frontiers | Research Topics

Advances in fluid-solid coupling processes between fractures and porous rocks: Experimental and numerical investigation

Edited by
Shiming Wei, Peng Tan, Xiang Rao, Yang Xia, Meng Meng,
Yuhan Huang and Bamidele Victor Ayodele

Published in
Frontiers in Earth Science
Frontiers in Environmental Science

ISSN 1664-8714
ISBN 978-2-8325-4165-4
DOI 10.3389/978-2-8325-4165-4

About Frontiers

Frontiers is more than just an open access publisher of scholarly articles: it is a pioneering approach to the world of academia, radically improving the way scholarly research is managed. The grand vision of Frontiers is a world where all people have an equal opportunity to seek, share and generate knowledge. Frontiers provides immediate and permanent online open access to all its publications, but this alone is not enough to realize our grand goals.

Frontiers journal series

The Frontiers journal series is a multi-tier and interdisciplinary set of open-access, online journals, promising a paradigm shift from the current review, selection and dissemination processes in academic publishing. All Frontiers journals are driven by researchers for researchers; therefore, they constitute a service to the scholarly community. At the same time, the *Frontiers journal series* operates on a revolutionary invention, the tiered publishing system, initially addressing specific communities of scholars, and gradually climbing up to broader public understanding, thus serving the interests of the lay society, too.

Dedication to quality

Each Frontiers article is a landmark of the highest quality, thanks to genuinely collaborative interactions between authors and review editors, who include some of the world's best academicians. Research must be certified by peers before entering a stream of knowledge that may eventually reach the public - and shape society; therefore, Frontiers only applies the most rigorous and unbiased reviews. Frontiers revolutionizes research publishing by freely delivering the most outstanding research, evaluated with no bias from both the academic and social point of view. By applying the most advanced information technologies, Frontiers is catapulting scholarly publishing into a new generation.

What are Frontiers Research Topics?

Frontiers Research Topics are very popular trademarks of the *Frontiers journals series*: they are collections of at least ten articles, all centered on a particular subject. With their unique mix of varied contributions from Original Research to Review Articles, Frontiers Research Topics unify the most influential researchers, the latest key findings and historical advances in a hot research area.

Find out more on how to host your own Frontiers Research Topic or contribute to one as an author by contacting the Frontiers editorial office: frontiersin.org/about/contact

Advances in fluid-solid coupling processes between fractures and porous rocks: Experimental and numerical investigation

Topic editors

Shiming Wei — China University of Petroleum, Beijing, China
Peng Tan — CNPC Engineering Technology R & D Company Limited, China
Xiang Rao — Yangtze University, China
Yang Xia — China University of Petroleum, China
Meng Meng — Los Alamos National Laboratory (DOE), United States
Yuhan Huang — University of Technology Sydney, Australia
Bamidele Victor Ayodele — University of Technology Petronas, Malaysia

Citation

Wei, S., Tan, P., Rao, X., Xia, Y., Meng, M., Huang, Y., Ayodele, B. V., eds. (2023). *Advances in fluid-solid coupling processes between fractures and porous rocks: Experimental and numerical investigation*. Lausanne: Frontiers Media SA. doi: 10.3389/978-2-8325-4165-4

Table of contents

frontiers | Frontiers in Earth Science

TYPE Original Research
PUBLISHED 20 January 2023
DOI 10.3389/feart.2023.1123620

OPEN ACCESS

EDITED BY
Shiming Wei,
China University of Petroleum, Beijing, China

REVIEWED BY
Kaixuan Qiu,
Jiangmen Laboratory of Carbon Science and Technology, China
Can Shi,
China University of Petroleum, China

*CORRESPONDENCE
Chuchu Cai,
842697979@qq.com

SPECIALTY SECTION
This article was submitted to Environmental Informatics and Remote Sensing, a section of the journal Frontiers in Earth Science

RECEIVED 14 December 2022
ACCEPTED 09 January 2023
PUBLISHED 20 January 2023

CITATION
Wang J, Cai C, Fu P, Deng S and Tang Z (2023), Study on simulation of cement plug—formation interface stripping failure and main influencing factors.
Front. Earth Sci. 11:1123620.
doi: 10.3389/feart.2023.1123620

Study on simulation of cement plug—formation interface stripping failure and main influencing factors

Jiangshuai Wang[1], Chuchu Cai[1]*, Pan Fu[2,3], Song Deng[1] and Zheng Tang[1]

[1]School of Petroleum and Natural Gas Engineering, Changzhou University, Changzhou, China, [2]CNPC Research Institute of Engineering Technology Co., Ltd., Beijing, China, [3]National Engineering Research Center for Oil and Gas Drilling and Completion Technology, Beijing, China

Among the existing gas storage facilities, salt cavern gas storage has the advantages of high injection production efficiency, low gas cushion volume, safety, flexibility, etc. It is of great significance to speed up the construction of underground gas storage by transforming abandoned salt caverns of salt industry into underground gas storage. However, old salt cavern wells cannot be directly converted into gas storage injection and production wells, so the old wellbore must be plugged to ensure the effectiveness of plugging. Therefore, a set of plugging optimization technology for salt cavern gas storage wells is urgently needed. In this paper, a 3D finite element model of the cement plug-formation system based on cohesive element method is established for the milling and plugging of the old well in the salt cavern gas storage section. The results show that under the condition of constant gas storage pressure, a certain degree of small deformation will occur at the bottom of the cement plug after compression, resulting in the shear direction deformation of the cement plug formation cementation interface, and peeling will occur after accumulation to a certain extent. With the increase of simulation time, the length of stripping section gradually increases and tends to be stable, and reaches the limit of stripping failure length. In the process of research, the factors and laws affecting the stripping failure length were also analyzed. It was found that the stripping failure length of cement plug formation cementation interface was related to the maximum operating pressure of gas storage, cement plug length, cement plug diameter, elastic modulus, Poisson's ratio and other factors. The research results are helpful to judge whether the milling and plugging length of the old well section is sufficient, and provide theoretical guidance for ensuring the long-term safe operation of the gas storage.

KEYWORDS

salt cavern gas storage, stripping failure length, cohesive element method, integrity of seal, cement plug-formation interface

1 Introduction

China's natural gas demand is increasing year by year, and the contradiction between supply and demand is becoming increasingly prominent. The construction of the gas storage is a key task for the development of China's natural gas industry (Shi et al., 2017; Dong et al., 2021). Salt cavern gas storage is considered the safest way to store large quantities of hydrocarbons. The transformation of abandoned salt caverns from salt-production industries into Underground Gas Storages (UGS) has a great significance for the full utilization of salt mine resources and accelerating the construction of UGS (Bai S et al., 2022). Among the existing storage facilities, salt cavern underground gas storage has greater

advantages with the characteristics of high injection-production efficiency, low cushion gas, volume, safety, and flexibility (Pamucar et al., 2020; Pinto et al., 2021). It is much safer in terms of safety and environmental protection: salt rock has extremely low permeability and better damage resistance and self-healing ability, which is a sealing material to ensure energy storage (Bérest and Brouard, 2003; Cornet et al., 2018). Although salt cavern reservoir has obvious advantages in energy storage, its complex geological conditions, lack of practical experience and imperfect theoretical system pose a great challenge to the sealing ability of salt cavern gas storage. There have been gas leaks due to the failure of the gas storage seal. Casing damage and cap fracture are the main causes of these accidents (Sovacool, 2008; Jing et al., 2011).

Due to the poor cementing quality of cap wells in some old gas storage wells, in the sealing of abandoned gas storage wells, it is necessary to section mill the casing in the section with poor cap cementing quality and then permanently seal the well in order to ensure the sealing quality of cap sealing and prevent gas from flowing out from casing and cementing cement ring to damage the sealing property of the reservoir. As the operation of gas storage is different from that of other operation wells, the reasons for the sealing integrity of old wells are also different. Ensuring borehole sealing is the basic premise of developing dissolved salt cavern. The key is casing/formation bonding and the integrity of the intermediate casing string (Benge, 2009; De Simone et al., 2017; Kiran et al., 2017). As a result, factors affecting well sealing include casing integrity, formation sealing, and the quality of cementation between casing and formation. The long-term integrity of the cemented surface of the cement plug is directly related to the risk of CO_2 leakage (Dian et al., 2022).

Generally, there is no macroscopic crack inside the cement plug of abandoned well, and the main failure mode is interface stripping (Akgün and Daemen, 1999). Several researchers have developed models to simulate cement interface debonding based on simplified models such as linear elastic casing, cement and rock, and initially complete cement rings. To determine borehole sealing performance, Bosma et al. (1999) used a non-linear material model, which can analyze the loss of sealing capacity due to cement cracking and or plastic deformation. For the casing-cement interface and cement-rock interface, a discrete crack description is used to simulate interface debonding, which is possible to analyze the phenomenon of micro-annulus at the interface due to disadhesion. Fleckenstein et al. (2001) used a 2D stress-distribution model to study the effects of cement slurry characteristics and formation confining stress on casing stress, and introduced the finite element results of casing resistance to implosion pressure under different conditions. This will contribute to a better understanding of casing stress conditions under blasting loads. Fourmaintraux et al. (2005) mainly studied the model of solid phase cement ring and used SRC method to evaluate the impact of production operations on the integrity of cement ring. Gray et al. (2009) established a framework for non-linear 3D wellbore analysis under various conditions, proposed and discussed in detail the phased finite element method, observed wellbore component behavior over the life of the well, and discussed the possibility of zonal isolation failure due to casing/cement interface debonding and material failure. Qiu and Li, 2018 take the microfracture into account and derive an approximate analytical solution to the triple-porosity model in the real-time space. Asala and Gupta (2019) used the modeling method of cross-section fluid driven interface debonding of the plugging system

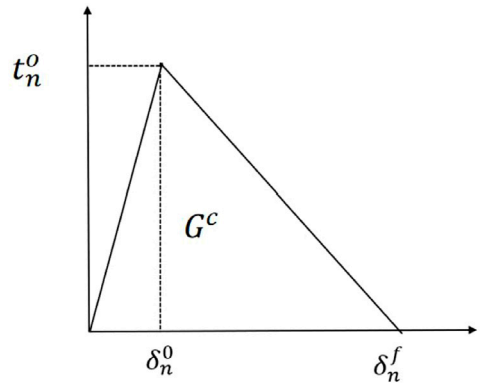

FIGURE 1
Typical traction—separation constitutive law.

and established a 2D semicircular bending (SCB) test model for two-material samples consisting of rock-cement, cement-casing and bush-plug interfaces. Lu et al. (2020) developed an adaptive model that couples multi-continuum matrix and discrete fractures, which is then validated to simulate hydromechanical coupling processes in fractured-shale reservoirs during the production period.

Through previous studies, it can be found that most of these problems revolve around sealing integrity failure of cement ring—formation interface, but there is a lack of relevant research on damage simulation of cement plug—formation interface during milling and plugging of old wells in salt caverns gas storage section. Using 2D models for well integrity analysis can lead to vague and often mislead conclusions about the behavior of near-wellbore rock, cement, and casing (Wang and Taleghani, 2014). The use of 3D symmetry models may be applicable on a case-by-case basis. Therefore, in order to properly study azimuth interface debonding, a complete 3D model is necessary. Besides, cohesive element method can accurately simulate crack propagation. Therefore, a 3D finite element model of the cement plug-formation system based on cohesive element method is proposed in this paper. The model can reflect the fracture growth pattern in the process of cement plug formation interface cementation failure, and quantitatively analyze its influencing factors. The cohesive failure behavior was simulated by inserting cohesive elements. The stripping failure law of cement plug—formation interface under constant pressure and dynamic pressure and the main controlling factors affecting the stripping failure were studied.

2 Cohesive element method

2.1 Sample description

Many scholars at home and abroad have applied cohesive unit method to research on hydraulic fracturing, CO_2 injection and fracture leakage, and it is proved that cohesive unit method can accurately simulate fracture propagation. Yao et al. (2010) established a 3D pore pressure cohesive layer model and applied the model to study the influence of different fracture and injection parameters on fracture geometry. Feng et al. (2017) established a 3D numerical simulation model of fluid driven debonding fractures using the coupled pore-pressure cohesive zone method. The effectiveness of

the proposed method is verified by replicating the experimental results of interface debonding in literature. The 3D model can be used to quantify the propagation pressure of debonding fractures in vertical wells. He and Arson. (2022) established a 2D cohesive zone model (CZM) coupled with a continuous damage mechanics model (CDM). The model can simulate diffusion damage and local fracture, and smooth the transfer of field variables between finite and cohesive elements.

2.2 The basic equations

Based on the tractor-separation constitutive law, the opening and extension of the fracture are modeled as the damage evolution between two initial bonding interfaces with zero interface thickness. The constitutive law consists of three parts: initial loading behavior (before damage), damage initiation and interface damage evolution (Feng et al., 2017). Figure 1 shows a typical traction—separation constitutive law. t^o and G^c are the critical strength and critical fracture energy of the cohesive interface; the subscripts n represent the corresponding parameters at the normal shear directions.

$$\mathrm{T} = \begin{Bmatrix} t_n \\ t_s \\ t_t \end{Bmatrix} = k\delta = \begin{pmatrix} k_{nn} & 0 & 0 \\ 0 & k_{ss} & 0 \\ 0 & 0 & k_{tt} \end{pmatrix} \begin{bmatrix} \delta_n \\ \delta_s \\ \delta_t \end{bmatrix}, \tag{1}$$

where t_n, t_s, and t_t are the maximum tractions on the interface in the normal, the first shear, and the second shear directions respectively; k_{nn}, k_{ss}, and k_{tt} are the initial cohesive stiffness on the interface in the normal, the first shear, and the second shear directions respectively; δ_n, δ_s, and δ_t are the separation on the interface in the normal, the first shear, and the second shear directions respectively.

According to Eq. 2, when the quadratic interaction function involving the contact stress ratio is equal to 1, damage occurs along the cohesive interface.

$$\left[\frac{t_n}{t_n^m}\right]^2 + \left[\frac{t_s}{t_s^m}\right]^2 + \left[\frac{t_t}{t_t^m}\right]^2 = 1, \tag{2}$$

Where t_n^m is the maximum nominal stress value for normal-only deformations, while t_s^m and t_t^m represent maximum nominal stress values for purely first or second shear direction deformations. The criterion considers the relationship between stresses in different directions.

The damage evolution of cohesion unit refers to the subsequent mechanical property degradation process after the initial damage of the unit. It is generally believed that cohesion unit has two evolution types, namely displacement damage evolution and energy damage evolution. Bilinear degradation mode in energy damage evolution is adopted in this paper. For energy-based damage evolution, the parameter describing the damage behavior of cohesion units is the fracture energy release rate. For bilinear degradation mode, the fracture energy release rate is defined as:

$$W_c = \frac{1}{2} t_s^m \delta_s^m, \tag{3}$$

Where, W_c is the release rate of fracture energy of the element, the area enclosed by the stress-displacement curve, J/m^2.

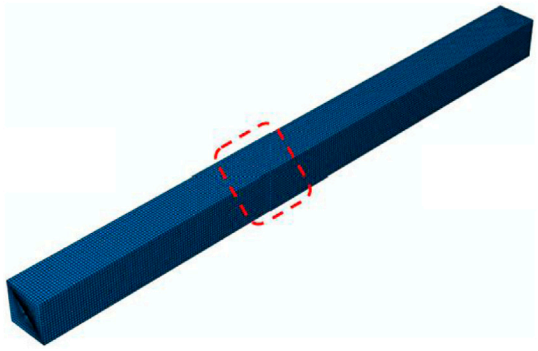

FIGURE 2
Overall finite element model grid diagram.

3 Finite element model building

3.1 Model establishment

Using Abaqus finite element software to establish the three-dimensional geometric model of cement plug formation interface as shown in Figure 2. Cement plug diameter 290 mm, overall 3D model size is 2 m × 2 m × 40 m.

In order to simulate the failure condition of cement stop-formation interface, the numerical model established in this paper adopts the cohesive contact theory and takes the secondary nominal stress criterion as the criterion to judge the damage. In the model, it is assumed that the cement plug and stratum are elastic-plastic porous materials, and the elastic properties and bonding interface properties of the materials are shown in Table 1.

If the bottom of the cement plug is poorly bonded to the formation, the cement plug—formation interface will appear micro-cracks, namely the existence of initial defects. A cohesive unit was inserted between the cement plug and the formation, and the initial break unit (the initial defect) was located at the bottom of the plug-casing interface. Structured grid and transition grid were used to discretize the model to improve the calculation accuracy (Figure 3).

Aiming at accurate calculation, a cohesive unit is inserted between the cement plug and formation interface, and a numerical damage model is established, which consists of three parts: the cement plug, the formation and the crack surface. The failure simulation of cement plug—formation interface bond under formation confining pressure and gas storage pressure is fully considered. The schematic diagram of the gas reservoir pressure on the cement plug-formation interface is shown in Figure 4.

The model restricts the rotational degrees of freedom of the three surfaces of xyz, that is, the translational displacement of the three surfaces in the direction of the outer normal and the rotational displacement around the direction of the outer normal. The specific boundary condition settings are shown in Figure 5. In the whole simulation process, the ground stress of xyz surface is 23, 23 and 2.58 Mpa respectively, and the pressure at the bottom of the cement plug is constant 20 Mpa.

TABLE 1 Setting of model parameters.

Material	Cement plug	Formation	Surface of bonding
Elasticity modulus/GPa	10	2	200
Poisson ratio	0.15	0.2	—
Shear bonding strength/Mpa	—	—	4.05
Tensile bonding strength/Mpa	—	—	1.71

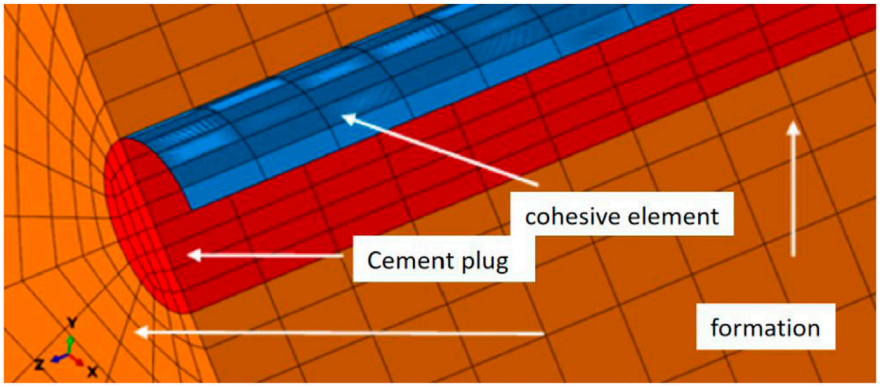

FIGURE 3
Grid diagram of the bottom of the finite element model.

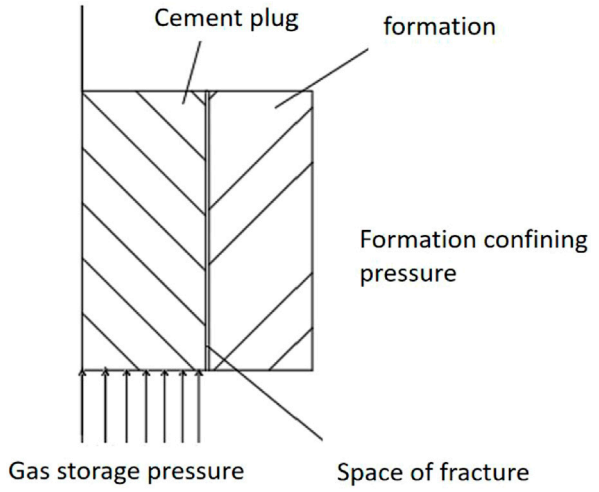

FIGURE 4
Schematic diagram of cement plug-formation interface subjected to gas storage pressure.

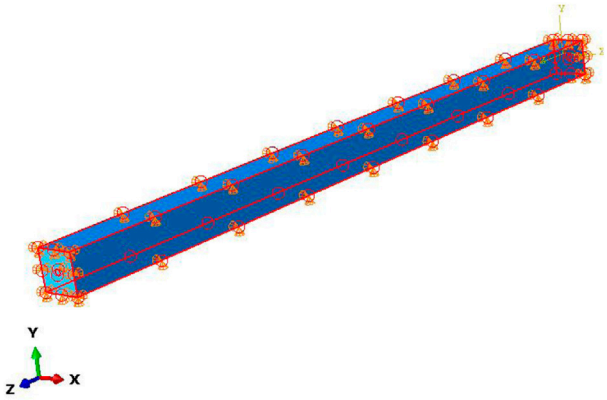

FIGURE 5
Boundary conditions of 3D finite element model.

3.2 Model verification

3.2.1 Bois model

Loizzo et al. (2015) described three basic requirements for an effective CMI simulator, namely: 1) the ability to evaluate the initial state of stress after cement sets; 2) The ability to estimate the position of cement design in the safe working envelope and the degree of approximation to the envelope limit; 3) The stiffness and failure behavior of all materials can be simulated to correctly locate the failure criterion limit. Bois et al. (2019) developed a model to simulate the mechanical and hydraulic integrity of a cement plug after cement setting, and simulated the micro-annulus generated by cement plug—formation interface stripping to understand how to prevent cement plug damage in the short and long term.

Modeling the cement plug-formation interface stripping process between 728 and 978 m in the vertical open hole shows that the most

TABLE 2 Comparison between numerical model and Bois model to calculate micro-ring gap size.

Well depth/mm	728	738	748	758	768	778
Bois model	0.563	0.555	0.553	0.538	0.532	0.527
Finite element model	0.552	0.542	0.537	0.510	0.509	0.507
D-value	0.011	0.013	0.016	0.028	0.023	0.020

important risk of damage to the integrity of the cement plug is the creation of micro-annulus in the cement plug/wellbore view, and shows the geometry of the micro-annulus after hydration at the cement plug-wellbore interface. This study mainly focused on qualitative analysis, and did not specifically describe the interface stripping process, nor did it conduct a quantitative analysis of its influencing factors.

3.2.2 Bois model vs. finite element model

In this section, the parameters of Axel Pierre Bois et al.'s (2019) cement plug case study are selected, as shown in Table 2. Bois model and finite element model are respectively used to simulate the cement plug formation interface peeling process of 728–778 m open hole, and the change of micro ring size with depth is compared. In this case, the hole has a diameter of 0.216 m, and the formation has Young's modulus and Poisson's ratio values of 5 GPa and 0.20 respectively. The cement is a 1.95-g/cm^3 API Class G cement system with Young's modulus and Poisson's ratio values of 10 GPa and 0.14. The applied WHP during the pressure test is 10 MPa.

As shown in Table 2, the maximum difference between the microannulus calculated by the finite element simulation and Bois model is 0.028 mm, and the maximum deviation is 5.12%, indicating that the established finite element model is basically reliable and can accurately simulate the cement stop-formation interface stripping.

3.3 Analysis of model results

According to the section milling hole size of a well in Jintan gas storage, Jiangsu Province, a 3D model of 290 mm × 40 m cement plug-formation system was established, and a cohesive unit was inserted to simulate the detachment failure of the cement plug-formation interface under constant pressure. The simulation results of the

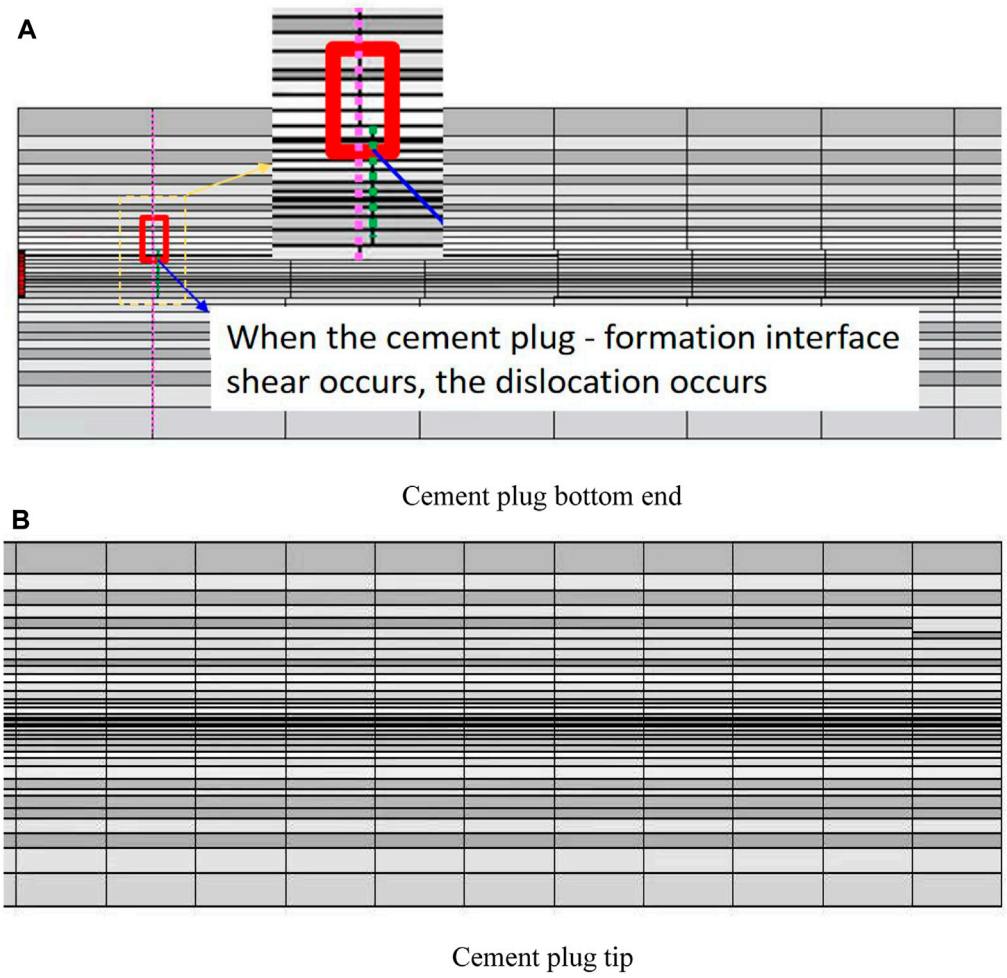

FIGURE 6
Schematic diagram of relative position after shear failure of cement plug-formation interface. **(A)** The simulation diagram of the relative position of the bottom of the cement plug after the shear failure of the cement plug-formation interface. **(B)** The simulation diagram of the relative position of the top of the cement plug after the shear failure of the cement plug-formation interface.

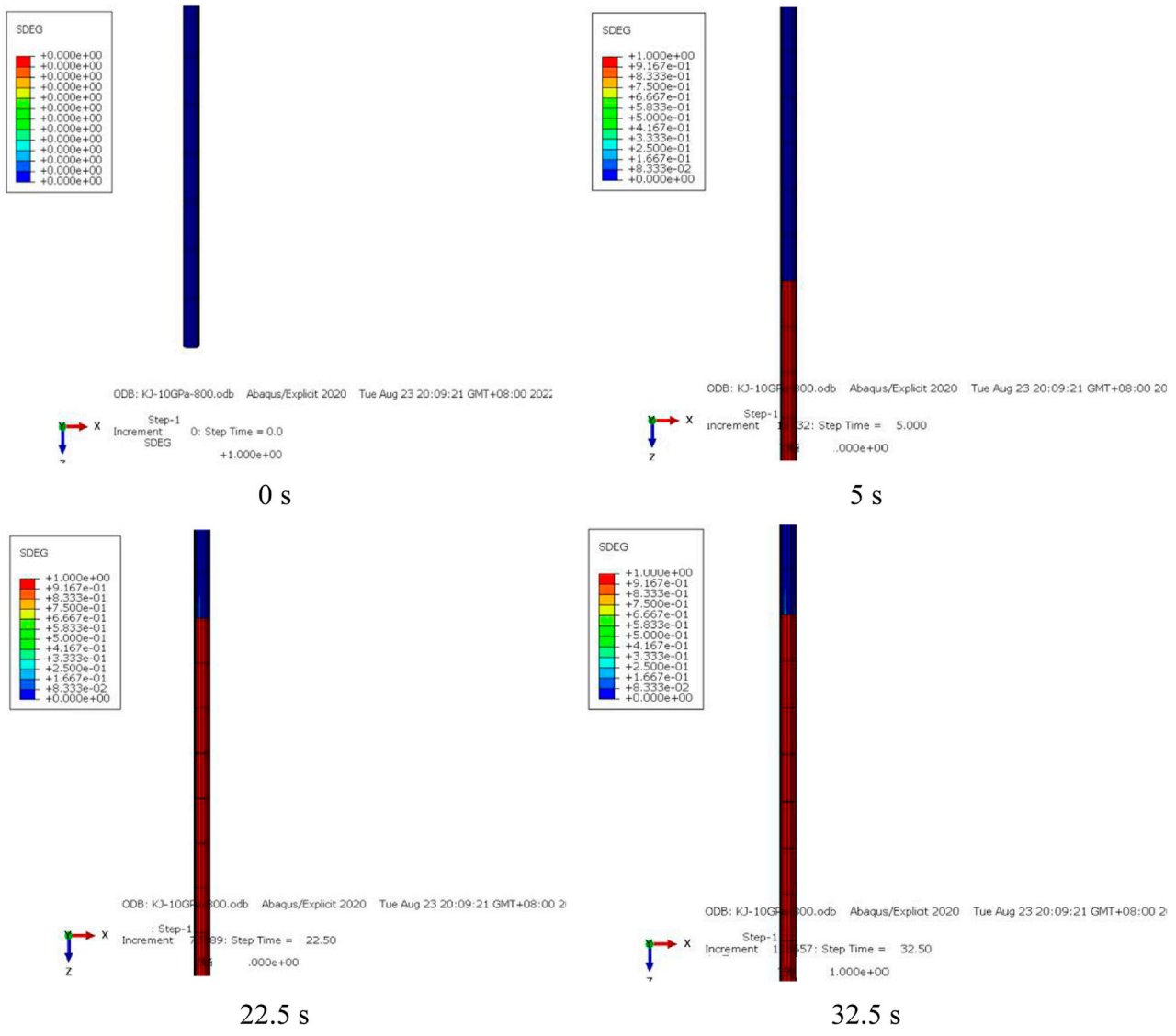

FIGURE 7
Stripping failure length vs. time.

relative positions of the cement plug-formation interface after shear failure are shown in Figure 6.

As shown in Figures 6A, the grid at the bottom of the cement plug is dislocated, which is because the cement plug is subjected to the gas storage pressure and causes cumulative deformation. With the increase of simulation time, the cement plug and the formation cementation surface will be sheared and dislocated along the borehole direction, resulting in the phenomenon of cement plug stripping. However, the stripping failure did not spread to the entire bonding surface (no longitudinal dislocation along the borehole occurred at the top of the cement plug in Figure 6B).

The length of cement stop-formation interface stripping failure over time is shown below.

As shown in Figure 7, according to the stiffness degradation coefficient SDEG of cement sheath interface, the failure of cement sheath interface is judged. When the cohesive damage parameter SDEG of the cement plug formation interface reaches 1, it indicates that the interface has been stripped at this time; 0 means

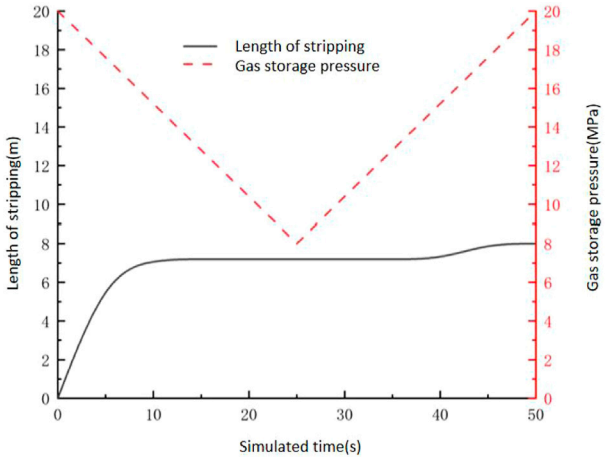

FIGURE 8
Stripping failure length vs. pressure.

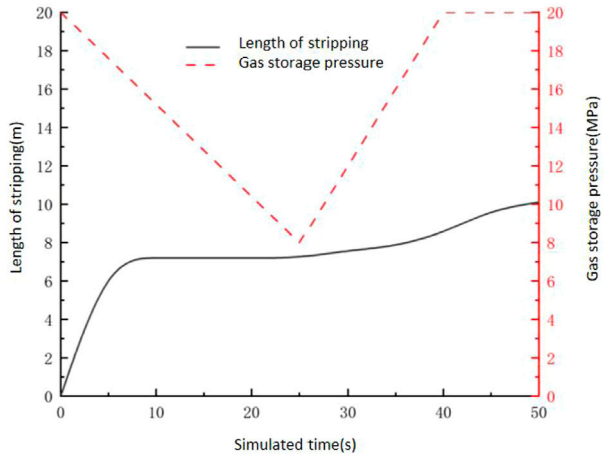

FIGURE 9
Stripping failure length vs. pressure.

no damage has occurred. The blue part represents the cement plug segment without stripping failure at the cement plug-formation interface, and the red part represents the cement plug segment with stripping failure. In the initial state (0 s), the cement plug did not undergo any deformation and was in a normal state without any peeling phenomenon. With the increase of the simulation time, the cement plug was subjected to the pressure of the gas reservoir at the bottom to produce a small deformation. When the simulation time reached 5 s, the cement plug was stripped, and the length of the red strip was 15.7 m. When the simulation time reached 22.5 s, the peel length of cement plug reaches 18.4 m, and when the simulation time reached 32.5 s, the peel length always stays at about 18.4 m, indicating that the ultimate peel length has been reached at this time.

In conclusion, under the constant pressure of 20 MPa, the cement plug—formation interface will have stripping failure, and there is a limit stripping failure length. When the cement plug is subjected to the bottom pressure, a certain degree of small deformation occurs, resulting in the shear direction deformation of the cement-plug interface. With the increase of simulation time, the length of the stripping segment gradually increased and tended to be stable, and the ultimate stripping failure length was 18.4 m. The model can determine the effective cementing length of cement plug for milling and plugging old wells in gas storage section. Effective cementation length is equal to section milling and plugging length (40 m) minus ultimate stripping length (18.4 m). Therefore, it is suggested that the length of cement plug in section milling should be greater than the ultimate stripping failure length, so as to ensure the safety and long-term effectiveness of plugging operation in the old wells.

4 Results and discussions

Since the 1960s, debonding of the cement/casing or cement/rock interface has been identified as a cause of wellbore leaks (Carter and Evans, 1964). The debonding of cementing-interface is mainly caused by the displacement difference between casing, cement ring and formation during perforation (Yan et al., 2020). This interface debonding may be caused by pressure and temperature changes and cement shrinkage during drilling operations (Lecampion et al., 2013). The degradation of cement strength has a significant influence on the occurrence of failure (debonding, radial crack, and disc) (Zhang et al., 2021). On the basis of previous researches, a 3D finite element model of the cement plug-formation system based on the cohesive

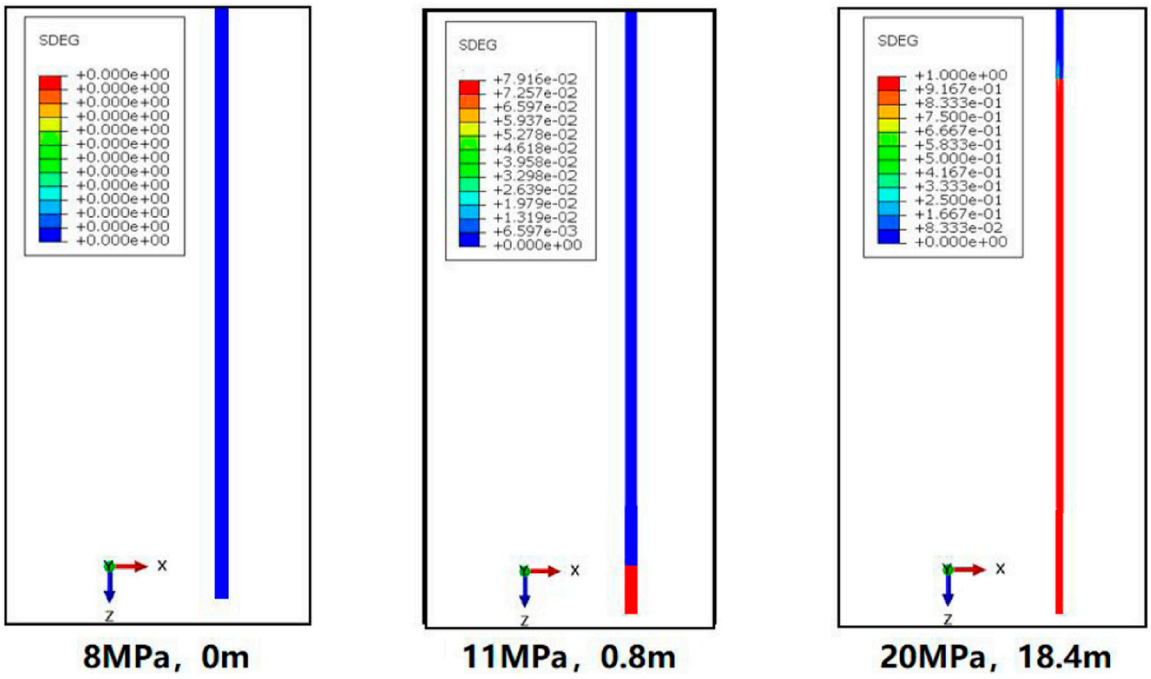

FIGURE 10
The stripping length varies with the gas storage pressure.

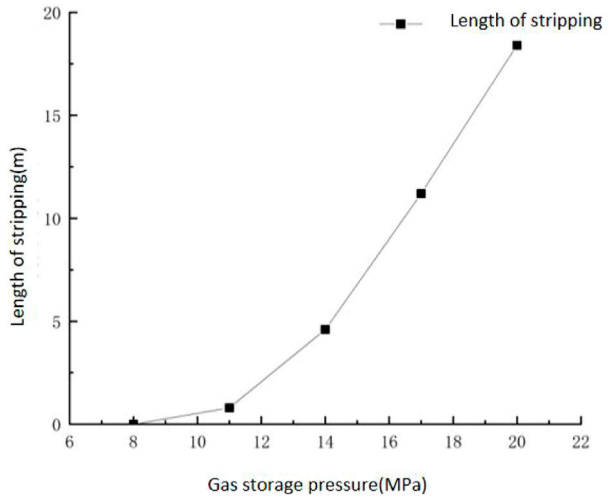

FIGURE 11
The stripping length varies with the gas storage pressure.

element method is used in this chapter to analyze the factors affecting the stripping failure length of the cement plug-formation interface.

4.1 Failure law of stripping under dynamic pressure

Lecampion et al. (2013) investigated what controls the propagation of this interfacial fluid disbonding at constant pressure injection conditions below the formation fracturing pressure. The aim is understanding the effects of this fluid-driven micro-annulus debonding in a CO_2 storage environment. This section mainly studies the peeling failure law of cement plug - formation interface under the dynamic change of the gas storage pressure.

The pressure of the gas storage tank will change dynamically during operation. As can be seen from Figures 8, 9, rapid stripping will occur at the cement stop-formation interface under higher pressure, and the stripping speed will slow down when the pressure decreases, and the stripping length will further increase when the pressure increases.

By comparing Figures 7, 8, it can be seen that the peel failure length (8 m) under pressure is smaller than that under constant pressure (18.4 m).

In Figure 8, the gas storage pressure first decreases to 8 MPa with the simulation time, increases after 25 s, and gradually increases to 20 MPa. After the simulation time (50 s) is over, the stripping failure length is 8 m. In Figure 9, the gas storage pressure decreases to 8 MPa with the simulation time at first, then increases to 20 MPa gradually after 25 s, and then becomes stable after 40 s. After the simulation time (50 s) is over, the stripping failure length is 10 m. The failure length (10 m) under decrease-augment-stable condition is greater than that under decrease-augmentation condition (8 m).

The dynamic change mode of the gas storage pressure during operation can be optimized and adjusted according to the needs.

4.2 Stripping main control factors of failure

4.2.1 Operating pressure

As shown in Figure 10, no stripping occurred at the cement-stop-formation bonding interface when the gas reservoir pressure was low (8 MPa). When the pressure reached about 11 Mpa, the interface began to peel (0.8 m) and rapidly increased. When it increased to 20 MPa, the stripping failure length reached the limit value (18.4 m). The cement plug - formation interface did not peel and fail under

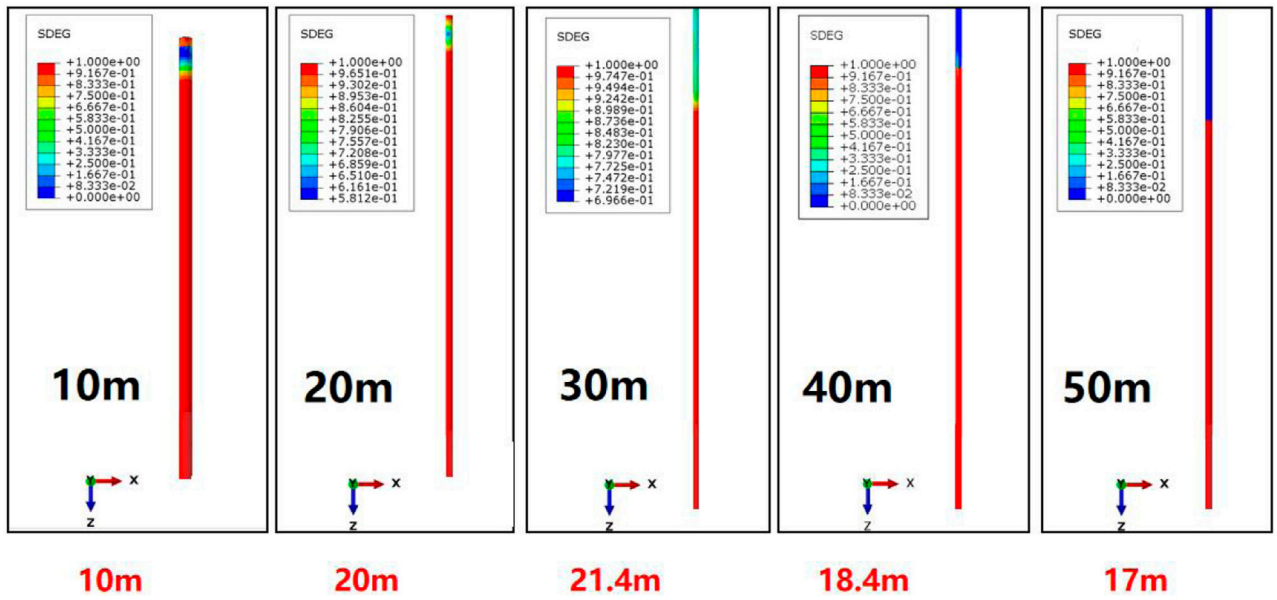

FIGURE 12
The stripping length varies with the length of the cement plug.

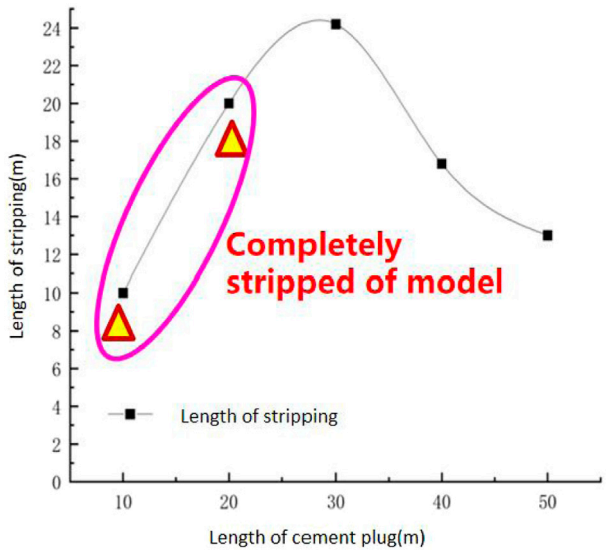

FIGURE 13
Line diagram of strip length changing with cement plug length.

lower pressure conditions because the gas reservoir pressure did not reach the failure strength of the bond surface.

It can be clearly seen from Figure 11 that the stripping failure length increases with the increase of gas storage pressure.

It can be concluded that reducing the maximum operating pressure of gas storage is beneficial to ensure the safe and long-term operation of gas storage.

4.2.2 Length of cement plug

As can be seen from Figure 12, under the same gas storage pressure, complete stripping will occur at the end of simulation when the length of cement plug is 10 and 20 m. When the cement plug length is 30 m, the stripping failure length is 21.4 m. When the cement plug length is 40 m, the stripping failure length is 18.4 m. When the length of cement plug is 50 m, the stripping failure length is 17 m. The change curve of the peeling failure length of the cement plug-formation interface with the length of the cement plug is shown in Figure 13.

In summary, the peel length of cement stop-formation interface decreases with the increase of cement stopper length, because the longer the cement stopper length is, the larger the equivalent cementing area is, and the smaller the peel failure length is under the same gas storage pressure. Therefore, the length of cement plug should not be too short during the section milling operation. According to different underground engineering geological conditions, it is suggested to optimize the length of section milling plugging operation, reduce the engineering operation cost as much as possible and shorten the construction cycle of gas storage.

4.2.3 Diameter of cement plug

As can be seen from Figure 14, when the diameter of cement plug is 118.6 mm, the cement plug does not peel. When the diameter of the cement plug is 157.1 mm, the stripping starts to occur and the stripping length of the cement plug is 8 m. When the cement plug diameter is 220.5 mm, the cement plug stripping length increases to 12 m. When the diameter of cement plug is 290 mm, the stripping length of cement plug reaches the ultimate stripping length of 18.4 m.

In conclusion, the peel length of cement stop-formation bond interface will increase with the increase of cement plug diameter. This is because the larger the diameter of cement plug is, the greater the equivalent thrust acting on the bottom of cement plug under the same gas storage pressure, resulting in the increase of the peel length. Therefore, when the hole size is small, the length of the section milling plug can be reduced appropriately.

4.2.4 Elastic modulus, Poisson's ratio

Boukhelifa et al. (2004) conducted large-scale annulus seal tests that showed that cement mechanical properties (such as elasticity, strength, and expansion) and rock properties were key parameters for maintaining the integrity of the cement ring over the life of the well.

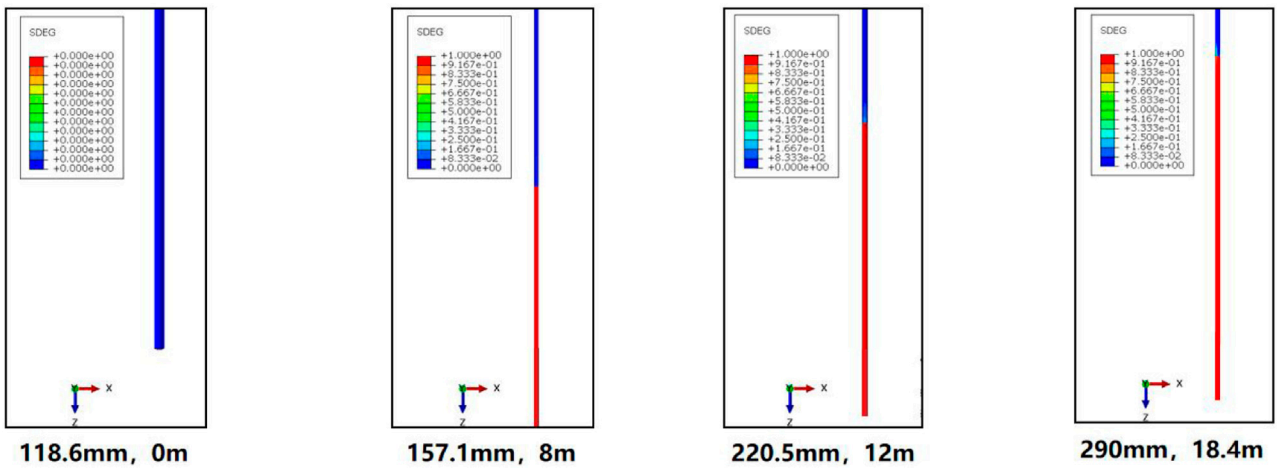

FIGURE 14
The strip length varies with the cement plug diameter.

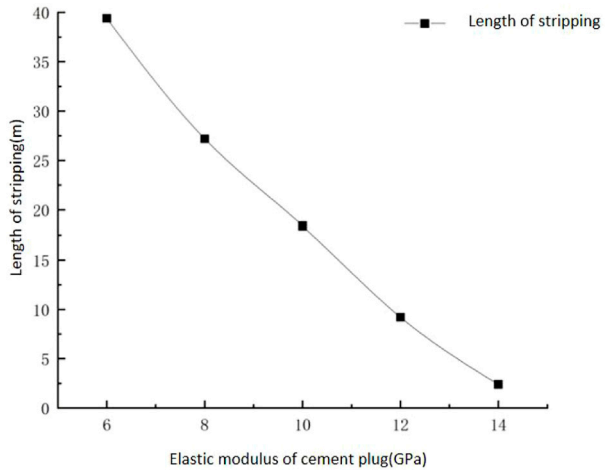

FIGURE 15
Influence of elastic modulus of cement plug on stripping length.

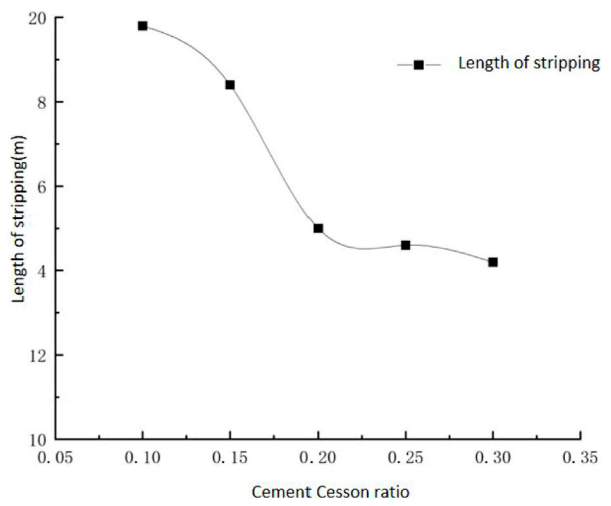

FIGURE 16
Influence of cement Poisson's ratio on the length of stripping.

However, the relationship between specific properties (such as elastic modulus, Poisson's ratio) and the length of cement plug stripping failure was not simulated. Therefore, this section mainly focuses on the influence of elastic modulus and Poisson's ratio of cement plug on stripping failure length.

As can be seen from Figure 15, with the increase of elastic modulus of cement plug, the peel failure length of cement plug-casing interface gradually decreases. When the elastic modulus increases from 6 GPa to 14 GPa, the stripping failure length decreases from 39.4 m to 2.4 m, which indicates that the elastic modulus of cement plug has a great influence on the crack stripping failure of cement plug-casing interface. This is because with the increase of elastic modulus, the deformation of cement plug becomes smaller, leading to the decrease of cumulative fracture energy. As a result, the use of a higher elastic modulus cement plug in well abandonment operations can improve the integrity of the cement-casing interface.

As can be seen from Figure 16, with the increase of cement Poisson's ratio, the peel failure length of cement plug-casing interface gradually decreases. When Poisson's ratio increases from 0.1 to 0.3, the stripping failure length decreases from 19.8 to 14.2 m, indicating that the cement plug Poisson's ratio has an effect on the cement-casing interface, but the effect is not as obvious as the elastic modulus of cement plug. The separation failure length of cement plug-casing interface will change with the change of Poisson's ratio, because the increase of Poisson's ratio will increase the transverse deformation of cement plug and lead to the increase of slip friction. As a result, high Poisson's ratio is more friendly to seal integrity at the cement stop-casing interface.

5 Conclusion

A total of 25 sets of simulation studies on cement stop-formation interface stripping failure under different cement plug lengths, diameters, gas storage pressure, pressure change modes and cement plug performance were carried out. The interface stripping failure rule under constant/dynamic pressure conditions was defined, the influence rule of different factors on stripping failure length was revealed, and the calculation method of effective cement plug bonding length for milling and plugging old wells in gas storage section was determined. Some meaningful conclusions are presented as follows.

(1) A 3D finite element model of the cement plug-formation system based on Cohesive element method in this research can accurately simulate the cement plug-formation interface bonding failure process, which is helpful to judge whether the milling and plugging length of the old well section is sufficient, and provide theoretical guidance for ensuring the long-term and safe operation of gas storage.
(2) Under the condition of constant pressure in gas storage tank, the bottom of cement plug will undergo a certain degree of minor deformation after compression, resulting in shear deformation of cement-stopper cement-formation bond interface. When accumulated to a certain degree, the cement-stopper cement-formation bond interface will be stripped. The stripping failure length increases gradually with time, and finally tends to be stable, reaching the ultimate stripping failure length.
(3) The ultimate peel length under dynamic pressure is smaller than that under constant pressure, and the peel length under "decrease-augmentation—stabilization" is larger than that under "decrease-augmentation."
(4) The operating pressure, cement plug length, cement plug diameter, elastic modulus of cement plug, Poisson's ratio and other factors of gas storage will also affect the stripping length of cement plug formation cementation interface. Therefore, it is recommended to use a cement slurry system with high elastic modulus and high Poisson's ratio, appropriately reduce the length of forging and milling plugging, reduce the maximum operating pressure of the gas storage, and optimize and adjust the dynamic change mode of the gas storage pressure during operation to reduce the length of interface failure and ensure the safe and long-term operation of the gas storage.

Data availability statement

The original contributions presented in the study are included in the article/supplementary material, further inquiries can be directed to the corresponding author.

Author contributions

JW: Conceptualization, Methodology, Writing—Review and Editing. CC: Software, Writing—Original Draft. PF: Resources, Formal analysis, Data Curation. SD: Project administration, Supervision. ZT: Investigation, Validation.

Funding

This research is supported by the Project of China National Petroleum Corporation (CNPC) (2021DJ5402), the Research Foundation of Changzhou University (ZMF22020060), and the Basic Science (Natural Science) Research Project of Jiangsu Higher Education (22KJD430001).

Conflict of interest

Author PF was employed by CNPC Research Institute of Engineering Technology Co., Ltd.

The remaining authors declare that the research was conducted in the absence of any commercial or financial relationships that could be construed as a potential conflict of interest.

Publisher's note

References

Akgün, H., and Daemen, J. J. (1999). Design implications of analytical and laboratory studies of permanent abandonment plugs. *Can. Geotechnical J.* 36 (1), 21–38. doi:10.1139/t98-089

Asala, H. I., and Gupta, I. (2019). "Numerical modeling aspects of fluid-driven interface debonding after wellbore plugging and abandonment," in *53rd US rock mechanics/geomechanics symposium* (OnePetro). New York, NY, USA.

Bai, S., Ding, G., Wanyan, Q., Li, K., and Li, H. (2022). "Feasibility study on transformation of abandoned salt caverns into underground gas storage in China," in *56th US rock mechanics/geomechanics symposium* (OnePetro). Santa Fe, New Mexico, USA.

Benge, G. (2009). Improving wellbore seal integrity in CO_2 injection wells. *Energy Procedia* 1 (1), 3523–3529. doi:10.2118/119267-MS

Bérest, P., and Brouard, B. (2003). Safety of salt caverns used for underground storage blow out; mechanical instability; seepage; cavern abandonment. *Oil Gas Sci. Technol.* 58 (3), 361–384.

Bois, A. P., Vu, M. H., Noël, K., Badalamenti, A., Delabroy, L., Therond, E., et al. (2019). Evaluating cement-plug mechanical and hydraulic integrity. *SPE Drill. Complet.* 34 (02), 92–102. doi:10.2118/191335-PA

Bosma, M., Ravi, K., van Driel, W., and Schreppers, G. J. (1999). "Design approach to sealant selection for the life of the well. Society of Petroleum Engineers," in Presented at the SPE annual technical conference and exhibition OnePetro (Houston, TX, USA: October 1999), 3–6. doi:10.2118/56536-MS

Boukhelifa, L., Moroni, N., James, S. G., Roy-Delage, L., Thiercelin, M. J., and Lemaire, G. (2004). "Evaluation of cement systems for oil and gas well zonal isolation in a full-scale annular geometry," in IADC/SPE drilling conference (OnePetro). Dallas, TX, USA. March, 2004. doi:10.2118/87195-MS

Carter, L. G., and Evans, G. W. (1964). A study of cement-pipe bonding. *J. Petroleum Technol.* 16 (02), 157–160. doi:10.2118/764-PA

Cornet, J. S., Dabrowski, M., and Schmid, D. W. (2018). Long term creep closure of salt cavities. *Int. J. Rock Mech. Min. Sci.* 103, 96–106. doi:10.1016/j.ijrmms.2018.01.025

De Simone, M., Pereira, F. L., and Roehl, D. M. (2017). Analytical methodology for wellbore integrity assessment considering casing-cementformation interaction. *Int. J. Rock Mech. Min. Sci.* 94, 112–122. doi:10.1016/j.ijrmms.2016.12.002

Dian, W., Jun, L., Xianbo, L., Tuo, L., Penglin, L., and Wei, L. (2022). Analysis of cement plug bonding surface integrity in CO_2 geological storage. In 56th US rock mechanics/geomechanics symposium. *OnePetro*. doi:10.56952/ARMA-2022-0213

Dong, J., Li, G., Liu, T., Li, J., and Zhang, Y. (2021). "Stability analysis of underground-gas-storage salt cavern based on similarity criterion," in *55th US rock mechanics/geomechanics symposium* (OnePetro). Richardson, TX, USA.

Feng, Y., Li, X., and Gray, K. E. (2017). Development of a 3D numerical model for quantifying fluid-driven interface debonding of an injector well. *Int. J. Greenh. Gas Control* 62, 76–90. doi:10.1016/j.ijggc.2017.04.008

Fleckenstein, W. W., Eustes, A. W., and Miller, M. G. (2001). Burst-induced stresses in cemented wellbores. *SPE Drill. Complet.* 16, 74–82. doi:10.2118/72059-PA

Fourmaintraux, D. M., Bois, A. P., and Fraboulet, B. (2005). "Efficient wellbore cement sheath design using the SRC (System Response Curve) method," in SPE europec/EAGE annual conference (OnePetro). Madrid, Spain, June 2005. doi:10.2118/94176-ms

Gray, K. E., Podnos, E., and Becker, E. (2009). Finite-element studies of near-wellbore region during cementing operations: Part I. *SPE Drill. Complet.* 24 (01), 127–136. doi:10.2118/106998-PA

He, H., and Arson, C. (2022). "Numerical implementation of a cohesive zone element coupled with continuum damage mechanics volume elements," in *56th US rock mechanics/geomechanics symposium*. OnePetro. Richardson, TX, USA. doi:10.56952/ARMA-2022-0324

Jing, W. J., Yang, C. H., and Chen, F. (2011). Risk assessment of salt cavern oil/gas storage based on accident statistical analysis. *Rock Soil Mech.* 32 (6), 1787–1793. doi:10.1631/jzus.B1000185

Kiran, R., Teodoriu, C., Dadmohammadi, Y., Nygaard, R., Wood, D., Mokhtari, M., et al. (2017). Identification and evaluation of well integrity and causes of failure of well integrity barriers (a review). *J. Nat. Gas. Sci. Eng.* 45, 511–526. doi:10.1016/j.jngse.2017.05.009

Lecampion, B., Bunger, A., Kear, J., and Quesada, D. (2013). Interface debonding driven by fluid injection in a cased and cemented wellbore: Modeling and experiments. *Int. J. Greenh. Gas. Control.* 18, 208–223. doi:10.1016/j.ijggc.2013.07.012

Loizzo, M., Bois, A. P., Etcheverry, P., and Lunn, M. G. (2015). An evidence-based approach to well-integrity risk management. *SPE Econ. Manag.* 7 (03), 100–111. doi:10.2118/170867-PA

Lu, Y. H., Wei, S. M., Xia, Y., and Jin, Y. (2020). Modeling of geomechanics and fluid flow in fractured shale reservoirs with deformable multi-continuum matrix. *J. Petroleum Sci. Eng.* 196, 107576. doi:10.1016/j.petrol.2020.107576

Pamucar, D., Deveci, M., Schitea, D., Eriskin, L., Iordache, M., and Iordache, I. (2020). Developing a novel fuzzy neutrosophic numbers based decision making analysis for prioritizing the energy storage technologies. *Int. J. Hydrog. Energy.* 45 (43), 23027–23047. doi:10.1016/j.ijhydene.2020.06.016

Pinto, J. S. R., Bachaud, P., Fargetton, T., Ferrando, N., Jeannin, L., and Louvet, F. (2021). Modeling phase equilibrium of hydrogen and natural gas in brines: Application to storage in salt caverns. *Int. J. Hydrogen Energy* 46 (5), 4229–4240. doi:10.1016/j.ijhydene.2020.10.242

Qiu, K. X., and Li, H. (2018). A new analytical solution of the triple-porosity model for history matching and performance forecasting in unconventional oil reservoirs. *SPE J.* 23, 2060–2079. doi:10.2118/191361-PA

Shi, X. L., Yang, C. H., Li, Y. P., Li, J. L., Ma, H. L., Wang, T. T., et al. (2017). "Development prospect of salt cavern gas storage and new research progress of salt cavern leaching in China," in *51st US rock mechanics/geomechanics symposium* (OnePetro). San Francisco, CA, USA.

Sovacool, B. K. (1907–20072008). The costs of failure: A preliminary assessment of major energy accidents. *Energy Policy* 36 (5), 1802–1820. doi:10.1016/j.enpol.2008.01.040

Wang, W., and Taleghani, A. D. (2014). Three-dimensional analysis of cement sheath integrity around Wellbores. *J. Petroleum Sci. Eng.* 121, 38–51. doi:10.1016/j.petrol.2014.05.024

Yan, Y., Guan, Z., Xu, Y., Yan, W., and Chen, W. (2020). Study on debonding issue of cementing interfaces caused by perforation with numerical simulation and experimental measures. *SPE Drill. Complet.* 35 (04), 684–695. doi:10.2118/201208-PA

Yao, Y., Gosavi, S. V., Searles, K. H., and Ellison, T. K. (2010). "Cohesive fracture mechanics based analysis to model ductile rock fracture," in *44th US rock mechanics symposium and 5th US-Canada rock mechanics symposium* (OnePetro). Salt Lake City, Utah.

Zhang, W., Eckert, A., and Ma, H. (2021). "Integrated experimental and numerical evaluation for wellbore integrity of wells under downhole conditions," in *55th US rock mechanics/geomechanics symposium* (OnePetro). Richardson, TX, USA.

frontiers | Frontiers in Earth Science

TYPE Original Research
PUBLISHED 20 January 2023
DOI 10.3389/feart.2023.1115054

OPEN ACCESS

EDITED BY
Peng Tan,
CNPC Engineering Technology R&D Company Limited, China

REVIEWED BY
Mengli Li,
The University of Newcastle, Australia
Chun Zhu,
Hohai University, China

*CORRESPONDENCE
Liuke Huang,
swpuhlk@126.com

SPECIALTY SECTION
This article was submitted to Environmental Informatics and Remote Sensing, a section of the journal Frontiers in Earth Science

RECEIVED 03 December 2022
ACCEPTED 06 January 2023
PUBLISHED 20 January 2023

CITATION
He R, Yang J, Li L, Yang Z, Chen W, Zeng J, Liao X and Huang L (2023), Investigating the simultaneous fracture propagation from multiple perforation clusters in horizontal wells using 3D block discrete element method.
Front. Earth Sci. 11:1115054.
doi: 10.3389/feart.2023.1115054

Investigating the simultaneous fracture propagation from multiple perforation clusters in horizontal wells using 3D block discrete element method

Rui He[1], Jian Yang[1], Li Li[1], Zhaozhong Yang[2], Weihua Chen[1], Ji Zeng[1], Xingchuan Liao[3] and Liuke Huang[3,4]*

[1]Engineering Technology Research Institute, PetroChina Southwest Oil and Gasfield Company, Chengdu, Sichuan, China, [2]State Key Laboratory of Oil and Gas Reservoir Geology and Exploitation, Southwest Petroleum University, Chengdu, Sichaun, China, [3]School of Civil Engineering and Geomatics, Southwest Petroleum University, Chengdu, Sichuan, China, [4]State Key Laboratory of Geomechanics and Geotechnical Engineering, Institute of Rock and Soil Mechanics, Chinese Academy of Sciences, Wuhan, China

Multi-cluster horizontal well fracturing is one of the key technologies to develop the unconventional reservoirs such as shales. However, the field data shows that some perforation clusters have little production contribution. In this study, a three-dimensional (3D) numerical model for simulating the multiple fracture propagation based on 3D block discrete element method was established, and this model considers the stress interference, perforation friction and fluid-mechanical coupling effect. In order to determine the most appropriate measures to improve the uniformity of multiple fracture propagation, the effect of the geologic and engineering parameters on the multiple fracture propagation in shale reservoirs is investigated. The modeling results show that the geometry of each fracture within a stage is different, and the outer fractures generally receive more fracturing fluid than the interior fractures. The vertical stress almost has no effect on the geometries of multiple fractures. However, higher horizontal stress difference, larger cluster spacing, smaller perforation number, higher injection rate, and smaller fracturing fluid viscosity are conducive to promote the uniform propagation of multiple fractures. The existence of bedding planes will increase the fluid filtration, resulting in a reduction in fracture length. The middle two fractures receive less fluid and the width of them is smaller. Through analyzing the numerical results, a large amount of fracturing fluid should be injected and the proppant with smaller size is suggested to be used to effectively prop the bedding planes. Cluster spacing and perforation number should be controlled in an appropriate range according to reservoir properties. Increasing the injection rate and reducing the viscosity of fracturing fluid are important means to improve the geometry of each fracture.

KEYWORDS

shale, horizontal well fracturing, multi-fracture propagation, 3D block discrete element method, fracture morphology

1 Introduction

As a kind of unconventional resources, shale reservoir is characterized by low porosity and ultra-low permeability (Huang et al., 2018; Wang et al., 2019; Song et al., 2021). Multi-stage hydraulic fracturing has become a standard technology to effectively exploit shale oil and gas (Luo et al., 2022; Zhang et al., 2022). In order to enlarge the fracture surface area, the scholars and companies continuously explore to generate multiple fractures with smaller cluster spacing, thus higher production can be achieved. According to the analysis results from distributed temperature sensing (DTS) and distributed acoustic sensing (DAS), some perforation clusters only receive a small proportion of fracturing fluid and proppant, and about one-third of the perforation clusters have no production contribution (Miller et al., 2011; Somanchi et al., 2017). That is to say, multiple hydraulic fractures cannot be uniformly generated within a stage, resulting in an obvious contrast in gas and oil production for each fracture along the wellbore. Previous studies show that stress interference among multiple fractures is an important factor affecting the geometry of each fracture (Ji et al., 2015; Wu and Olson, 2016; Tang et al., 2019). Fundamentally, the effectiveness of hydraulic fracturing is determined by many factors, such as perforation parameters, rock properties, *in-situ* stress, and fracturing treatment parameters. Meanwhile, hydraulic fracturing is a highly non-linear and fluid-mechanical coupling process (Zhu et al., 2019). Therefore, an integrated model which can accurately simulate the three-dimensional fracture propagation of horizontal wells is required. How to reduce the stress interference and improve the fracture geometry is a concern of engineers. In recent years, investigation of simultaneous multiple fracture propagation in horizontal well has been a hot issue.

The results of multiple fracture propagation can be directly observed through the physical experiment (Tan et al., 2020; Wang et al., 2022a). Bunger et al. studied the interaction among closely spaced hydraulic fractures through triaxial apparatus, and several preexisting notches on the wellbore were designed to represent the perforation holes (Bunger et al., 2011). Liu et al. conducted triaxial experiments on tight sandstone to investigate the geometries of multiple fractures and the pattern of fracturing curves. The influencing factors including net pressure, fracture spacing, perforation parameter, *in-situ* stress and well cementation quality were analyzed (Liu et al., 2018). However, the physical experiments can only qualitatively study the fracture propagation because of scale effect, and the experimental preparation is complicated and high cost is required. Therefore, few scholars carry out physical experiments to study multiple fracture propagation. In contrast, theoretical research tends to be an economic method.

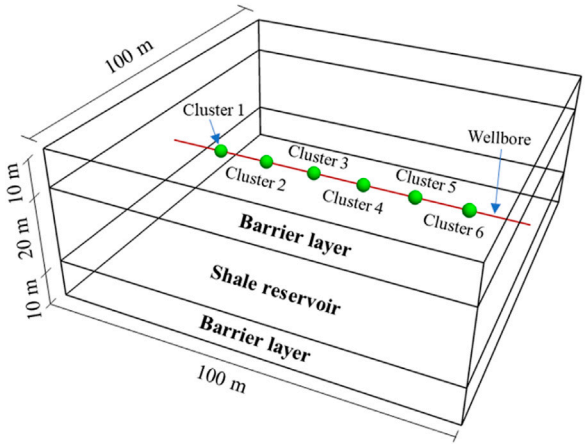

FIGURE 1
Physical model of horizontal well fracturing with six clusters in a stage.

At present, numerical models to simulate fracture propagation mainly include 2D, pseudo 3D and planar 3D models. Various 2D hydraulic fracturing models were developed to simulate the multiple fracture propagation. As an indirect boundary element method (BEM), the displacement discontinuity method (DDM) was earlier used to simulate the competitive propagation of multiple fractures considering the stress interference (Crouch, 1976). Wu and Olson proposed a fully coupled hydraulic fracture propagation model using 2D-DDM, and revealed the influencing mechanism of unbalanced fracture propagation (Wu and Olson, 2013). Sesetty and Ghassemi investigated the fracture propagation in sequential and simultaneous fracturing for single and multiple horizontal wells using fully coupled 2D-DDM (Sesetty and Ghassemi, 2015). In addition, two dimensional analysis of the uneven growth of multiple fracture have been conducted by some scholars using extended finite element method (XFEM) (Shi et al., 2016; Li et al., 2017; Tan et al., 2021). However, the 2D model has a fatal flaw in modeling the fracture height growth although it can reflect the physical mechanism of multiple fracture propagation under a great computing speed. Settari et al. proposed Pseudo 3D models for hydraulic fracturing design in the 1980s, which can simulate fracture height growth based on the analytical solution of stress intensity factor (Palmer et al., 1983; Settari and Cleary, 1986). Linkov et al. proposed an improved pseudo 3D model based on equivalent KGD model to calculate fracture height propagation under stress contrast (Linkov and Markov, 2020). Zhao et al.(2016) established a pseudo 3D model to simulate simultaneous propagation of multiple fractures in horizontal wells, coupling the influence of many factors including elastic deformation of rock, stress interaction among fractures and fluid flow. Yang et al. (2018) proposed a pseudo-3D multi-cluster fracturing model based on 2D-DDM and the criterion of energy release rate, and the measures to promote the uniform propagation of multiple fractures were put forward. However, the calculation accuracy of pseudo 3D model is insufficient in the stress field of multiple fracture because of the plane strain assumption, and this method is not applicable to simulate the fracture height growth in high stress layer. The planar 3D model, which applies the 3D solid-mechanical equation to calculate the rock deformation while

TABLE 1 The input parameters for hydraulic fracturing simulation.

Parameters	Unit	Value
Injection rate	m^3/min	0.6
Fracturing fluid viscosity	cP	5
Total injection time	s	30
Young's modulus	GPa	46
Poisson's ratio	/	0.224

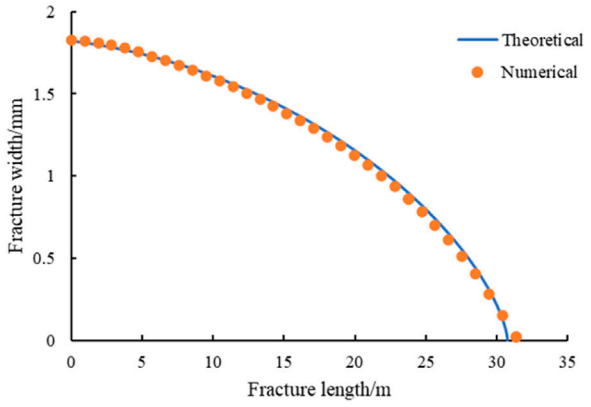

FIGURE 2
Comparison between the theoretical solution and the numerical solution for hydraulic fracture width versus fracture position.

allowing two-dimensional fluid flows, provide better description of fluid behaviors in the fracture. Barree (1983) established a planar 3D numerical simulator using the fixed grid method in heterogenous media. Peirce and Bunger (2014) investigated the influence of non-uniform cluster space on increasing the fracture uniformity using a developed, fully coupled, planar 3D fracturing model. Tang et al. (2016) analyzed the multiple fracture propagation using a planar 3D-DDM based thermal-hydro-mechanical model and non-uniform distribution of proppant was observed. However, the planar 3D model has a disadvantage that the curving of fracture caused by stress interference and stress heterogeneity cannot be considered. In recent years, in order to simulate the multiple fracture propagation more accurately, some new 3D models were developed by scholars (Li et al., 2016; Huang et al., 2020).

In 1970s, Cundall (1971) first developed the discrete element method (DEM) to describe the non-linear mechanical behavior of non-continuum. In recent years, the scholars have begun to investigate the hydraulic fracture propagation using the DEM (Zhang et al., 2017; He et al., 2020; Huang et al., 2022). As a typical DEM, the block discrete element method (BDEM) is suitable for characterizing discontinuities (such as shale reservoirs) fully coupled with fluid-mechanical effect. This model is composed of a number of deformable blocks, which are connected by contacts to characterize the rock formation. This method does not require sophisticated constitutive equations and adopts explicit solution with strong convergence, which greatly reduces the calculation amount. Compared with other DEM methods (such as particle flow code method), the BDEM method can better simulate the fracture height growth and multiple fracture propagation. Zhang and Dontsov (2018) used the BDEM to study the 3D fracture propagation and proppant transport in a layered reservoir considering the influencing of stress distribution. Yin et al. (2020) investigated the fault reactivation and induced seismicity caused by hydraulic fracturing using the BDEM. Zheng et al. (2022) explored the effect of fracturing fluid viscosity and injection rate on the vertical propagation of hydraulic fracture in shale reservoirs with developed bedding planes. Although the BDEM method has been widely used to analyze the mechanical behavior of fracture propagation, there are few studies on simultaneous 3D propagation of multiple fractures taking account of stress interference among fractures, and the effect of bedding planes on the multiple fracture propagation were less studied.

TABLE 2 Summary of the input parameters of each modeling case.

Cases	*In-situ* stress $\sigma_h/\sigma_v/\sigma_H$ (MPa)	Bedding plane	Cluster spacing (m)	Perforation number of each cluster	Injection rate (m^3/min)	Fluid viscosity (cP)
A	59/64/69	No bedding plane	10	8	18	5
B	59/61/69	No bedding plane	10	8	18	5
C	59/67/69	No bedding plane	10	8	18	5
D	63/64/69	No bedding plane	10	8	18	5
E	55/64/69	No bedding plane	10	8	18	5
F	59/64/69	Strongly bedding plane	10	8	18	5
G	59/64/69	Weakly bedding plane	10	8	18	5
H	59/64/69	No bedding plane	6	8	18	5
I	59/64/69	No bedding plane	14	8	18	5
J	59/64/69	No bedding plane	10	6	18	5
K	59/64/69	No bedding plane	10	12	18	5
L	59/64/69	No bedding plane	10	8	6	5
M	59/64/69	No bedding plane	10	8	12	5
N	59/64/69	No bedding plane	10	8	18	30
O	59/64/69	No bedding plane	10	8	18	100

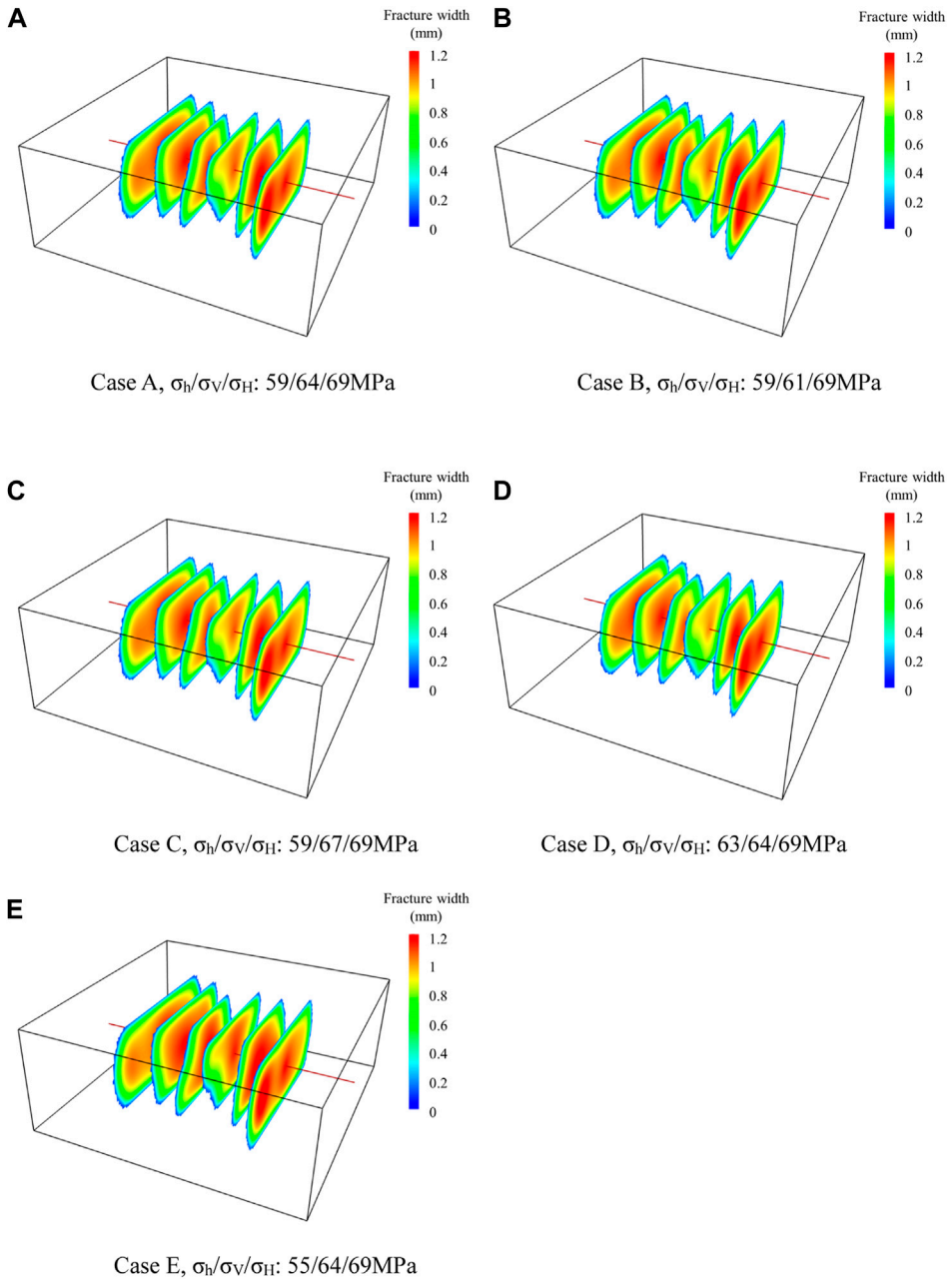

FIGURE 3
Fracture morphology for five cases with different *in-situ* stress combination states. **(A)** Case A, $\sigma_h/\sigma_V/\sigma_H$: 59/64/69 MPa. **(B)** Case B, $\sigma_h/\sigma_V/\sigma_H$: 59/61/69 MPa. **(C)** Case C, $\sigma_h/\sigma_V/\sigma_H$: 59/67/69 MPa. **(D)** Case D, $\sigma_h/\sigma_V/\sigma_H$: 63/64/69 MPa. **(E)** Case E, $\sigma_h/\sigma_V/\sigma_H$: 55/64/69 MPa.

In order to investigate the effect of the geologic and engineering parameters on the multiple fracture propagation in shale reservoirs, we established a fracturing model of horizontal wells considering the influence of stress interference effect, perforation friction and fluid-mechanical coupling effect using the 3D-BDEM. Based on this model, a sensitivity analysis of the key influencing parameters including *in-situ* stress, bedding plane, cluster spacing, perforation number, injection rate and fracturing fluid viscosity on multiple fracture propagation in the shale reservoirs are systematically studied. The uniformity of multiple fracture and dynamic flow rate distribution between clusters within a stage are analyzed. Based on the research results, the engineering measures to adjust the flow rate in each cluster and improve the fracture geometries of horizontal shale wells are put forward.

2 Numerical modeling methodology

For the block DEM, it is assumed that the rock is divided into many blocks by the joints, and the interaction between the blocks satisfies Newton's second law. In the model, the forces exerted on the blocks are balanced under initial state conditions. When the forces or

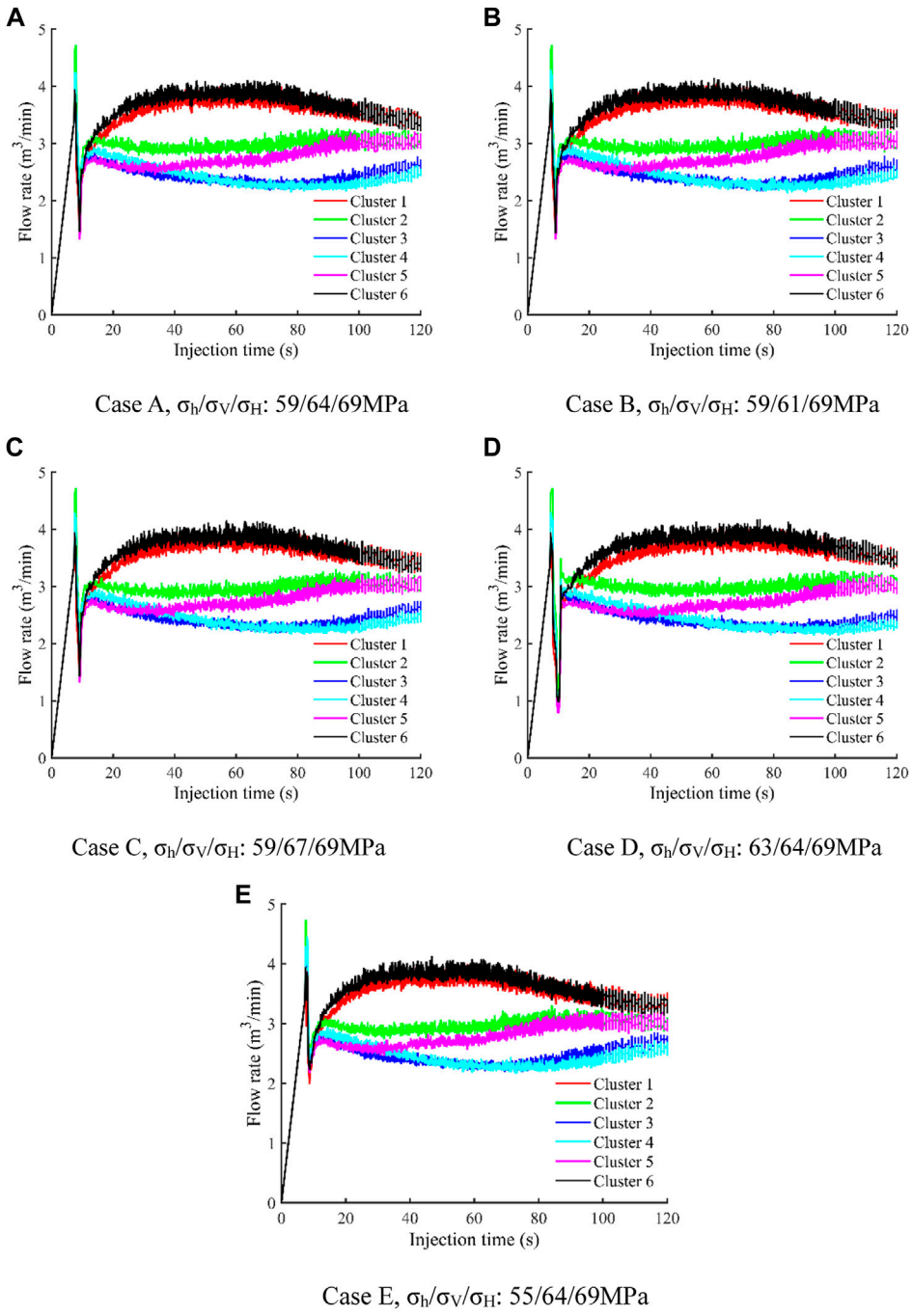

FIGURE 4
Flow rate into each cluster as a function of time for five cases with different *in-situ* stress combination states. **(A)** Case A, $\sigma_h/\sigma_V/\sigma_H$: 59/64/69 MPa. **(B)** Case B, $\sigma_h/\sigma_V/\sigma_H$: 59/61/69 MPa. **(C)** Case C, $\sigma_h/\sigma_V/\sigma_H$: 59/67/69 MPa. **(D)** Case D, $\sigma_h/\sigma_V/\sigma_H$: 63/64/69 MPa. **(E)** Case E, $\sigma_h/\sigma_V/\sigma_H$: 55/64/69 MPa.

constraints of the system are changed, the blocks move or rotate, resulting in the change of force exerted on the blocks. The system finally reaches a new balance after the interaction between the blocks.

For rigid blocks, the plane motion equation and rotation equation of the block are respectively expressed as:

$$\ddot{x}_i + \eta\dot{x}_i = \frac{F_i}{m} - g_i \tag{1}$$

$$\dot{\omega}_i + \eta\omega_i = \frac{M_i}{I} \tag{2}$$

where $\ddot{x}_i$ is the acceleration, $\dot{x}_i$ is the velocity, η is the damping coefficient, F_i is the resultant force acting on the center of the block, m is the mass of block, g_i is the gravitational acceleration, $\dot{\omega}_i$ is the angular acceleration, ω_i is the angular velocity, M_i is bending moment, I is the moment of inertia.

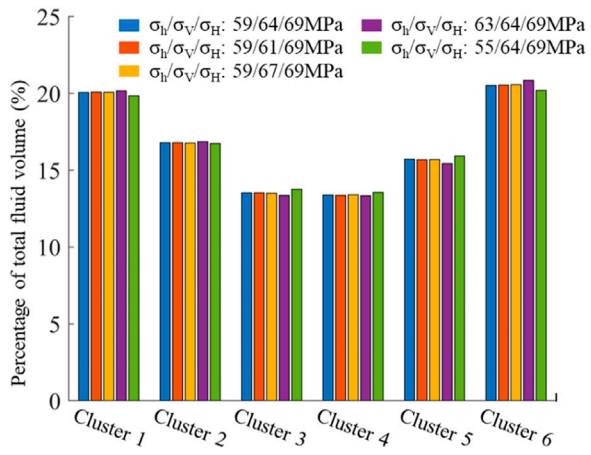

FIGURE 5
The total fluid volume distribution of each cluster for five cases with different *in-situ* stress combination states.

In block DEM, each deformable block is composed of several tetrahedron finite element grids. The complexity of block deformation is directly related to the number of the divided elements. Similar to the finite element method (FEM), the vertices in the tetrahedron element are called nodes.

Under equilibrium condition, the resultant force on the node is 0. Conversely, if the resultant force is not 0, then there is an acceleration at the node. The explicit difference method (EDM) is used to solve the model, and the linear momentum balance equation and displacement-velocity relationship are adopted to calculate the translational degrees of the freedom of nodes, as shown in follows:

$$\dot{u}_i^{(t+\Delta t/2)} = \dot{u}_i^{(t-\Delta t/2)} + \sum F_i^{(t)} \Delta t / m \tag{3}$$

$$u_i^{(t+\Delta t)} = u_i^{(t)} + \dot{u}_i^{(t+\Delta t/2)} \Delta t \tag{4}$$

where $\dot{u}_i{}^t$, $u_i{}^t$ are respectively the velocity and displacement of i (i = 1, 2, 3) component at time t, $\sum F_i^{(t)}$ is the resultant force of i (i = 1, 2, 3) component at the node at time t, and Δt is the time step.

The angular velocity of component i at time t is calculated by the central difference equation:

$$\omega_i{}^{(t+\Delta t/2)} = \omega_i{}^{(t-\Delta t/2)} + \frac{\sum M_i{}^{(t)}}{I} \Delta t \tag{5}$$

The incremental equation of constitutive relation of deformable blocks can be described as:

$$\Delta \sigma_{ij}^e = \lambda_0 \Delta \varepsilon_v \delta_{ij} + 2\mu_0 \Delta \varepsilon_{ij} \tag{6}$$

where λ_0 and μ_0 are the Lame constants; $\Delta \sigma_{ij}^e$ is the increment of the stress tensor; $\Delta \varepsilon_v$ is the increment of the volume strain; δ_{ij} is the Kronecker function, $\Delta \varepsilon_{ij}$ is the increment of strain.

In block DEM, any two blocks are connected by a contact, where can be set as a joint. The fracture propagates along the joint when the joint is broken. The deformation and failure of joints follow the Coulomb slip joint contact behaviour. In this paper, the constitutive model takes account of shear and tensile failure, also the joint expansion is considered. The contact deformation is described by the normal and shear relationships.

The increments of normal force is given by:

$$\Delta F_n = k_n A \Delta U_n \tag{7}$$

where ΔF_n is the increment of normal force acting on the contact, k_n is the normal stiffness, A is the contact area, and ΔU_n is the increment of the normal displacement.

The increments of shear force is given by:

$$\Delta F_S = -k_S A \Delta U_S \tag{8}$$

where ΔF_S the increment of shear force acting on the contact, k_S is the shear stiffness, ΔU_S is the increment of the shear displacement.

For an original joint, the maximum normal tensile force can be calculated as:

$$F^n_{\max} = -S_t A \tag{9}$$

where $F^n_{\max}$ is the maximum normal tensile force, and S_t is the tensile strength.

The maximum shear force can be calculated as:

$$F^S_{\max} = CA + F^n \tan \varphi \tag{10}$$

where $F^S_{\max}$ is the maximum shear force, C is the joint Cohesion, F^n is the normal force acting on the joint, and φ is the internal friction angle.

When the maximum normal stress reaches or exceeds the normal strength of the joint, or the maximum shear stress reaches or exceeds the shear strength of the joint, the contact of joint will be broken by tensile or shear force, then the tensile strength and joint cohesion decrease to zero.

The criterions of tensile and shear breakage of the joint contact are described as follows:

$$F_n \geq F^n_{\max} \quad F_S \geq F^S_{\max} \tag{11}$$

where F_n is the normal force acting on the contact, F_S the shear force acting on the contact.

After the failure of joint contacts, the deformation of the joint is determined by block deformation, as shown in Eq. 6

The fluid flow in the joint satisfies the Navier-Stokes equation (Jin and Chen, 2019). When the two joint faces are approximately parallel and impermeable, and the fluid is incompressible, the Navier-Stokes equation can be simplified to the Reynolds equation. The fluid flow rate can be expressed as:

$$q = \frac{b^3 \Delta P}{12 \mu L} \tag{12}$$

where b is the joint aperture (fracture width), q is the fluid flow rate, ΔP is the pressure difference of the fluid domain, μ is the fracturing fluid viscosity, and L is the length of fluid domain.

Fluid flow in the fracture is a fluid-mechanical coupling process. In a time step, the fluid pressure acts on the joint surface and causes rock deformation, resulting in the update of fluid pressure. After a time step, the updated fluid pressure leads to the variation of fracture width, thus changing the fracture permeability. The effective stress is often used to calculate the deformation of solids under the action of fluid, which can be given as:

$$\sigma' = \sigma + \alpha P_p \tag{13}$$

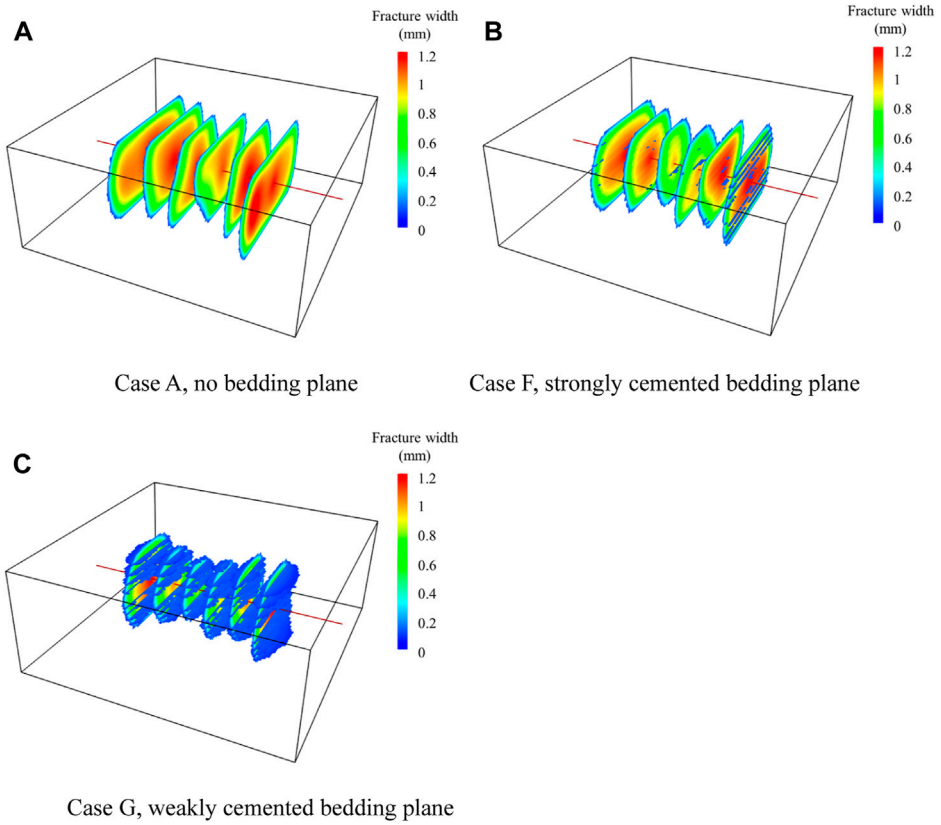

FIGURE 6
Fracture morphology for three cases with different bedding development level. **(A)** Case A, no bedding plane. **(B)** Case F, strongly cemented bedding plane. **(C)** Case G, weakly cemented bedding plane.

where σ' is the effective stress, σ is the total stress, α is the Boit coefficient, and P_p is the reservoir pressure.

The fracture width is defined as the average distance between the two parallel joint surfaces, which is related to the deformation of rock mass. It is known that the fluid flow rate is related to the fracture width. Therefore, the influence of rock deformation on the fracture permeability is mainly characterized by the change of joint aperture. The joint aperture is described by:

$$b = b_0 \Delta U_n + \Delta U_S \tan \phi \tag{14}$$

where b_0 is the initial joint aperture, and ϕ is the dilation angle.

The pressure is changed with the fluid volume and injection parameters. The domain pressure is described by:

$$P = P_0 + K_f \frac{Q\Delta t}{V} + K_f \frac{\Delta V}{V_0} \tag{15}$$

where P is the domain pressure, P_0 is the domain pressure at previous time step, K_f is the bulk modulus of fluid, Q is the sum of flow rate of the domain, V is the domain volume, V_0 is the domain volume at previous time step, and ΔV is the volume variation of domain.

The perforation frictional pressure drop can be predicted using the equation proposed by Crump and Conway (Crump and Conway, 1988):

$$P_f = \frac{0.2369 q^2 \rho}{K_d{}^2 d^4 N^2} \tag{16}$$

where P_f is the perforation frictional pressure drop, ρ is the fluid density, K_d is the discharge coefficient, N is the number of perforations, and d is the perforation diameter.

3 Model verification

A shale reservoir model with dimensions of 100 m × 100 m × 40 m is established based on the BDEM, as shown in Figure 1. In the model, it is vertically divided into three layers, in which the top and bottom parts are barrier layers, and the thickness of each barrier layer is 10 m. Shale reservoir is located in the middle of the model, with a thickness of 20 m. A horizontal wellbore (red line) is established, and there are six perforation clusters (green balls) within a fracturing stage are set along the wellbore. In the location of each cluster, a hydraulic fracture will initiate and propagate perpendicular to the wellbore. Among the six clusters, Cluster 6 is near the heel of the wellbore, and Cluster 1 is near the toe of wellbore. To model the shale reservoir which contains bedding planes, several horizontal joints are preset in the model to study multiple fracture propagation.

In 1950s, the plane strain KGD fracture propagation model was proposed by Khristianovic and Zheltov (Khristianovic and Zheltov, 1955). Then, Donstov developed a quick solution for a propagating penny-shaped hydraulic fracture, considering fracture toughness, fluid viscosity, and leak-off (Dontsov, 2016). In order to validate the BDEM-based fracture propagation model, we compared it with

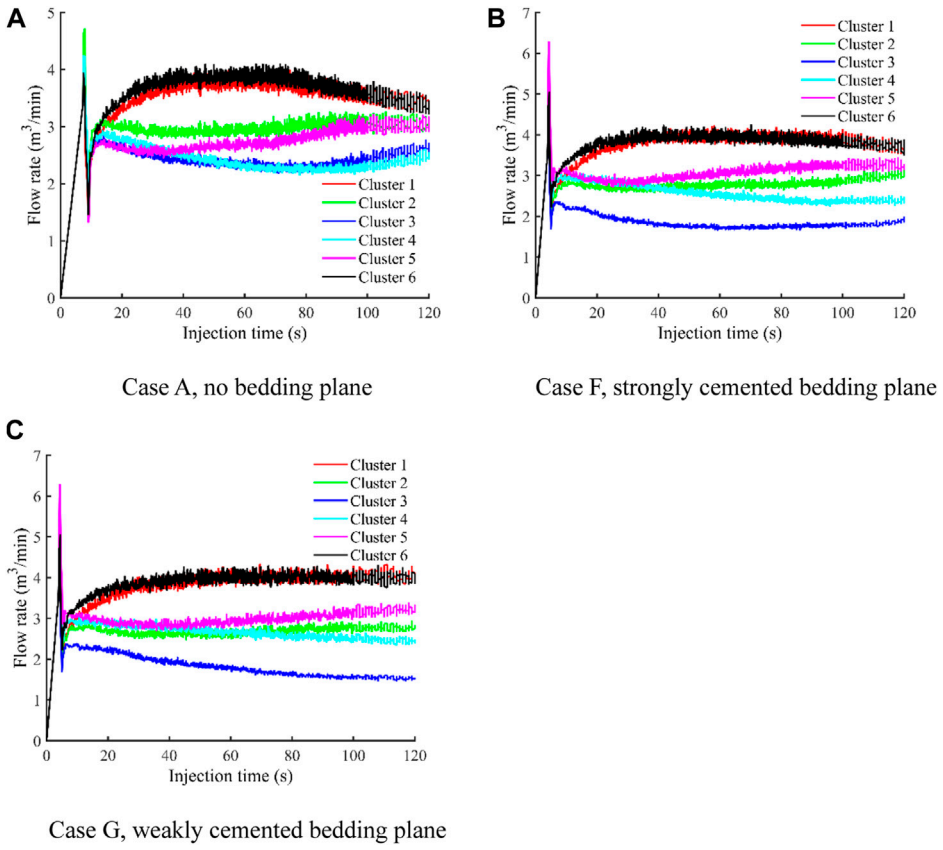

FIGURE 7
Flow rate into each cluster as a function of time for three cases with different bedding development levels. **(A)** Case A, no bedding plane. **(B)** Case F, strongly cemented bedding plane. **(C)** Case G, weakly cemented bedding plane.

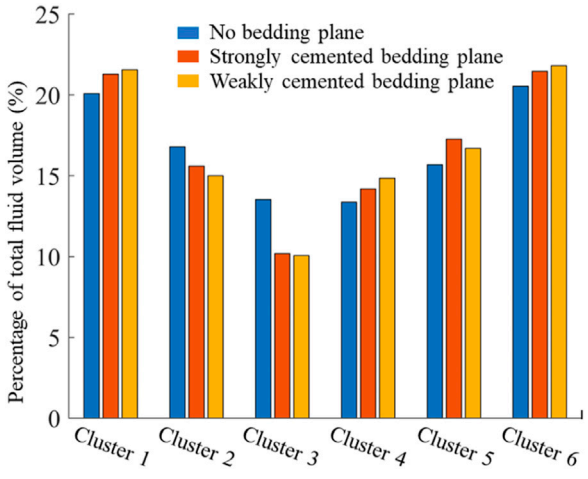

FIGURE 8
The total fluid volume distribution of each cluster for three cases with different bedding development level.

analytical model under viscosity-dominated regime. The analytical expression for the fracture width and fracture length can be described as (Huang et al., 2019; Huang et al., 2022):

$$w = 1.1901\left(\frac{\mu'^2 Q_0^3 t}{E'^2}\right)^{1/9}\left(1+\frac{x}{L}\right)^{0.487}\left(1-\frac{x}{L}\right)^{2/3} \quad (17)$$

$$l = 0.6944\left(\frac{Q_0^3 E' t^4}{\mu'}\right)^{1/9} \quad (18)$$

$$\mu' = 12\mu \qquad E' = \frac{E}{1-\nu^2} \quad (19)$$

where w is the fracture width, Q_0 is the injection rate, t is the injection time, x is distance between a certain position of hydraulic fracture and the injection point, L is the half fracture length, E is the Young's modulus, and υ is the Poisson's ratio.

The input parameters for model validation are shown in Table 1. Figure 2 shows a comparison between the numerical solution by BDEM and the modeling results of analytical model. The results show that there is good agreement on the fracture width calculated by these two methods, showing that the BDEM model established in this paper is reliable.

4 Modeling results and discussion

4.1 Input parameters

The multiple fracture propagation during hydraulic fracturing process is largely influenced by geological and engineering

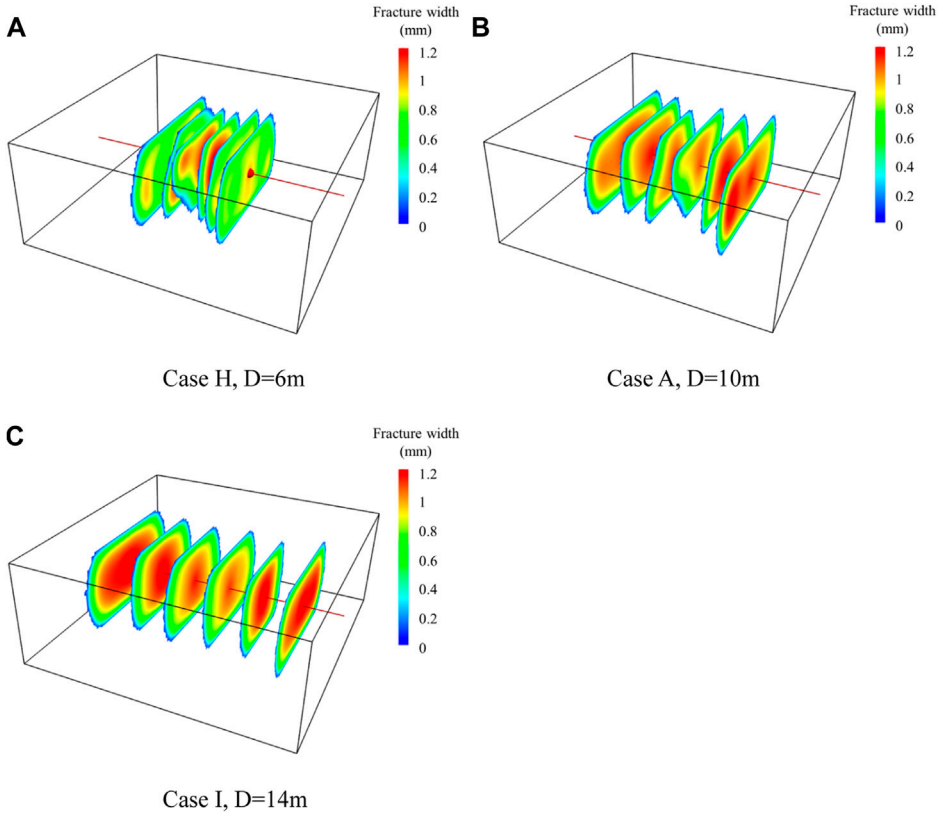

FIGURE 9
Fracture morphology for three cases with different cluster spacing. **(A)** Case H, D = 6 m. **(B)** Case A, D = 10 m. **(C)** Case I, D = 14 m.

parameters (Tan et al., 2017; Zhang et al., 2021; Wang et al., 2022b; Guo et al., 2022; Dou and Wang, 2022; Zhou and Yang, 2022; Huang et al., 2023). In this paper, the effects of these parameters including *in-situ* stress, bedding plane, cluster spacing, perforation number, injection rate and fracturing fluid viscosity on multiple fracture propagation within a stage were investigated using the numerical model established above. A series of numerical simulations (Case A to Case O) of multiple fracture propagation were conducted through changing the value of each parameter separately. Table 2 shows the input parameters of each modeling case. For this study, the basic parameters were taken from the shale oil reservoirs in western China, as shown in Case A in Table 1. In each case, the Young's modulus of the shale reservoir is set at 46 GPa, and the Poisson's ratio is 0.224. The Young's modulus of the barrier layer is set at 51 GPa, and the Poisson's ratio is 0.263. The minimum principal stress of the barrier layer is 5 MPa larger than that of the shale reservoir. Comparing the results of other cases with that of the base case (Case A), the effect of factors can be analyzed. To study the effect of bedding planes on the multiple fracture propagation, Case F gives the shale reservoir model with strongly cemented bedding planes, where the shear resistance of bedding planes is stronger, and the internal friction angle is set at 30°. Case G gives the shale reservoir model with weakly cemented bedding planes, where the shear resistance of bedding planes is weaker, and the internal friction angle is set at 10°. In the above two cases, the tensile strength of the bedding planes is 6 MPa, and the cohesion of bedding planes is 1.5 MPa.

4.2 Effect of geologic parameters

Based on the input parameters in Table 2, the numerical simulations of Case A to Case O were carried out. The fracture morphology of multiple fracture for each case is as shown in this section, and the variation of flow rate into each cluster is plotted and discussed in this section. In the figures of facture morphologies below, the colors at different fracture positions represent the value of fracture width (aperture).

4.2.1 *In-situ* stress

In this section, we will study the effect of *in-situ* stress combination on the multiple fracture propagation under the condition of keeping other parameters constant. Figure 3 shows the fracture morphologies at the end of injection for five different *in-situ* stress combination states. It can be seen that multiple bi-wing fractures initiated and propagated perpendicular to the wellbore in each case. The geometries of each fracture within a stage are different due to the difference in received fracturing fluid. From Figure 3, the fracture length of the outer two fractures are slightly greater than that of the interior fractures, which means that a wider area is stimulated on both sides within a fracturing stage. In addition, the interior four clusters are suppressed to a certain extent, resulting in significantly smaller fracture

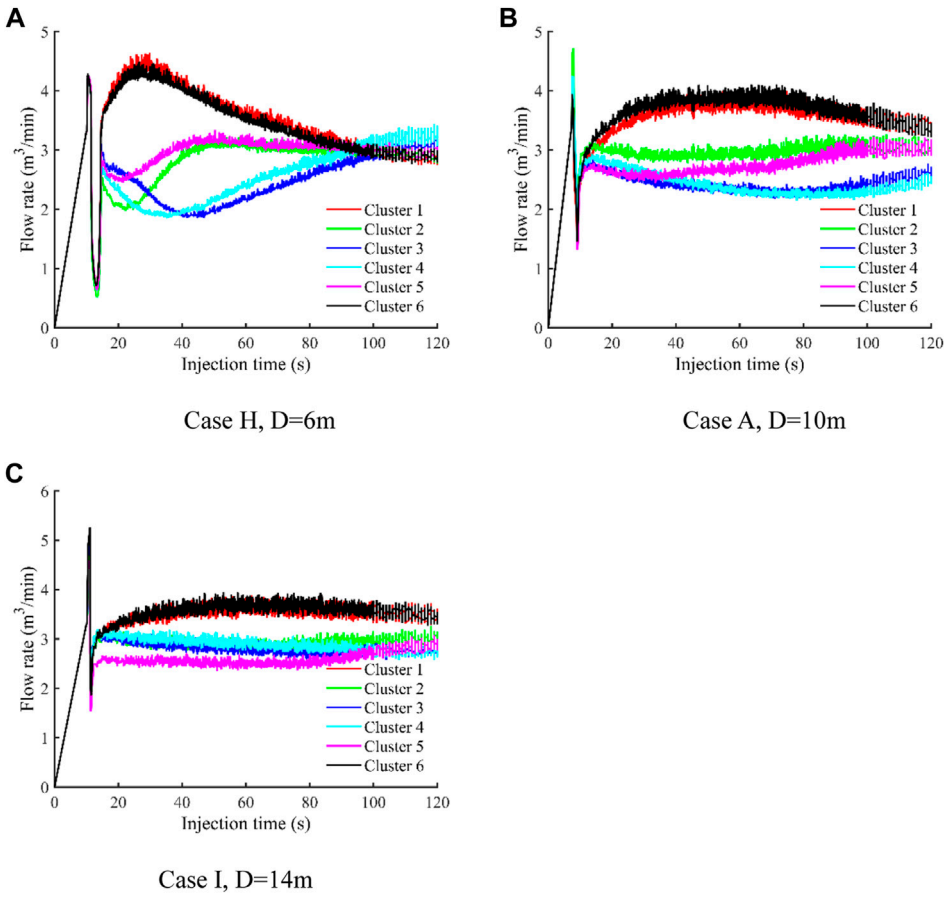

FIGURE 10
Flow rate into each cluster as a function of time for three cases with different cluster spacing. **(A)** Case H, D = 6 m. **(B)** Case A, D = 10 m. **(C)** Case I, D = 14 m.

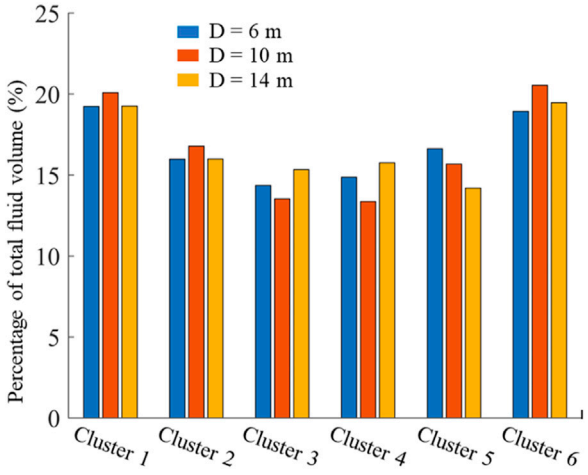

FIGURE 11
The total fluid volume distribution of each cluster for three cases with different cluster spacing.

width and larger area of inefficient fracture width (less than 1 mm). This phenomenon has been confirmed by some previous studies (Wu and Olson, 2016; Yang et al., 2018), showing that it is caused by competitive fracture propagation due to stress interference and friction effect.

Cases A, B, and C compare the effect of vertical *in-situ* stress at a horizontal stress difference of 10 MPa. The numerical simulation results show that the fracture geometries obtained by the above three cases are very close, indicating that the vertical stress has little influence on the propagation of vertical fracture in homogeneous reservoirs. On the other hand, Cases A, D, and E compare the effect of horizontal stress difference when the vertical stress stays at 64 MPa. The results show that when the horizontal stress difference is higher, the length of each fracture slightly increases and the width of interior fractures is significantly greater, which means the fractures are more easily to propagate along the maximum principal stress direction under higher horizontal stress difference. The middle two fractures are greatly restrained when the horizontal stress difference is only 6 MPa. In this case, the fracture width of the middle two fractures are smaller, especially the areas near the injection point are not effectively opened. However when the horizontal stress difference reaches 14 MPa, the multiple fracture propagation is comparatively more

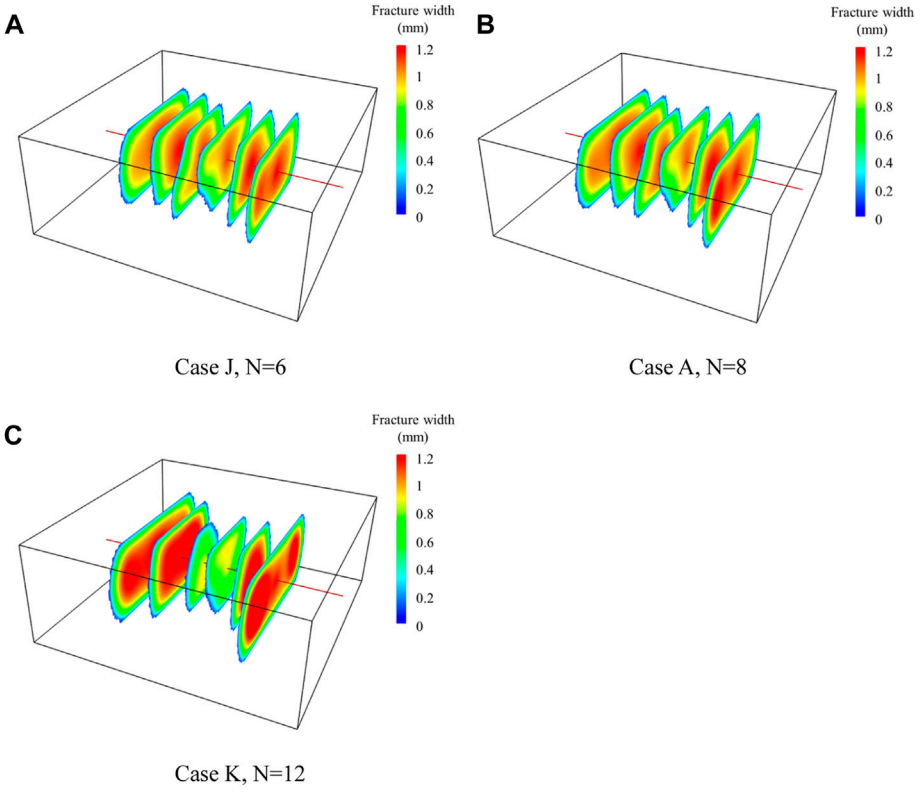

FIGURE 12
Fracture morphology for three cases with different perforation numbers. **(A)** Case J, *N* = 6. **(B)** Case A, *N* = 8. **(C)** Case K, *N* = 12.

uniform, indicating that higher horizontal stress difference can reduce the inhibition of interior fractures.

In order to better understand the dynamic propagation process of multiple fractures, the change of flow rate with injection time in each cluster is plotted in Figure 4. The total fluid volume distribution of each cluster for the five different cases is shown in Figure 5. It can be seen that in each case, the two fractures on the outside always receive more fluid than the other four fractures during all the injection process. The flow rate of the outer two fractures increases rapidly first and then decrease gradually. Conversely, the flow rate obtained by the interior four fractures decreases slightly at first, and increases gradually after half of the total fluid is injected. At the end of injection, the flow rate of the outer fractures is obviously larger than that of interior fractures. Taking Case A as an example, the total fluid volume percentage received by the fractures are 20.09%, 16.79%, 13.53%, 13.37%, 15.68%, and 20.54%, respectively. Comparing cases A, B, and C, it can be seen that the vertical stress has little influence on the flow rate distribution, and the flow rate curves of each case are very similar, and these fractures finally receive almost the same volume of fracturing fluid. Comparing cases A, D, and E, we can find the difference between the shapes of each flow rate curve slightly decreases with the increase of horizontal stress difference, and the volume of fracturing fluid received by each fracture is closer under higher horizontal stress difference. When the horizontal stress difference is 14 MPa, the total fluid volume percentage received by the fractures are 19.84%, 16.74%, 13.76%, 13.55%, 15.92%, and 20.19%, respectively. The results verify that the flow distribution of each fracture is more uniform under the condition of higher horizontal stress difference.

4.2.2 Bedding plane

Some shale reservoirs contain numerous bedding planes with lower strength and the existence of bedding planes will have an influence on the vertical growth of hydraulic fractures. The activation of bedding planes often promotes the formation of a complex fracture network, which is beneficial to increase the stimulated reservoir volume (SRV). In this section, several horizontal bedding planes are preset in the model to investigate the effect of bedding plane on the multiple fracture propagation. Figure 6 shows the fracture morphologies at the end of injection for three different bedding development levels. For comparison, Case A shows the fracture propagation results without bedding planes. It can be seen that for the shale reservoirs with strongly cemented bedding planes, just a few bedding planes are activated by fracturing fluid (Figure 6B). The fractures near the heel of wellbore can connect several bedding planes, but the distance of fracturing fluid flowing through the bedding planes is very short. Moreover, the closer to the toe of the wellbore, the more difficult it is to activate the bedding planes.

On the other side, for the shale reservoir with weakly cemented bedding planes, a lot of bedding planes are effectively activated and opened by the hydraulic fractures, and a fence-like fracture network is generated (Figure 6C). Similarly, the fractures near the heel of wellbore can communicate more bedding planes than the other fractures. It can also be found that the length of each fracture is smaller because of fluid filtration into the bedding planes. Compared with the shale reservoir

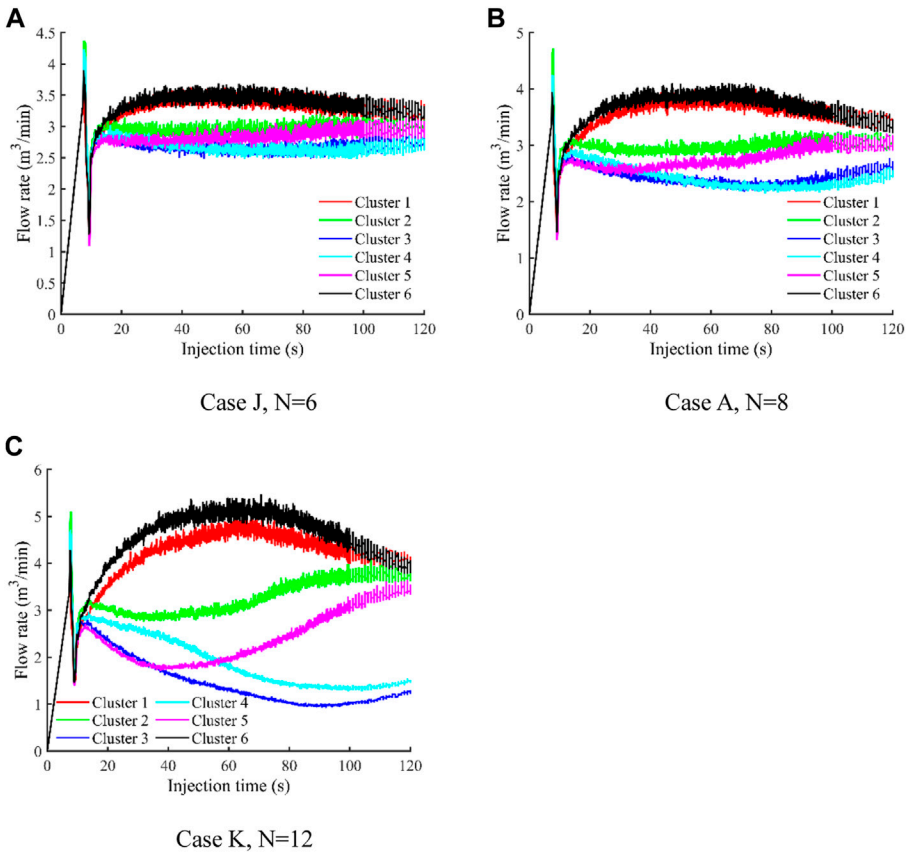

FIGURE 13
Flow rate into each cluster as a function of time for three cases with different perforation numbers. **(A)** Case J, *N* = 6. **(B)** Case A, *N* = 8. **(C)** Case K, *N* = 12.

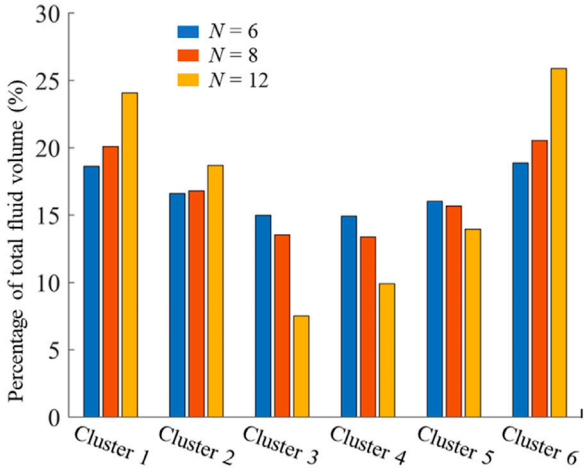

FIGURE 14
The total fluid volume distribution of each cluster for three cases with different perforation numbers.

with no bedding planes, the width of the middle two fractures is obviously lower for the shale reservoir with bedding planes, which indicates that the existence of bedding planes increases the effect of stress interference, even in the bedding planes which are relatively strongly cemented. For the above two cases, the width of activated bedding planes is very low (blue color). This is because the normal stress will decrease and the shear stress increase near the intersection line of the bedding plane when the hydraulic fracture approaches the bedding plane, and the shear failure is more easily to occur at bedding plane when the fracturing fluid flows from the hydraulic fracture to the bedding planes (Zheng et al., 2022). That means the bedding planes will be activated and they will tend to move along the shear direction, however it will not be opened to a great level. Thus, it is suggested that using the proppant with smaller particle size to effectively support the opened bedding planes. For shale reservoirs with bedding planes, as much fracturing fluid as possible should be injected to ensure the propagation of both hydraulic fractures and bedding planes, especially to improve the width of bedding planes.

Figure 7 shows the change of flow rate with injection time in each cluster with different bedding development levels. Compared with shale reservoir without bedding planes, the flow rate obtained by each fracture in shale reservoir with bedding planes is smaller because of fluid filtration into the bedding planes. In addition, the difference of flow rate obtained by each fracture in shale reservoir with bedding planes is greater, which means the existence of bedding planes will promote the non-uniform distribution of flow rates in each fracture. Particularly, the flow rate of the interior four fractures varies greatly, and the amount of fracturing fluid received by the Cluster 3 is far lower

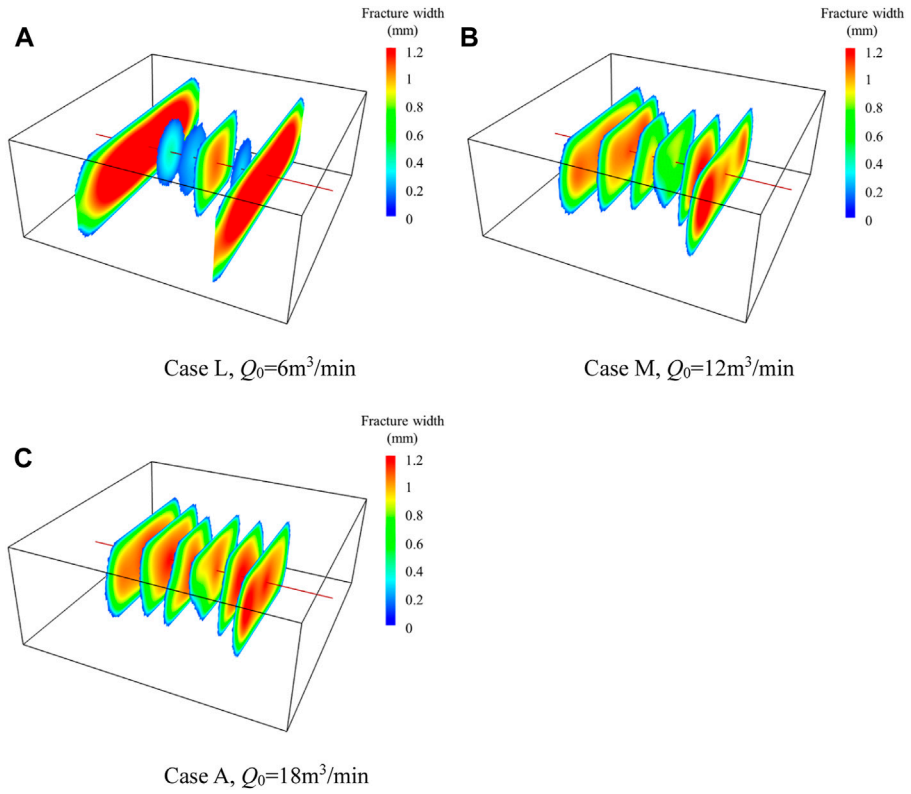

FIGURE 15
Fracture morphology for three cases with different injection rates. **(A)** Case L, Q_0 = 6 m^3/min. **(B)** Case M, Q_0=12 m^3/min. **(C)** Case A, Q_0 = 18 m^3/min.

than that of other fractures. However, the existence of bedding planes has little influence on the flow rate of the outer two fractures. According to the statistical results of total fluid volume for Case F and Case G (Figure 8), it can be seen that the percentage of flow rates received by the interior four fractures varies more greatly when the bedding plane is more developed. For Case F, the total fluid volume percentage received by the fractures are 21.29%, 15.60%, 10.18%, 14.18%, 17.27%, and 21.47%, respectively. For Case G, the total fluid volume percentage received by the fractures are 21.56%, 15.00%, 10.07%, 14.85%, 16.70%, and 21.82%, respectively.

4.3 Effect of engineering parameters

4.3.1 Cluster spacing

The above investigations mainly focus on the influence of inherent geologic parameters on the multiple fracture propagation. The parameters that we can control are the engineering parameters such as perforation parameters (cluster spacing and perforation number) and injection parameters (injection rate and fracturing fluid viscosity). In this section, we will study the effect of cluster spacing on the multiple fracture propagation under the condition of keeping other parameters constant. Figure 9 shows the fracture morphologies at the end of injection for three different cluster spacing. It can be seen that the geometry of each fracture within a stage are significantly different under three different clustering spacing (D = 6 m, D = 10 m, and D = 14 m). The interior four clusters are greatly suppressed when the cluster spacing is 6 m. In this case, the fracture length of the interior four fractures is shorter than that of the outer two fractures, although the fracture width is larger. At the same time, the outer two fractures obviously grow preferentially. However, the difference of fracture length of each fracture decreases with the increase of cluster spacing. When the cluster spacing is 14 m, the geometries of different fractures are relatively similar, and the multiple fracture propagation is much more uniform. In this case, the stress interference between adjacent fractures is quite weak. The results show that increasing the cluster spacing is beneficial to the uniform propagation of each fracture within a stage. However, larger cluster spacing means fewer fractures within a stage, which results in that some reservoir areas have not been effectively stimulated. At this time, the distance between some matrix areas and the hydraulic fractures is farther, which makes it difficult for oil to flow from the matrix to hydraulic fractures. How to optimize the treatment parameters to obtain a reasonable fracture geometries without expanding the cluster spacing is an important prerequisite for the optimal design of multi-cluster fracturing.

The change of flow rate with injection time in each cluster is plotted in Figure 10. It can be seen that the overall curve shapes of flow rate in each case differ a lot. The flow rate curves show obvious peaks and troughs when the cluster spacing is 6 m. In this case, the flow rate of outer two fractures increases sharply, while the flow rate of interior fractures becomes smaller. With the fluid injection for a period of time, the outer two fractures gradually begin to receive less fluid, and the middle two fractures receive more fluid. At the end of injection, the flow rate of the middle two fractures is slightly larger than that of other four fractures. During the whole injection process, the flow rate curve

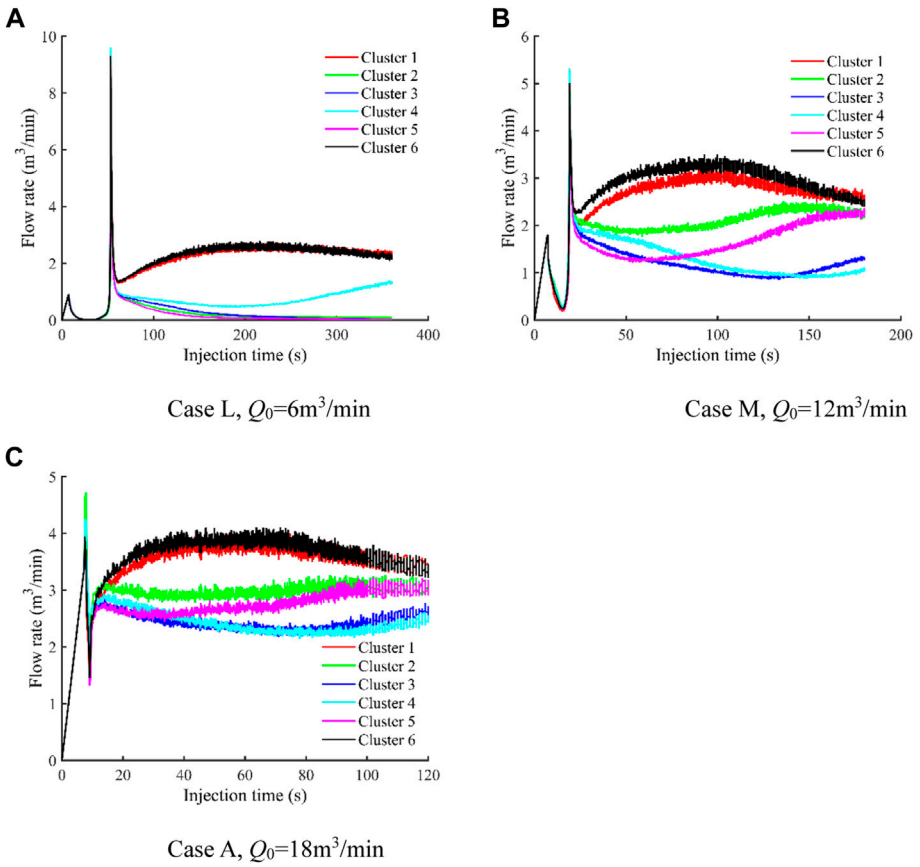

FIGURE 16
Flow rate into each cluster as a function of time for three cases with different injection rates. **(A)** Case L, Q_0 = 6 m³/min. **(B)** Case M, Q_0 = 12 m³/min. **(C)** Case A, Q_0 = 18 m³/min.

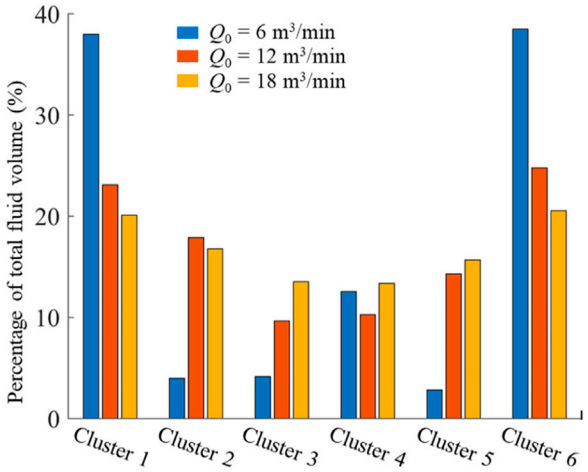

FIGURE 17
The total fluid volume distribution of each cluster for three cases with different injection rates.

of the outer two fractures shows the opposite trend to that of the other four fractures. With the increase of cluster spacing, the curves become flatter. The fracturing fluid received by each fracture within a stage is more similar, indicating that these fractures can propagate more evenly. The total fluid volume distribution of each cluster for the three different cases is shown in Figure 11. The results show that the outer two fractures finally receive much more fracturing fluid than the interior fractures. In addition, the flow volume difference between different fractures decreases with the increase of cluster spacing. When the cluster spacing is 6m, the total fluid volume percentage received by the fractures are 19.23%, 15.98%, 14.36%, 14.87%, 16.62%, and 18.93%, respectively. When the cluster spacing is 14m, the total fluid volume percentage received by the fractures are 19.25%, 16.00%, 15.34%, 15.76%, 14.19%, and 19.46%, respectively. In a word, the flow rate obtained by each fracture is closer with the increase of cluster spacing.

4.3.2 Perforation number

In this section, we will study the effect of perforation number on the multiple fracture propagation under the condition of keeping other parameters constant. Figure 12 shows the fracture morphologies at the end of injection for three different perforation numbers. It can be seen that the difference of geometry of each fracture within a stage becomes smaller with the decrease of the perforation number. Specially, when the number of perforations in each cluster is greater than 8, the perforation number has an obvious impact on the fracture morphologies. When the perforation number of each cluster reaches 12 (1.5 times of Case A), the length and width of the

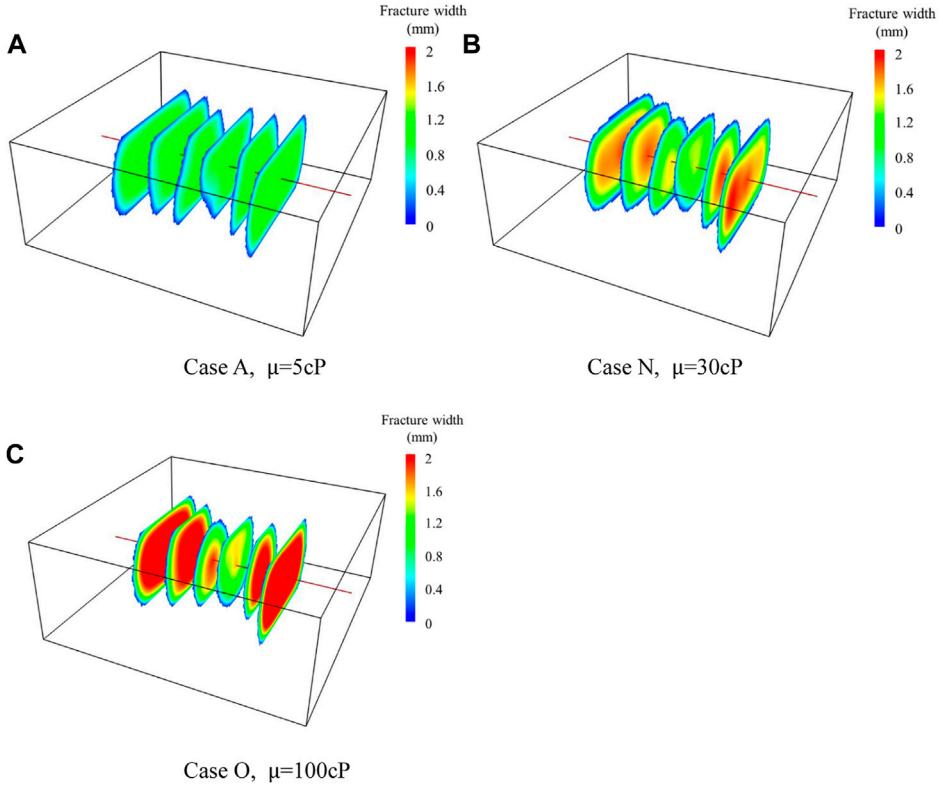

FIGURE 18
Fracture morphology for three cases with different fracturing fluid viscosity. **(A)** Case A, μ = 5 cP. **(B)** Case N, μ = 30 cP. **(C)** Case O, μ = 100 cP.

middle two fractures are significantly smaller than that of the other four fractures. The results can be explained by the theory of limited entry perforation. The perforation hole friction will be increased by reducing the number of perforations. At this time, the resistance of fluid flowing through the holes will increase, and the difference of fluid pressure in the outer and interior fractures will be smaller, thus promoting the uniform propagation of each fracture within a stage. However, comparing Cases J and A, it can be seen that reducing the number of perforations has little effect on the fracture morphologies when the perforation number of each cluster is less than 8. At this time, the influence of perforation friction on fracture propagation is weaker than that of stress interference. In this case, it is necessary to improve the fracture geometries by other measures such as adjusting the cluster spacing. Although the simulation results show that reducing the number of perforations is conducive to promoting the uniform propagation of multiple fractures, significantly reducing the number of perforations will cause high perforation friction and a remarkable increase in wellhead pressure during fracturing treatment. Therefore, the number of perforations should be controlled within a reasonable range.

The change of flow rate with injection time in each cluster is plotted in Figure 13. It can be seen that as the number of perforations decreases, the difference of received fracturing fluid by each fracture is smaller. When the perforation number of each cluster is 6, the total fluid volume percentage received by the fractures are 18.62%, 16.60%, 14.98%, 14.91%, 16.02%, and 18.87%, respectively (As shown in Figure 14). At this time, the flow rate obtained by each fracture within a stage is relatively close. However, the change range of the flow rate curves becomes larger with the increase of perforation number, and the flow rate obtained by each fracture differs a lot during all the injection process. Taking Case K as an example, the number of perforations for each cluster in this case is 12. According to the modeling results, the flow rates of Cluster 1 and Cluster 6 increase rapidly first and then decrease. Different from the simulation results of other cases, the flow rate obtained by these two fractures shows obvious differences due to the effect of wellbore friction. However, wellbore friction plays a small role in other cases. In Case K, the total fluid volume percentage received by the fractures are 24.07%, 18.69%, 7.51%, 9.91%, 13.95%, and 25.88%, respectively (As shown in Figure 14). The results show that increasing the number of perforations can significantly cause the more uneven distribution of flow rate.

4.3.3 Injection rate

In this section, the effect of injection rate on the multiple fracture propagation is investigated keeping other parameters constant. According to the theory of hydraulic fracture, increasing the injection rate will lead to a higher net pressure in the fractures, thus affecting the distribution of stress field near the wellbore and changing the geometries of fractures. In this paper, three cases with different injection rates are investigated. The injection rates are 6 m^3/min, 12 m^3/min, and 18 m^3/min, respectively. Figure 15 illustrates the fracture morphologies under three different injection rates. The results show that the fracture uniformity within a stage increases with an

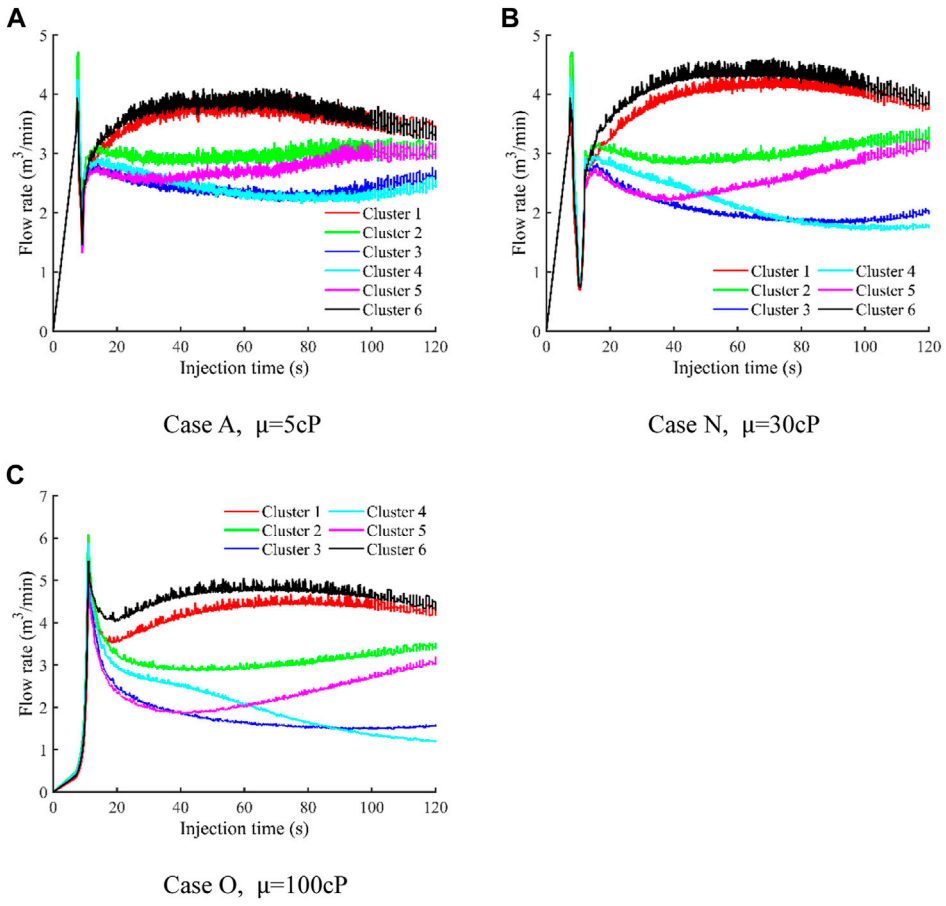

FIGURE 19
Flow rate into each cluster as a function of time for three cases with different fracturing fluid viscosity. **(A)** Case A, μ = 5 cP. **(B)** Case N, μ = 30 cP. **(C)** Case O, μ = 100 cP.

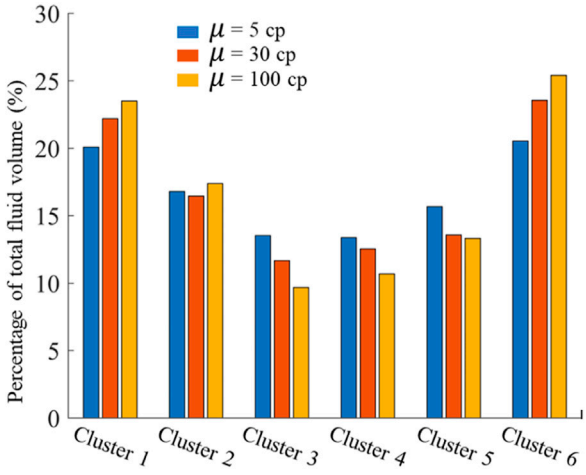

FIGURE 20
The total fluid volume distribution of each cluster for three cases with different fracturing fluid viscosity.

increase in injection rate, especially compared the case L and case M. When the injection rate is 6 m^3/min, the length and width of the outer two fractures are obviously larger than those of the interior fractures, showing remarkable difference of geometric sizes between the outer and interior fractures. For the interior fractures, three of them hardly propagate forward after the initiation, which are greatly restricted, and the other one (Cluster 4) only extends a short distance away the wellbore. When the injection rate increases to 12 m^3/min, the fracture length is more evenly distributed. In the case, the width of interior fractures is increased a lot. The comparison between Case M and Case A shows that the fracture length slightly increases, but the width of the middle two fractures is much higher with the increase of injection rate from 12 m^3/min to 18 m^3/min. In a word, the injection rate has a very significant impact on multiple fracture propagation, and it is beneficial to promote the uniform growth of fractures within a stage by increasing the injection rate.

The change of flow rate with injection time in each cluster is plotted in Figure 16. It can be seen that when the injection rate is 6 m^3/min, the outer two fracture always receive much more fluid during all the injection process even if the curves of flow rate have a slight

downward trend at the final stage. However, only a small proportion of fluid flow into the interior four fractures. The flow rate of three of the four fractures rapidly decreases to nearly zero, which indicates that there will be almost no fluid entering these fractures at that time. However, another fracture (Cluster 4) is less inhibited, and the flow rate is relatively stable at the initial stage and gradually increases at the later. Comparing Cases L, M, and A, it can be seen that much more fluid is received by the interior fractures with the increase of injection rate, and the difference between the shape of each flow rate curve decreases. The results show that the stress interference is weaker under higher injection rate.

The total fluid volume distribution of each cluster for the three different cases is shown in Figure 17. It can be seen that the fluid flows into each fracture more evenly with the increase of injection rate. When the injection rate is 6 m^3/min, the percentage of total fluid volume into different fractures are 37.99%, 3.99%, 4.16%, 12.55%, 2.83%, and 38.50%, respectively. The results indicate that the proportion of flow rate of different fractures varies greatly. When the injection rate reaches 12 m^3/min, the percentage of total fluid volume into different fractures are 23.10%, 17.88%, 9.65%, 10.28%, 14.30%, 24.79%, respectively. This demonstrates that fluid received by the interior inhibited fractures is significantly improved by increasing the injection rate from 6 m^3/min to 12 m^3/min, showing increasing injection rate is one of effective measures to improve the uniformity of multiple fracture growth. In addition, the fluid received by the interior fractures can be further increased with the increase of injection rate from 12 m^3/min to 18 m^3/min. The results show that increasing the injection rate can not only improve the fracture geometries, but also effectively adjust the flow rate received by the fractures. Therefore, the injection rate should be increased as much as possible within the limit of treatment equipment.

4.3.4 Fracturing fluid viscosity

In this section, three cases with different fracturing fluid viscosities are investigated, and the fluid viscosities are 5 cP, 30 cP, and 100 cP, respectively. Figure 18 illustrates the fracture morphologies under three different fracturing fluid viscosities. The results show that the fracture geometry is greatly affected by the fluid viscosity. It can be seen that the increase of fluid viscosity will inhibit the hydraulic fracture to propagate along the direction of the maximum principal stress to a certain extent. However, the fracture width of each fracture is significantly expanded with the increase of fluid viscosity. Comparing Case A and Case N, the length of each fracture decreases in some extent when the fluid viscosity increases from 5 cP to 30 cP. Except that the width of the middle two fractures has hardly changed, the width of the other four fractures increases. Comparing Case N and Case O, the fracture length of each fracture is only slightly decreased when the fluid viscosity increases from 30 cP to 100 cP. The width of the outer four fractures increases largely. However, the width of the middle two fractures only increases a little. By comparison, the generated multiple fractures are more uniform under lower fracturing fluid viscosity. For low-permeability shale reservoirs, the main target is to create long fractures rather than increase conductivity. Therefore, fracturing fluid with lower viscosity is conducive to increase fracture length and multiple fracture uniformity in shale reservoirs, so high injection rate needs to be adopted to increase proppant carrying capacity.

The change of flow rate with injection time in each cluster is plotted in Figure 19. The results show that the difference of dynamic flow rate between the fractures increases with the increase of fracturing fluid viscosity. When the fracturing fluid viscosity increases, the proportion of fracturing fluid obtained by the middle two fractures decreases continuously. The total fluid volume distribution of each fracture for the three different cases is shown in Figure 20. It can be seen that when the fluid viscosity is 5 cP, the percentage of total fluid volume into different fractures are 20.09%, 16.79%, 13.53%, 13.37%, 15.68%, and 20.54%, respectively. When the fluid viscosity reaches 100 cP, the percentage of total fluid volume into different fractures are 23.50%, 17.38%, 9.69%, 10.69%, 13.32%, and 25.40%, respectively. This demonstrates that the outer fractures receive more fluid and the interior fractures receive less fluid with the increase of fracturing fluid viscosity. The results indicate that increasing the viscosity of fracturing fluid will aggravate the stress interference and increase the difference of geometric size between different fractures.

5 Conclusion

The block discrete element method (BDEM) is used to establish a 3D multi-cluster fracturing model of a horizontal well. The effects of various geologic and engineering parameters on the multiple simultaneous fracture propagation within a stage were studied. The suggestions to improve the fracture geometries were proposed according to the modeling results. The main conclusions are as follows:

1) The geometry of each fracture within a stage is different, and the outer fractures generally receive more fracturing fluid than the interior fractures, resulting in the length and width of the outer fracture are generally larger than that of the interior fractures. According to the modeling results, the vertical stress almost has no effect on the geometries of multiple fractures, and higher horizontal stress difference is beneficial to the uniform propagation of multiple fractures, and the width of the middle two fractures is improved with the increase of horizontal stress difference. The existence of bedding planes will aggravate the stress interference effect and decrease the width of the middle two fractures. The activation and propagation along the bedding planes will increase the fluid filtration, resulting in a reduction in hydraulic fracture length.
2) Increasing the cluster spacing can effectively promote the propagation of each fracture, and the inhibition on the interior fractures can be reduced. The difference of received fluid between different fractures decreases with the increase of cluster spacing due to weaker stress interference. The difference of geometry of each fracture becomes smaller with the decrease of perforation number due to effect of limited entry perforation. With the increase of the fracturing fluid viscosity, the fracture length decreases to a certain extent and the fracture width increases significantly. At this time, the squeezing effect of the outer fractures on the middle fractures increases, and the flow rate distribution is much more uneven.
3) For shale reservoirs with bedding planes, a large amount of fracturing fluid should be injected to ensure the propagation of hydraulic fractures and the activation of bedding planes. It is

necessary to use the proppant with smaller size to support the bedding planes. Only increasing cluster spacing is not the primary method to promote uniform propagation of multiple fractures because the seepage distance is farther. Reducing the number of perforations is conducive to the even distribution of flow rates, but causing higher treatment pressure. Therefore, cluster spacing and perforation number should be controlled in an appropriate range according to reservoir properties. On the other hand, increasing the injection rate and reducing the viscosity of fracturing fluid are important means to improve the geometry of each fracture.

Data availability statement

The original contributions presented in the study are included in the article/supplementary material, further inquiries can be directed to the corresponding author.

Author contributions

RH: Investigation, Writing—original draft. JY: Writing—review and editing. LL: Visualization, Writing—review and editing. ZY: Writing—Reviewing and Editing. WC: Writing—original draft. JZ: Writing—review and editing. XL: Validation. LH: Writing—original draft, Conceptualization, Supervision.

Funding

The authors acknowledge the support provided by the National Natural Science Foundation of China (Grant No. 42002271 and 42202314), and natural science starting project of SWPU (No. 2022QHZ009), and Open Research Fund of State Key Laboratory of Geomechanics and Geotechnical Engineering, Institute of Rock and Soil Mechanics, Chinese Academy of Sciences (Grant No. Z020009).

Conflict of interest

Authors RH, JY, LL, WC, and JZ were employed in the company PetroChina Southwest Oil and Gasfield Company.

The remaining authors declare that the research was conducted in the absence of any commercial or financial relationships that could be construed as a potential conflict of interest.

Publisher's note

References

Barree, R. (1983). "A practical numerical simulator for three-dimensional fracture propagation in heterogenous media," in Paper presented at the Reservoir Simulation Symposium, San Francisco, USA, November 1983 (One Petro).

Bunger, A. P., Jeffrey, R. G., Kear, J., and Zhang, X. (2011). "Experimental investigation of the interaction among closely spaced hydraulic fractures," in Paper presented at the 45th US Rock Mechanics/Geomechanics Symposium, San Francisco, USA, June 2011 (One Petro).

Crouch, S. L. (1976). Solution of plane elasticity problems by the displacement discontinuity method. I. Infinite body solution. *Int. J. Numer. Methods Eng.* 10, 301–343. doi:10.1002/nme.1620100206

Crump, J. B., and Conway, M. W. (1988). Effects of perforation-entry friction on bottomhole treating analysis. *J. Petroleum Technol.* 40 (8), 1041–1048. doi:10.2118/15474-pa

Cundall, P. A. (1971). "A computer model for simulating progressive, large-scale movements in blocky rock systems," in Paper presented at the Symposium of International Society of Rock Mechanics, Nancy, France (One Petro).

Dontsov, E. V. (2016). An approximate solution for a penny-shaped hydraulic fracture that accounts for fracture toughness, fluid viscosity and leak-off. *R. Soc. open Sci.* 3 (12), 160737. doi:10.1098/rsos.160737

Dou, F., and Wang, J. (2022). A numerical investigation for the impacts of shale matrix heterogeneity on hydraulic fracturing with a two-dimensional particle assemblage simulation model. *J. Nat. Gas Sci. Eng.* 104, 104678. doi:10.1016/j.jngse.2022.104678

Guo, X., Cheng, M., Zhang, J., Li, H., and Li, Y. (2022). Numerical simulation study of hole erosion under directional perforating conditions. *Xinjiang Oil & Gas* 18 (4), 56–61.

He, R., Yang, Z., Li, X., Liu, C., Sun, Z., and Li, W. (2020). Numerical investigation of interaction between hydraulic and natural fractures under various geologic and engineering parameters using particle flow code method. *Energy Sources, Part A Recovery, Util. Environ. Eff.*, 1757790. doi:10.1080/15567036.2020.1757790

Huang, L., Liu, J., Ji, Y., Gong, X., and Qin, L. (2018). A review of multiscale expansion of low permeability reservoir cracks. *Petroleum* 4 (2), 115–125. doi:10.1016/j.petlm.2017.09.002

Huang, L., Liu, J., Zhang, F., Donstov, E., and Damjanac, B. (2019). Exploring the influence of rock inherent heterogeneity and grain size on hydraulic fracturing using discrete element modeling. *Int. J. Solids Struct.* 176, 207–220. doi:10.1016/j.ijsolstr.2019.06.018

Huang, L., Liu, J., Zhang, F., Fu, H., Zhu, H., and Damjanac, B. (2020). 3D lattice modeling of hydraulic fracture initiation and near-wellbore propagation for different perforation models. *J. Petroleum Sci. Eng.* 191, 107169. doi:10.1016/j.petrol.2020.107169

Huang, L., Donstov, E., Fu, H., Lei, Y., Weng, D., and Zhang, F. (2022). Hydraulic fracture height growth in layered rocks: Perspective from DEM simulation of different propagation regimes. *Int. J. Solids Struct.* 238, 111395. doi:10.1016/j.ijsolstr.2021.111395

Huang, L., He, R., Yang, Z., Tan, P., Chen, W., Li, X., et al. (2023). Exploring hydraulic fracture behavior in glutenite formation with strong heterogeneity and variable lithology based on DEM simulation. *Eng. Fract. Mech.* 278, 109020. doi:10.1016/j.engfracmech.2022.109020

Ji, Y., Wang, Y., and Huang, L. (2015). Analysis on inflowing of the injecting water in faulted formation. *Adv. Mech. Eng.* 7 (6), 168781401559029–10. doi:10.1177/1687814015590294

Jin, Y., and Chen, K. (2019). Fundamental equations for primary fluid recovery from porous media. *J. Fluid Mech.* 860, 300–317. doi:10.1017/jfm.2018.874

Khristianovic, S., and Zheltov, Y. (1955). "Formation of vertical fractures by means of highly viscous fluids," in Paper presented at 4th World Petroleum Congress, Rome, Italy, June 1955 (One Petro).

Li, S., Li, X., and Zhang, D. (2016). A fully coupled thermo-hydro-mechanical, three-dimensional model for hydraulic stimulation treatments. *J. Nat. Gas Sci. Eng.* 34, 64–84. doi:10.1016/j.jngse.2016.06.046

Li, X., Yi, L., Yang, Z., Liu, C., and Yuan, P. (2017). A coupling algorithm for simulating multiple hydraulic fracture propagation based on extended finite element method. *Environ. Earth Sci.* 76, 725. doi:10.1007/s12665-017-7092-9

Linkov, A. M., and Markov, N. S. (2020). Improved pseudo three-dimensional model for hydraulic fractures under stress contrast. *Int. J. Rock Mech. Min. Sci.* 130, 104316. doi:10.1016/j.ijrmms.2020.104316

Liu, N., Zhang, Z., Zou, Y., Ma, X., and Zhang, Y. (2018). Propagation law of hydraulic fractures during multi-staged horizontal well fracturing in a tight reservoir. *Petroleum Explor. Dev.* 45 (6), 1129–1138. doi:10.1016/s1876-3804(18)30116-2

Luo, H., Xie, J., Huang, L., Wu, J., Shi, X., Bai, Y., et al. (2022). Multiscale sensitivity analysis of hydraulic fracturing parameters based on dimensionless analysis method. *Lithosphere* 2022, 9708300. doi:10.2113/2022/9708300

Miller, C., Waters, G., and Rylander, E. (2011). "Evaluation of production log data from horizontal wells drilled in organic shales," in Paper presented at the SPE North American Unconventional Gas Conference and Exhibition, Woodlands, USA, June 2011 (One Petro).

Palmer, I. D., Roberts, O., and Carroll, H. B. (1983). "Numerical solution for height and elongated hydraulic fractures," in Paper presented at the 1983 SPE/DOE Symposium on Low Permeability, Denver, USA, March 1983 (One Petro).

Peirce, A., and Bunger, A. P. (2014). Interference fracturing: Nonuniform distributions of perforation clusters that promote simultaneous growth of multiple hydraulic fractures. *SPE J.* 20 (2), 384–395. doi:10.2118/172500-pa

Sesetty, V., and Ghassemi, A. (2015). A numerical study of sequential and simultaneous hydraulic fracturing in single and multi-lateral horizontal wells. *J. Petroleum Sci. Eng.* 132, 65–76. doi:10.1016/j.petrol.2015.04.020

Settari, A., and Cleary, M. P. (1986). Development and testing of a pseudo-three-dimensional model of hydraulic fracture geometry. *SPE Prod. Eng.* 1 (6), 449–466. doi:10.2118/10505-pa

Shi, F., Wang, X., Liu, C., Liu, H., and Wu, H. (2016). A coupled extended finite element approach for modeling hydraulic fracturing in consideration of proppant. *J. Nat. Gas Sci. Eng.* 33, 885–897. doi:10.1016/j.jngse.2016.06.031

Somanchi, K., Brewer, J., and Reynolds, A. (2017). "Extreme limited entry design improves distribution efficiency in plug-n-perf completions: Insights from fiber-optic diagnostics," in Paper presented at the SPE Hydraulic Fracturing Technology Conference and Exhibition, Woodlands, USA, January 2017 (One Petro).

Song, R., Wang, Y., Sun, S., and Liu, J. (2021). Characterization and microfabrication of natural porous rocks: From micro-CT imaging and digital rock modelling to micro-3D-printed rock analogs. *J. Petroleum Sci. Eng.* 205, 108827. doi:10.1016/j.petrol.2021.108827

Tan, P., Jin, Y., Han, K., Hou, B., Chen, M., Guo, X., et al. (2017). Analysis of hydraulic fracture initiation and vertical propagation behavior in laminated shale formation. *Fuel* 206, 482–493. doi:10.1016/j.fuel.2017.05.033

Tan, P., Pang, H., Zhang, R., Jin, Y., Zhou, Y., Kao, J., et al. (2020). Experimental investigation into hydraulic fracture geometry and proppant migration characteristics for southeastern Sichuan deep shale reservoirs. *J. Petroleum Sci. Eng.* 184, 106517. doi:10.1016/j.petrol.2019.106517

Tan, P., Jin, Y., and Pang, H. (2021). Hydraulic fracture vertical propagation behavior in transversely isotropic layered shale formation with transition zone using XFEM-based CZM method. *Eng. Fract. Mech.* 248, 107707. doi:10.1016/j.engfracmech.2021.107707

Tang, H., Winterfeld, P., Wu, Y., Huang, Z., Di, Y., Pan, Z., et al. (2016). Integrated simulation of multi-stage hydraulic fracturing in unconventional reservoirs. *J. Nat. Gas Sci. Eng.* 36, 875–892. doi:10.1016/j.jngse.2016.11.018

Tang, H., Wang, S., Zhang, R., Li, S., Zhang, L., and Wu, Y. (2019). Analysis of stress interference among multiple hydraulic fractures using a fully three-dimensional displacement discontinuity method. *J. Petroleum Sci. Eng.* 179, 378–393. doi:10.1016/j.petrol.2019.04.050

Wang, Y., Song, R., Liu, J., Cui, M., and Ranjith, P. G. (2019). Pore scale investigation on scaling-up micro-macro capillary number and wettability on trapping and mobilization of residual fluid. *J. Contam. Hydrology* 225, 103499. doi:10.1016/j.jconhyd.2019.103499

Wang, Y., Zhu, C., He, M., Wang, X., and Le, H. (2022). Macro-meso dynamic fracture behaviors of xinjiang marble exposed to freeze thaw and frequent impact disturbance loads: A lab-scale testing. *Geomechanics Geophys. Geo-Energy Geo-Resources* 8 (5), 154. doi:10.1007/s40948-022-00472-5

Wang, H., Li, H., Tang, L., Ren, X., Meng, Q., and Zhu, C. (2022). Fracture of two three-dimensional parallel internal cracks in brittle solid under ultrasonic fracturing. *J. Rock Mech. Geotechnical Eng.* 14 (3), 757–769. doi:10.1016/j.jrmge.2021.11.002

Wu, K., and Olson, J. E. (2013). Investigation of the impact of fracture spacing and fluid properties for interfering simultaneously or sequentially generated hydraulic fractures. *SPE Prod. Operations* 28 (4), 427–436. doi:10.2118/163821-pa

Wu, K., and Olson, J. E. (2016). Mechanisms of simultaneous hydraulic-fracture propagation from multiple perforation clusters in horizontal wells. *SPE J.* 21 (3), 1000–1008. doi:10.2118/178925-pa

Yang, Z., Yi, L., Li, X., and He, W. (2018). Pseudo-three-dimensional numerical model and investigation of multi-cluster fracturing within a stage in a horizontal well. *J. Petroleum Sci. Eng.* 162, 190–213. doi:10.1016/j.petrol.2017.12.034

Yin, Z., Huang, H., Zhang, F., Zhang, L., and Maxwell, S. (2020). Three-dimensional distinct element modeling of fault reactivation and induced seismicity due to hydraulic fracturing injection and backflow. *Geotech. Eng.* 12, 752–767. doi:10.1016/j.jrmge.2019.12.009

Zhang, F., and Dontsov, E. (2018). Modeling hydraulic fracture propagation and proppant transport in a two-layer formation with stress drop. *Eng. Fract. Mech.* 199, 705–720. doi:10.1016/j.engfracmech.2018.07.008

Zhang, F., Dontsov, E., and Mack, M. (2017). Fully coupled simulation of a hydraulic fracture interacting with natural fractures with a hybrid discrete-continuum method. *Int. J. Numer. Anal. Methods Geomechanics* 41 (13), 1430–1452. doi:10.1002/nag.2682

Zhang, S., Chen, M., Ma, X., Zou, Y., and Guo, T. (2021). Research progress and development direction of hydrofracturing design models. *Xinjiang Oil & Gas* 17 (3), 67–73.

Zhang, F., Huang, L., Yang, L., Dontsov, E., Weng, D., Liang, H., et al. (2022). Numerical investigation on the effect of depletion-induced stress reorientation on infill well hydraulic fracture propagation. *Petroleum Sci.* 19 (1), 296–308. doi:10.1016/j.petsci.2021.09.014

Zhao, J., Chen, X., Li, Y., and Fu, B. (2016). Simulation of simultaneous propagation of multiple hydraulic fractures in horizontal wells. *J. Petroleum Sci. Eng.* 147, 788–800. doi:10.1016/j.petrol.2016.09.021

Zheng, Y., He, R., Huang, L., Bai, Y., Wang, C., Chen, W., et al. (2022). Exploring the effect of engineering parameters on the penetration of hydraulic fractures through bedding planes in different propagation regimes. *Comput. Geotechnics* 146, 104736. doi:10.1016/j.compgeo.2022.104736

Zhou, Y., and Yang, D. (2022). A fast simulation method for hydraulic-fracture-network generation in fractured rock based on fully coupled XFEM. *Comput. Geotechnics* 150, 104892. doi:10.1016/j.compgeo.2022.104892

Zhu, C., Xu, X., Wang, X., Xiong, F., Tao, Z., Lin, Y., et al. (2019). Experimental investigation on nonlinear flow anisotropy behavior in fracture media. *Geofluids* 2019 (9), 1–9. doi:10.1155/2019/5874849

frontiers | Frontiers in Earth Science

TYPE Original Research
PUBLISHED 25 January 2023
DOI 10.3389/feart.2023.1119946

OPEN ACCESS

EDITED BY
Peng Tan,
CNPC Engineering Technology R & D Company Limited, China

REVIEWED BY
Xian Shi,
China University of Petroleum, Huadong, China
Hao Yang,
China University of Geosciences, China
Zhang Yan,
Yangtze University, China

*CORRESPONDENCE
Mian Chen,
chenm@cup.edu.cn

SPECIALTY SECTION
This article was submitted to Environmental Informatics and Remote Sensing, a section of the journal Frontiers in Earth Science

RECEIVED 09 December 2022
ACCEPTED 10 January 2023
PUBLISHED 25 January 2023

CITATION
Jiang H, Chen M, Hua C, Li X and Zhang Y (2023), Analysis of influencing factors on wellbore instability for high-pressure gas well during testing and production. *Front. Earth Sci.* 11:1119946. doi: 10.3389/feart.2023.1119946

Analysis of influencing factors on wellbore instability for high-pressure gas well during testing and production

Hailong Jiang[1,2], Mian Chen[1]*, Chao Hua[3], Xiao Li[2] and Yong Zhang[2]

[1]State Key Laboratory of Petroleum Resources and Prospecting, China University of Petroleum, Beijing, China, [2]College of Mechanical Engineering, Xi'an Shiyou University, Xi'an, Shannxi, China, [3]Xi'an Qing'an Electrical Control Co., Ltd, Xi'an, Shannxi, China

Unlike normal-pressure gas wells, wellbore instability is more likely to occur during testing for high-pressure gas wells. Gas acceleration effect exists in gas flow during high-pressure gas well testing, which was ignored in previous wellbore instability analysis. In this paper, the developments of effective circumferential stress and effective radial stress are analyzed in the near-wellbore area of high-pressure gas well, considering the influence of *in-situ* stress non-uniformity and acceleration effect. To analyze the effective circumferential stress and the effective radial stress more accurately, it is established that the fluid-structure coupling stress field of the finite large thick wall cylinder The flow field considers three cases, namely Darcy's law, Darcy–Forchheimer model and Darcy-Forchheime model considering gas acceleration. The results show that *in-situ* stress non-uniformity has a similar influence on tensile failure and shear failure. It is observed that the location of occurring shear failure and tensile failure may not be on the wellbore wall. When the formation fluid is under abnormally high pressure, it is more likely to have a tensile failure, while when the formation fluid is under abnormally low pressure, it is more likely to have a shear failure. The Biot parameter has the same effect on tensile failure and shear failure. These results are helpful to control sand production during testing and production for high-pressure gas wells.

KEYWORDS

acceleration effect, non-uniform *in situ* stress, wellbore instability, tensile failure, shear failure

1 Introduction

High-pressure gas reservoirs are characterized by natural fractures, high formation pressure and large variation of a production pressure difference which is on account of depletion production. In the process of gas test production, the non-Darcy characteristic of high speed is the prominent characteristic of high-pressure gas flow, which is not only manifested in the inertial resistance, but also in the significant gas acceleration effect induced by the rapid expansion of the gas volume (Jin et al., 2011a; Chen et al., 2011; Jin et al., 2012). The characteristic makes the spatio-temporal evolution of gas pressure more complex (Jin et al., 2019; Zhang et al., 2021; Hou et al., 2022a; Zhang et al., 2022). Traditionally, the inertial effect of near-wellbore gas flow is simply expressed by adding the Forchheimer inertial drag to Darcy's Law. However, this description of the inertial effects of compressible fluid flows is incomplete. Wooding (1957) might be the first to add an accelerated-inertial term to the gas momentum equation. The model with the accelerated-inertial term has been discussed in detail for a high-speed compressible flow in porous media (Nield, 1994; Levy et al., 1995; Chang and Hou, 2022). Jiang et al. (2015a; 2015b; 2015c; 2016) finds the reason why the gas

acceleration effect was ignored in the past literature and analyzes the importance of the gas acceleration effect in detail. Jin et al. (2011b) establishes a plane radial model considering the acceleration effect and presents a method for quantitative evaluation of the gas acceleration effect. Tensile stress is easy to form in the surrounding rock stress of the wellbore wall considering the acceleration effect by analyzing the fluid-structure coupling stress equation in the infinite thick-walled cylinder. The relationship of effective radial stress under different seepage models is not pointed out. Wellbore instability failure is usually divided into two categories, one is a shear failure, and the other is a tension failure. The current research focuses on shear failure (Zhao et al., 2021; Hou et al., 2022b; Hou et al., 2022c; Warsitzka et al., 2022), while the strength of extension is frequently used in analyzing tensile failure for wellbore instability during testing and production (Tan et al., 2021; Hou et al., 2022d; Sun et al., 2022; Hou et al., 2022e; Huang et al., 2023).

In this paper, we investigate the properties of near-wellbore stress using a set of equations that is built in the finite thick-walled cylinder in the non-uniform *in-situ* stress field. It is proved that the acceleration effect increases the possibility of tensile and shear failure. It is shown that the two types of failure do not necessarily occur on the wellbore wall. It is also shown that when the formation fluid is under abnormally high pressure, it is more likely to have a tensile failure, while when the formation fluid is under abnormally low pressure, it is more likely to have a shear failure. The Biot parameter has the same effect on tensile failure and shear failure.

2 Wellbore stress distributions in the finite large thick wall cylinder model

The stratum is assumed to be a uniform isotropic, linear elastic porous material, and the surrounding rock is considered to be in a plane strain state. σ_H is the horizontal maximum stress and σ_h is the horizontal minimum stress. The stress distributions for a radially varying pore pressure given by Eqs. (4.51)–(4.52) in the literature (Fjaer et al., 2008) is under the uniform stress field. The wellbore stress under the non-uniform *in-situ* stress can be obtained by changing both equations according to the theory of elasticity. The new wellbore stress distributions are:

$$\begin{aligned}
\sigma_r &= \frac{(\sigma_H+\sigma_h)}{2}\left(\frac{{R_e}^2}{{R_e}^2-{R_w}^2}-\frac{{R_e}^2{R_w}^2}{({R_e}^2-{R_w}^2)r^2}\right)+\frac{R_w^2({R_e}^2-r^2)p_w}{r^2(R_e^2-R_w^2)}\\
&+\frac{(\sigma_H-\sigma_h)}{2}\left(\frac{{R_e}^2({R_e}^4+{R_e}^2{R_w}^2+4{R_w}^4)}{(R_e^2-R_w^2)^3}+\frac{3{R_e}^4{R_w}^4({R_e}^2+{R_w}^2)}{(R_e^2-R_w^2)^3r^4}\right.\\
&\left.-4\frac{{R_e}^2{R_w}^2({R_e}^4+R_e^2R_w^2+{R_w}^4)}{(R_e^2-R_w^2)^3r^2}\right)\cos 2\theta\\
&+\frac{2\eta}{r^2}\left[\int_{R_w}^{r} r'\Delta p(r')dr'-\frac{r^2-{R_w}^2}{R_e^2-{R_w}^2}\int_{R_w}^{R_e} r'\Delta p(r')dr'\right]\\
\sigma_\theta &= \frac{(\sigma_H+\sigma_h)}{2}\left(\frac{{R_e}^2}{{R_e}^2-{R_w}^2}+\frac{{R_e}^2{R_w}^2}{({R_e}^2-{R_w}^2)r^2}\right)-\frac{R_w^2({R_e}^2+r^2)p_w}{r^2(R_e^2-R_w^2)}\\
&-\frac{(\sigma_H-\sigma_h)}{2}\left(\frac{{R_e}^2({R_e}^4+{R_e}^2{R_w}^2+4{R_w}^4)}{(R_e^2-R_w^2)^3}+\frac{3{R_e}^4{R_w}^4({R_e}^2+{R_w}^2)}{(R_e^2-R_w^2)^3r^4}\right.\\
&\left.-\frac{12{R_e}^2{R_w}^2r^2}{(R_e^2-R_w^2)^3}\right)\cos 2\theta+2\eta\Delta p(r\\
&-\frac{2\eta}{r^2}\left[\int_{R_w}^{r} r'\Delta p(r')dr'+\frac{r^2+{R_w}^2}{R_e^2-{R_w}^2}\int_{R_w}^{R_e} r'\Delta p(r')dr'\right]
\end{aligned}\tag{1}$$

where $\eta=(1-2\nu_{fr})\alpha_B/2(1-\nu_{fr})$ is the poroelastic coefficient, $\Delta p(r)=p(r)-p_e$, and υ_{fr} is the rock frame Poisson ratio.

When σ_H is equal to σ_h, Equation 1 will be simplified to Eqs. (4.51)–(4.52) in the literature (Fjaer et al., 2008). The dimensionless stress distributions related to Equation 1 are:

$$\begin{aligned}
\sigma_r &= \frac{A}{2}\left(\frac{{R_e}^2}{{R_e}^2-1}-\frac{{R_e}^2}{({R_e}^2-1)r^2}\right)+\frac{({R_e}^2-r^2)D}{r^2({R_e}^2-1)}\\
&+\frac{B}{2}\left(\frac{{R_e}^2({R_e}^4+{R_e}^2+4)}{({R_e}^2-1)^3}+\frac{3{R_e}^4({R_e}^2+1)}{({R_e}^2-1)^3r^4}-4\frac{{R_e}^2({R_e}^4+{R_e}^2+1)}{({R_e}^2-1)^3r^2}\right)\cos 2\theta\\
&+\frac{2\eta}{r^2}\left[\int_1^r r'\Delta p(r')dr'-\frac{r^2-1}{R_e^2-1}\int_1^{R_e} r'\Delta p(r')dr'\right]\\
\sigma_\theta &= \frac{A}{2}\left(\frac{{R_e}^2}{{R_e}^2-1}+\frac{{R_e}^2}{({R_e}^2-1)r^2}\right)-\frac{({R_e}^2+r^2)D}{r^2({R_e}^2-1)}\\
&-\frac{B}{2}\left(\frac{{R_e}^2({R_e}^4+{R_e}^2+4)}{({R_e}^2-1)^3}+\frac{3{R_e}^4({R_e}^2+1)}{({R_e}^2-1)^3r^4}-\frac{12{R_e}^2r^2}{({R_e}^2-1)^3}\right)\cos 2\theta\\
&+2\eta\Delta p(r)-\frac{2\eta}{r^2}\left[\int_1^r r'\Delta p(r')dr'+\frac{r^2-1}{R_e^2-1}\int_1^{R_e} r'\Delta p(r')dr'\right]
\end{aligned}\tag{2}$$

where $A=\sigma_H+\sigma_h/p_e$, where $(A>2)$, $B=\sigma_H+\sigma_h/p_e$, $D=p_w/p_e$, where $(D<1)$, and $\Delta p(r)=p(r)-1$.

The dimensionless effective stress distributions are:

$$\begin{aligned}
{\sigma_r}' &= \sigma_r-\alpha_B p(r)=\frac{A}{2}\left(\frac{{r_e}^2}{{r_e}^2-1}-\frac{{r_e}^2}{({r_e}^2-1)r^2}\right)+\frac{({r_e}^2-r^2)D}{r^2({r_e}^2-1)}\\
&+\frac{B}{2}\left(\frac{{r_e}^2({r_e}^4+{r_e}^2+4)}{({r_e}^2-1)^3}+\frac{3{r_e}^4({r_e}^2+1)}{({r_e}^2-1)^3r^4}-4\frac{{r_e}^2({r_e}^4+{r_e}^2+1)}{({r_e}^2-1)^3r^2}\right)\cos 2\theta\\
&+\frac{2\eta}{r^2}\left[\int_1^r r'\Delta p(r')dr'-\frac{r^2-1}{r_e^2-1}\int_1^{r_e} r'\Delta p(r')dr'\right]-\alpha_B p(r)\\
{\sigma_\theta}' &= \sigma_\theta-\alpha_B p(r)=\frac{A}{2}\left(\frac{{r_e}^2}{{r_e}^2-1}+\frac{{r_e}^2}{({r_e}^2-1)r^2}\right)-\frac{({r_e}^2+r^2)D}{r^2({r_e}^2-1)}\\
&-\frac{B}{2}\left(\frac{r_e^2({r_e}^4+r_e^2+4)}{({r_e}^2-1)^3}+\frac{3{r_e}^4({r_e}^2+1)}{({r_e}^2-1)^3r^4}-\frac{12r_e^2r^2}{({r_e}^2-1)^3}\right)\cos 2\theta\\
&+2\eta\Delta p(r)-\frac{2\eta}{r^2}\left[\int_1^r r'\Delta p(r')dr'+\frac{r^2-1}{r_e^2-1}\int_1^{r_e} r'\Delta p(r')dr'\right]-\alpha_B p(r)
\end{aligned}\tag{3}$$

where α_B is the Biot parameter.

3 Analysis of the influence of acceleration effect on the wellbore stress

The traditional Darcy–Forchheimer model is not suitable for characterizing the flow of high-pressure gas into the well, so the acceleration effect of gas should be considered (Jin et al., 2011; Chen et al., 2011; Jin et al., 202). The acceleration effect of near-wellbore gas can be characterized by the dimensionless quantity λ. After considering the acceleration effect, the three characteristics of gas flow in high-pressure gas wells are:

1) With the decrease of bottomhole pressure, there is a maximum mass flow rate of fluid into the well, $m_{\max}$.

$$m_{\max}=\sqrt{\lambda}D \tag{4}$$

2) The gas pressure gradient of the three flow models which are Darcy's law, the Darcy-Forchheime model and the Darcy-Forchheime model considering gas acceleration has the

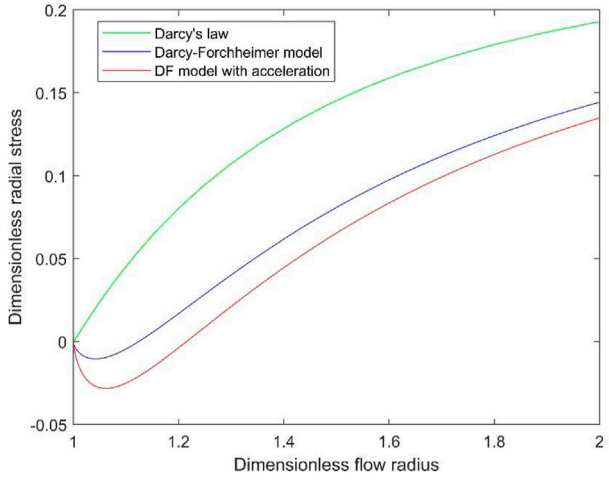

FIGURE 1
The effective radial stress distribution for the three flow models.

following relation when the mass flow is the same. The subscript *AC* stands for the Darcy-Forchheime model considering gas acceleration, *DF* is the Darcy-Forchheime model, and *D* points to Darcy's law.

$$\left(\frac{dp}{dr}\right)_{AC} > \left(\frac{dp}{dr}\right)_{DF} > \left(\frac{dp}{dr}\right)_{D} \tag{5}$$

3) Under the same mass flow rate, the bottomhole pressure of the three models has the following relationship.

$$(D)_{AC} < (D)_{DF} < (D)_{D} \tag{6}$$

3.1 Comparative analysis of effective radial stress

Jin et al. (2011b) believed that the effective radial stress in the near-wellbore zone is more likely to change into tensile stress after considering the acceleration effect, but he did not give the relative size for the effective radial stress of the three flow models. To facilitate the analysis of this relationship, the inhomogeneity of *in-situ* stress is ignored, i.e., *B*=0, and the Biot parameter is equal to 1. According to Eq. 3, $\sigma_r'|_{r=1,\alpha_B=1} = 0$ for the three flow models.

The derivative of effective radial stress for Darcy's law is:

$$\left(\frac{d\sigma_r'}{dr}|_{r=1}\right)_D = \frac{d\sigma_r}{dr}|_{r=1} - \frac{dp}{dr}|_{r=1} = \frac{r_e{}^2 A}{r_e{}^2-1} - 2\left(\frac{r_e{}^2}{r_e{}^2-1}-\eta\right)D_D - 2\eta\bar{p}_D - \frac{m_D}{D_D} \tag{7}$$

where $\bar{p}_D = 2/r_e^2 - 1\int_1^{r_e}(r'p(r'))dr'$.

The derivative of effective radial stress for the Darcy–Forchheimer model can be given by

$$\left(\frac{d\sigma_r'}{dr}|_{r=1}\right)_{DF} = \frac{d\sigma_r}{dr}|_{r=1} - \frac{dp}{dr}|_{r=1} = \frac{r_e{}^2 A}{r_e{}^2-1} - 2\left(\frac{r_e{}^2}{r_e{}^2-1}-\eta\right)D_{DF} - 2\eta\bar{p}_{DF} - \frac{1}{D_{DF}}\left(m_{DF} + \frac{\delta}{\lambda}m_{DF}{}^2\right) \tag{8}$$

where δ/λ is constant.

The derivative of effective radial stress for the Darcy–Forchheimer model considering gas acceleration becomes

$$\left(\frac{d\sigma_r'}{dr}|_{r=1}\right)_{AC} = \frac{d\sigma_r}{dr}|_{r=1} - \frac{dp}{dr}|_{r=1} = \frac{r_e{}^2 A}{r_e{}^2-1} - 2\left(\frac{r_e{}^2}{r_e{}^2-1}-\eta\right)D_{AC} - 2\eta\bar{p}_{AC} - \frac{1}{D_{AC}}\frac{m_{AC}+\frac{\delta}{\lambda}m_{AC}{}^2 + m_{AC}{}^2/\lambda}{1-(m_{AC}{}^2/(\lambda D_{AC}^2))} \tag{9}$$

The difference in derivative of effective stress on the wellbore between Darcy's law and Darcy–Forchheimer model with the same mass flow rate is:

$$\left(\frac{d\sigma_r'}{dr}|_{r=1}\right)_D - \left(\frac{d\sigma_r'}{dr}|_{r=1}\right)_{DF} = m\left(\frac{1}{D_{DF}}-\frac{1}{D_D}\right) + \frac{\delta}{\lambda}\frac{m^2}{D_{DF}} - \left[2\eta\left(\bar{p}_D-\bar{p}_{DF}\right) + 2\left(\frac{r_e{}^2}{r_e{}^2-1}-\eta\right)(D_D-D_{DF})\right] \tag{10}$$

where, $2\eta(\bar{p}_D-\bar{p}_{DF}) + 2(r_e{}^2/r_e{}^2-1-\eta)(D_D-D_{DF}) < 2(r_e{}^2/r_e{}^2-1-\eta)(D_D-D_{DF})$.

We can obtain $(d\sigma_r'/dr|_{r=1})_D - (d\sigma_r'/dr|_{r=1})_{DF} > 0$ labeled Equation 11, when $m \geq \frac{\frac{1}{D_D}-\frac{1}{D_{DF}} + \sqrt{(\frac{1}{D_{DF}}-\frac{1}{D_D})^2 + 8\frac{\delta}{\lambda D_{DF}}(\frac{r_e{}^2}{r_e{}^2-1}-\eta)(D_D-D_{DF})}}{2\delta/\lambda/D_{DF}} = m_1$.

The given distance r_a must exist. $(\sigma_r')_D > (\sigma_r')_{DF}$, when the radius in polar coordinates is between 1 and r_a, i.e., $1 < r < r_a$, combining $\sigma_r'|_{r=1,\alpha_B=1} = 0$.

The difference in derivative of effective stress on the wellbore between Darcy–Forchheimer model and Darcy–Forchheimer model considering gas acceleration with the same mass flow rate is:

$$\left(\frac{d\sigma_r'}{dr}|_{r=1}\right)_{DF} - \left(\frac{d\sigma_r'}{dr}|_{r=1}\right)_{AC} = \frac{1}{D_{AC}}\frac{m+\frac{\delta}{\lambda}m^2+m^2/\lambda}{1-(m_{AC}^2/(\lambda D_{AC}^2))} - \frac{1}{D_{DF}}\left(m+\frac{\delta}{\lambda}m^2\right) - \left[2\eta\left(\bar{p}_{DF}-\bar{p}_{AC}\right) + 2\left(\frac{r_e{}^2}{r_e{}^2-1}-\eta\right)(D_{DF}-D_{AC})\right]$$

where $\frac{1}{D_{AC}}\frac{m+\frac{\delta}{\lambda}m^2+m^2/\lambda}{1-(m^2/(\lambda D_{AC}^2))} - \frac{1}{D_{DF}}(m+\frac{\delta}{\lambda}m^2) > \frac{m+\frac{\delta}{\lambda}m^2+m^2/\lambda}{D_{AC}} - \frac{1}{D_{DF}}(m+\frac{\delta}{\lambda}m^2) > m^2[\frac{\delta}{\lambda}(\frac{1}{D_{AC}}-\frac{1}{D_{DF}}) + \frac{1}{\lambda D_{AC}}]$, and $2\eta(\bar{p}_{DF}-\bar{p}_{AC}) + 2(\frac{r_e^2}{r_e^2-1}-\eta)(D_{DF}-D_{AC}) < 2(\frac{r_e^2}{r_e^2-1}-\eta)(D_{DF}-D_{AC})$.

We can find $(\frac{d\sigma_r'}{dr}|_{r=1})_{DF} - (\frac{d\sigma_r'}{dr}|_{r=1})_{AC} > 0$, which is marked as Equation 12 when $m \geq \sqrt{\frac{2(r_e^2/r_e^2-1-\eta)(D_{DF}-D_{AC})}{\frac{\delta}{\lambda}(1/D_{AC}-1/D_{DC})+1/D_{\lambda AC}}} = m_2$.

As well, the given distance r_b must exist. $(\sigma_r')_{DF} > (\sigma_r')_{AC}$, when the radius in polar coordinates is between 1 and r_b, i.e., $1 < r < r_b$, combining $\sigma_r'|_{r=1,\alpha_B=1} = 0$.

Combining equation 11 and 12, we can get $(\sigma_r')_D > (\sigma_r')_{DF} > (\sigma_r')_{AC}$, when $\sqrt{\lambda}D_{AC} \geq m \geq \max(m_1, m_2)$ and $1 < r < \min(r_a, r_b)$.

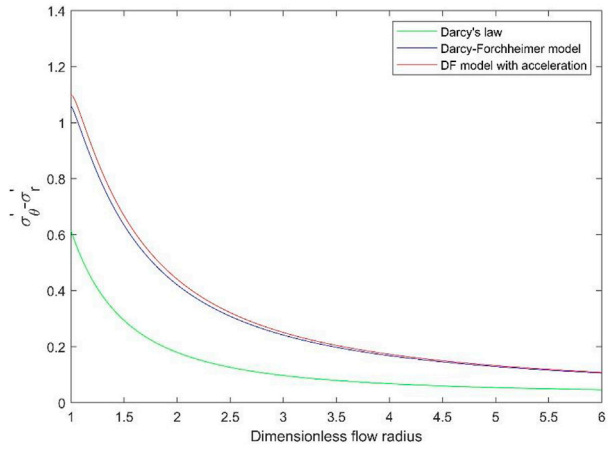

FIGURE 2
Difference between effective circumferential stress and effective radial stress for the three flow models.

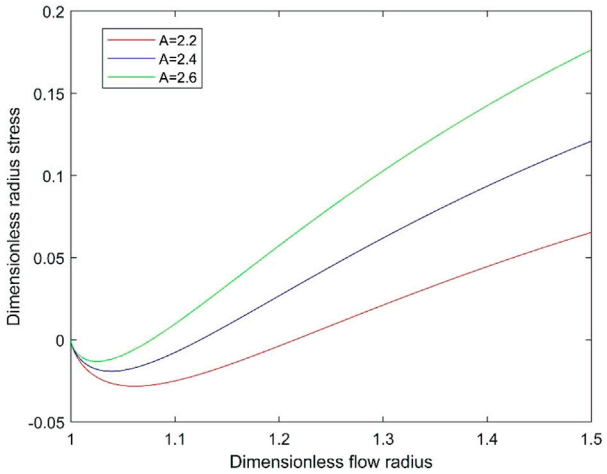

FIGURE 3
The effective radial stress distribution the acceleration flow for various *A*

It is quite clear that $(\sigma_r')_D > (\sigma_r')_{DF} > (\sigma_r')_{AC}$ even if $\alpha_B < 1$.

Effective radial stress near the wellbore must be a negative value when $d(\sigma_r')_{AC}/dr|_{r=1} < 0$. We can find that the effective radial stress is minimal for the Darcy–Forchheimer model considering gas acceleration because $(\sigma_r')_D > (\sigma_r')_{DF} > (\sigma_r')_{AC}$. In other words, the tensile stress is minimal for the Darcy–Forchheimer model considering gas acceleration.

According to Equations 7 and 8 and 9, we can obtain $(d\sigma_r/dr)_D < (\sigma_r/dr)_{DF} < (\sigma_r/dr)_{AC}$ and the pore pressure gradient plays a decisive role in the effective radial stress by using Equation 5.

To better observe the variation in tensile stress, a case is presented. The mass flow rate, m, equals 0.0412 which is bigger than the maximum between m_1 equal to 0.0232 and m_2.given by 0.0245. Set other parameters as follows. $r_e = 2000$, $\eta = 0.5$, $\lambda = 0.5$, $\delta = 50$, $A = 2.2$, and $B = 0$. In the above parameters, the distribution of the stress for the three flow models is illustrated in Figure 1. Firstly, for Darcy's law, the effective radial stress on the wellbore is zero, which is the minimum in the stress distribution. Secondly, for the Darcy-Forchheimer model, the effective radial stress at r=1.0395 equals −0.0105, which is the minimum. Finally, for the Darcy-Forchheimer model, the effective radial stress is equal to −0.0282 at r=1.0568, which is the minimum, i.e., it is 2.82MPA when the formation pressure is 100 MPa.

3.2 Difference between effective circumferential stress and effective radial stress

For the convenience of comparative analysis, the inhomogeneity of *in-situ* stress is not considered here, and the Biot parameter is assumed to be one.

From Equation 2, we can conclude that

$$\sigma_\theta|_{r=1} = \frac{r_e{}^2 A - (r_e{}^2+1)D}{r_e{}^2-1} + 2\eta(D-1) = \left(\frac{A}{1-\frac{1}{r_e^2}} - 2\eta\right) - \left(\frac{1+\frac{1}{r_e^2}}{1-\frac{1}{r_e^2}} - 2\eta\right)D$$

where $\frac{A}{1-\frac{1}{r_e^2}} - 2\eta > 0$, and $\frac{1+\frac{1}{r_e^2}}{1-\frac{1}{r_e^2}} - 2\eta > 0$.

When the mass flow rates of the three flow models are the same, the wellbore pressure can be written as $(D)_{AC} < (D)_{DF} < (D)_D$. Then, we have $(\sigma_\theta|_{r=1})_{AC} > (\sigma_\theta|_{r=1})_{DF} > (\sigma_\theta|_{r=1})_D$ and $(\sigma_\theta'|_{r=1})_{AC} > (\sigma_\theta'|_{r=1})_{DF} > (\sigma_\theta'|_{r=1})_D$.

Because the effective radial stresses on the wellbore for the three flow models are zero, it can be obtained that

$$\left(\sigma_\theta'|_{r=1} - \sigma_r'|_{r=1}\right) > {}_{AC}\left(\sigma_\theta'|_{r=1} - \sigma_r'|_{r=1}\right)_{DF} > \left(\sigma_\theta'|_{r=1} - \sigma_r'|_{r=1}\right)_D \quad (11)$$

It is quite clear that Equation 13 is correct, even if $\alpha_B < 1$.

When $1 < r < r_e$, from Equation 3, we have

$$\sigma_\theta' = \frac{r_e^2(r^2+1)A}{2r^2(r_e^2-1)} - \frac{r_e^2+r^2}{r^2(r_e^2-1)}D + (2\eta-\alpha_B)p(r) - \frac{2\eta}{r^2}\left[\int_1^r r'p(r')dr' + \frac{r^2-1}{r_e^2-1}\int_1^{r_e} r'p(r')dr'\right] - \frac{2\eta}{r^2}$$

As long as $\eta \le \alpha_B/2$, σ_θ' and $p(r)$ are negatively correlated for the same mass flow rate. Then we can conclude that $(\sigma_\theta')_{AC} > (\sigma_\theta')_{DF} > (\sigma_\theta')_D$, where $1 \le r < r_e$. The accelerating flow has the highest difference:

$$\left(\sigma_\theta' - \sigma_r'\right)_{AC} > \left(\sigma_\theta' - \sigma_r'\right)_{DF} > \left(\sigma_\theta' - \sigma_r'\right)_D \quad (12)$$

To better observe the variation in the difference between effective circumferential stress and effective radial stress, a case is presented. When the other parameters are set to $m = 0.0412$, $r_e = 2000$, $\eta = 0.5$, $\lambda = 0.5$, $\delta = 50$, $A = 2.2$, and $B = 0$, the difference is shown in Figure 2. The difference between effective circumferential stress and effective radial stress reaches the maximum at r=1, which is equal to 0.6147, for Darcy's law. It becomes 1.0004 reaching the maximum at r=1.0584 for Darcy–Forchheimer models. Meanwhile, For the acceleration flow, this difference equals 1.0980 at r=1.0063 which is the maximum in the distribution. When the formation pressure is 100MPa, the maximum for the three flow models is 61.47MPa, 100.04 MPa and 109.80 MPa respectively.

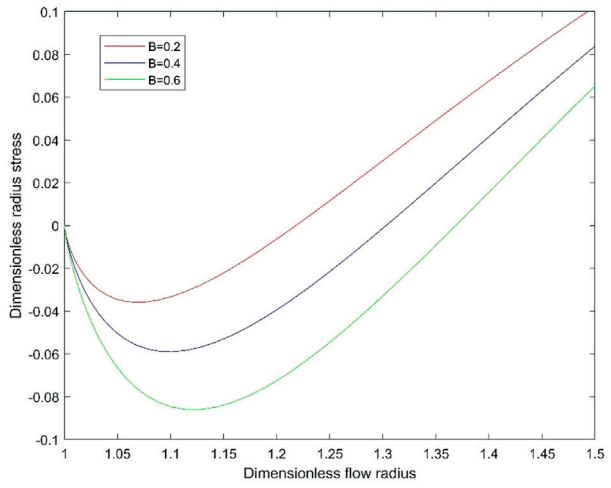

FIGURE 4
The effective radial stress distribution in the acceleration flow for various *B*

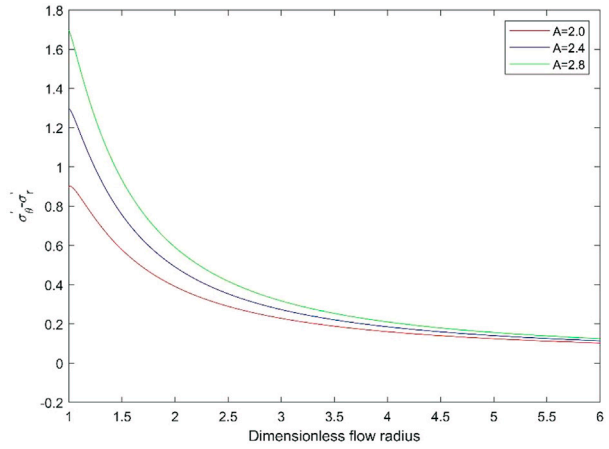

FIGURE 5
Difference between effective circumferential stress and effective radial stress in the acceleration flow for various A.

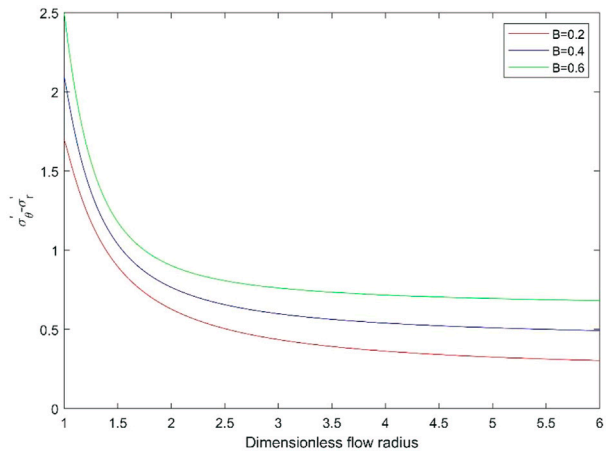

FIGURE 6
Difference between effective circumferential stress and effective radial stress in the acceleration flow for various B.

4 Analysis of the influence of *in situ* stress on the wellbore stress

4.1 Comparative analysis of effective radial stress

Since $r_e^2/r_e^2 - 1 - r_e^2/(r_e^2-1)r^2 > 0$, we have $\frac{d\sigma_r'}{dA} > 0$. Thus, the effective radial stress considering the acceleration effect is the monotone-increasing function of A. When the effective radial stress is negative, the smaller A is, the greater the tensile stress is, indicating that the formation fluid is under abnormally high pressure, while the tensile stress is greater.

We plot the effective radial stress for $m = 0.0412$, $r_e = 2000$, $\eta = 0.5$, $\lambda = 0.5$, $\delta = 50$ and $B = 0$ in Figure 3. It shows that the effective radial stress is the minimum at r=1.0568, which is −0.0282 when A=2.2. While A=2.4, the effective radial stress is −0.0191 at r=1.0395 which is also minimum. When A=2.6, the mini effective radial stress is −0.0132 at r=1.0253. When $1 < r < \sqrt{\frac{3+3/r_e^2}{1+1/r_e^2+4/r_e^4}}$ and $\cos 2\theta > 0$, we have $(\frac{r_e^2(r_e^4+r_e^2+4)}{(r_e^2-1)^3} + \frac{3r_e^4(r_e^2+1)}{(r_e^2-1)^3 r^4} - \frac{12r_e^2r^2}{(r_e^2-1)^3})\cos 2\theta < 0$.

Thus, $d\sigma_r'/dB < 0$. It can be seen that the effective radial stress considering the acceleration effect is a monotone-decreasing function of B. When the effective radial stress is tensile, the stronger the non-uniformity of *in-situ* stress is, the smaller the effective radial stress is, that is, the greater the tensile stress is and the maximum tensile stress is obtained in the direction of the maximum horizontal principal stress.

In Figure 4, we plot the effective circumferential stress for $m = 0.0412$, $r_e = 2000$, $\eta = 0.5$, $\lambda = 0.5$, $\delta = 50$, $A = 2.4$ and $\theta = 0$. In the direction of the maximum horizontal principal stress, the minimum effective radial stress is −0.0359 at r=1.0667 when B=0.2. When B=0.4, the effective radial stress is the minimum at r=1.1010, which is −0.0590. When B=0.6, it is the minimum at r=1.1278, which is −0.0859.

4.2 Difference between effective circumferential stress and effective radial stress

From Equation 3, the difference between effective circumferential stress and effective radial stress in the acceleration flow is given by

$$\sigma_\theta' - \sigma_r' = \frac{A{r_e}^2}{({r_e}^2-1)r^2} - \frac{2D}{(r_e^2-1)} + 2\eta\Delta p(r) - \frac{4\eta}{r^2}\int_1^r r'\Delta p(r')dr' - B\cos 2\theta\left[\frac{r_e^2(r_e^4+r_e^2+4)}{(r_e^2-1)^3} + \frac{3{r_e}^4(r_e^2+1)}{(r_e^2-1)^3 r^4} - \frac{6r_e^2r^2}{(r_e^2-1)^3} + 2\frac{r_e^2(r_e^4+r_e^2+1)}{(r_e^2-1)^3 r^2}\right] \quad (13)$$

It is obvious that $d(\sigma_\theta^{'}-\sigma_r^{'})/dA>0$, so the value, $\sigma_\theta^{'}-\sigma_r^{'}$, is smaller when the formation pressure is from the normal pressure to the abnormally high pressure.

The parameters in Figure 5 are the same as that in Figure 3. When A=2.0, the maximum stress is 0.9014 at r=1.0142. When A=2.4, when r= 1.0036, the value, $\sigma_\theta^{'}-\sigma_r^{'}$, is 1.2963. When A=2.8, $\sigma_\theta^{'}-\sigma_r^{'}$ reaches its maximum value at r=1.004, which is 1.6950.

It can be written as $F(r)=\frac{r_e^2(r_e^4+r_e^2+4)}{(r_e^2-1)^3}+\frac{3r_e^4(r_e^2+1)}{(r_e^2-1)^3r^4}-\frac{6r_e^2r^2}{(r_e^2-1)^3}+2\frac{r_e^2(r_e^4+r_e^2+1)}{(r_e^2-1)^3r^2}$.

When $1\le r\le r_e$, $\frac{dF(r)}{dr}<0$ and $F(r)\ge\frac{r_e^6-3r_e^4+9r_e^2+5}{(r_e^2-1)^3}>0$. Thus, $\frac{d(\sigma_\theta^{'}-\sigma_r^{'})}{dB}>0$, for $\cos 2\theta<0$. These imply that the greater the stress non-uniform, the greater the value $\sigma_\theta^{'}-\sigma_r^{'}$.

In Figure 6, we plot the difference between effective circumferential stress and effective radial stress in the acceleration flow for m = 0.0412, r_e = 2000, η = 0.5, λ = 0.5, δ = 50, A = 2.4 and $\theta=\pi/2$. When B=0.2, the maximum stress is 1.6947 at r=1.0004. When B=0.4, when r=1.0004, the value, $\sigma_\theta^{'}-\sigma_r^{'}$, is 2.0940. When B=0.6, $\sigma_\theta^{'}-\sigma_r^{'}$ reaches its maximum value at r=1, which is 2.4938.

5 Wellbore stability of uncased hole in the high-pressure gas wells

5.1 Tensile fracture

According to the analysis in section 3.1 of this paper, when the stress of the surrounding rock near the wellbore reaches the tensile strength, the acceleration flow requires less mass flow than the Darcy model and the Darcy-Forhheimer model, that is, the surrounding rock near the wellbore is the first to fail in the s acceleration flow. According to the analysis in section 4.1 of this paper, tensile failure occurs first in the surrounding rock near the wellbore in the direction of maximum horizontal principal stress.

We will assume the Biot parameter α_B = 1, so $\sigma_r^{'}|_{r=1,\alpha_B=1}=0$. Thus, the effective tensile stress depends on the positive or negative sign of the effective radial stress derivative at the wellbore. In other words, the condition for the onset of effective tensile stress is $d\sigma_r^{'}/dr|_{r=1}=0$. Combining the condition, Equation 9 can be written as

$$\frac{-r_e{}^{2*}(A-2D-Ar_e{}^2+2Dr_e{}^2+4B\cos 2\theta+2Br_e{}^2\cos 2\theta)}{(r_e{}^2-1)^2}-2D$$
$$-\frac{2D}{r_e{}^2-1}-2\eta\left(\bar{p}-D\right)-\frac{1-D^2}{2D\ln r_e}=0$$

The critical bottomhole pressure, D, for the onset of tensile stress is determined from the above equation.

5.2 Shear failure

It is assumed that the shear failure of rock follows the weak surface failure criterion (Zeng et al., 2021). The Mohr-Coulomb failure criterion for $\beta<\beta_1$ or $\beta>\beta_2$ is defined as

$$\sigma_1-\sigma_3=\frac{2\left(C_w+\tan\phi_w\sigma_3\right)}{\left(1-\tan\phi_w\cot\beta\right)\sin 2\beta}$$
$$\beta_1=\frac{\phi_w}{2}+\frac{1}{2}\arcsin\left[\frac{\left(\sigma_1+\sigma_3+2C_w\cot\phi_w\right)\sin\phi_w}{\sigma_1-\sigma_3}\right]$$
$$\beta_2=\frac{\pi}{2}+\frac{\phi_w}{2}-\frac{1}{2}\arcsin\left[\frac{\left(\sigma_1+\sigma_3+2C_w\cot\phi_w\right)\sin\phi_w}{\sigma_1-\sigma_3}\right]$$

where C_o is the cohesion of the rock, ϕ_o is the friction angle of the rock, C_w is the cohesion of the weak plane, ϕ_w is the friction angle of the weak plane, and β is the angle between maximum principal stress and weak plane normal, related to the failure mode of the anisotropic mudstone with the weak plane.

Only the case is discussed where $\sigma_\theta^{'}>\sigma_z^{'}>\sigma_r^{'}$ and weak plane shear failure occurred in the rock. According to the analysis in section 3.2, shear failure occurs first in the surrounding rock of the acceleration flow when the mass flow rate increases and shear failure occurs first in the minimum horizontal direction of the surrounding rock according to the analysis in section 4.2.

Thus, when r=1, Equation 13 can be written as

$$\left(\sigma_\theta^{'}-\sigma_r^{'}\right)_{r=1}=A\frac{r_e^2}{r_e^2-1}-\frac{B}{2}\frac{4r_e^2\left(r_e^2+2\right)}{\left(r_e^2-1\right)^2}\cos 2\theta$$
$$-D\frac{r_e^2+2}{r_e^2-1}-\left(1-2\eta\right)D-2\eta \quad (14)$$

Thus, $D=\frac{\sin 2\beta(1-\mu_w\cot\beta)(A\frac{r_e^2}{r_e^2-1}-2B\frac{r_e^2(r_e^2+2)}{(r_e^2-1)^2}\cos 2\theta-2\eta)+2C_w}{\frac{r_e^2+2}{r_e^2-1}+(1-2\eta)+2\mu_w(1-\alpha_B)}$.

The critical bottomhole pressure is proportional to the Biot parameter, that is, when the Biot parameter increases, the mass flow required for shear failure decreases. When the Biot parameter increases, the effective radial stress decreases, the tensile stress increases and the required pore pressure gradient decreases. In other words, when the Biot parameter increases, the mass flow rate required for tensile failure decreases. Therefore, the Biot parameter has the same effect on tensile failure and shear failure.

6 Conclusion

Considering the dual effects of non-uniformity of *in-situ* stress and acceleration effect in the process of seepage, the stress state of surrounding rock suitable for high-pressure gas well and its influence on tensile failure and shear failure in the process of gas test of the high-pressure gas well are analyzed, and the following conclusions are as following.

1) Considering the acceleration effect, the difference between effective circumferential stress and effective radial stress at any flow radius is larger than that in the other two flow models, which is more likely to cause shear failure. The difference between the effective circumferential stress and the effective radial stress does not reach the maximum value at the wellbore wall.
2) The pore pressure gradient plays a decisive role in the effective radial stress. Considering the acceleration effect, the minimum effective radial stress is smaller than that of the other two flow models, which is more likely to lead to tensile failure. The conditional expression of tensile stress generation considering the non-uniformity of *in-situ* stress is given.
3) The influence of Biot parameter on tensile failure and shear failure is the same.

Data availability statement

The original contributions presented in the study are included in the article/supplementary material, further inquiries can be directed to the corresponding author.

Author contributions

HJ and MC contributed to conception and design of the study. CH organized the database. XL performed the statistical analysis. YZ wrote the first draft of the manuscript. All authors contributed to manuscript revision, read, and approved the submitted version.

Funding

This study is supported by the Open Fund (Program No. PRP/open-2009) of State Key Laboratory of Petroleum Resources and Prospecting, National Natural Science Foundation of China (Grant No. 52104005), Natural Science Basic Research Plan in Shaanxi Province of China (Program No. 2021JM-407), Key Research and Development Program of Shaanxi Province (grant number 2023-YBGY-312).

Conflict of interest

Author CH was employed by the company Xi'an Qing'an Electrical Control Co., Ltd., China.

The remaining authors declare that the research was conducted in the absence of any commercial or financial relationships that could be construed as a potential conflict of interest.

Publisher's note

References

Chang, Z., and Hou, B. (2022). Numerical simulation on cracked shale oil reservoirs multi-cluster fracturing under inter-well and inter-cluster stress interferences. *Rock Mech. Rock Eng.* In Press. doi:10.1007/s00603-022-03145-7

Chen, K. P. (2011). A new mechanistic model for prediction of instantaneous coal outbursts—dedicated to the memory of prof. Daniel D. Joseph. *Int. J. Coal Geol.* 87 (2), 72–79. doi:10.1016/j.coal.2011.04.012

Fjaer, E., Holt, R. M., Horsrud, P., Raaen, A. M., and Risnes, R. (2008). *Petroleum related rock mechanics*. 2nd ed. Amsterdam: Elsevier.

Hou, B., Chang, Z., and Wu, A. (2022b). Simulation of competitive propagation of multi-fractures on shale oil reservoir multi-clustered fracturing in Jimsar sag. *Acta Pet. Sin.* 43 (01), 75–90. doi:10.7623/xyxb202201007

Hou, B., Cui, Z., Ding, J. H., Zhang, F. S., Zhuang, L., and Elsworth, D. (2022a). Perforation optimization of layer-penetration fracturing for commingling gas production in coal measure strata. *Petroleum Sci.* 19 (4), 1718–1734. doi:10.1016/j.petsci.2022.03.014

Hou, B., and Cui, Z. (2022e). Vertical fracture propagation behavior upon supercritical carbon dioxide fracturing of multiple layers. *Eng. Fract. Mech.*, 108913. In Press. doi:10.1016/j.engfracmech.2022.108913

Hou, B., Dai, Y., Fan, M., Zhang, K., Wick, T., and Lee, S. (2022c). Numerical simulation of pores connection by acid fracturing based on phase field method. *Acta Pet. Sin.* 43 (6), 849–859. doi:10.7623/syxb202206009

Hou, B., Zhang, Q., Liu, X., Pang, H., and Zeng, Y. (2022d). Integration analysis of 3D fractures network reconstruction and frac hits response in shale wells. *Energy* 260, 124906. doi:10.1016/j.energy.2022.124906

Huang, L., He, R., Yang, Z., Tan, P., Chen, W., Li, X., et al. (2022). Exploring hydraulic fracture behavior in glutenite formation with strong heterogeneity and variable lithology based on DEM simulation. *Eng. Fract. Mech.* 278, 109020. doi:10.1016/j.engfracmech.2022.109020

Jiang, H., Chen, M., Jin, Y., and Chen, K. P. (2015a). Analytical modeling of acceleration-induced conductivity damage in a propped hydraulic fracture of a high-pressure gas well. *J. Nat. Gas Sci. Eng.* 26, 185–192. doi:10.1016/j.jngse.2015.06.019

Jiang, H., Chen, M., Jin, Y., and Chen, K. P. (2015c). Gas expansion-induced acceleration effect of a highly compressible gas flow in porous media. *J. Porous Media* 18 (8), 825–834. doi:10.1615/jpormedia.v18.i8.70

Jiang, H., Chen, M., Jin, Y., and Chen, K. P. (2015b). Importance of gas acceleration near the wellbore in radial compressible porous media flows for a vertical gas well. *Transp. Porous Media* 110 (1), 127–140. doi:10.1007/s11242-015-0559-9

Jiang, H., Dou, Y., Xi, Z., Chen, M., and Jin, Y. (2016). Microscopic choked flow for a highly compressible gas in porous media. *J. Nat. Gas Sci. Eng.* 35, 42–53. doi:10.1016/j.jngse.2016.08.039

Jin, Y., Chen, K. P., and Chen, M. (2011b). Development of tensile stress near a wellbore in radial porous media flows of a high pressure gas. *Int. J. Rock Mech. Min. Sci.* 48 (8), 1313–1319. doi:10.1016/j.ijrmms.2011.09.013

Jin, Y., Chen, K. P., Chen, M., and Grapsas, N. (2012). Gas expansion-induced acceleration effect in high-pressure gas flows near a wellbore. *J. porous media* 15 (4), 317–328. doi:10.1615/jpormedia.v15.i4.20

Jin, Y., Chen, K. P., Chen, M., Grapsas, N., and Zhang, F. X. (2011a). Short-time pressure response during the start-up of a constant-rate production of a high pressure gas well. *Phys. Fluids* 23 (4), 043101. doi:10.1063/1.3571494

Jin, Y., and Chen, K. P. (2019). Fundamental equations for primary fluid recovery from porous media. *J. Fluid Mech.* 860, 300–317. doi:10.1017/jfm.2018.874

Levy, A., Sorek, S., Ben-Dor, G., and Bear, J. (1995). Evolution of the balance equations in saturated thermoelastic porous media following abrupt simultaneous changes in pressure and temperature. *Transp. Porous Media* 21 (3), 241–268. doi:10.1007/BF00617408

Nield, D. A. (1994). Modelling high speed flow of a compressible fluid in a saturated porous medium. *Transp. porous media* 14 (1), 85–88. doi:10.1007/BF00617029

Sun, S., Wang, J., Le, H., Fan, H., and Wang, W. (2022). Experimental and numerical investigation on compressive strength and crack behavior of rock-like specimens with open flaws under confining loads. *Front. Earth Sci.* 10. doi:10.3389/feart.2022.972194

Tan, P., Jin, Y., and Pang, H. (2021). Hydraulic fracture vertical propagation behavior in transversely isotropic layered shale formation with transition zone using XFEM-based CZM method. *Eng. Fract. Mech.* 248, 107707. doi:10.1016/j.engfracmech.2021.107707

Warsitzka, M., Kukowski, N., and May, F. (2022). Patterns and failure modes of fractures resulting from forced folding of cohesive caprocks–comparison of 2D vs. 3D and single-vs. Multi-layered analog experiments. *Front. Earth Sci.* 10. doi:10.3389/feart.2022.881134

Wooding, R. (1957). Steady state free thermal convection of liquid in a saturated permeable medium. *J. Fluid Mech.* 2 (3), 273–285. doi:10.1017/S0022112057000129

Zeng, Y., Jiang, H., Ding, S., Chen, J., Wang, Y., and Zheng, J. (2021). Analytical and experimental investigations on mechanical properties of weak plane bedding in mudstone. *Geofluids* 2021, 5408701–5408705. doi:10.1155/2021/5408701

Zhang, Q., Hou, B., Lin, B., Liu, X., and Gao, Y. (2021). Integration of discrete fracture reconstruction and dual porosity/dual permeability models for gas production analysis in a deformable fractured shale reservoir. *J. Nat. Gas Sci. Eng.* 93, 104028. doi:10.1016/j.jngse.2021.104028

Zhang, W., Xue, X., Zhang, C., Qu, Y., Ke, K., Pan, S., et al. (2022). A drilling wellbore pressure calculation model considering the effect of gas dissolution and suspension. *Front. Earth Sci.* 10. doi:10.3389/feart.2022.993876

Zhao, X., Huang, B., and Grasselli, G. (2021). Numerical investigation of the fracturing effect induced by disturbing stress of hydrofracturing. *Front. Earth Sci.* 9. doi:10.3389/feart.2021.751626

frontiers | Frontiers in Earth Science

TYPE Original Research
PUBLISHED 01 March 2023
DOI 10.3389/feart.2023.1143541

OPEN ACCESS

EDITED BY
Shiming Wei,
China University of Petroleum, Beijing, China

REVIEWED BY
Can Shi,
China University of Petroleum, Beijing, China
Xiang Rao,
Yangtze University, China

*CORRESPONDENCE
Kaixuan Qiu,
qiukx940908@163.com

SPECIALTY SECTION
This article was submitted to Environmental Informatics and Remote Sensing, a section of the journal Frontiers in Earth Science

RECEIVED 13 January 2023
ACCEPTED 13 February 2023
PUBLISHED 01 March 2023

CITATION
Qiu K (2023), A practical analytical model for performance prediction in unconventional gas reservoir. *Front. Earth Sci.* 11:1143541. doi: 10.3389/feart.2023.1143541

A practical analytical model for performance prediction in unconventional gas reservoir

Kaixuan Qiu*

Jiangmen Laboratory of Carbon Science and Technology, Jiangmen, China

Ninety percentage of newly proven natural gas reservoirs of China are mainly unconventional resources, which can be typically developed by multi-stage fracturing horizontal well technology. Two regions typically occur near each fracture after hydraulic fracturing, in which the lower permeability region is considered as the storage source and the higher permeability region as the flow channel. The existed analytical models so far are mainly derived by Laplace transforming. In this paper, an improved practical analytical solution is derived for unconventional gas reservoirs bypassing the Laplace transform and numerical inversion. Through solving material balance equation and adopting the integration, a rate vs. pseudo-time solution in real-time domain can be directly obtained. Five numerical cases are created to verify the accuracy of the proposed analytical solution and the ratio of regular/irregular region pore volume is also proved to be derived reversely by the output parameters, which is significant for the field engineers to evaluate the effect of hydraulic fracturing. Moreover, a field example of a multi-fractured horizontal well in a tight gas reservoir is provided for demonstrate application.

KEYWORDS

analytical model, performance prediction, unconventional reservoir, history matching, hydraulic fracturing

1 Introduction

Unconventional resources including tight gas and shale gas have become a significant source of global hydrocarbon supply due to advanced reservoir evaluation and drilling/completion/fracturing technology (Clarkson, 2013; Dejam et al., 2018). As for the ultra-low permeability in unconventional reservoirs, the volume fracturing technology is adopted extensively to improve reservoir properties and achieve economic exploitation. Due to the dense distribution of the pre-existing natural fractures, the complex fracture geometry with high permeability will be created around the hydraulic fractures after fracturing operation (Wei et al., 2019; Xia et al., 2019; Liu et al., 2021), which is significant for fluid flow and resource extraction.

In order to make accurate reservoir evaluation, a large number of studies have been conducted for production data analysis. The popular techniques for quantitative production data

Abbreviations: t, production time, days; ta, pseudo-time, days; k_1, region 1 permeability, mD; $m_2(p)$, pseudo-pressure in region 2,psi; k_2, region 2 permeability, mD; T_r, transmissibility between region 1 and 2, STB/D/psi; J, production index, STB/D/psi; $m_1(p)$, pseudo-pressure in region 1,psi; τ_1, region 1 constant time, days; τ_2, region 2 constant time, days; V_{p_1}, pore volumes of region 1, ft^3; μ, fluid viscosity, cp; V_{p_2}, pore volumes of region 2, ft^3; ϕ, porosity; q_i, initial production rate, Mscf/D; C_t, total compressibility, Psi^{-1}.

analysis including empirical methods, numerical methods and analytical models. Firstly, the typical empirical methods, firstly proposed by Arps (1945), have been evolved by many researchers (Fetkovich, 1980; Blasingame et al., 1991; Duong, 2011). These decline curve analysis methods remain commonly used because of their simple and fast empirical regression. However, these methods will result in significant errors especially when applied to unconventional reservoirs. Numerical simulation for unconventional reservoirs has received extensive attention (Cipolla et al., 2010; Ding et al., 2014; Rao et al., 2022). However, it is a time-consuming process and depends on numerous original physical parameters. Compared with the numerical simulation, the analytical methods are models that derive analytically solutions to mathematical models including reservoir behavior as well as flow behavior associated with complex fracture geometry. Therefore, many scholars have focused on analytical models for production data analysis in unconventional reservoirs. Ci-qun (1983) proposed the analytical solution considering the two-dimensional pseudo steady state flow from two matrix blocks to the fracture. Lee and Brockenbrough, (1983) derived a tri-linear model to represent the transient flow behavior within the single fracture in an infinite homogeneous reservoir. Wattenbarger et al. (1998) represented an analytical solution accounting for linear flow in fractures with infinite conductivity applied in tight gas wells. Brown et al. (2011) presented a three-region analytical model considering the hydraulic fracture region, the stimulated region including dense branch fractures as well as the outer region containing low permeability matrix beyond the tip of hydraulic fractures. Stalgorova and Mattar, (2012) also introduced a three-region analytical model to consider complex fracture geometry. The outer region in their model adjacent to the stimulated region, which is the only difference from Brown et al. (2011) model. Stalgorova and Mattar, (2013) extended the three-region model to five-region model. Three outer regions are considered in their model. And it notes that the contribution from the outer regions may be negligible except for very late in the production life of the well. Abbassi et al. (2019) put forward a three-region model considering the transient flow among matrix, vugs and fractures. The analytical relationship for calculating the shape factor between different regions is also presented.

The analytical solutions mentioned above were derived analytically based on Laplace-transform technique and the final solution in real-time domain can be obtained by Stehfest numerical inversion (Stehfest, 1970). Development of a straightforward solution for analytical model considering the complex fracture geometry is still lacking. Ogunyomi et al. (2016) and Qiu andLi, (2018) presented the approximate analytical solutions to the dual-porosity model and triple-porosity model in real-time domain separately by adopting the integration and average pressure replacement. However, their solutions are applicable for tight oil reservoirs because the pressure-dependent properties in their model are not taken into consideration.

In this paper, our goal is to derive a straightforward solution in real-time domain for unconventional gas reservoirs considering complex fractures. Firstly, we define two regions and the high permeability regions contains hydraulic fractures and complex branch fractures as well as the low permeability region which adjacent to the high permeability region contains the matrix. Then the pseudo-variables (Anderson and Mattar, 2005) are introduced to eliminate the non-linearity caused by the pressure-dependent properties of gas. The derivation is based on the integration in real-time domain bypassing Laplace transform and numerical inversion. Lastly, the accuracy of the analytical solution is validated with equivalent numerical model.

2 Model description

In order to improve gas production in unconventional reservoirs, it is necessary to create as much connection between the unconventional gas reservoir and artificial or natural fractures as possible. Therefore, multistage hydraulic fracturing technology is applied to generate the hydraulic fractures and complex fracture networks to improve gas recovery. As shown in Figure 1A, there is a network of branch fractures forming the flow channel within the tight matrix. By virtue of the highly connected and high conductivity of the network of fractures, the oil/gas stored in ultra-tight matrix can flow into the wellbore. The black arrows represent the flow directions. Obviously, the flow in fractures network is complex and it is impossible to describe each flow process using mathematical models. Therefore, we simplified the complex flow system into two-region system, in which the defined high permeability region (Region 1) includes all the fractures and the low permeability region (Region 2) is the aggregated volume of the matrix directly connected to the high permeability region. Because the contribution of regions beyond hydraulic fractures is validated to be negligible after comparing the results of numerical simulation with and without region beyond fractures (Stalgorova and Mattar, 2012; Abbassi et al., 2019). Figure 1B is a 3D schematic of the reservoir with a multi-stage horizontal well, which is the conceptual model for constructing analytical model.

In this paper, our analytical model is derived analytically based on the following assumption.

1. The reservoir is homogeneous, and isothermal.
2. Flow process is linear in each region.
3. Flow is single gas phase.
4. Flow within the hydraulic fracture is neglected for the high-speed gas flow rate.
5. Flow process is under constant bottom-hole pressure.
6. Pressure at the interface between two regions is constant.
7. Gravity effect is neglected.

Once the gas flow reaches the boundary and reservoir average pressure will decrease, and meanwhile the gas properties such as gas viscosity (μ), gas compressibility (C_t) and gas compressibility (Z) is varying with reservoir pressure. Consequently, the gas diffusivity equation will be non-linear which is impossible to derive the analytical solution directly. In order to deal with this problem, the pseudo-pressure and pseudo-time (Anderson and Mattar, 2005) are adopted to linearize the equation. The equations for pseudo-pressure and pseudo-time can be expressed as,

$$m(p) = 2\int_0^p \frac{p}{\mu z} dp \tag{1}$$

$$t_a = \int_0^t \frac{(\mu C_t)_i}{\mu(\bar{p}) C_t(\bar{p})} dt \tag{2}$$

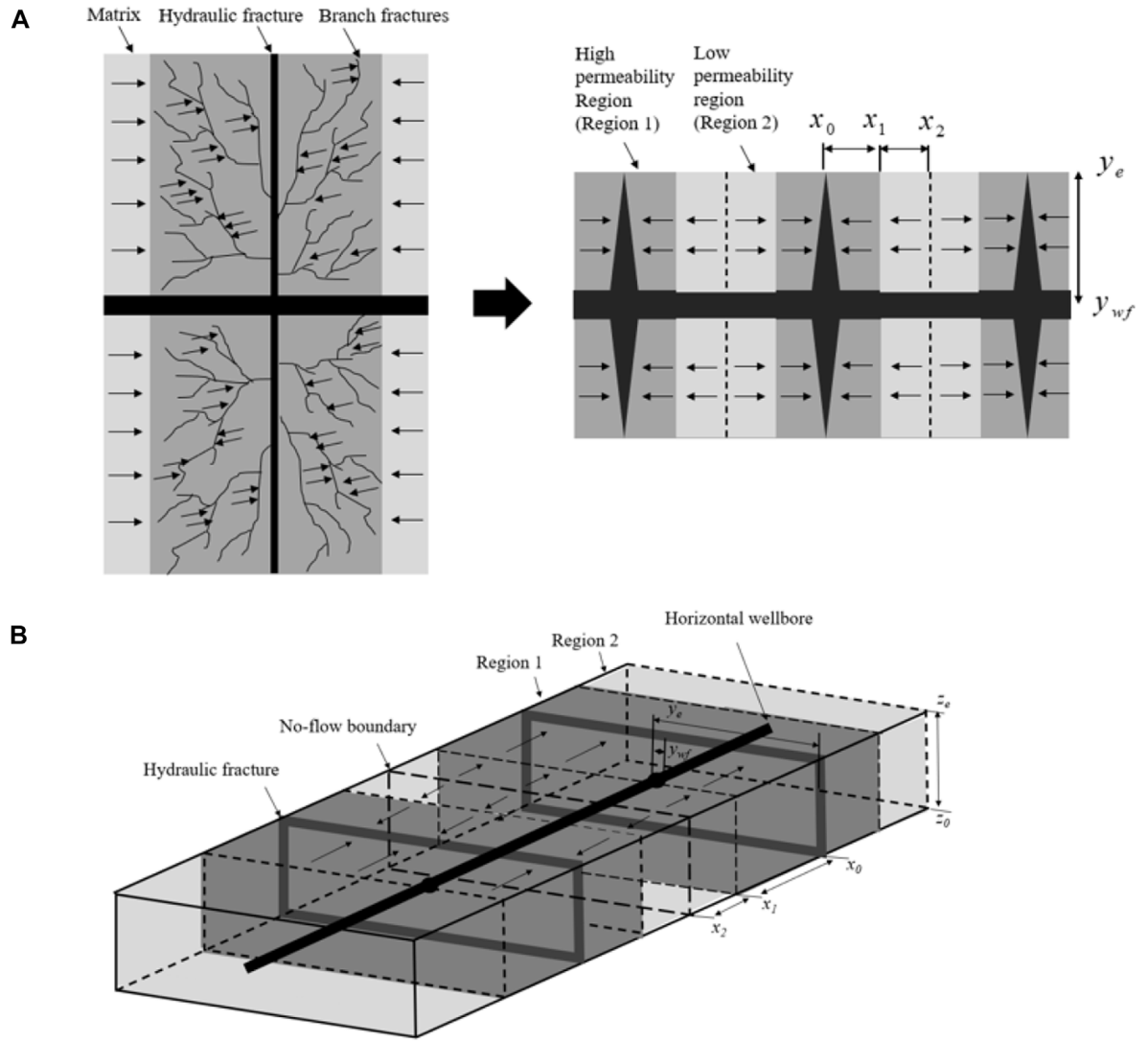

FIGURE 1
Schematic of a multi-stage fractured horizontal well with complex fractures. **(A)** The complex fractures after hydraulic fracturing. **(B)** 3D schematic of a multi-stage fractured horizontal well with two-regions around the hydraulic fractures.

3 Model development

The system of equations based on the conceptual model is presented below. In the low-permeability region (Region 2), the governing equation for gas flow after substituting the Eqs 1, 2 is expressed as:

$$\frac{\partial^2 m_2(p)}{\partial x^2} + \frac{\partial^2 m_2(p)}{\partial y^2} + \frac{\partial^2 m_2(p)}{\partial z^2} = \frac{(\phi\mu C_t)_2}{k_2} \frac{\partial m_2(p)}{t_a} \tag{3}$$

Where $m_2(p)$ is the pseudo-pressure in region 2, x, y and z are Cartesian coordinates, t_a is the pseudo-time for gas flow, k_2 and Φ is the permeability and porosity, respectively, of region 2.

The initial condition for the region 2 is equal to initial reservoir pseudo-pressure before the production start.

$$m_2(p)(x, y, z, 0) = m(p_i) \tag{4}$$

Where $m(p_i)$ is the initial reservoir pseudo-pressure.

The closed boundary is defined for the top and bottom of the reservoir. Therefore, the outer boundary conditions are regarded as no-flow boundaries.

$$\left.\frac{\partial m_2(p)}{\partial y}\right|_{y=y_{wf},y_e} = 0 \tag{5}$$

$$\left.\frac{\partial m_2(p)}{\partial z}\right|_{z=z_0,z_e} = 0 \tag{6}$$

Considering the symmetry between adjacent hydraulic fractures, the location of $x = x_2$ is also regarded as no-flow boundary.

$$\left.\frac{\partial m_2(p)}{\partial x}\right|_{x=x_2} = 0 \tag{7}$$

Continuity of the flux and pressure across the boundaries between two regions is assumed. Therefore, the inner boundary condition can be written as,

$$\frac{k_2}{\mu}\frac{\partial m_2(p)}{\partial x}\bigg|_{x=x_1} = \frac{k_1}{\mu}\frac{\partial m_1(p)}{\partial x}\bigg|_{x=x_1} \tag{8}$$

Similarly, the governing equation for gas flow in region 1 can be also expressed as,

$$\frac{\partial^2 m_1(p)}{\partial x^2} + \frac{\partial^2 m_1(p)}{\partial y^2} + \frac{\partial^2 m_1(p)}{\partial z^2} = \frac{(\phi\mu C_t)_1}{k_1}\frac{\partial m_1(p)}{t_a} \tag{9}$$

Where $m_1(p)$ is the pseudo-pressure in region 1, x, y and z are Cartesian coordinates, t_a is the pseudo-time for gas flow, k_1 and Φ is the permeability and porosity in region 1 respectively.

In regard to the whole flow process, the initial condition of two regions is identical. And the constant bottom-hole pressure is assumed. Thus, the pressure is equal to the bottom-hole pressure at the location of $x = x_0$.

$$m_1(p)(x, y, z, 0) = m(p_i) \tag{10}$$

$$m_1(p)(x = x_0, y, z, t_a) = m(p_{wf}) \tag{11}$$

Where $m(p_{wf})$ is the bottom-hole pseudo-pressure.

The flow in two regions is both 1D linear flow in the x-direction. Therefore, the outer boundary conditions are identical to those of region 2.

$$\frac{\partial m_1(p)}{\partial y}\bigg|_{y=y_{wf},y_e} = 0 \tag{12}$$

$$\frac{\partial m_1(p)}{\partial z}\bigg|_{z=z_0,z_e} = 0 \tag{13}$$

The inner boundary condition based on the continuity of flux at the location of $x=x_1$ is expressed as:

$$\frac{k_1}{\mu}\frac{\partial m_1(p)}{\partial x}\bigg|_{x=x_1} = \frac{k_2}{\mu}\frac{\partial m_2(p)}{\partial x}\bigg|_{x=x_1} \tag{14}$$

4 Analytical solution

The equations mentioned above used for mathematical model are partial differential equations (PDEs). To solve mathematical model analytically, the system of PDEs must be transformed into the system of ordinary differential equations (ODEs). Considering the Laplace transform and numerical inversion are time-consuming, the integration method is adopted in this paper to eliminate the spatial dependences and obtain the ODEs directly. Integrating the governing equation with respect to spatial coordinates for region 2:

$$\begin{aligned}&\int_{x_1}^{x_2}\int_{y_{wf}}^{y_e}\int_{z_o}^{z_e}\frac{\partial}{\partial x}\left(\frac{\partial m_2(p)}{\partial x}\right)dxdydz + \int_{x_1}^{x_2}\int_{y_{wf}}^{y_e}\int_{z_o}^{z_e}\frac{\partial}{\partial y}\left(\frac{\partial m_2(p)}{\partial y}\right)dxdydz\\ &+\int_{x_1}^{x_2}\int_{y_{wf}}^{y_e}\int_{z_o}^{z_e}\frac{\partial}{\partial z}\left(\frac{\partial m_2(p)}{\partial z}\right)dxdydz\\ &= \frac{(\phi\mu C_t)_2}{k_2}\frac{\partial}{\partial t_a}\int_{x_1}^{x_2}\int_{y_{wf}}^{y_e}\int_{z_o}^{z_e}m_2(p)dxdydz\end{aligned} \tag{15}$$

The pseudo-time can be moved outside the spatial integral because the pseudo-time is independent of the spatial coordinates. To obtain a simplified equation, we define the average pseudo-pressure and the effective pore volume as:

$$\bar{m}(p) = \frac{\iiint m(p)}{\iiint dxdydz} = \frac{\iiint m(p)}{V_b} \tag{16}$$

$$V_p = \phi V_b \tag{17}$$

Where V_b is the volume of the region and V_p is the pore volume of the region.

Substituting the Eqs 15–17 can be rewritten as:

$$\begin{aligned}&\int_{y_{wf}}^{y_e}\int_{z_0}^{z_e}\left(\frac{\partial m_2(p)}{\partial x}\bigg|_{x_2} - \frac{\partial m_2(p)}{\partial x}\bigg|_{x_1}\right)dydz\\ &+\int_{x_1}^{x_2}\int_{z_0}^{z_e}\left(\frac{\partial m_2(p)}{\partial y}\bigg|_{y_e} - \frac{\partial m_2(p)}{\partial y}\bigg|_{y_{wf}}\right)dxdz\\ &+\int_{x_1}^{x_2}\int_{y_{wf}}^{y_e}\left(\frac{\partial m_2(p)}{\partial z}\bigg|_{z_e} - \frac{\partial m_2(p)}{\partial y}\bigg|_{z_0}\right)dxdy\\ &= \frac{(\phi\mu C_t)_2 V_{b_2}}{k_2}\frac{d\bar{m}_2(p)}{dt_a}\end{aligned} \tag{18}$$

With the use of the initial and boundary conditions, Eq. 18 can be simplified as:

$$-\int_{y_{wf}}^{y_e}\int_{z_0}^{z_e}\left(\frac{k_2}{\mu}\frac{\partial m_2(p)}{\partial y}\bigg|_{x_1}\right)dydz = \left(V_{p_2}C_t\right)_2\frac{d\bar{m}_2(p)}{dt_a} \tag{19}$$

According to the Darcy's law, the following applies:

$$q_2 = \int_{y_{wf}}^{y_e}\int_{z_0}^{z_e}\frac{k_2}{\mu}\frac{\partial m_2(p)}{\partial y}\bigg|_{x_1}dydz \tag{20}$$

Therefore, Eq. 19 can be rewritten as:

$$\left(V_{p_2}C_t\right)_2\frac{d\bar{m}(p)}{dt_a} = -q_2 \tag{21}$$

Where V_{p2} is the pore volume of region 2 and q_2 is the flow rate in region 2.

In region 1, we also apply the integration method to address the diffusion equation as:

$$\begin{aligned}&\int_{y_{wf}}^{y_e}\int_{z_0}^{z_e}\left(\frac{\partial m_1(p)}{\partial x}\bigg|_{x_1} - \frac{\partial m_1(p)}{\partial x}\bigg|_{x_0}\right)dydz\\ &+\int_{x_0}^{x_1}\int_{z_0}^{z_e}\left(\frac{\partial m_1(p)}{\partial y}\bigg|_{y_e} - \frac{\partial m_1(p)}{\partial y}\bigg|_{y_{wf}}\right)dxdz\\ &+\int_{x_0}^{x_1}\int_{y_0}^{y_1}\left(\frac{\partial m_1(p)}{\partial z}\bigg|_{z_e} - \frac{\partial m_1(p)}{\partial y}\bigg|_{z_0}\right)dxdy\\ &= \frac{(\phi\mu C_t)_1 V_{b_1}}{k_1}\frac{d\bar{m}_1(p)}{dt_a}\end{aligned} \tag{22}$$

After applying the initial and boundary conditions, Eq. 22 can be rewritten as,

TABLE 1 Summary of the synthetic numerical model parameters.

Parameters	Value
Model dimension (X × Y × Z) (ft)	150 × 400 × 10
Initial pressure (psi)	2,500
Bottom-hole pressure (psi)	500
Viscosity (cp)	0.0174
Compressibility (10^{-5} psi^{-1})	9.75
Porosity	0.06
Permeability of Region 2 (mD)	0.0005
Permeability of Region 1 (mD)	1
Volume in Region 2 (10^4 ft^3)	18
Volume in Region 1 (10^4 ft^3)	42

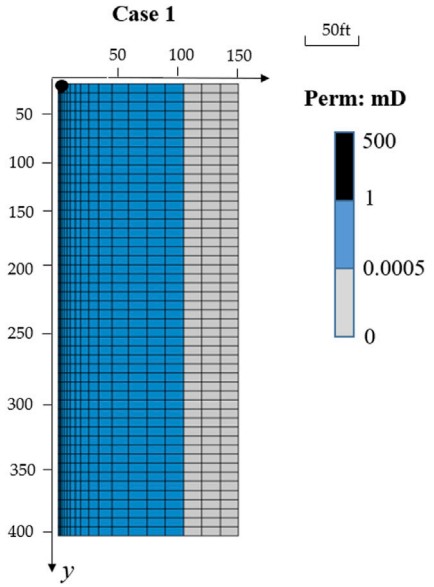

FIGURE 2
Reservoir grid of the numerical model. The blue grids represent the high-permeability region and the gray grids represent the low-permeability region.

$$-\int_{y_{wf}}^{y_e}\int_{z_0}^{z_e}\left(\frac{k_1}{\mu}\frac{\partial m_1(p)}{\partial x}\bigg|_{x_1}-\frac{k_1}{\mu}\frac{\partial m_1(p)}{\partial x}\bigg|_{x_0}\right)dydz=\left(V_{p_1}C_t\right)_1\frac{d\bar{m}_1(p)}{dt_a} \tag{23}$$

Note that the following applies:

$$q_1=\int_{y_0}^{y_1}\int_{z_0}^{z_e}\left(\frac{k_1}{\mu}\frac{\partial m_1(p)}{\partial x}\bigg|_{x_0}\right)dydz \tag{24}$$

Substituting Eqs 9, 16, 34, 38 into Eq. 24 results in:

$$\left(V_{p_1}C_t\right)_1\frac{d\bar{m}_1(p)}{dt_a}=-q_1+q_2 \tag{25}$$

Where V_{p1} is the pore volume of region 1, q_1 is the flow rate in region 1.

Obviously, the next step involves the substitution of the average pseudo-pressure with the relationship between the pressure and flow rate. Since it is assumed that gas flows sequentially from region 2 into region 1, a general analytical solution for 1D linear gas flow is derived to solve the problem (Details are provided in Supplementary Appendix SA), which is given by:

$$\bar{m}(p)=m\left(p_{wf}\right)+\frac{4}{\pi^2}\left[m(p_i)-m\left(p_{wf}\right)\right]\sum_{n=1}^{\infty}\frac{q_{D_n}}{(2n-1)^2} \tag{26}$$

Where $\bar{m}(p)$ is the average pseudo-pressure, q_{Dn} is the dimensionless production of the *nth* mode.

Based on the model assumptions, the average pseudo-pressure in each region can be expressed as:

$$\bar{m}_1(p)=m\left(p_{wf}\right)+\frac{4}{\pi^2}\left[m(p_i)-m\left(p_{wf}\right)\right]\sum_{n=1}^{\infty}\frac{q_{D1_n}}{(2n-1)^2} \tag{27}$$

$$\bar{m}_2(p)=\bar{m}_1(p)+\frac{4}{\pi^2}\left[m(p_i)-\bar{m}_1(p)\right]\sum_{n=1}^{\infty}\frac{q_{D2_n}}{(2n-1)^2} \tag{28}$$

We define the productivity index (J) and transmissibility (T_r) between region 1 and region 2 as:

$$J=\frac{\pi^2}{4}\frac{q_i}{m(p_i)-m\left(p_{wf}\right)} \tag{29}$$

$$T_r=\frac{\pi^2}{4}\frac{q_i{}'}{m(p_i)-\bar{m}_1(p)} \tag{30}$$

Where $\bar{m}_1(p)$ is the average pseudo-pressure in region 1, q_i and $q_i{}'$ is the initial production rate from the region 1 and region 2 respectively.

Substituting Eqs 27, 28 into Eqs 21, 25 results in:

$$q_i\sum_{n=1}^{\infty}\frac{1}{(2n-1)^2}\frac{dq_{D1_n}}{dt_a}=-\frac{J}{\left(\nu_pC_t\right)_1}q_i\sum_{n=1}^{\infty}q_{D1_n}+\frac{J}{\left(\nu_pC_t\right)_1}q_i{}'\sum_{n=1}^{\infty}q_{D2_n} \tag{31}$$

$$q_i{}'\sum_{n=1}^{\infty}\frac{1}{(2n-1)^2}\frac{dq_{D2_n}}{dt_a}=-\frac{J}{\left(\nu_pC_t\right)_1}\frac{T_r}{J}q_i\sum_{n=1}^{\infty}q_{D1_n}-\left(\frac{T_r}{\left(\nu_pC_t\right)_2}+\frac{J}{\left(\nu_pC_t\right)_1}\frac{T_r}{J}\right)q_i{}'\sum_{n=1}^{\infty}q_{D2_n} \tag{32}$$

Where q_{D1_n} and q_{D2_n} is the initial production rate from the nth mode in region 1 and region 2 respectively.

We can rewrite this set of ODEs in the following matrix form:

$$\begin{pmatrix}\frac{dq_{1_n}}{dt_a}\\ \frac{dq_{2_n}}{dt_a}\end{pmatrix}=(2n-1)^2\begin{pmatrix}-\frac{J}{\left(\nu_pC_t\right)_1} & \frac{J}{\left(\nu_pC_t\right)_1}\\ -\frac{J}{\left(\nu_pC_t\right)_1}\frac{T_r}{J} & -\left(\frac{T_r}{\left(\nu_pC_t\right)_2}+\frac{J}{\left(\nu_pC_t\right)_1}\frac{T_r}{J}\right)\end{pmatrix}\times\begin{pmatrix}q_{1_n}\\ q_{2_n}\end{pmatrix} \tag{33}$$

Where the initial conditions to solve the system of equations are,

$$q_1(t_a=0)=q_i \tag{34}$$

$$q_2(t_a=0)=0 \tag{35}$$

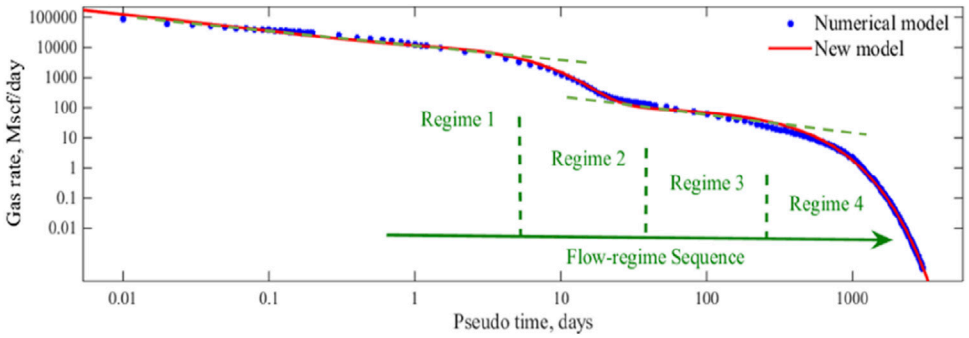

FIGURE 3
Analysis results in Case 1. (Regime 1: transient linear flow in region 1. Regime 2: boundary-dominated flow in region 1. Regime 3: transient linear flow in region 2. Regime 4: boundary-dominated flow in region 2).

TABLE 2 Model output parameters after fitting.

Parameter	Value
τ_1 (days)	4
τ_2 (days)	246
T_r/J	0.007289
q_i (Mscf/D)	13,540

After solving Eq. 33, we can obtain the *nth* flow rate in combination with the initial conditions. The production rate is the summation of all production rate terms. By converting the summation to an indefinite integral, the analytical solution in real-time domain can be derived below (Details are provided in Supplementary Appendix SB),

$$q = q_i \frac{a_1}{a_1 - a_2} e^{\lambda_1 t_a} - q_i \frac{a_2}{a_1 - a_2} e^{\lambda_2 t_a} + \frac{q_i}{4} \frac{a_1}{a_1 - a_2} \sqrt{\frac{\pi}{|\lambda_1 t_a|}} erfc\left(3\sqrt{|\lambda_1 t_a|}\right) - \frac{q_i}{4} \frac{a_2}{a_1 - a_2} \sqrt{\frac{\pi}{|\lambda_2 t_a|}} erfc\left(3\sqrt{|\lambda_2 t_a|}\right) \tag{36}$$

Where the defined parameters are expressed as:

$$\tau_1 = \frac{\left(V_p C_t\right)_1}{J} \tag{37}$$

$$\tau_2 = \frac{\left(V_p C_t\right)_2}{T_r} \tag{38}$$

$$\lambda_1 = \frac{1}{2}\left(-\frac{1}{\tau_1} - \frac{1}{\tau_2} - \frac{1}{\tau_1}\frac{T_r}{J} + \sqrt{\left(\frac{1}{\tau_1} - \frac{1}{\tau_2}\right)^2 + \frac{2}{\tau_1^2}\frac{T_r}{J} + \frac{2}{\tau_1 \tau_2}\frac{T_r}{J} + \left(\frac{1}{\tau_1}\frac{T_r}{J}\right)^2}\right) \tag{39}$$

$$\lambda_2 = \frac{1}{2}\left(-\frac{1}{\tau_1} - \frac{1}{\tau_2} - \frac{1}{\tau_1}\frac{T_r}{J} - \sqrt{\left(\frac{1}{\tau_1} - \frac{1}{\tau_2}\right)^2 + \frac{2}{\tau_1^2}\frac{T_r}{J} + \frac{2}{\tau_1 \tau_2}\frac{T_r}{J} + \left(\frac{1}{\tau_1}\frac{T_r}{J}\right)^2}\right) \tag{40}$$

$$a_1 = \frac{\tau_1}{2}\frac{J}{T_r}\left(-\frac{1}{\tau_1} + \frac{1}{\tau_2} + \frac{1}{\tau_1}\frac{T_r}{J} + \sqrt{\left(\frac{1}{\tau_1} - \frac{1}{\tau_2}\right)^2 + \frac{2}{\tau_1^2}\frac{T_r}{J} + \frac{2}{\tau_1 \tau_2}\frac{T_r}{J} + \left(\frac{1}{\tau_1}\frac{T_r}{J}\right)^2}\right) \tag{41}$$

$$a_2 = \frac{\tau_f}{2}\frac{J}{T_r}\left(-\frac{1}{\tau_1} + \frac{1}{\tau_2} + \frac{1}{\tau_1}\frac{T_r}{J} - \sqrt{\left(\frac{1}{\tau_1} - \frac{1}{\tau_2}\right)^2 + \frac{2}{\tau_1^2}\frac{T_r}{J} + \frac{2}{\tau_1 \tau_2}\frac{T_r}{J} + \left(\frac{1}{\tau_1}\frac{T_r}{J}\right)^2}\right) \tag{42}$$

Where λ_1 and λ_2 are both the eigenvalue in the matrix, a_1 and a_2 are both the factor in the eigenvector in the matrix, τ_1 and τ_2 is the time constant in region 1 and region 2 respectively.

Based on the final solution in Eq. 36, it reveals that the production rate is related to four variables (productivity index (J), transmissibility between region 1 and region 2 (T_r), time constant in region 1 (τ_1) and time constant in region 2 (τ_2)). By fitting production data, four variables can be determined and the analytical solution can be applied for performance prediction.

5 Model validation

5.1 Validation against numerical cases

To verify the derived analytical solution, one numerical model contains 35 grid cells in the *x*-direction, 50 grid cells in the *y*-direction and only one grid cell in the *z*-direction is built with Eclipse reservoir simulator and the model parameters are summarized in Table 1. Considering the symmetry of the conceptual model and computational convenience, one-quarter of the region 1 and region 2 around one hydraulic fracture exhibited in Figure 1A is extracted for comparison. A top view of the numerical model is shown in Figure 2, where the first column of grids represents the half-length of the hydraulic fracture and the first row of grids in the *x*-direction represents the horizontal wellbore only connected with the region 1. The gray region represents region 2, while the blue region represents region 1.

Pressure-dependent properties is considered and linearized using the pseudo-pressure and pseudo-time during the derivation of the new analytical solution. It is essential to transform the results obtained with numerical models into production rate over pseudo-time and then fit the transformed results with the derived analytical solution. A comparison of the production rates obtained with the numerical simulation and our analytical model is shown in Figure 3. The blue dotted line indicates the relationship between the gas rate and pseudo-

TABLE 3 Summary of model parameters obtained from the four additional numerical cases.

Case	V_{p2}/V_{p1}	τ_1 (days)	τ_2 (days)	T_r/J	q_i (Mscf/D)	Calculated result	Ratio
							Error (%)
Case 2	1	3	727	0.0041	13,700	0.994	0.6
Case 3	1/9	5	117	0.00472	13,550	0.11	1.0
Case 4	3/2	3	1,022	0.0044	15,390	1.499	0.1
Case 5	2/3	3	448	0.0045	13,580	0.672	0.8

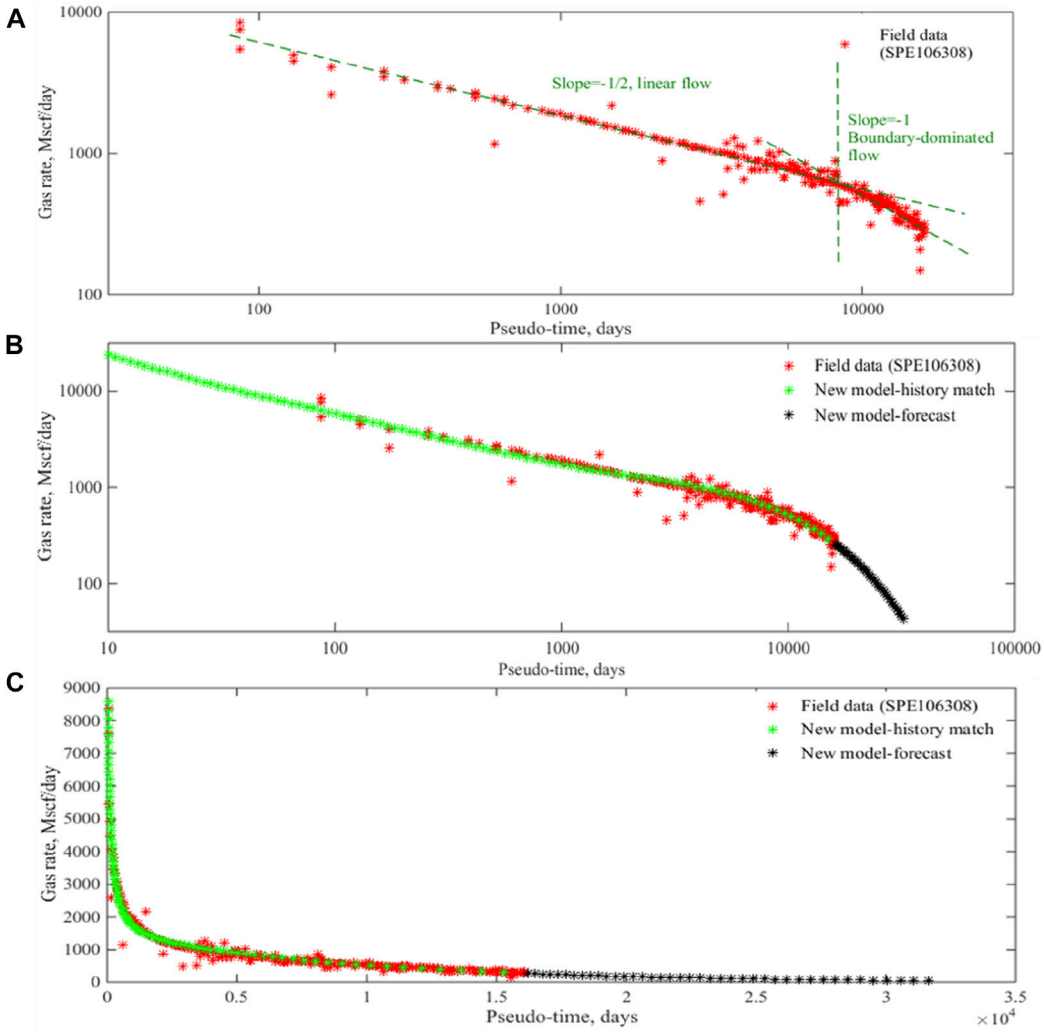

FIGURE 4
Summary of the production profiles in field example. **(A)** The flow regimes diagnosis. **(B,C)** The history-matching and forecasting results on a log-log and Cartesian plots.

time whereas the red dotted line indicates that determined from the derived analytical solution. The simulation and analytical results agree well. As shown in Figure 3, four flow regimes are identified. Regime 1 exhibits a half-slope straight line in a log-log plot which represents the transient linear flow in region 1. The permeability in this region is relatively high and hence the time constant in this region is relatively short and equals nearly 4 days. Then, the exponential curve of Regime 2 represents the boundary of region 1 is reached, which is referred to as boundary-dominated flow in region 1 or inner-boundary-dominated flow. Regime 3 exhibits the expected straight line with a half-slope signature. In our model, the permeability of region 2 is low and thus the time constant is relatively long (246 days). Regime 4 experiences

TABLE 4 Model output parameters after fitting.

Parameter	Value
τ_1 (days)	8
τ_2 (days)	8,130
T_r/J	0.102
q_i (Mscf/D)	16,980

outer-boundary-dominated flow, which is caused by the boundary of region 2. Table 2 summarizes the four variables after fitting.

5.2 Validation for the pore volume ratio

According to Eqs 37, 38 the time constants in region 1 and region 2 are defined to relate strongly with the pore volumes of regions. When Eq. 37 is divided by Eq. 38, we can derive the pore volume ratio of two regions as below:

$$\frac{V_{p_2}}{V_{p_1}} = \frac{\tau_2}{\tau_1}\frac{T_r}{J} \tag{43}$$

Substituting the model parameters in Table 2 into Eq. 43, the pore volume ratio can be obtained. We compare it to the given value from the numerical model which is proved correct within the accepted error bound.

$$\frac{V_{p_2}}{V_{p_1}} = \frac{246}{4} \times 0.007289 = 0.44 \approx \frac{18}{42} \tag{44}$$

The calculated pore volume ratio is nearly equal to the given value in Case 1. To further verify the accuracy of Eq. 43, four more numerical cases are conducted based on the previous numerical model parameters. Table 3 summarizes all the output values from these four numerical cases. Through comparing the given pore volume ratio to the calculated results, the comparison reveals that the accuracy of the calculated results is higher than 95% and thus the model parameters from our new analytical solution can be applied to estimate the pore volume ratio.

6 Application to field example

In this section, we apply the practical analytical solution to field data. The Mexico gas well is a 'near textbook' quality tight gas well with long production history and high quality data, which is operated under a constant bottom-hole pressure of 920 Psi. Several analyses have shown that the reservoir has an ultra-low permeability less than 0.001 md and there is only one well in this field. The original production data is from Blasingame et al. (2007). First, we transform time into the pseudo-time and then the log-log diagnostic plot of gas rate versus pseudo-time is obtained, which exhibit a half-slope straight line and a nearly unit-slope line in Figure 4A indicating linear and boundary-dominated flow. Since the linear flow lasts for nearly 10,000 days, this linear flow regime is identified as Regime 3 and the boundary-dominated flow represents Regime 4. The next step involved matching our model to the production data. The history matching and forecasting results is shown in Figure 4B. The red marks in Figure 4B indicate the production data and the green marks indicate the analytical solution of the history match. A suitable matching degree is revealed. The four model parameters obtained from the history matching process is summarized in Table 4. Based on these output parameters, we forecast the gas rate until 30,000 days, indicated by the black markers in Figure 4B. The more intuitive results are shown in Figure 4C by Cartesian plots. Meanwhile, we can calculate the ratio of region pore volume by Eq. 43 as V_{p2}/V_{p1}=104. The ratio can also be used to explain why only two flow regions can be observed rather than four regimes as seen in the previous numerical models. From the ratio, we can obtain that the volume of high permeability region is far smaller than the matrix region and thus the flow in region 1 with high permeability is too fast to be observed.

7 Conclusion

In this paper, a practical analytical model is presented for performance prediction in unconventional gas reservoirs under constant bottomhole pressure. Numerical models were employed to verify the accuracy of derived analytical solution and an excellent agreement was revealed. The following conclusions are drawn:

(1) The proposed analytical solution is derived in real-time domain bypassing Laplace transform and numerical inversion, which is highly suitable for field applications.
(2) Pressure-dependent properties is considered and linearized using the pseudo-pressure and pseudo-time in the analytical model and it is applicable for performance prediction in unconventional gas reservoirs.
(3) The pore volume ratio of different regions can be calculated reversely and the relative error is less than 10%, which is helpful for rapidly evaluating the effect of hydraulic fracturing.

Data availability statement

The original contributions presented in the study are included in the article/Supplementary Material, further inquiries can be directed to the corresponding author.

Author contributions

Conceptualization; methodology and investigation; writing—original draft preparation; project administration; funding acquisition-KQ.

Funding

This study was supported by Basic Research Project from Jiangmen Science and Technology Bureau (Grant No. 2220002000356).

Conflict of interest

The author declares that the research was conducted in the absence of any commercial or financial relationships that could be construed as a potential conflict of interest.

Publisher's note

All claims expressed in this article are solely those of the authors and do not necessarily represent those of their affiliated organizations, or those of the publisher, the editors and the reviewers. Any product that may be evaluated in this article, or claim that may be made by its manufacturer, is not guaranteed or endorsed by the publisher.

Supplementary material

The Supplementary Material for this article can be found online at: https://www.frontiersin.org/articles/10.3389/feart.2023.1143541/full#supplementary-material

References

Abassi, M., Sharifi, M., and Kazemi, A. (2019). Development of new analytical model for series and parallel triple porosity models and providing transient shape factor between different regions. *J. Hydrol.* 574, 683–698. doi:10.1016/j.jhydrol.2019.04.038

Anderson, D. M., and Mattar, L. (2005). "An improved pseudo-time for gas ReservoirsWith significant transient flow," in Canadian International Petroleum Conference, Calgary, Alberta (Calgary: Society of Petroleum Engineers).

Arps, J. J. (1945). Analysis of decline curves. *Trans. AIME* 160 (01), 228–247. doi:10.2118/945228-g

Blasingame, T. A., Amini, S., and Rushing, J. (2007). "Evaluation of the elliptical flow period for hydraulically-fractured wells in tight gas sands -- theoretical aspects and practical considerations," in SPE Hydraulic Fracturing Technology Conference, College Station, Texas, U.S.A. (College Station: Society of Petroleum Engineers).

Blasingame, T. A., McCray, T. L., and Lee, W. J. (1991). "Decline curve analysis for variable pressure drop/variable flowrate systems," in SPE Gas Technology Symposium (Houston, Texas, USA: Society of Petroleum Engineers).

Brown, M., Ozkan, E., Raghavan, R., and Kazemi, H. (2011). Practical solutions for pressure-transient responses of fractured horizontal wells in unconventional shale reservoirs. *SPE Res Eval Eng* 14 (06), 663–676. doi:10.2118/125043-pa

Ci-qun, L. (1983). Exact solution of unsteady axisymmetrical two-dimensional flow through triple porous media. *Appl. Math. Mech.* 4 (5), 717–724. doi:10.1007/bf02432083

Cipolla, C. L., Lolon, E. P., Erdle, J. C., and Rubin, B. (2010). Reservoir modeling in shale-gas reservoirs. *SPE Res Eval Eng.* 13 (4), 638–653. doi:10.2118/125530-pa

Clarkson, C. R. (2013). Production data analysis of unconventional gas wells: Review of theory and best practices. *Int. J. COAL Geol.* 110, 101–146. doi:10.1016/j.coal.2013.01.002

Dejam, M., Hassanzadeh, H., and Chen, Z. (2018). Semi-analytical solution for pressure transient analysis of A hydraulically fractured vertical well in A bounded dual-porosity reservoir. *J. Hydrol.* 565, 289–301. doi:10.1016/j.jhydrol.2018.08.020

Ding, Y., Wu, Y. S., Farah, N., Wang, C., and Bourbiaux, B. (2014). "Numerical simulation of low permeability unconventional gas reservoirs," in SPE/EAGE European Unconventional Resources Conference and Exhibition (Vienna, Austria: Society of Petroleum Engineers).

Duong, A. N. (2011). Rate-decline analysis for fracture-dominated shale reservoirs. *SPE Res. Eval. Eng.* 14 (03), 377–387. doi:10.2118/137748-pa

Fetkovich, M. J. (1980). Decline curve analysis using type curves. *J. Pet. Technol.* 32 (06), 1065–1077. doi:10.2118/4629-pa

Lee, S. T., and Brockenbrough, J. (1983). "A new analytic solution for finite conductivity vertical fractures with real time and Laplace space parameter estimation," in SPE Annual Technical Conference and Exhibition, San Francisco, California (San Francisco: Society of Petroleum Engineers).

Liu, J. H., Lu, M. J., and Sheng, G. L. (2021). Description of fracture network of hydraulic fracturing vertical wells in unconventional reservoirs. *Fron Earth S. C.* 07, 749181.

Ogunyomi, B. A., Patzek, T. W., Lake, L. W., and Kabir, C. S. (2016). History matching and rate forecasting in unconventional oil reservoirs with an approximate analytical solution to the double-porosity model. *SPE Res Eval Eng.* 19 (01), 070–082. doi:10.2118/171031-pa

Qiu, K. X., and Li, H. (2018). A new analytical solution of the triple-porosity model for history matching and performance forecasting in unconventional oil reservoirs. *SPE J.* 23 (06), 2060–2079. doi:10.2118/191361-pa

Rao, X., Xin, L. Y., He, Y. X., Fang, X., Gong, R., Wang, F., et al. (2022). Numerical simulation of two-phase heat and mass transfer in fractured reservoirs based on projection-based embedded discrete fracture model (pEDFM). *J. Pet. Sci. Eng.* 208, 109323. doi:10.1016/j.petrol.2021.109323

Stalgorova, E., and Mattar, L. (2012). "Practical analytical model to simulate production of horizontal wells with branch fractures," in SPE Canadian Unconventional Resources Conference, Calgary, Canada (Calgary: Society of Petroleum Engineers).

Stalgorova, K., and Mattar, L. (2013). Analytical model for unconventional multifractured composite systems. *SPE Res Eval Eng.* 16 (3), 246–256. doi:10.2118/162516-pa

Stehfest, H. (1970). Algorithm 368: Numerical inversion of Laplace transforms [D5]. *Commun. ACM.* 13 (1), 47–49. doi:10.1145/361953.361969

Wattenbarger, R. A., El-Banbi, A. H., Villegas, M. E., and Maggard, J. B. (1998). "Production analysis of linear flow into fractured tight gas wells," in SPE Rocky Mountain Regional/Low-Permeability Reservoirs Symposium (Denver, Colorado: Society of Petroleum Engineers).

Wei, S. M., Xia, Y., Jin, Y., Chen, M., and Chen, K. (2019). Quantitative study in shale gas behaviors using A coupled triple-continuum and discrete fracture model. *J. Pet. Sci. Eng.* 174, 49–69. doi:10.1016/j.petrol.2018.10.084

Xia, Y., Jin, Y., Chen, M., and Chen, K. P. (2019). An enriched approach for modeling multiscale discrete-fracture/matrix interaction for unconventional reservoir simulations. *SPE J.* 24, 1349–1374. doi:10.2118/194012-pa

frontiers | Frontiers in Earth Science

TYPE Original Research
PUBLISHED 16 March 2023
DOI 10.3389/feart.2023.1163295

OPEN ACCESS

EDITED BY
Peng Tan,
CNPC Engineering Technology R & D Company Limited, China

REVIEWED BY
Yanfang Gao,
Northwest University, China
Mengli Li,
The University of Newcastle, Australia

*CORRESPONDENCE
Yongxiang Zheng,
zhengyx@stdu.edu.cn

SPECIALTY SECTION
This article was submitted to Environmental Informatics and Remote Sensing, a section of the journal Frontiers in Earth Science

RECEIVED 10 February 2023
ACCEPTED 06 March 2023
PUBLISHED 16 March 2023

CITATION
Bai Y, Hu Y, Liao X, Tan J, Zheng Y and Wang W (2023), Research on the influence of stress on the penetration behavior of hydraulic fracture: Perspective from failure type of beddings. *Front. Earth Sci.* 11:1163295. doi: 10.3389/feart.2023.1163295

Research on the influence of stress on the penetration behavior of hydraulic fracture: Perspective from failure type of beddings

Yuesong Bai[1,2], Yaoqing Hu[1], Xingchuan Liao[3], Jin Tan[3], Yongxiang Zheng[4]* and Wei Wang[4]

[1]Institute of Mining Technology, Taiyuan University of Technology, Taiyuan, China, [2]Shanxi Wangjialing Coal Industry Co., Ltd., Xinzhou, China, [3]School of Civil Engineering and Geomatics, Southwest Petroleum University, Chengdu, Sichuan, China, [4]Key Laboratory of Roads and Railway Engineering Safety Control (Shijiazhuang Tiedao University), Ministry of Education, Shijiazhuang, Hebei, China

The failure types of bedding determine the penetration behavior of hydraulic fracture. A stratum model containing bedding was established based on the 3D block distinct element method to explore the penetration behavior of hydraulic fractures with different types of bedding. The mechanics of hydraulic fractures penetrating the shear- failure bedding plane and tensile-failure bedding plane were analyzed. The results showed that the shear-failure bedding plane was more difficult to expand than the tensile-failure bedding plane after the hydraulic fracture turns to bedding plane. The initial stress magnitude controls the expansion difficulty of hydraulic fractures, and the high stress magnitude attenuated penetration behavior. The vertical stress affected the shear failure by increasing the shear strength of the bedding plane. It affected the tensile failure by increasing the initiation stress of the bedding plane. The effect of horizontal stress on the penetration behavior included the influence on the initiation stress of vertical joints and the enhancement of the interference stress on the horizontal bedding plane. The conclusions can provide the guidance for hydraulic fracturing in reservoir with bedding planes.

KEYWORDS

failure types of bedding, penetration behavior, shear-failure bedding plane, tensile-failure bedding plane, stress

1 Introduction

Bedding planes is widely developed in shale. The penetration behavior of hydraulic fractures refers to the behavior of whether hydraulic fractures can cross the bedding plane. It has an important influence on the network of hydraulic fractures (Zhang et al., 2019; Huang et al., 2020; Tan et al., 2020). If the hydraulic fracture cannot cross the bedding plane, the fracture height is limited. Conversely, if the hydraulic fractures can cross the bedding plane, the hydraulic fracture can connect multiple layers (Tong et al., 2020). The complexity of fracture network requires both fracture height and multiple fracturing (Shicheng et al., 2021). Consequently, it is meaningful to explore the influence of the bedding plane on the formation of fracture network (Xiao et al., 2019).

Previous studies largely focused on the influence factors of penetration behavior of hydraulic fracture. The influence factors can be divided into three types, the stress difference (Warpinski et al., 1982; Huang et al., 2016; Weng et al., 2018), the difference of rock properties (Huang et al.,

2018; Xu et al., 2019; Huang et al., 2023), and the weak bedding planes (Tang and Wu, 2018; Xing et al., 2018; Zhang et al., 2022). Some numerical simulation and physical experiments about the penetration behavior of hydraulic fractures showed that the filtration of fracturing fluid into the bedding plane reduces the penetration ability (Ji et al., 2015; Huang et al., 2019; Gao and Ahmad, 2020; Luo et al., 2022). It mainly describes the phenomenon that the bedding planes hindered fracture propagation, but fails to explain the control mechanism of bedding on hydraulic fracture. Actually, the penetration behavior of hydraulic fractures is mainly related to the mechanical behavior of the weak bedding plane. Heng et al. (2021) believe that the penetration behavior of hydraulic fractures is controlled by the mechanical properties of the bedding joint and the local stress state of the fracture tip. And the penetration behavior of hydraulic fractures is a path selection problem. It means that the hydraulic fractures usually propagate along the path with the least resistance. Zhang et al. (2021a) and Zhang et al. (2021b) believe that the stress disturbance induced by weak plane before hydraulic fractures approach the weak bedding plane results in the energy dissipation on the bedding plane. Huang et al. (2022) analyzed the penetration law in the layered rock mass under different regimes based on the particle distinct element method. Zheng et al. (2019) and Zheng et al. (2022) analyzed the evolution of normal stress and shear stress on the bedding plane when the hydraulic fracture approached through the block distinct element method, and identified the discontinuous deformation (slip or shear failure) at the fracture tip as the main reason why the hydraulic fracture could not cross the bedding. Wang et al. (2019) also showed that the increase of shear stress on the bedding plane and the passivation of fracture tip affect the penetration of hydraulic fractures. Tan et al. (2021) proposed the notion of transition zone in the layered formation and investigated the effects of multiple influencing factors on hydraulic fracture vertical propagation behavior based on XFEM-based CZM method. Zhao et al. (2022) given a new pseudo 3D hydraulic fracture propagation model for sandstone reservoirs considering fracture penetrating height. In conclusion, the mechanism of weak bedding plane hindering vertical propagation of fractures has been preliminarily understood, that is, the shear behavior on the bedding plane increases the difficulty of hydraulic fracture penetration. Therefore, the penetration behavior of hydraulic fractures can be determined by stress state at connection point between hydraulic fracture and bedding plane.

The stress state in the formation determines the choice of the path after the hydraulic fracture meets the bedding plane. If the stress field meets the failure criterion of the bedding plane first, the bedding planes open and the hydraulic fracture turns to spread along the bedding plane. If the stress filed meets the failure criterion of the fracture tip, the fractures propagate along the original path and cross the bedding plane. Therefore, the strength of the bedding plane plays an important role in fracture penetration. According to the strength characteristics, the bedding plane can be divided into two categories. They are shear-failure bedding plane (the shear strength of the bedding plane is low) and tensile-failure bedding plane (the tensile strength of bedding plane is low). However, the existing researches mainly focus on the shear failure of bedding plane. There are few discussions about the failure types of bedding plane and penetration behavior of fracture.

Here, the penetration behavior of hydraulic fractures is calculated by the 3D block distinct element method (3D DEM) considering the failure type of bedding plane and *in-situ* stress conditions. The influence of stress filed on fracture propagation path under different failure types of bedding plane was analyzed. The structure of this paper is as follow. Firstly, the 3D DEM is introduced and the block model with bedding plane is established. Then, the stress evolution of fracture penetration behavior in shear-failure bedding plane is studied. Finally, the stress evolution of fracture penetration behavior in tensile-failure bedding plane is analyzed. In conclusion, this paper analyzes the influence mechanism of bedding failure type and stress state on the penetration behavior of hydraulic fractures, which has important theoretical guiding significance for the hydraulic fracturing construction of layered rock mass.

2 Method and model

2.1 Block distinct element method

The block distinct element method has an advantage in simulating the hydro-mechanic coupling behavior in the fracture. In this paper, the block distinct element method was used to simulate the hydraulic fracturing. The block distinct element describes the discontinuity by a set of distinct blocks. So, it has significant advantages in modeling discontinuities. Each block is subdivided into finite difference elements consisting of tetrahedral regions and nodes. The velocities, displacements and joint forces of all nodes at different time steps follow the Newton's laws of motion. The discontinuity is expressed by the boundary between blocks. The 3D DEM have been used by Zheng. See literature (Zheng et al., 2019; Zheng et al., 2022) for details about the validation of this method.

(1) The failure of joints

The failure of the joint represents the opening of the fracture. In the block distinct element method, joints are described by contacts. The constitutive model of joint is the Coulomb slip joint model. This model considers shear failure, tensile failure and dilation. During the elastic stage, the contact is described by the normal stiffness and tangential stiffness. The normal behavior of the joint can be expressed as (Tang and Wu, 2018)

$$\Delta F^n = -K_n \Delta U^n A_c \tag{1}$$

The shear behavior can be expressed as:

$$\Delta F_i^s = -K_s \Delta U_i^s A_c \tag{2}$$

Where, A_c is the area of contact. ΔF^n is the increment of normal force, ΔF_i^s is the shear stress increment, K_n is the normal stiffness, K_s is tangential stiffness, ΔU^n is the normal displacement increment, ΔU_i^s is tangential displacement increment.

The maximum normal tensile force of the joint (without slip or cracking) is:

$$T_{\max} = -TA_c \tag{3}$$

Where, T is the tensile strength.

The maximum shear force allowed by the joint is:

$$F^s_{\max} = cA_c + F^n \tan\varphi \tag{4}$$

Where, c is the cohesion of the joint and φ is the friction angle.

The contact fails when the stress on the joint equals to its tensile or shear strength. Then the tensile strength and cohesion of the joint equals to zero after failure. Here, the maximum tensile and shear force on the joint plane can be expressed as:

$$T_{\max} = 0 \tag{5}$$

$$F^{s}_{\max} = F^{n} \tan \phi \tag{6}$$

The instantaneous loss of strength after failure is the "displacement-weaken" behavior of joint plane. Here, the new contact force between the blocks will be updated (assume that the compression is positive). For tensile failure, the update mode of contact force is:

If $F^n < T_{\max}$, then the normal force $F^n = 0$, shear force $F^s_i = 0$.

For shear failure, the update mode of the contact force is:

If $F^s > F^s_{\max}$, then the shear force is $F^s_i := F^s_i \frac{F^s_{\max}}{F^s}$.

Where, the shear force is $F^s = (F^s_i F^s_i)^{1/2}$.

Shear dilation occurs only in the slip mode. Then, the shear displacement increment can be expressed as:

$$\Delta U^s = \left(\Delta U^s_i \Delta U^s_i\right)^{1/2} \tag{7}$$

The shear displacement causes the change in normal displacement considering dilation. The relationship can be characterized by the dilation angle ψ. And their relationship is:

$$\Delta U^n (\mathrm{dil}) = \Delta U^s \tan \psi \tag{8}$$

Where, $\Delta U^n(dil)$ is normal displacement considering dilation. Ψ is the dilation angle.

Here, the influence of dilation should be considered in the normal force, and the normal force becomes:

$$F^n := F^n + K_n A_c \Delta U^s \tan \psi \tag{9}$$

(2) Fluid flow in joints

The fluid flow in the joint follows to the Navier-Stokes equation. When the joint surfaces are approximately parallel non-permeable and the fluid is incompressible, the Navier-Stokes equation can be simplified to the Reynolds equation.

$$\left(\frac{u^3 \rho g}{12\mu} \phi, i\right), i = 0 \tag{10}$$

where $u = u(x_i)$ is the distance of the two non-permeable surfaces at a point x_i on the plane. ϕ, ρ and μ are the head height, fluid density, and fluid viscosity, respectively.

$$q_i = -\frac{u^3 \rho g}{12\mu} \phi, i = -k_H \phi, i \tag{11}$$

Where, the permeability of a single fracture is $u^2/12$, and the hydraulic conductivity is $k_H = \frac{u^3 \rho g}{12\mu}$.

2.2 Modelling

The essence of the fracture height containment is the interaction between the hydraulic fracture and bedding plane. In order to reveal the behavior of hydraulic fractures before and after encountering bedding, a base model of bedding stratum (shown in Figure 1) is established. The size of model is 1 m*1 m*1 m. It contains two horizontal joints and one vertical joint (shown in Figure 1B). Among them, the vertical joint is set to simulate the preset hydraulic fracture, while the horizontal joints are set to simulate the horizontal bedding plane. The distance between two horizontal joints is 0.3 m. The injection point is located between two bedding planes. Based on the established model, different injection rates and fracturing fluid viscosities can be set according to the experiment plan.

2.3 Basic parameters

We focus on the influence of failure type of bedding plane and *in-situ* stress on the penetration behavior of hydraulic fractures. The failure type can be divided into shear failure and tensile failure. The shear-failure bedding plane always has the high tensile strength and low shear strength. Therefore, the shear failure is the main type when the hydraulic fracturing approaches bedding plane. The tensile failure bedding plane always has the high shear strength and low tensile strength. So, the tensile failure is the main failure type. According to their types, the parameters for the shear-failure bedding plane and tensile-failure bedding plane are list in Table 1.

In addition to the failure type, the *in-situ* stress is also of great importance. The stress includes the magnitude and difference of the initial *in-situ* stress. Consequently, the effects of the stress magnitude and difference are discussed separately with two types of failure. The influence mechanism of horizontal stress and vertical stress variation is also discussed in detail.

Other parameters are set according to the laboratory data and previous literatures. The rock density is 2,600 kg/m^3. The rock elastic modulus is 20 × 10^3 MPa. The pore pressure is 1 MPa. And the Poisson's ratio is 0.25.

2.4 The stress state at intersection

No matter how the fracture propagates, the hydraulic fracture will eventually encounter the bedding plane at the intersection of the horizontal bedding and vertical joints. Then, the fracture chooses propagation path according to the stress state and strength of the horizontal and vertical joints. So, the stress state is of great significance for the penetration behavior. In order to investigate the stress state before and after the hydraulic fracture meeting the intersection, the different stress states of the vertical joints and horizontal joints at the intersection of the hydraulic fracture in the model are extracted. The details are shown in Figure 2 (Zheng et al., 2022). The solid black line in the figure represents the hydraulic fracture, and the dashed blue line indicates the location of the horizontal bedding plane. Here, the hydraulic fracture has reached but not yet crosses the bedding plane. Next, the hydraulic fracture will continue to expand, it may pass through the bedding plane or be captured by the bedding plane. The right-hand picture in Figure 2 gives the connection between different elements. If the connections (block1 and block3, or block2 and block4) on the horizontal bedding plane are broken, the bedding plane are damaged and the hydraulic

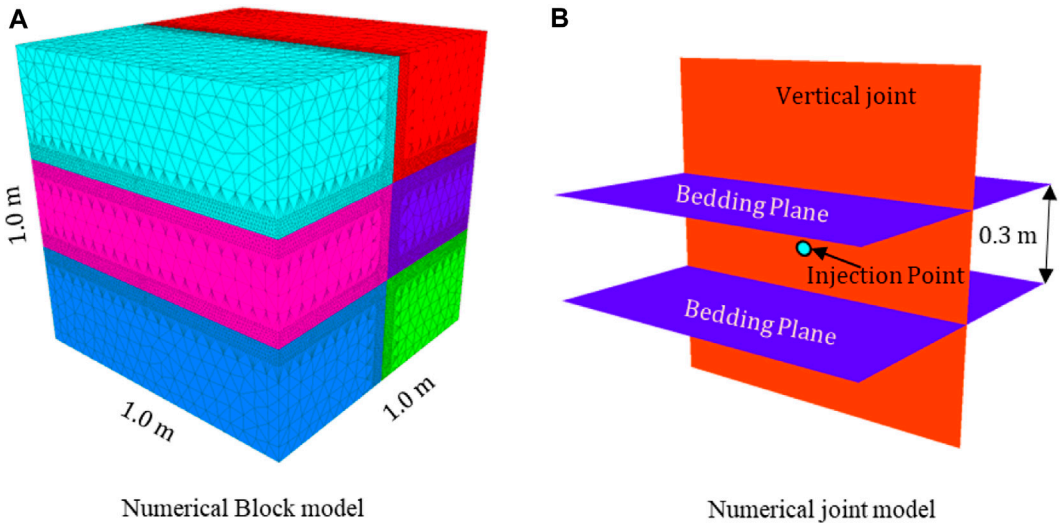

FIGURE 1
Stratum and joint model. **(A)** Numerical block model. **(B)** Numerical joint model.

TABLE 1 Base parameters for two types of bedding planes.

Failure type	Vertical joint			Horizontal joint		
	Cohesion (MPa)	Friction angle	Tensile strength (MPa)	Cohesion (MPa)	Friction angle	Tensile strength (MPa)
Shear Failure	5	20°	10	4	20°	5
Tensile Failure	10	20°	10	10	20°	3

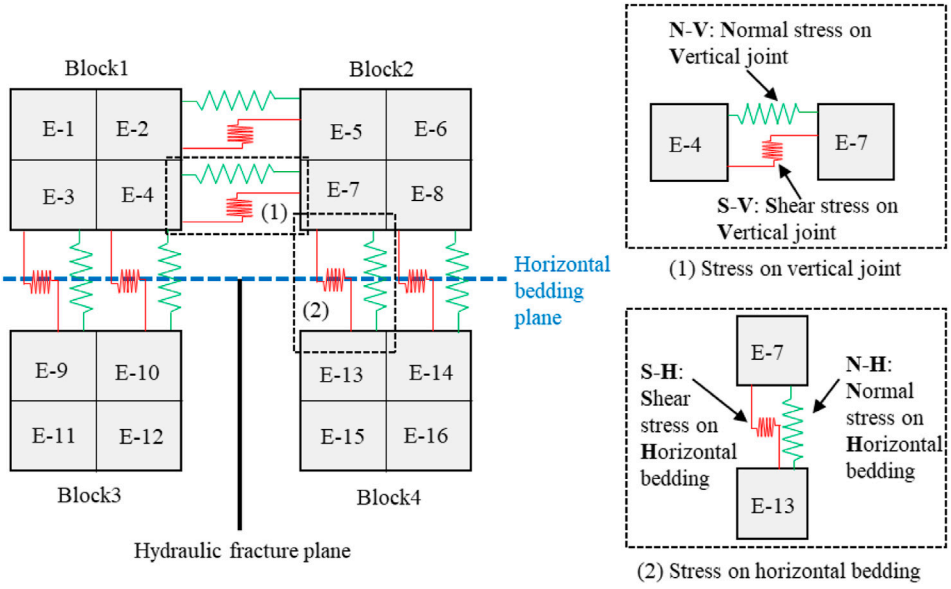

FIGURE 2
Schematic diagram of stress location (Zheng et al., 2022).

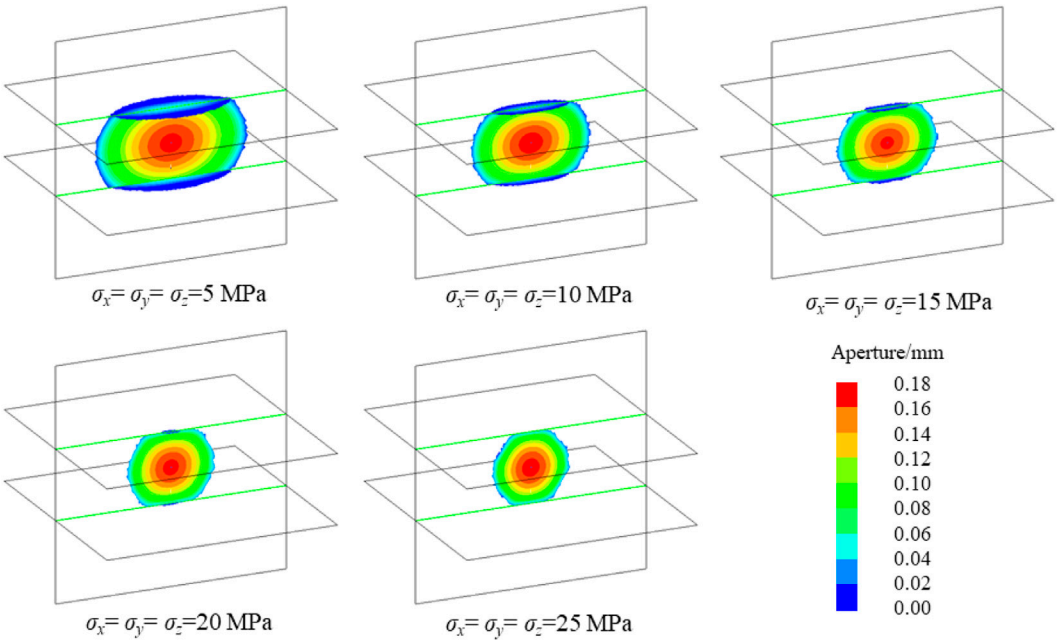

FIGURE 3
Fracture propagation morphology under uniform *in-situ* stress.

fracture is captured by the bedding. If the connections (block1 and block2) in the propagation direction of the hydraulic fracture are broken, the hydraulic fracture crosses the bedding. Based on this, the stresses on the horizontal bedding plane and vertical fracture plane are defined as N-H (normal stress on the horizontal bedding plane), S-H (shear stress on the horizontal bedding plane), N-V (normal stress on the vertical joint) and S-V (shear stress on the vertical joint) respectively. Where S denotes shear stress, N means normal stress, H indicates horizontal bedding plane, and V refers to vertical joint.

3 The effect of stress on penetration behavior with shear-failure bedding plane

In shear-failure bedding, hydraulic fracture failure mainly includes two forms. One is the tensile failure caused by the tensile stress at the front edge of the hydraulic fracture in the propagation direction. And the other is the shear failure of the bedding under the combined action of normal stress and shear stress on the bedding plane.

The effect of *in-situ* stress can be analyzed in terms of both the magnitude of the stress and the stress difference. The magnitude of the stress characterizes the initial value of the *in-situ* stress and its magnitude is mainly influenced by the burial depth of the reservoir. The difference of *in-situ* stress characterizes the stress difference reflected by tectonic stress in the reservoir. Consequently, the effects of the initial *in-situ* stress value and the *in-situ* stress difference on the hydraulic fracture propagation are analyzed separately.

3.1 The effect of initial stress on fracture propagation

3.1.1 Uniform *in-situ* stress conditions

To investigate the effect of stress magnitude on the hydraulic fracture propagation under uniform stress conditions, we assume that the stress is equal in three directions. Five cases with stress of 5 MPa, 10 MPa, 15 MPa, 20 MPa and 25 MPa are established. The injection rate is 5 mL/s. The fluid viscosity is 10 cp and the injection time is 20 s. Then the above five cases are calculated separately.

The propagation results are shown in Figure 3. In the all 5 cases, the hydraulic fractures fail to cross bedding plane. However, the fracture morphology varies under different stress conditions. When the stress is low (5 MPa), the hydraulic fracture fails to pass through the bedding plane after encountering it. Due to the barrier effect of bedding plane, hydraulic fractures propagate laterally. The hydraulic fractures turn and propagate along the bedding plane, but the extension range is not far. With the increase of *in-situ* stress, the extension range of hydraulic fractures decreases. In addition, when the stress is 5 MPa, the length of hydraulic fracture is the largest. With the increase of stress, the fracture length becomes shorter. The reduction of extension area on bedding plane and fracture length means that the fracturing volume is reduced. When the stress is 25 MPa, the hydraulic fracture has not yet propagated to the bedding plane under the same liquid injection volume. In conclusion, the initial stress magnitude controls the extension range of hydraulic fractures. Under high stress conditions, the propagation difficulty of hydraulic fractures increases, so the propagation speed of hydraulic fractures slows down and the extension range decreases.

The magnitude of *in-situ* stress reflects the burial depth of the reservoir. And the deeper the reservoir, the greater the *in-situ* stress.

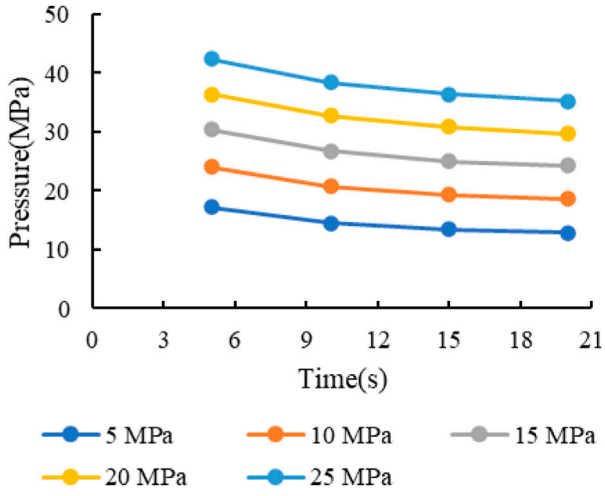

FIGURE 4
Fluid injection pressure under uniform *in-situ* stress.

Therefore, with the increase of burial depth, the difficulty of propagation increases. To obtain the same extension range, more liquid injection is required. When the stress is different, the fracture extension range is different for the same liquid injection volume. Since the stress induced by the fluid in the formation is caused by fluid compression, the formation pressure will be higher under the condition of high *in-situ* stress. Therefore, the evolution of injection pressure under different stress states is analyzed in Figure 4. The liquid injection pressure increases with the increase of stress. Therefore, fracturing in deep reservoirs requires higher pressure and higher power equipment.

In conclusion, high stress reservoirs require higher injection pressure. In this simulation, the initiation strength of the five cases is the same, so the fracture initiation is controlled by the stress state. The stress state on the joint is the result of the combined effect of the initial stress field of the formation and the included stress by liquid injection. The formation is compressed and the opening of the fracture is the result of the tension of the fracture surface. Therefore, the opening of the fracture requires the induced stress by liquid injection to overcome the initial stress. Taking N-V stress as an example, the initial N-V is the compressive stress, and the opening of hydraulic fractures requires N-V to change into a tensile state and be greater than the tensile strength of the joint (10 MPa in this cases). Therefore, the larger the initial stress, the larger the range of N-V from compression to tension. This explains why it is more difficult to propagate for hydraulic fractures under high *in-situ* stress conditions.

Hydraulic fracture propagation is the result of stress action. Its propagation behavior at the bedding plane is determined by the stress state at the intersection of hydraulic fracture and bedding plane. As mentioned above, the failure in the failure of shear-failure bedding is mainly the tensile failure of vertical joints and the shear failure of horizontal beddings. The tensile failure of vertical joints is determined by N-V. According to Coulomb slip criterion of bedding plane, shear failure of horizontal bedding is determined by normal stress (N-H) and shear stress (S-H) on bedding plane. Therefore, the stress curve at the intersection is extracted and summarized in Figure 5.

Figure 5A shows the N-V stress curve at the intersection. According to the figure, the N-V curve can be divided into three stages. The first stage is the slight decrease stage, in which the fracture tip is far from the intersection point. The induced stress caused by hydraulic fractures is small and has little influence on the total stress at the intersection point. The second stage is the rapid decrease stage, in which the fracture tip approaches and finally reaches the intersection point. At this time, the induced stress by hydraulic fracture has a great influence on this point, so the stress curve drops rapidly. According to the minimum value of each curve in Figure 5, the N-V fails to meet the tensile strength of the vertical joint. Consequently, the hydraulic fracture cannot propagate vertically and cross the bedding plane. In addition, the analysis of the starting time of this stage (when the curve starts to drop rapidly) shows that the greater the stress, the later the starting time. The late starting time means that it takes more time for the fracture to meet the bedding plane, which is caused by the slow propagation speed of hydraulic fracture under high stress conditions. The third stage is the gradual recovery stage. In this stage, N-V does not reach the tensile strength of the vertical joint, and the hydraulic fracture turns to the bedding plane. It results that the interference stress of the hydraulic fracture mainly acts on the bedding plane. Therefore, the tensile stress on the stress curve gradually decreases, and it shows a slow recovery on the curve. Finally, the curve finally approaches zero.

Figure 5B shows the N-H stress curve. Similar to the N-V curve, the N-H curve shows a slight decrease at the early stage. When the hydraulic fractures approach the intersection, the stress drops rapidly. When the bedding plane is sheared, the connection at this point is broken. Now, N-H becomes 0. Compared with the initial stage, the N-H has a greater drop than the initial stress. According to the Coulomb slip criterion, if the normal stress on the bedding plane decreases, the shear strength of the plane decreases. In conclusion, the N-H curve is higher under high stress conditions.

Figure 5C shows the S-H stress evolution curve. When the hydraulic fracture is far from the intersection, the value of shear stress is low. With the approaching of hydraulic fracture, the shear stress increases gradually. When the hydraulic fracture reaches the bedding plane, the shear stress increases rapidly. Finally, shear failure occurs at the intersection, and the shear stress decreases. It can be seen from the figure that the maximum shear stress increases with the increase of initial stress.

Figure 5D shows the N-H and S-H stress evolution. The dotted line in the figure is the critical curve for the failure of the bedding plane. The vertical dotted line on the left side of the curve indicates the tensile failure of the bedding plane, while the diagonal dotted line on the right side indicates the shear failure of the bedding plane. It can be seen from the figure that shear failure occurred to the bedding plane in all five cases. It can also be seen from the evolution law of the curve that the normal stress on the bedding plane decreases and the shear stress increases with time. Under low stress conditions (5 MPa and 10 MPa), N-H is in tension when it is damaged. Under high stress conditions (20 MPa and 25 MPa), N-H is under compression when the bedding plane is damaged. From the analysis of stress variation difference, the normal stress reduction value and the shear stress increase value on the bedding plane are

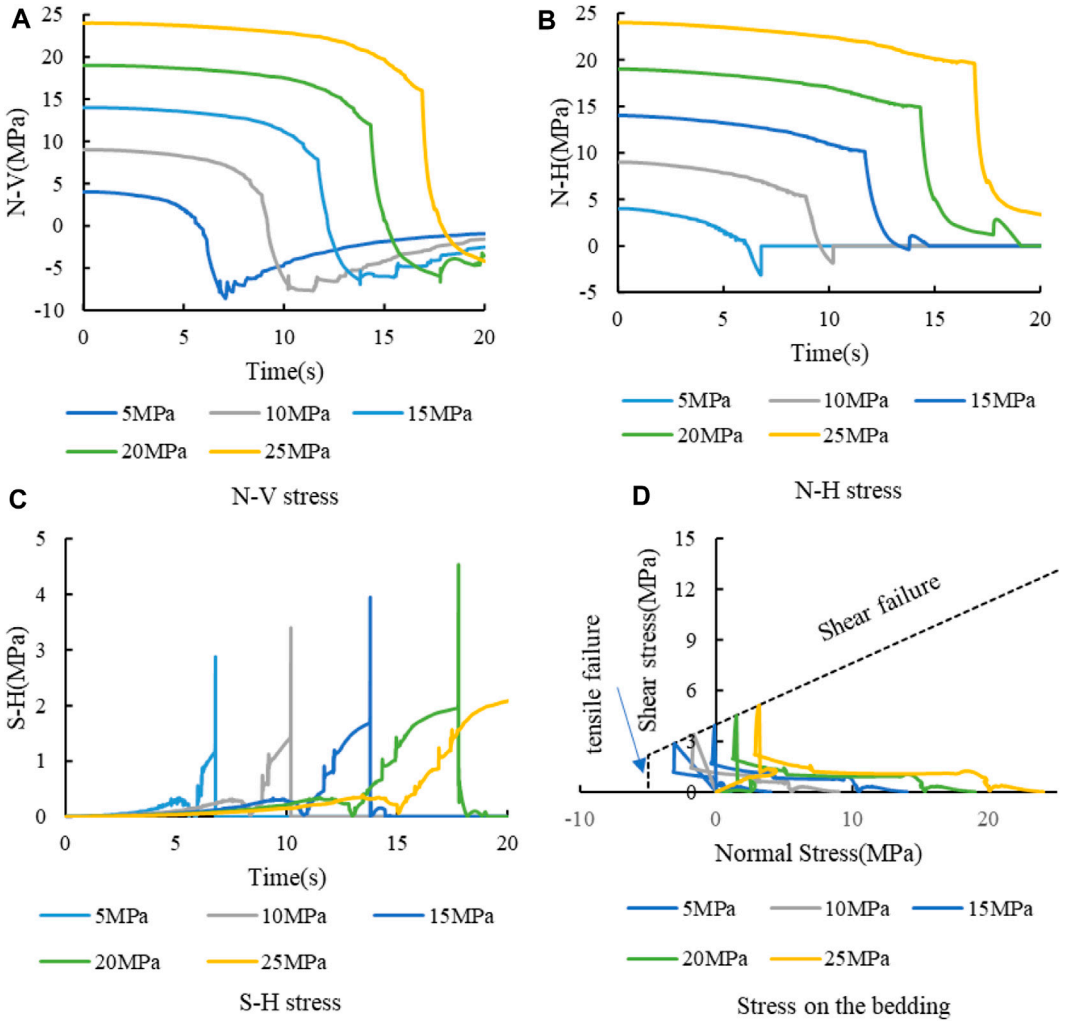

FIGURE 5
Stress curve at the intersection of hydraulic fracture and bedding plane. **(A)** N-V stress. **(B)** N-H stress. **(C)** S-H stress. **(D)** Stress on the bedding.

higher under high stress conditions. The change of stress requires the supply of injected fracturing fluid, so the difficulty of hydraulic fracture expansion under high stress conditions increases.

3.1.2 Non-uniform *in-situ* stress condition

The influence of different initial stresses on fracture propagation with uniform *in-situ* stress has been investigated. Based on the simulation scheme in the previous section, we set the difference between vertical stress and horizontal stress as 5 MPa, and the fluid injection time is increased to 30 s. But other parameters are consistent with those in the previous section. The details about simulation cases are shown in Figure 6.

Figure 6 shows the fracture propagation under non-uniform *in-situ* stress. In the five cases, due to the difference between the vertical stress and the horizontal stress, the hydraulic fracture can cross the bedding plane. The increase of vertical stress leads to the increase of normal stress on the bedding plane, which improves the shear strength of the bedding plane. From the perspective of initial stress, when the initial stress is low, the hydraulic fracture has a large expansion range and the fracture is uniform and circular. With the increase of initial stress magnitude, the difficulty of hydraulic fracture propagation increases, and the expansion range decreases gradually. In addition, when the initial horizontal stress is 25 MPa, the propagation of the hydraulic fracture is hindered when it meets the bedding plane. The hydraulic fractures first extend along the length of the fractures, and then gradually break through the bedding plane and expand vertically. In conclusion, the initial *in-situ* stress mainly affects the difficulty of hydraulic fracture propagation. The higher the initial stress is, the slower the propagation speed of hydraulic fracture is under the same construction parameters. Therefore, according to different *in-situ* stress conditions, appropriate construction parameters should be determined. On the basis of ensuring the shape of hydraulic fractures, parameters such as fluid injection rate should be appropriately increased to improve the efficiency of fracturing construction.

Figure 7 illustrates the injection pressure under different horizontal stress conditions. Similarly, the injection pressure decreases as the fracture propagates. It is easy to know that the

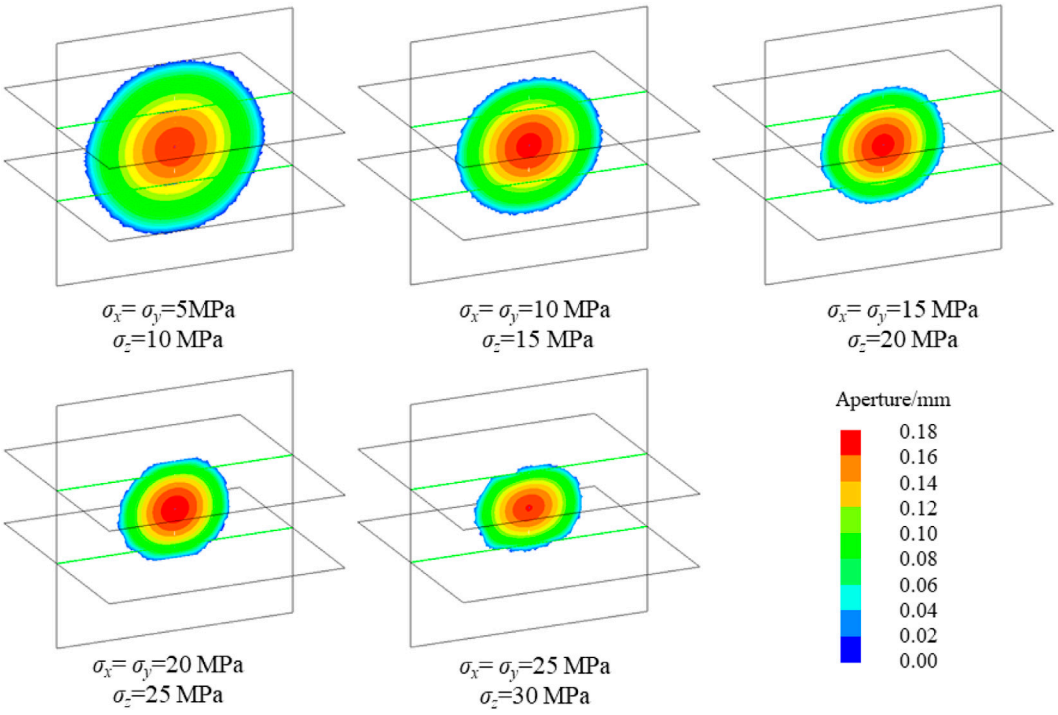

FIGURE 6
Fracture propagation with non-uniform stress (difference is 5 MPa).

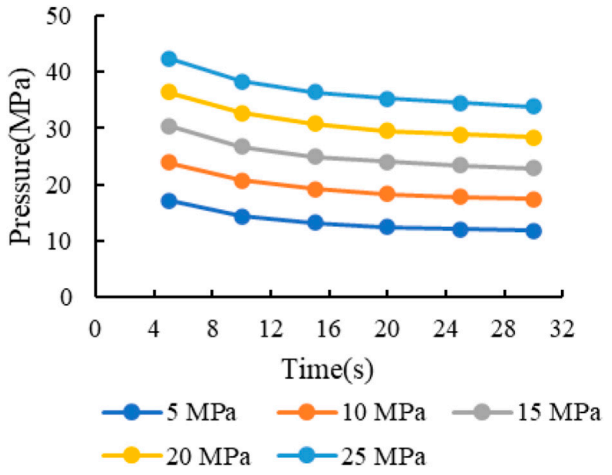

FIGURE 7
Injection pressure change with different horizontal stress σ_x (difference is 5 MPa).

injection pressure is positively correlated with the initial stress by analyzing different cases. The higher the initial stress is, the greater the stress difference required for N-V to decrease from the initial value to cracking. It results in the higher induced stress by pressure in fracture. Analysis of the stress differences among the cases demonstrates that the differences between adjacent curves are relatively uniform at the same time point.

Figure 8 presents the stress curves at the intersection. Figure 8A illustrates the N-V curve. All the hydraulic fractures cross the bedding plane and propagate along the vertical joints, so N-V is the key factor to determine the fracture propagation. From the figure, N-V are reduced from the initial stress to −10 MPa. By analyzing the curves, it can be obtained that the N-V curve is basically decreased directly to −10 MPa in the rapid decrease stage when the initial horizontal stresses is 5 MPa and 10 MPa. And as the initial stress rises, the falling rate of the N-V curve slows down in the later part of the rapid decrease stage. The duration of the slowing zone increases significantly with the increase of the initial stress. Combined with the change of fracture propagation pattern analyzed in Figure 6, the reason for the slowing down of the interval may be related to the obstruction of hydraulic fractures on the bedding plane. According to the stress curve, the N-V at the intersection has not yet reduced to −10 MPa when the hydraulic fracture approaches the bedding plane. So, the fracture cannot continue to propagate upward. However, due to the high vertical initial stress, the hydraulic fractures also cannot meet the condition of turning toward the bedding. So, the fracture expansion is hindered in vertical and horizontal direction and it can only propagate along the length direction. The N-V at the intersection reduces to −10 MPa when the fracture propagates for a certain length, and at this time the hydraulic fracture crosses the bedding plane. It is noteworthy that the duration of slowing zone increases due to the higher difficulty of fracture propagation under high stress conditions. That means the obstruction of bedding is slight after encountering the bedding plane and hydraulic fracture can cross the bedding plane rapidly when the initial stress is low. While under

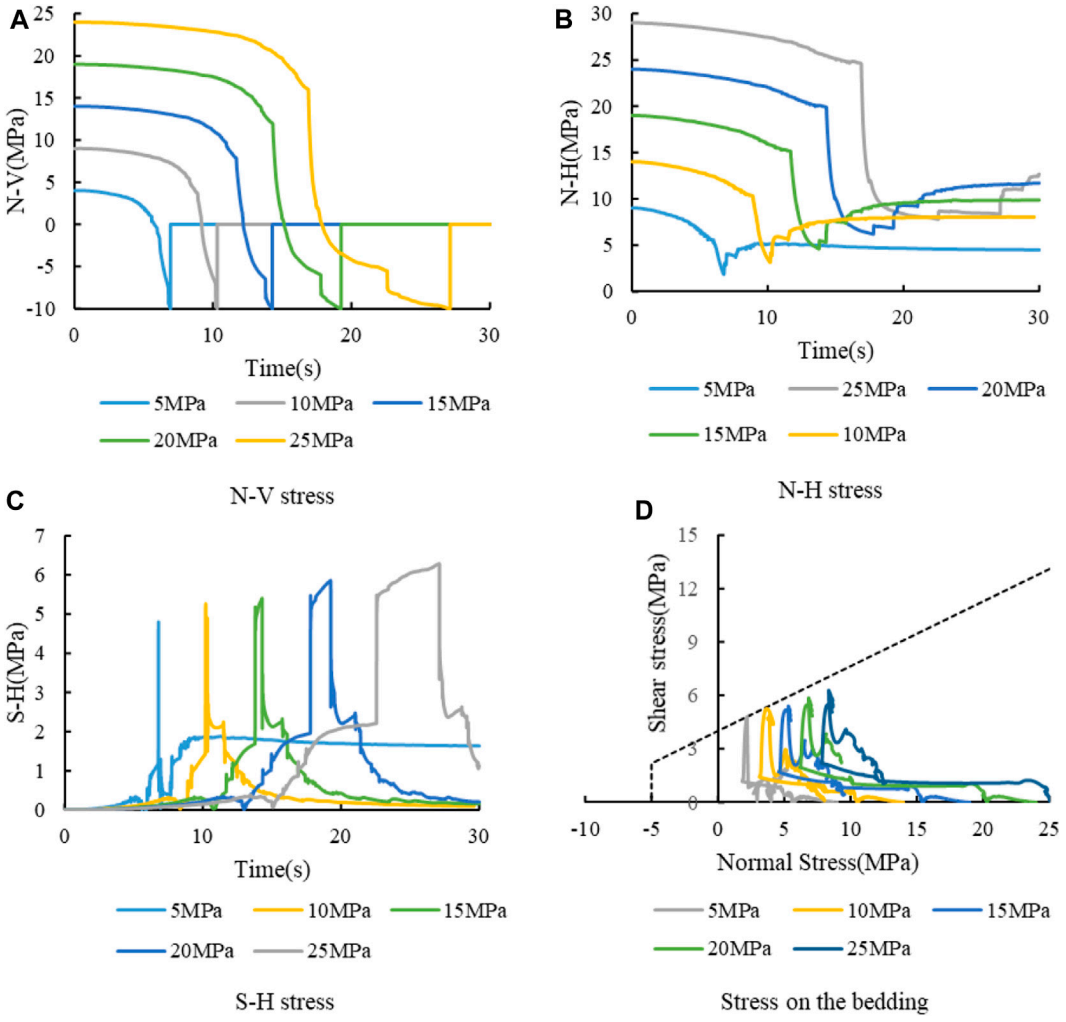

FIGURE 8
Stress curve at the intersection with different horizontal stress σ_x. **(A)** N-V stress. **(B)** N-H stress. **(C)** S-H stress. **(D)** Stress on the bedding.

high stress conditions, the hydraulic fracture is hindered by the bedding plane, and it takes some time for the hydraulic fracture to pass through the bedding plane.

Figure 8B shows the N-H stress evolution curve. Similar to Figure 5B, N-H stress decreases gradually. However, due to the high initial stress, the lowest value of the stress curve is still greater than 0, which means that the bedding plane is always in compression. When the initial stress is low, the reduction of N-H curve is low. However, due to the low initial value, its minimum value is the lowest. With the increase of initial stress, the reduction of N-H stress increases. However, due to the increase of the initial value, the minimum value of the final N-H stress increases with the increase of the initial stress.

Figure 8C presents the S-H curve. The shear stress has a jump rise when the hydraulic fracture reaches the intersection point. However, it still cannot meet the shear failure strength yet. Consequently, the shear stress remains at a higher value and increases slightly. Similar to the flat phase of N-V, there is also a slightly rising phase in S-H. When the hydraulic fracture crosses the bedding plane, the S-H curve drops suddenly. As can be seen from the figure, the duration of the flat phase becomes longer as the initial stress value rises. This is same as the N-V curve, both are influenced by the fracture barrier effect. That is, the barrier effect of bedding plane on hydraulic fracture is enhanced under high stress conditions.

Figure 8D shows the evolution curves of the normal and shear stresses on the bedding plane. At the low stress condition, the bedding plane reached the condition of shear failure, but the hydraulic fracture did not propagate along the bedding plane due to the presence of stress difference. At high initial stress, the stress on the bedding plane does not reach the shear failure condition. Due to the high initial vertical stress, the bedding plane is always under compression.

3.2 Effect of stress difference on fracture propagation

The effect of the initial stress magnitude was explored in the previous section, and the result shows that the magnitude of the initial stress value affects the propagation difficulty of the hydraulic fracture. The greater the initial stress, the more difficult it is for the hydraulic fracture to propagate. In addition to the initial stress

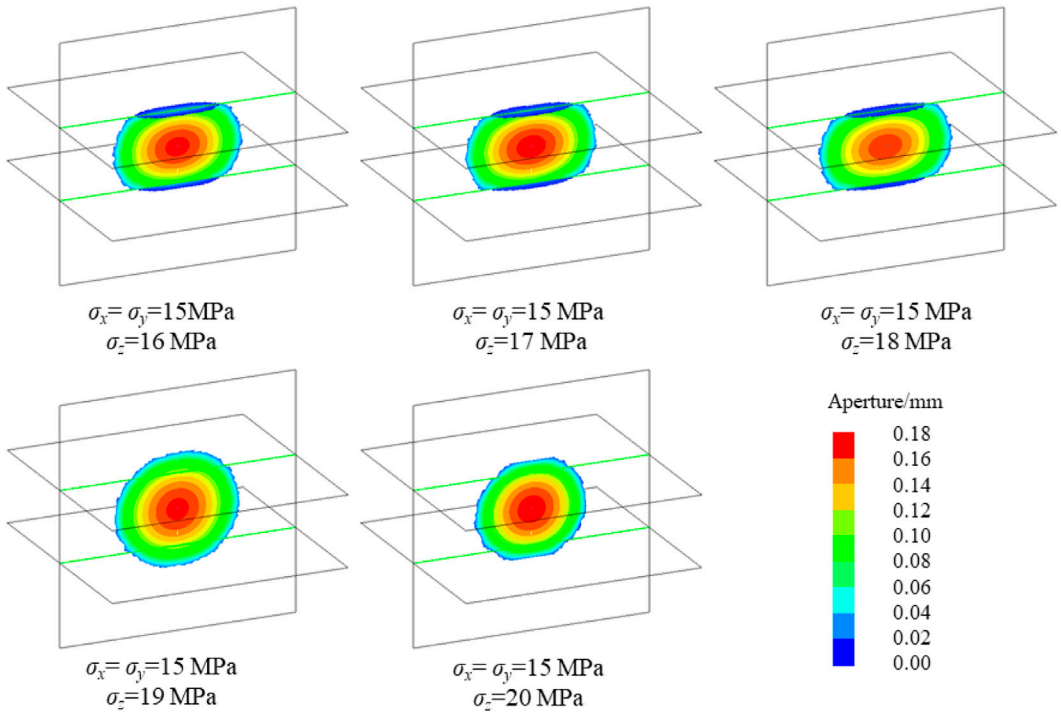

FIGURE 9
Fracture propagation of different vertical stresses (σ_x=15 MPa).

magnitude, stress difference has an important effect on the propagation morphology of hydraulic fractures. Therefore, this section addresses the effect of stress difference. Stress difference refers to the difference between vertical stress and horizontal stress. Changes in both vertical stress and horizontal stress will cause changes in stress difference, so the influence of vertical stress and horizontal stress are analyzed separately here.

3.2.1 Effect of vertical stress

In order to investigate the effect of vertical stress on hydraulic fracture propagation, the horizontal stress was set to 15 MPa and the vertical stress was set to 16 MPa, 17 MPa, 18 MPa, 19 MPa, and 20 MPa, respectively, which means the stress difference was 1–5 MPa. The injection time was 30 s. The hydraulic fracture propagation patterns under different cases are presented in Figure 9. When the vertical stress is low, the stress difference is small and the hydraulic fracture fails to cross the bedding plane, but turns to the bedding plane. Meanwhile, the hydraulic fracture propagates along the length direction. When the vertical stress is high, the stress difference is large and the hydraulic fracture cross the bedding plane directly. In summary, the hydraulic fracture penetration behavior is influenced by the stress difference, and the tendency of hydraulic fracture penetration increases when the difference between vertical stress and horizontal stress grows.

Figure 10 illustrates the injection pressure under different cases. The figure shows that the injection pressure curve is basically the same. It can be divided into two groups according to fracture morphology (cross and capture, in Figure 9). The pressure curves of the two groups were

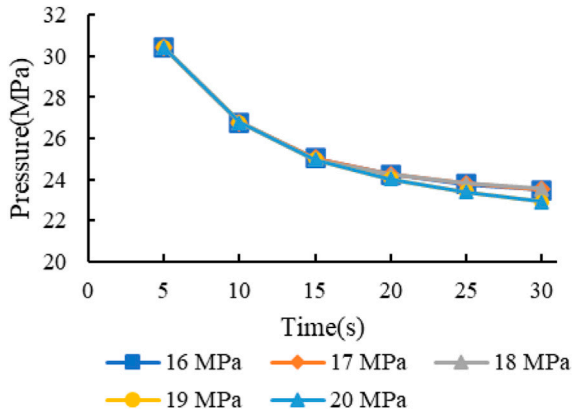

FIGURE 10
Injection pressure with different vertical stresses σ_z (σ_x=15 MPa).

basically the same before 15 s. Then the injection pressure of capture is slightly higher than that of the cross during 15 s–30 s. In the same group, the injection pressure increased slightly with the growth of vertical stress, but the difference was not obvious. Hence, if hydraulic fracture mainly propagates in the vertical joints, the injection pressure is mainly controlled by the horizontal stress and is little influenced by the vertical stress. The vertical stress mainly affects the normal stress on the bedding plane. It limits the fracture turning to bedding plane by increase the normal stress on the bedding plane.

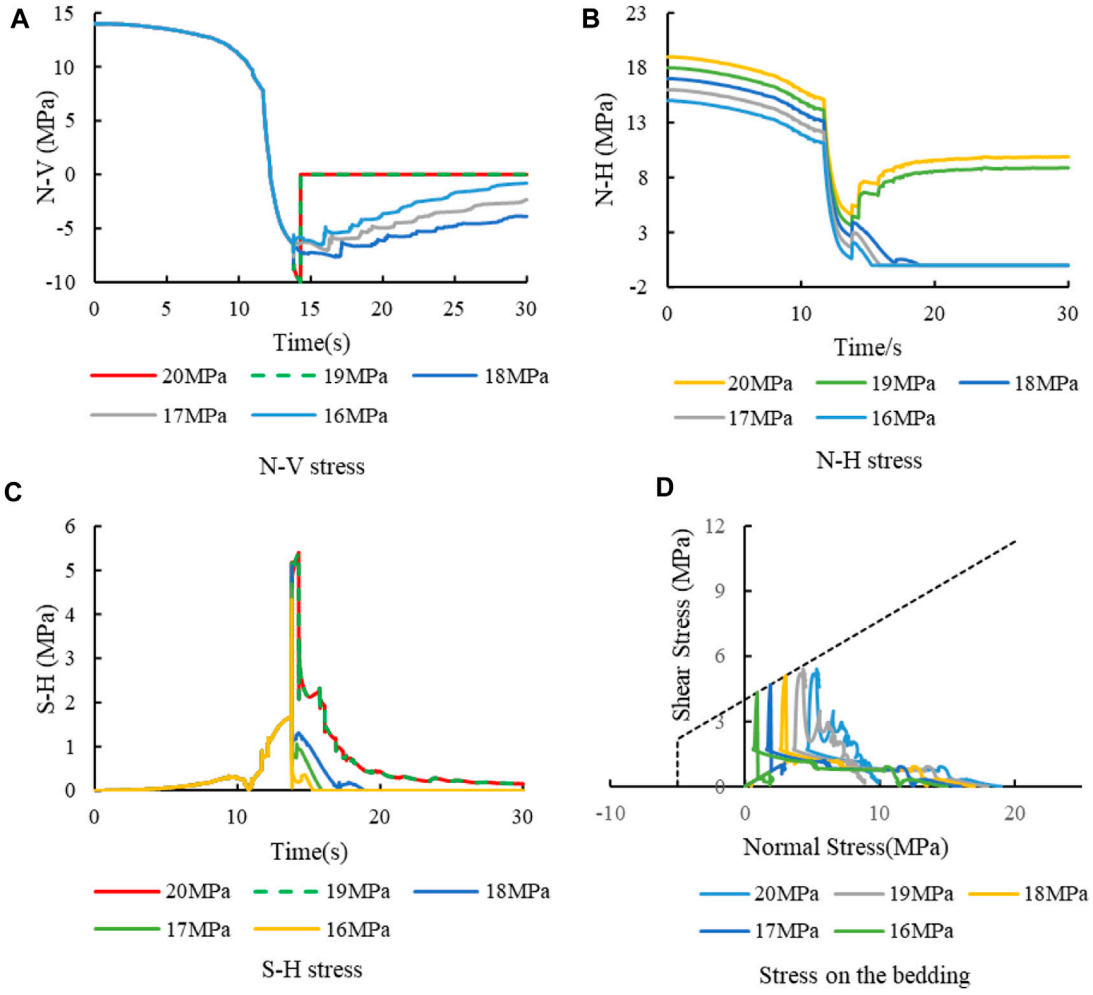

FIGURE 11
Stress curve at intersection with different vertical stresses σ_z (σ_x=15 MPa). **(A)** N-V stress. **(B)** N-H stress. **(C)** S-H stress. **(D)** Stress on the bedding.

Figure 11 shows the stress curve at the intersection. Figure 11A shows the N-V stress evolution curve. The stress curve overlaps before 15 s, indicating that the fracture propagation is controlled by horizontal stress before the hydraulic fracture encounters the bedding plane. During 15–30 s, the fractures can be divided into 2 groups according to their morphologies (cross and capture). The fracture turns to the bedding plane under the condition of low vertical stress, so the N-V can continue to maintain a certain stress and gradually tends to 0. Under the high vertical stress condition (19 MPa and 20 MPa), the hydraulic fracture crosses the bedding plane, that is why N-V becomes 0 directly and the two curves coincide. This is due to the fact that the propagation is not affected by vertical stress when a hydraulic fracture crosses the layer.

Figure 11B shows the N-H stress evolution curve. In the first half of the curve (0–15 s), the difference between the curves remains the same. It results that the minimum value of N-H under low vertical stress is small. Low N-H stress means that the shear strength of the bedding is not high and the bedding is more prone to shear failure resulting in the propagation of hydraulic fractures along the bedding plane. In conclusion, the effect of vertical stress on hydraulic fracture penetration is mainly through influencing the normal stress on the bedding plane, which then influences the shear strength of the bedding plane and finally determines the penetration behavior of the hydraulic fracture. During 15–30 s, the curves can be divided into two groups according to the failure state. However, the stress has no significant effect on the fracture propagation in this stage.

Figure 11C shows the S-H stress evolution curve. The shear stress curves coincide before the hydraulic fractures reach the bedding plane. After the hydraulic fracture meets the bedding plane, the shear stress shows slight difference. Figure 11D shows the stress path on the bedding plane. It can be seen from the figure that in the cases where fractures are captured (vertical stress is 16–18 MPa), the shear stress increases slightly with the increase of vertical stress. However, the main reason for its shear failure is that the low N-H leads to the reduction of the shear strength of the bedding plane. In this case, the shear failure of the bedding can occur under the condition of low shear stress.

In conclusion, the essence of the influence mechanism of vertical stress on the bedding behavior of hydraulic fractures is to change the normal stress on the bedding plane, and then affect the shear strength of the horizontal bedding plane. For bedding plane, the vertical stress is the normal stress on the surface. Under the

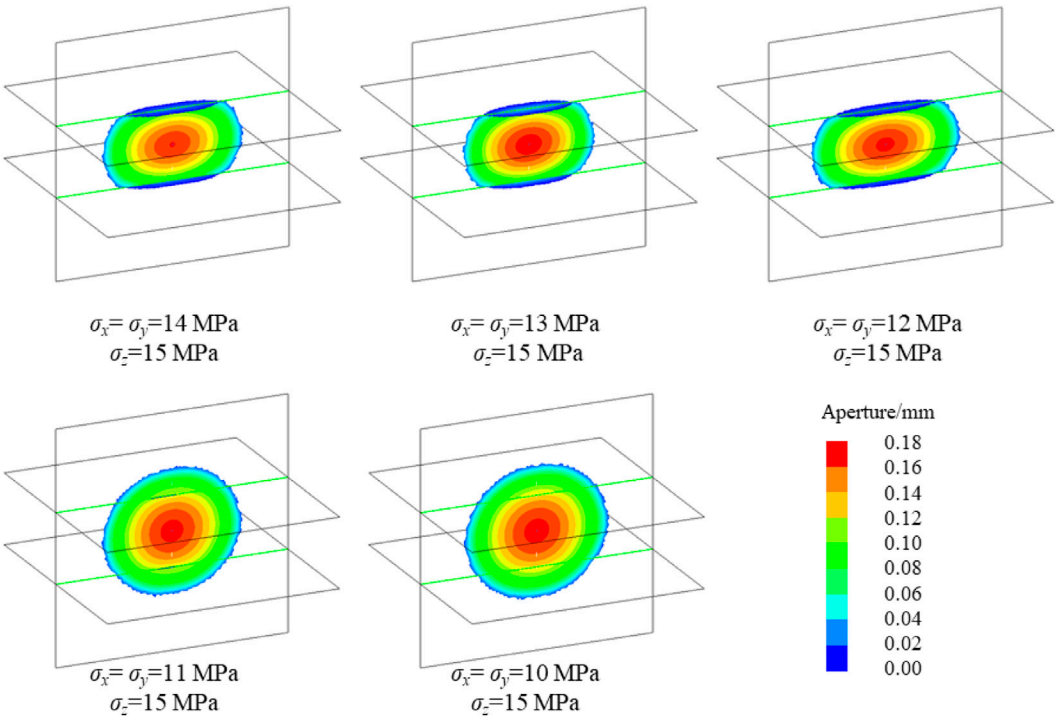

FIGURE 12
Fracture propagation under different horizontal stresses (σ_z=15 MPa).

condition of low stress difference, the vertical stress is small. So, the normal stress on the bedding plane is small. It results in the low shear strength of bedding. Therefore, the bedding plane is prone to shear failure in this case. After the shear failure of the bedding plane, the hydraulic fracture can expand along the bedding plane. In this way, the normal stress on the vertical joint cannot be transferred effectively. Therefore, the hydraulic fractures cannot continue to expand vertically.

3.2.2 Effect of horizontal stress

In addition to the vertical stress, the horizontal stress is another key to the stress difference. In order to analyze the influence of horizontal stress, the vertical stress is set as 15 MPa, and the horizontal stress is set as 14 MPa, 13 MPa, 12 MPa, 11 MPa and 10 MPa respectively, that is, the stress difference is 1–5 MPa. And other parameters are the same as 3.2.1.

Figure 12 presents the fracture propagation under five cases. From the perspective of stress difference, the results are similar to those in Section 3.2.1. Under the condition of low stress difference, the hydraulic fractures fail to cross the bedding plane. And the hydraulic fractures propagate along the bedding plane and mainly along the fracture length. However, under the condition of high stress difference, the hydraulic fractures continue to propagate vertically through the bedding plane. From the perspective of horizontal stress, the reduction of horizontal stress increases the possibility of hydraulic fracture penetrating the bedding plane.

Figure 13 shows the fluid injection pressure under different horizontal stress. As can be seen from the figure, the injection pressure drops with the decrease of horizontal stress. This is because

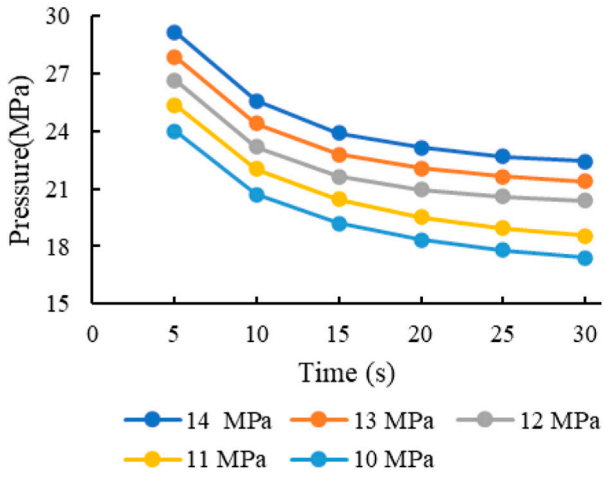

FIGURE 13
Injection pressure with different horizontal stresses σ_x (σ_z=15 MPa).

the expansion of hydraulic fractures is mainly in the vertical joint plane, so the injection pressure is mainly related to the normal stress (for vertical joint, the normal stress is horizontal stress) of the fracture plane. Note the difference between adjacent curves at the same time point. At the beginning, the difference between the curves is basically the same. In the later stage (such as 30 s), it is divided into two groups according to the fracture morphology. The maximum

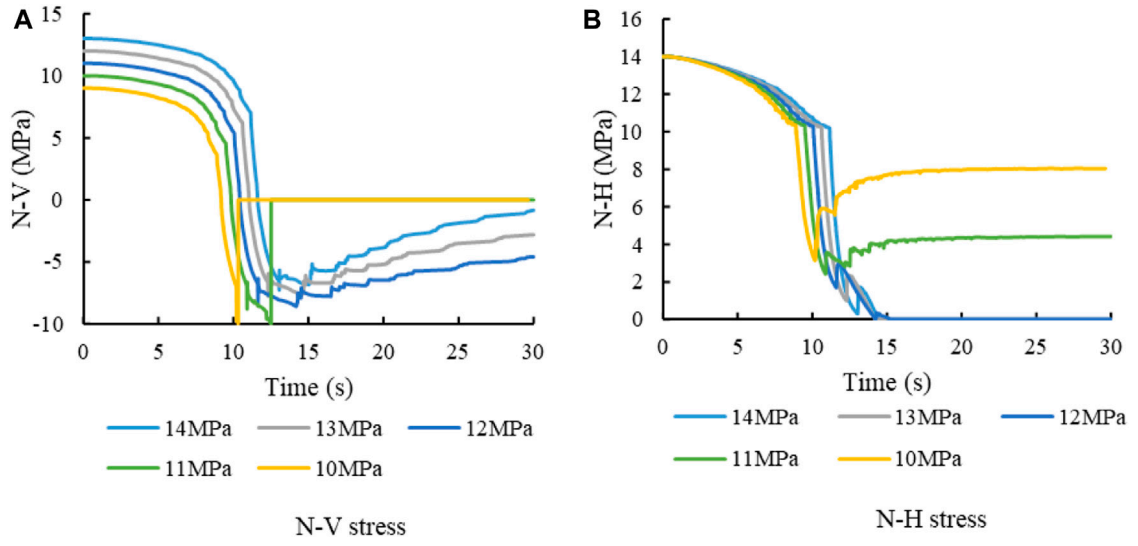

FIGURE 14
Stress curve at intersection with different horizontal stresses σ_x (σ_z=15 MPa). **(A)** N-V stress. **(B)** N-H stress.

spacing is between 11 MPa and 12 MPa. The fracture shape corresponding to 11 MPa is crossing, and the fracture shape corresponding to 12 MPa is captured. According to the pressure difference, the pressure of the hydraulic fracture after penetrating the bedding is low. This shows that the expansion difficulty of hydraulic fracture after penetrating the bedding is lower than that of capture in this case.

Figure 14 shows the stress evolution curve at intersection. And Figure 14A shows the N-V stress evolution curve. The curves in the figure can be divided into two categories according to the fracture morphology. The hydraulic fracture crosses the bedding plane when the horizontal stress is low (10 MPa and 11 MPa). When the N-V curve is reduced to −10 MPa, the tensile strength of the vertical joint is reached. After fracture cracking, the joint connection fails and the normal stress becomes 0. The stress is not reduced to −10 MPa when the horizontal stress is high because of the high initial value of N-V. At this time, the bedding plane meets the shear failure, so the hydraulic fracture turns toward the bedding plane. Consequently, the mechanism of horizontal stress on hydraulic fracture penetration is mainly the evolution of N-V stress. When the horizontal stress is low, the reduction value of N-V from the initial value to the failure criterion is small. On the contrary, when the horizontal stress is high, the initial stress of N-V is high, which rises the range of stress reduction and makes it difficult for the hydraulic fracture to continue vertical propagation.

Figure 14B shows the N-H curve. It can be seen from the figure that the lowest value of the curve before failure decreases with the increase of horizontal stress. This shows that the higher the horizontal stress is, the greater the reduction of N-H. According to Figure 13, the higher the horizontal stress, the greater the injection pressure. Stress disturbance was caused by fracturing fluid injection. The N-H reduction is the result of induced stress by injection. Therefore, the high horizontal stress leads to a large decrease of N-H. Under low horizontal stress, N-H only decreases slightly. This leads to high N-H. According to Coulomb slip theory, high N-H means high shear strength of bedding plane. Here, the difficulty of shear failure of bedding plane increases. It results in an increase in the probability of hydraulic fracture crossing the bedding plane.

The influence of horizontal stress on N-V and N-H are comprehensively considered. On the one hand, low horizontal stress results in low initial value of N-V. The low N-V reduces the tensile strength of vertical joints. This is conducive to the vertical propagation of hydraulic fractures. On the other hand, low horizontal stress leads to a higher value of N-H, which increases the shear strength of the bedding plane and is not conducive to the hydraulic fracture turning to the bedding plane. In conclusion, low horizontal stress is conducive to hydraulic fracture penetration.

4 The effect of stress on penetration behavior with tensile-failure bedding plane

The fracture propagation law of shear-failure bedding plane is analyzed above. Combined with stress analysis, it can be seen that the normal stress on the bedding plane decreases gradually in the process of hydraulic fracture propagation. With the decrease of stress, the bedding plane changes from compression to tension. If the tensile strength of bedding plane is low, tensile failure may occur on the bedding plane. Therefore, the analysis of tensile failure bedding is carried out to explore the influence mechanism of stress on the fracture propagation law in tensile-failure bedding plane. There are two main propagation modes of hydraulics fractures in the tensile-failure bedding model. One is the tensile failure of the vertical bedding plane. The hydraulic fracture propagating vertically and crosses the bedding plane in this model. Another is the tensile failure of the bedding plane. The hydraulic fractures will turn and propagating along the bedding plane in this model.

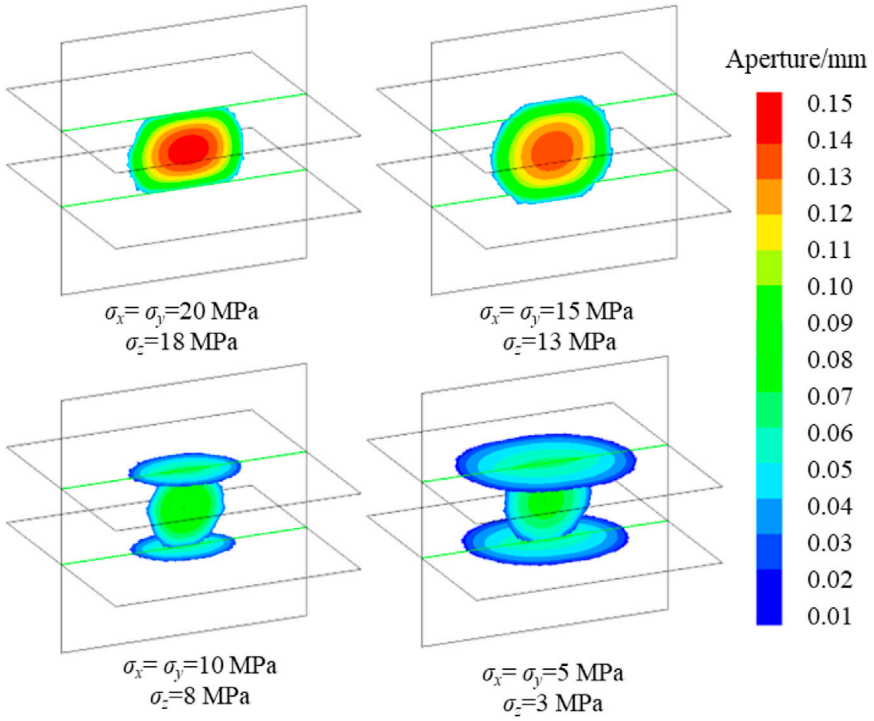

FIGURE 15
Fracture morphology of different initial stress.

4.1 The effect of initial stress magnitude on fracture propagation

Studies have shown that the initial stress magnitude has a significant impact on fracture morphology. In order to analyze the influence of initial stress on fracture morphology, the difference between horizontal stress and vertical stress is set to 2 MPa. The initial horizontal stress is 20 MPa, 15 MPa, 10 MPa and 5 MPa respectively. The injection rate is 5 mL/s. The viscosity of fracturing fluid is 1 cp. And the injection time is 25 s. The results of the above 4 cases are shown in Figure 15.

The results show that the initial stress affects the fracture propagation. When the initial horizontal stress is 20 MPa, the hydraulic fracture cannot cross the bedding plane, and the fractures mainly propagating along the length direction and the fracture height is limited. When the initial horizontal stress is 15 MPa, the hydraulic fracture crosses the bedding plane and continues to propagate vertically. As the initial horizontal stress decreases, the fracture morphology changes, and the hydraulic fracture cannot cross the bedding plane. The hydraulic fracture turns and spreads along the bedding plane. When the initial horizontal stress is 5 MPa, the range of fracture is obviously larger than that of 10 MPa. From the perspective of fracture range, it is affected by the initial stress. The higher the initial stress is, the smaller the fracture range is. This is consistent with the conclusion in the shear-failure bedding plane. In addition to the influence on the propagation range, the initial stress value also affects the fracture morphology. A small initial stress value will increase the tendency of hydraulic fractures to be captured. From the analysis of fracture aperture, it can be seen that the increase of initial stress will increase the aperture. As discussed in last section, the initial stress affects the fluid pressure in the fracture. The greater the pressure in the fracture, the greater the fracture deformation. For this kind of bedding, the stress difference is not the only factor that affects the fracture penetration behavior. When fracturing is carried out in reservoirs with different burial depths, the stress of the formation shall be evaluated in detail. Then fracturing design is carried out according to different initial stresses.

Stress is the essence of fracture propagation. And in the simulation of tensile-failure bedding, it is mainly the vertical propagation of hydraulic fracture (tensile failure) and the tensile failure of horizontal bedding. Therefore, only the normal stress at the intersection should be analyzed. The stress evolution curves of the four cases are extracted respectively, and the results are shown in Figure 16.

It can be seen from the figure that in the early stage of hydraulic fracture propagation, the normal stress N-H and N-V are in a slow decline stage. When the hydraulic fracture approaches the bedding plane, the normal stress enters a rapid decline stage. Figure 16A shows the stress evolution curve with an initial horizontal stress of 20 MPa. After the hydraulic fracture encounters the bedding plane (after the rapid decline stage, about 14 s later), the N-H stress on the bedding plane does not reach −3 MPa (tensile strength for tensile-failure bedding), and N-V does not drop to −10 MPa (tensile strength for vertical joint). Therefore, both tensile failures will not occur. Due to the high shear strength of the bedding plane, shear failure will not occur, so the fracture is limited to the bedding plane and can only propagate in the length direction. At this stage,

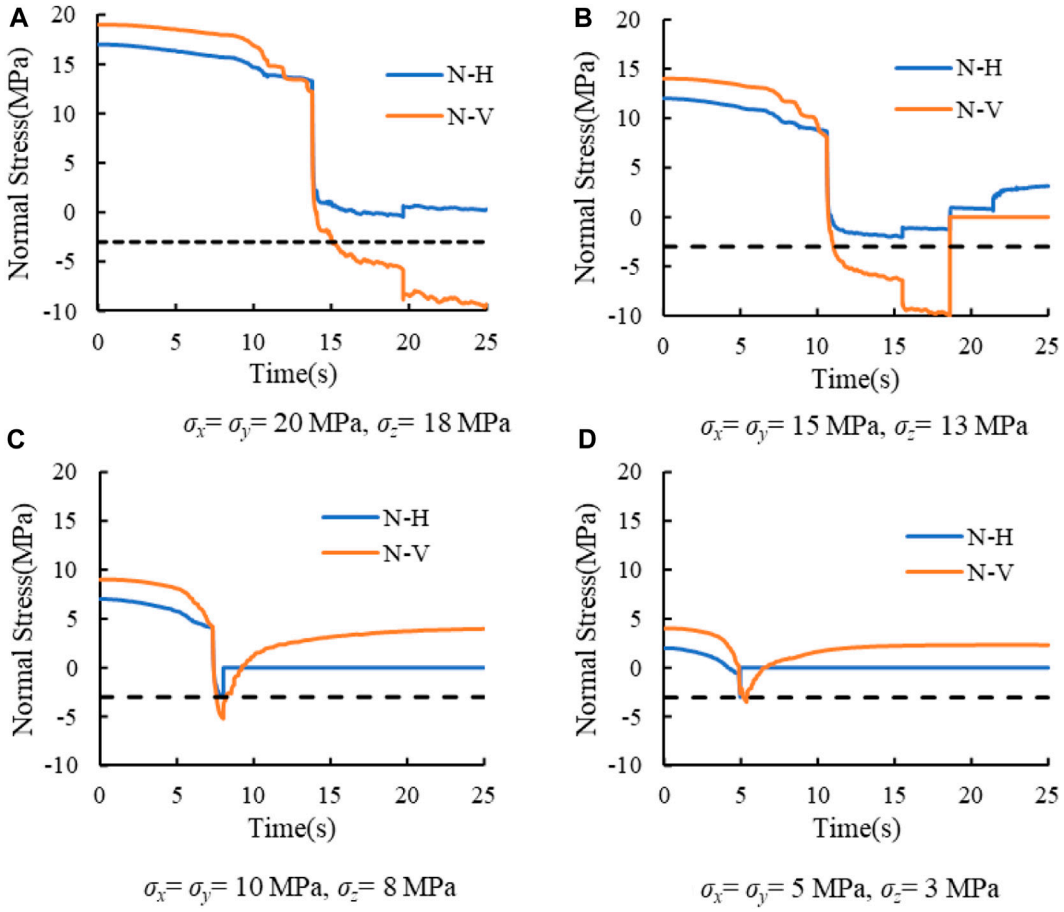

FIGURE 16
Stress curves of different initial stress values. **(A)** $\sigma_x = \sigma_y = 20$ MPa, $\sigma_z = 18$ MPa. **(B)** $\sigma_x = \sigma_y = 15$ MPa, $\sigma_z = 13$ MPa. **(C)** $\sigma_x = \sigma_y$ 10 MPa, $\sigma_z = 8$ MPa. **(D)** $\sigma_x = \sigma_y = 5$ MPa, $\sigma_z = 3$ MPa.

both N-H and N-V decrease slowly, and when one stress meets the failure criterion, the hydraulic fracture continues to propagate outward. According to the curve in the figure, N-V can reach −10 MPa. Therefore, it can be predicted that under this case, the hydraulic fracture will eventually cross the bedding plane and continue to propagate vertically.

Figure 16B shows the stress curve under the condition that the horizontal stress is 15 MPa. In those cases, the stress does not meet any failure criterion after the hydraulic fracture meets the bedding plane. So, N-H and N-V enter the slightly decline stage. Finally, the N-V reaches −10 MPa, and the hydraulic fracture crosses the bedding plane.

Figure 16C is the stress evolution curve with an initial horizontal stress of 10 MPa. Due to the low initial stress, the N-H has been reduced to-3 MPa in the rapid decline stage. So, the tensile failure of the bedding plane occurs. Then the fracturing fluid enters the bedding plane, and the hydraulic fracture continues to propagate along the bedding plane.

Similarly, Figure 16D shows the stress curve under the condition that the initial horizontal stress is 5 MPa. N-H first decreases to −3 MPa, tensile failure occurs on the bedding surface, and hydraulic fractures propagate along the bedding plane. Comparing Figures 16C, 16d, the latter has a shorter initial time. There are two reasons for it. First, fractures are easy to expand under low stress conditions. Second, the initial value of N-H is small, and the required reduction range to reduce to—3 MPa is small.

The cross or captured of hydraulic fractures is related to the decrease of N-H and N-V. The higher the initial stress, the greater the required reduction range to reach the critical stress. Figure 17 analyzes the initial values, minimum values and stress drops of N-H and N-V under different cases. According to the figure, and the decreases of N-H and N-V increased with the increase of initial stress. Therefore, the increase of initial stress will increase the difficulty of fracture failure. By comparing N-H and N-V, it can be seen that the reduction of N-V is greater than that of N-H. Combined with the stress curve, when the initial horizontal stress is 20 MPa and 15 MPa, the reduction rate of N-H is smaller than that of N-V. Therefore, N-V first reaches the failure condition, and the hydraulic fracture will directly cross the bedding plane. When the initial horizontal stress is 10 MPa and 5 MPa, both N-H and N-V are in the rapid reduction stage, and the initial value of stress is low. N-H can reach—3 MPa in the rapid reduction stage, so the bedding is first subject to tensile failure. In conclusion, the internal reason for the influence of initial stress on the behavior of hydraulic fracture

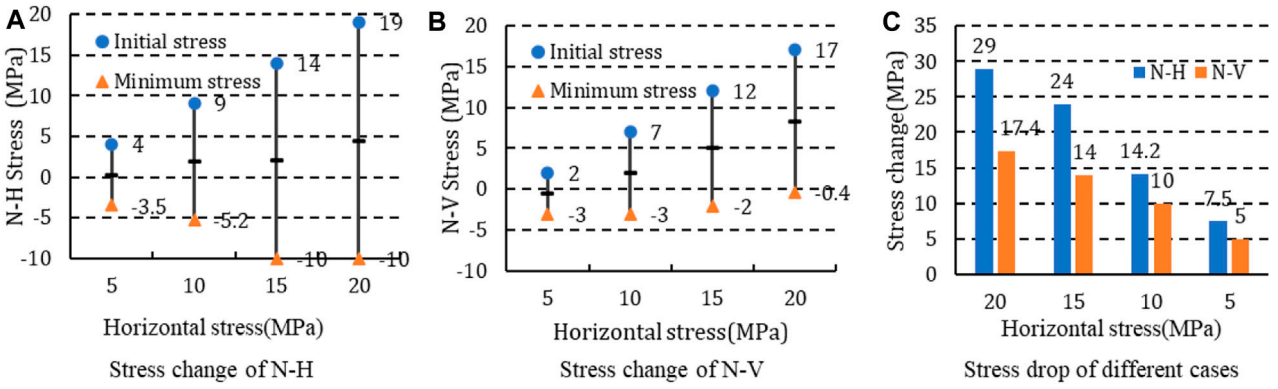

FIGURE 17
Stress drop under different cases (stress difference is 2 MPa). **(A)** Stress change of N-H. **(B)** Stress change of N-V. **(C)** Stress drop of different cases.

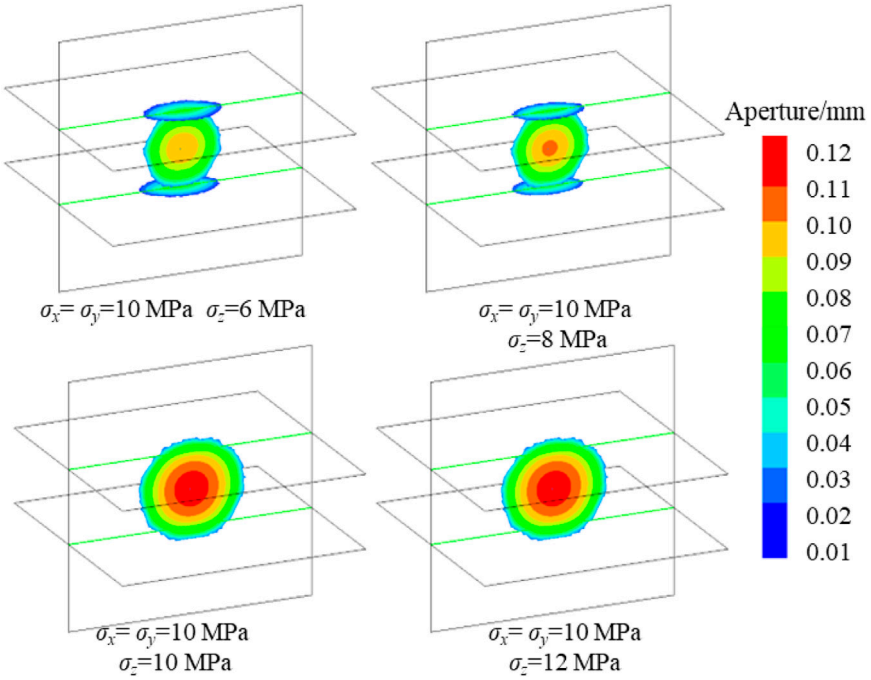

FIGURE 18
Fracture morphology with different vertical stresses.

penetration is that the lower initial stress can ensure that the N-H stress has reached the tensile strength of the bedding plane in the rapid reduction stage.

4.2 Effect of stress difference on fracture propagation

4.2.1 Effect of vertical stress

The stress difference has a significant effect on the penetration behavior of hydraulic fractures. In order to analyze the influence of vertical stress on the behavior of hydraulic fractures, the horizontal stress is set to 10 MPa, and the vertical stresses are 6 MPa, 8 MPa, 10 MPa and 12 MPa, respectively. The corresponding stress differences (the vertical stress minus the horizontal stress) are −4 MPa, −2 MPa, 0 MPa and 2 MPa. The injection time is set to 15 s, and other parameters are consistent with above. Fracture propagation morphology under four cases is shown in Figure 18.

The forms of hydraulic fractures are different with different vertical stress. When the vertical stress is small (6 MPa and 8 MPa), the hydraulic fractures propagate along the bedding plane. When the

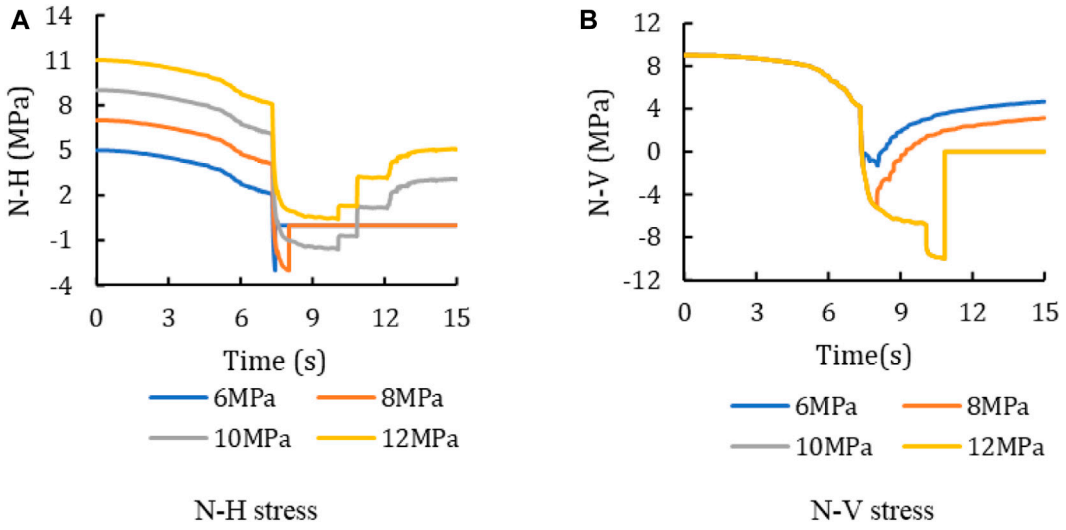

FIGURE 19
Stress evolution curve at intersection with different vertical stress σ_z (σ_x=σ_y=10 MPa). **(A)** N-H stress. **(B)** N-V stress.

vertical stress is large (10 MPa and 12 MPa), the hydraulic fractures propagate vertically through the bedding plane. This shows that with the increase of vertical stress, the difficulty of hydraulic fracture turning to bedding plane increases. And the vertical stress affects the aperture of the fracture. The smaller the vertical stress, the smaller the maximum aperture of the fracture.

Comparing the morphology of captured fracture in shear-failure bedding (e.g., Figure 3; Figure 9; Figure 12) and tensile-failure bedding (e.g., Figure 15; Figure 18), the former will still propagate in the direction of fracture length after shear failure on the bedding plane, while the propagation distance on the bedding plane is shorter. The fracture morphology of the latter tends to extend along the bedding plane, and the fracture length is shorter than shear-failure type. This is related to the failure form of both. The failure mode of shear-failure type bedding is shear failure. However, the fractures may not open after the shear failure of bedding. When the pressure inside the fractures overcomes the normal stress of the fracture surface, the fracture opens. The shear stress caused by hydraulic fractures mainly acts near the intersection line. The shear stress far away from the intersection line decreases, which cannot cause the shear failure of the bedding plane. In addition, the tensile strength of the bedding is high, and the bedding is difficult to meet the requirements of tensile failure. Therefore, the fractures are limited between bedding planes and can only extend along the length direction. In tension-failure bedding, the failure mode of bedding is tension failure. And the fracturing fluid directly enters the bedding plane after failure. The tensile strength of the bedding plane is low, so the fluid pressure in the bedding plane can ensure the fracture expansion. Even because the strength of bedding plane is far lower than that of rock mass, bedding plane has become the main channel for hydraulic fracture expansion.

According to the stress evolution curves (summarized in Figure 19), N-H is divided into two categories according to the fracture morphology. When the vertical stress is low, the N-H curve can be divided into slightly reduction stage, rapid reduction stage and flat stage. Firstly, before the hydraulic fracture reaches the bedding plane, the induced stress of N-H is small, and the curve shows a slow decline. When the hydraulic fracture approaches the bedding plane, the N-H decreases rapidly due to the induced stress caused by the fracture. When it is reduced to −3 MPa, the fracture opens due to tensile failure of bedding plane. Then the N-H becomes 0. When the bedding plane is opened, the fracturing fluid enters the bedding plane. Because of the low tensile strength of the bedding plane, the hydraulic fractures propagate along the horizontal bedding plane. When the vertical stress is large, N-H is always greater than −3 MPa, so no tensile failure occurs on the bedding plane.

The analysis of the N-V curve shows that before the hydraulic fracture meets the bedding plane (about 7 s), the stress curves coincide. After encountering the bedding plane, N-H is reduced to −3 MPa during rapid reduction stage due to the small initial N-H of the low vertical stress, resulting in bedding failure and fracture deflection. Therefore, N-V cannot be further reduced. However, when the vertical stress is high, the initial N-H is high, and the N-H is still greater than-3 MPa after the rapid reduction stage. The bedding plane is not destroyed, and the N-H enters the slow reduction stage. Therefore, N-V can continue to decline. When N-V drops to −10 MPa, the hydraulic fractures propagate vertically.

In conclusion, the effect of vertical stress on the penetration behavior of hydraulic fractures is mainly to affect the initial value of N-H. When the vertical stress is low, the initial value of N-H is small. Therefore, it is easy for the bedding plane to change from compression to tension. On the contrary, when the vertical stress is high, the initial value of N-H is large, and the compressive stress on the bedding is large. So, it is difficult to change from compression to tension. If the bedding plane is not subject to tensile failure, the

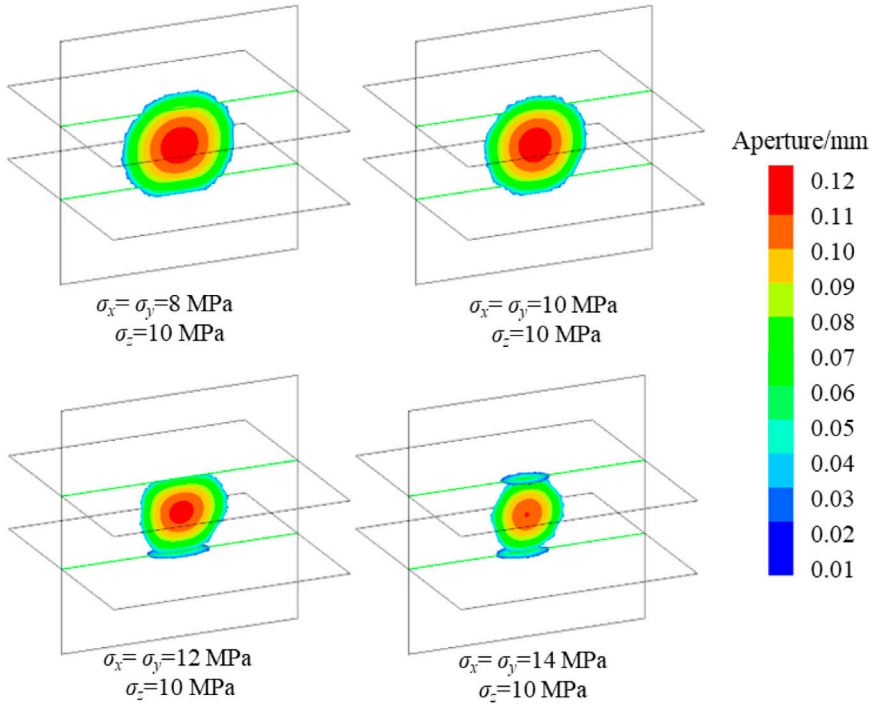

FIGURE 20
Fracture morphology under different vertical stresses.

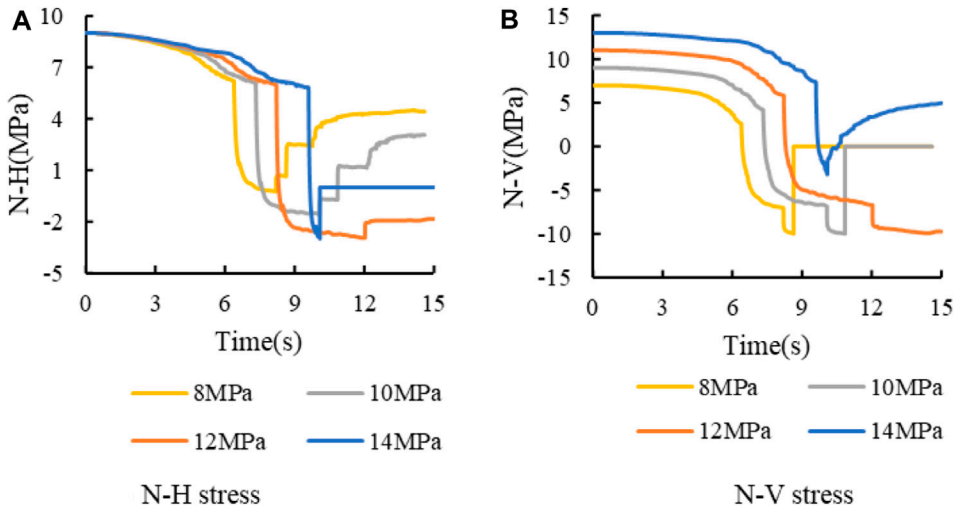

FIGURE 21
Stress curve at intersection with different horizontal stress σ_x (σ_z =10 MPa). **(A)** N-H stress. **(B)** N-V stress.

hydraulic fracture will expand vertically. In a word, with the increase of vertical stress, hydraulic fractures are easier to cross the bedding.

4.2.2 Effect of horizontal stress

Horizontal stress is another key factor causing stress difference. In order to analyze the influence of horizontal stress on fracture propagation, the vertical stress is set to 10 MPa. And the horizontal stresses are 8 MPa, 10 MPa, 12 MPa and 14 MPa, respectively. The difference between vertical stress and horizontal stress is 2 MPa, 0 MPa, −2 MPa and −4 MPa, respectively. The injection time is 15 s, and the other parameters are the same as the previous section. The results are shown in Figure 20.

According to the figure, when the horizontal stress is small (8 MPa and 10 MPa), the hydraulic fractures cross the bedding

plane. As the horizontal stress increases (12 MPa and 14 MPa), the hydraulic fractures are captured by the bedding plane. Combined with the stress evolution curve (Figure 21), when the horizontal stress is small, the initial value of N-V is low. Therefore, the pressure in the fracture required for the vertical propagation of the fracture is small. The decrease of N-V required for vertical fracture propagation is small, which leads to the small induced stress by hydraulic fractures. However, the initial value of N-H is the same, and the N-H cannot be reduced to −3 MPa under low stress conditions. So, the bedding plane will not be damaged. Owing to the low initial value of N-V, the hydraulic fracture first reaches −10 MPa, resulting in vertical propagation of hydraulic fracture. On the contrary, if the horizontal stress is high, the fracture pressure during the vertical propagation is large. High pressure leads large induced stress, resulting in the N-H decreasing to −3 MPa at first. Then, the hydraulic fractures will propagate along the bedding plane.

To sum up, the influence of vertical stress on fracture morphology is mainly on the initial value of N-H. The higher vertical stress leads to the increase of the initial normal stress on the bedding plane, which increases the opening difficulty of the bedding plane. The influence of horizontal stress is divided into two aspects. On the one hand, horizontal stress affects the initial value of N-V, lower horizontal stress results in lower initial N-V value and less stress reduction required for N-V. On the other hand, if the horizontal stress is small, the vertical propagation difficulty of hydraulic fracture is low. So, the fracture pressure is small. Then the induced stress by pressure is small. As a result, the reduction of N-H is small and cannot meet the tensile criterion of bedding plane. It can be concluded that the increase of vertical stress or the decrease of horizontal stress will increase the tendency of hydraulic fractures crossing the bedding.

5 Conclusion

(1) According to the failure characteristics of the bedding plane, it can be divided into shear-failure bedding and tensile-failure bedding. The shear-failure bedding mainly considers the shear failure behavior on the bedding plane. While the tensile-failure bedding mainly focuses on the tensile behavior on the bedding plane. The failure characteristics of the two are also different. After the shear failure of the bedding plane, it is difficult for the bedding plane to maintain the shear failure, so the hydraulic fracture will propagate in the length direction. However, the tensile strength of tensile failure bedding plane is small in tensile-failure bedding. So, the bedding plane is the dominant path of fracture propagation, and the length of hydraulic fractures is shorter than the shear-failure bedding.

(2) The initial stress mainly affects the difficulty of hydraulic fracture propagation. The inherent mechanism is that the normal stress on the fracture needs to be reduced from the initial stress to the failure stress during the fracking. Therefore, the greater the initial stress, the greater the stress reduction required for fracture propagation. Therefore, the effect of initial stress on the fracture penetrating is summarized as follows: the smaller the initial stress is, the smaller the barrier effect of bedding plane on the hydraulic fracture penetration.

(3) The vertical stress mainly affects the normal stress on the bedding plane. For the shear-failure bedding plane, the vertical stress determines the shear strength of the bedding plane by affecting the normal stress on the bedding plane. The smaller the vertical stress, the lower the shear strength of the bedding plane. For tensile-failure bedding planes, vertical stress affects the difficulty of tensile failure of bedding planes. When vertical stress is small, the difficulty of tensile failure of bedding planes decreases. In consequence, the low vertical stress is conducive to the propagation of hydraulic fractures along the bedding plane, and the fractures are easier to be captured.

(4) The horizontal stress affects normal stress on vertical bedding planes. The large horizontal stress increases the difficulty of vertical propagation of hydraulic fractures. So, the increase of horizontal stress will aggravate the difficulty of hydraulic fracture crossing the bedding. In addition, due to the increase of the pressure in the fracture, the induced stress increases. Then, the stress reduction on the bedding plane increases, which reduces the difficulty of the failure of the bedding plane and is conducive to the hydraulic fracture turning to the bedding plane.

Data availability statement

The original contributions presented in the study are included in the article/Supplementary Material, further inquiries can be directed to the corresponding author.

Author contributions

YB: Investigation, writing—original draft. YH: Writing—review and editing. XL: Visualization, writing—review and editing. JT: Writing—reviewing and editing. YZ: Writing—original draft, conceptualization, WW: supervision.

Funding

This work is supported by the Natural Science Starting Project of SWPU (No. 2022QHZ009).

Conflict of interest

YB was employed by Shanxi Wangjialing Coal Industry Co., Ltd.

The remaining authors declare that the research was conducted in the absence of any commercial or financial relationships that could be construed as a potential conflict of interest.

Publisher's note

References

Gao, Q., and Ahmad, G. (2020). Three dimensional finite element simulations of hydraulic fracture height growth in layered formations using a coupled hydro-mechanical model. *Int. J. Rock Mech. Min. Sci.* 125, 104137. doi:10.1016/j.ijrmms.2019.104137

Heng, S., Li, X., Zhang, X., and Li, Z. (2021). Mechanisms for the control of the complex propagation behaviour of hydraulic fractures in shale. *J. Petroleum Sci. Eng.* 200, 108417. doi:10.1016/j.petrol.2021.108417

Huang, J., Ma, X., Shahri, M., Safari, R., Yue, K., Mutlu, U., et al. (2016). in Hydraulic fracture growth and containment design in unconventional reservoirs[C]//50th Us Rock mechanics/geomechanics symposium, American Rock Mechanics Association.

Huang, L., Dontsov, E., Fu, H., Lei, Y., Weng, D., and Zhang, F. (2022). Hydraulic fracture height growth in layered rocks: Perspective from DEM simulation of different propagation regimes. *Int. J. Solids Struct.* 238, 111395. doi:10.1016/j.ijsolstr.2021.111395

Huang, L., He, R., Yang, Z., Tan, P., Chen, W., Li, X., et al. (2023). Exploring hydraulic fracture behavior in glutenite formation with strong heterogeneity and variable lithology based on DEM simulation. *Eng. Fract. Mech.* 278, 109020. doi:10.1016/j.engfracmech.2022.109020

Huang, L., Liu, J., Ji, Y., Gong, X., and Qin, L. (2018). A review of multiscale expansion of low permeability reservoir cracks. *Petroleum* 4, 115–125. doi:10.1016/j.petlm.2017.09.002

Huang, L., Liu, J., Zhang, F., Dontsov, E., and Damjanac, B. (2019). Exploring the influence of rock inherent heterogeneity and grain size on hydraulic fracturing using discrete element modeling. *Int. J. Solids Struct.* 176, 207–220. doi:10.1016/j.ijsolstr.2019.06.018

Huang, L., Liu, J., Zhang, F., Fu, H., Zhu, H., and Damjanac, B. (2020). 3D lattice modeling of hydraulic fracture initiation and near-wellbore propagation for different perforation models. *J. Petroleum Sci. Eng.* 191, 107169. doi:10.1016/j.petrol.2020.107169

Ji, Y., Wang, J., and Huang, L. (2015). Analysis on inflowing of the injecting Water in faulted formation[J]. *Adv. Mech. Eng.* 7 (6), 405–407. doi:10.1177/1687814015590294

Luo, H., Xie, J., Huang, L., Wu, J., Shi, X., Bai, X., et al. (2022). Multiscale sensitivity analysis of hydraulic fracturing parameters based on dimensionless analysis method[J]. *Lithosphere* 2022, 9708300. doi:10.2113/2022/9708300

Shicheng, Z., Sihai, L., and Yushi, Z. (2021). Experimental study on fracture height propagation during multi-stage fractu-ring of horizontal wells in shale oil reservoirs[J]. *J. China Univ. Petroleum (Ed. Nat. Sci.* 45 (1), 77–86.

Tan, P., Jin, Y., and Pang, H. (2021). Hydraulic fracture vertical propagation behavior in transversely isotropic layered shale formation with transition zone using XFEM-based CZM method. *Eng. Fract. Mech.* 248, 107707. doi:10.1016/j.engfracmech.2021.107707

Tan, P., Pang, H., Zhang, R., Jin, Y., Zhou, Y., Kao, J., et al. (2020). Experimental investigation into hydraulic fracture geometry and proppant migration characteristics for southeastern Sichuan deep shale reservoirs. *J. Petroleum Sci. Eng.* 184, 106517. doi:10.1016/j.petrol.2019.106517

Tang, J., and Wu, K. (2018). A 3-D model for simulation of weak interface slippage for fracture height containment in shale reservoirs. *Int. J. Solids Struct.* 144, 248–264. doi:10.1016/j.ijsolstr.2018.05.007

Tong, Z., Wang, H., Li, F., Yuanzhao, L., Yushi, Z., and Chi, Z. (2020). Numerical simulation of hydraulic fracture propagation in laminated shale reservoirs[J]. *Petroleum Explor. Dev.* 47 (5), 1039–1051. doi:10.1016/s1876-3804(20)60122-7

Wang, S., Li, J., Dong, K., and Yang, Q. (2019). Research on the expansion mechanism of hydraulic fracture branching induced by weak bedding shear slip. *Desalination Water Treat.* 157, 219–227. doi:10.5004/dwt.2019.23849

Warpinski, N. R., Schmidt, R. A., and Northrop, D. A. (1982). *In-situ* stresses: The predominant influence on hydraulic fracture containment. *J. Petroleum Technol.* 34 (3), 653–664. doi:10.2118/8932-pa

Weng, X., Dimitry, C., Kresse, O., Prioul, R., and Wang, H. (2018). Hydraulic fracture-height containment by permeable weak bedding interfaces. *Geophysics* 83 (3), 137–152. doi:10.1190/geo2017-0048.1

Xiao, L., Hao, J., Yin, C., Huang, B., Li, G., Zhang, Z., et al. (2019). Characteristics of the shale bedding planes and their control on hydraulic fracturing[J]. *Oil Gas Geol.* 40, 1–8. doi:10.11743/ogg20190320

Xing, P., Yoshioka, K., Adachi, J., El-Fayoumi, A., Bunger, A. P., et al. (2018). Laboratory demonstration of hydraulic fracture height growth across weak discontinuitieshf height growth with weak interfaces[J]. *Geophysics* 83 (2), 1–36. 10.1190/geo2016-0713.1.

Xu, W., Prioul, R., Berard, T., Weng, X., and Kresse, O. (2019). in Barriers to Hydraulic Fracture Height Growth: a New Model for Sliding Interfaces[C]//SPE Hydraulic fracturing technology conference and exhibition: Society of Petroleum Engineers. doi:10.2118/194327-MS

Zhang, F., Damjanac, B., and Maxwell, S. (2019). Investigating hydraulic fracturing complexity in naturally fractured rock masses using fully coupled multiscale numerical modeling. *Rock Mech. Rock Eng.* 52, 5137–5160. doi:10.1007/s00603-019-01851-3

Zhang, F-S., Huang, L-K., Yang, L., Dontsov, E., Weng, D. W., Liang, H. B., et al. (2022). Numerical investigation on the effect of depletion-induced stress reorientation on infill well hydraulic fracture propagation. *Petroleum Sci.* 19 (1), 296–308. doi:10.1016/j.petsci.2021.09.014

Zhang, X., Zhang, Y., and Huang, B. (2021). Investigation of the fracturing effect induced by the disturbing stress of hydrofracturing using the bonded-particle model[J]. *Geofluids* 2021, 9988748. doi:10.1155/2021/9988748

Zhang, X., Zhang, Y., and Zhang, T. (2021). Experimental and numerical investigation on hydraulic fracture propagation law of composite rock materials considering the disturbing stress effect. *J. Geofluids* 2021, 1–20. doi:10.1155/2021/9920633

Zhao, W., Ji, G., Li, K., Liu, W., Xiong, L., and Xiao, J. (2022). A new pseudo 3D hydraulic fracture propagation model for sandstone reservoirs considering fracture penetrating height. *Eng. Fract. Mech.* 264, 108358. doi:10.1016/j.engfracmech.2022.108358

Zheng, Y., He, R., Huang, L., Bai, Y., Wang, C., Chen, W., et al. (2022). Exploring the effect of engineering parameters on the penetration of hydraulic fractures through bedding planes in different propagation regimes. *Comput. Geotechnics* 146, 104736. doi:10.1016/j.compgeo.2022.104736

Zheng, Y., Liu, J., and Zhang, B. (2019). An investigation into the effects of weak interfaces on fracture height containment in hydraulic fracturing. *Energies* 12 (17), 3245. doi:10.3390/en12173245

frontiers | Frontiers in Earth Science

TYPE Original Research
PUBLISHED 13 April 2023
DOI 10.3389/feart.2023.1188302

OPEN ACCESS

EDITED BY
Peng Tan,
CNPC Engineering Technology R&D Company Limited, China

REVIEWED BY
Wang Zepeng,
Henan Polytechnic University, China
Jianghui Ding,
CNPC Engineering Technology R&D Company Limited, China

*CORRESPONDENCE
Jingwei Zheng,
zhengjingwei@cqu.edu.cn
Saipeng Huang,
huangspcugb@hotmail.com

RECEIVED 17 March 2023
ACCEPTED 03 April 2023
PUBLISHED 13 April 2023

CITATION
Li C, Zheng J and Huang S (2023), The effects of supercritical CO_2 on the seepage characteristics and microstructure of water-bearing bituminous coal at *in-situ* stress conditions.
Front. Earth Sci. 11:1188302.
doi: 10.3389/feart.2023.1188302

The effects of supercritical CO_2 on the seepage characteristics and microstructure of water-bearing bituminous coal at *in-situ* stress conditions

Chengtian Li[1,2], Jingwei Zheng[1,2]* and Saipeng Huang[3,4]*

[1]State Key Laboratory of Coal Mine Disaster Dynamics and Control, Chongqing University, Chongqing, China, [2]School of Resources and Safety Engineering, Chongqing University, Chongqing, China, [3]Key Laboratory of Continental Shale Hydrocarbon Accumulation and Efficient Development, Ministry of Education, Northeast Petroleum University, Daqing, China, [4]Department de Mineralogia, Petrologia i Geologia Aplicada, Facultat de Ciències de la Terra, Universitat de Barcelona (UB), Barcelona, Spain

CO_2 geological storage (CGS) is considered to be an important technology for achieving carbon peak and carbon neutralization goals. Injecting CO_2 into deep unminable coal seams can achieve both CGS and enhance coalbed methane (ECBM) production. Therefore, the deep unminable coal seams are considered as promising geological reservoirs. CO_2 exists in a supercritical CO_2 ($ScCO_2$) when it was injected into deep unminable coal seams. The injection of $ScCO_2$ can induce changes in the seepage characteristics and microstructure of deep water-bearing coal seams. In this study, typical bituminous coal from Shenmu, Shanxi Province was used to investigate the effects of $ScCO_2$ on seepage characteristics, pore characteristics, and mineral composition through experiments such as seepage tests, low-temperature liquid nitrogen adsorption, and X-ray diffraction (XRD). The results indicate that $ScCO_2$ treatment of dry and saturated coal samples caused a significant increase in clay mineral content due to the dissolution of carbonates, leading to the conversion of adsorption pores to seepage pores and an improvement in seepage pore connectivity. Therefore, the Brunauer-Emmett-Teller (BET) specific surface area and pore volume of the two coal samples both decreased after $ScCO_2$ treatment. Moreover, the permeability of dry and saturated coal samples increased by 191.53% and 231.71% at 10 MPa effective stress respectively. In semi-saturated coal samples, a large amount of dolomite dissolved, leading to the precipitation of Ca^{2+} and CO_3^{2-} to form calcite. This caused pore throats to clog and macropores to divide. The results show that the pore volume and average pore size of coal samples decrease, while the specific surface area increases after $ScCO_2$ treatment, providing more space for gas adsorption. However, the pore changes also reduced the permeability of the coal samples by 32.21% and 7.72% at effective stresses of 3 MPa and 10 MPa, respectively. The results enhance our understanding of carbon sequestration through $ScCO_2$ injection into water-bearing bituminous coal seams.

KEYWORDS

bituminous coal, *in situ* stress, supercritical CO_2, seepage characteristics, pore characteristics, mineral composition

1 Introduction

Massive CO_2 emissions contribute to the global greenhouse effect, which in turn causes a series of climate catastrophes. Scholars worldwide have proposed many carbon reduction options in response (Liu et al., 2019; Li X. et al., 2022; Xu et al., 2022), including carbon geological storage (CGS), which has gained recognition as an effective way to achieve CO_2 sequestration and reduce greenhouse gas emissions (Wang Y. et al., 2021; Liu et al., 2021). In particular, CO_2 injection into deep unminable coal seams offers a promising geological reservoir for simultaneous CO_2 storage and coalbed methane (CBM) recovery (Chiquet et al., 2007; Li et al., 2009; Zepeng et al., 2022). CO_2 exists in the form of $ScCO_2$ when the depth of the coal seams exceeds 800 m, and the pressure and temperature exceed the critical conditions of 7.38 MPa and 31°C (Zhang et al., 2017). Injection of $ScCO_2$ into coal seams, especially those containing water, can cause significant modifications to the pore and fracture structure of the coal due to mineralization reactions between $ScCO_2$-H_2O and minerals. These changes can impact permeability and adsorption capacity in turn (Dawson et al., 2011; Wang Z. et al., 2022). Scholars have conducted extensive research on the interaction of $ScCO_2$ with coal. $ScCO_2$ geochemical reaction experiment on typical high-rank coal of Qinshui Basin was conducted and it is found that $ScCO_2$ dissolved minerals and change the porosity, pore volume and specific surface area of coal (Du et al., 2018). The seepage test before and after CO_2 adsorption were conducted to found that CO_2 adsorption increases the permeability anisotropy of coal due to the high permeability adsorption sensitivity of low permeability cleats and the low permeability adsorption sensitivity of high permeability bedding (Niu et al., 2018). Xiaolei Wang et al. treated coal with subcritical CO_2 and $ScCO_2$, respectively, and found that the solubility of minerals in $ScCO_2$-treated coal is stronger. Furthermore, the total pore volume and BET specific surface area of coal gradually increase with the increase of CO_2 intrusion pressure (Wang X. et al., 2022). Yugang Cheng et al. studied the effects of subcritical and supercritical CO_2 on the pore structure of coal and found that the porosity and pore volume of coal showed an inverted "U" shaped change which first increased and then decreased with the increase of CO_2 pressure (Cheng et al., 2021). M.S.A. Perera et al. conducted adsorption experiments of coal at different CO_2 pressures, indicating that the maximum swelling of coal occurs within 3–4 h after CO_2 injection. And the swelling strain increases while the permeability decreases as CO_2 pressure increases (Perera et al., 2011).

Several studies have highlighted the important role of water in geochemical interactions (Li et al., 2019). Renxia Jiang et al. conducted a $ScCO_2$-H_2O interaction experiment on coal to investigate the effect of $ScCO_2$-H_2O on the primary mineral composition of coal. And the study found that $ScCO_2$ effectively improves the solubility of various elements of coal in water (Jiang et al., 2019). Ruihui Li et al. conducted $ScCO_2$ soaking experiments on bituminous coals with varying moisture contents and investigated the modification of pore characteristics and microcrystalline structure of bituminous coals with the effect of $ScCO_2$ under different moisture conditions (Li R. et al., 2022). Guodong Cui et al. injected water and CO_2 into rock samples, respectively, to investigate the effects of water and CO_2 injection on minerals. The results indicated that mixing the injected water with the original formation water results in significant mineral precipitation, while acidification resulting from the injection of CO_2 leads to the dissolution of some minerals and the precipitation of dolomite, altering the composition of the formation water (Cui et al., 2021). Shasha Gao et al. studied the

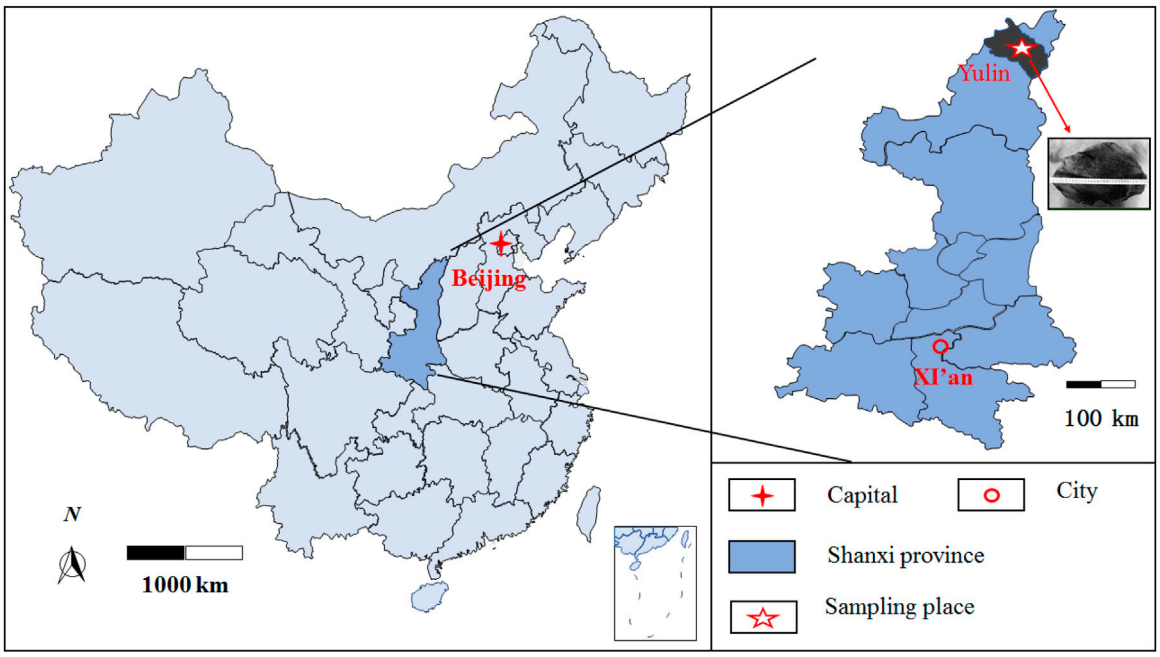

FIGURE 1
Location of coal samples collection.

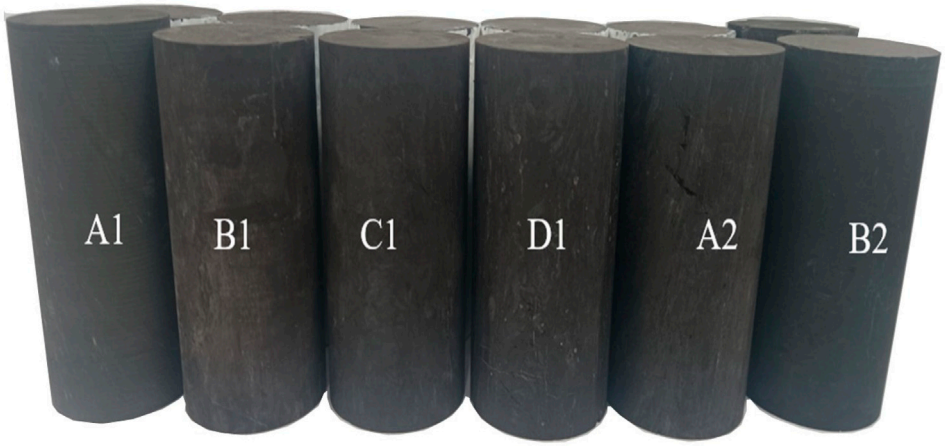

FIGURE 2
The coal samples from Ningtiaota coal mine.

TABLE 1 The groups and treatment conditions of coal samples.

Group	Water-bearing condition	CO_2 pressure/MPa
A	untreated	—
B	dry	8
C	Semi-saturation	8
D	saturation	8

effect of CO_2-H_2O interaction on the pore structure and mineral composition of coal. The results show that the pore structures of coal become more complex due to the geochemical reaction between CO_2-H_2O and carbonate minerals, and the fractures expands and develops after CO_2-H_2O treatment which is positive for permeability (Gao et al., 2022). Yao Song et al. analyzed the influences of the $ScCO_2$–H_2O coupling effect on the microstructures of low-rank coal samples and found that mineral dissolution increases as the CO_2 pressure increases, resulting in an increase in porosity and macropore ratio in the coal samples (Song et al., 2020).

Although the effects of $ScCO_2$ on the pore structure and mineral composition of coal have been extensively studied, most experiments are based on soaking treatment. The hydrological and *in situ* stress conditions of actual coal seams are not be considered (Mirzaeian et al., 2006; Qu et al., 2012; Song et al., 2020; Gao et al., 2022). Therefore, this paper conducted $ScCO_2$ injection experiments on bituminous coal with varying water saturation under *in situ* stress to investigate the influence of $ScCO_2$-H_2O interaction on coal seepage characteristics, pore characteristics, and mineral composition through seepage, low-temperature liquid nitrogen adsorption, and XRD experiments. The findings of this study provide a theoretical guideline for CO_2 geological storage (CGS) and CO_2-enhanced coal bed methane recovery (CO_2-ECBM).

2 Material and methods

2.1 Coal samples

The experiments in this study utilized typical bituminous coal samples from Ningtiaota coal mine, Yulin City, Shanxi Province. The coal was taken from Yan'an Formation. The coal samples were as shown in Figure 1.

Upon on-site collection, the coal was immediately wrapped with plastic and transported to the laboratory. Subsequently, it was cored, polished, and processed into standard cylindrical samples of 50 × 100 dimensions. And the experiments were repeated 2–3 times to ensure the validity of the experimental results. Coal is a natural organic rock with anisotropy. The coal samples used in the tests were all sampled perpendicular to the bedding direction in order to avoid the influence of coal anisotropy on the experimental results (Perera et al., 2011). And the coal samples are depicted in Figure 2.

2.2 Seepage test

The coal samples were divided into different groups based on their water saturation levels achieved through soaking for varying periods of time before the $ScCO_2$ treatment. The specific group numbers and treatment conditions are presented in Table 1.

The coal rock rheology seepage system which was independently developed by the laboratory to simulate the geological environment was used to conduct the seepage tests. And the experimental equipment is illustrated in Figure 3.

Seepage tests were conducted at different axial and confining pressures namely 2.8 MPa and 5.5 MPa as well as 9.8 MPa and 12.5 MPa respectively. The seepage gas pressure was maintained at 3.1 MPa to study changes at different effective stresses. The effective stress acting on the coal sample was calculated using the Terzaghi effective stress formula (Liu Z. et al., 2020):

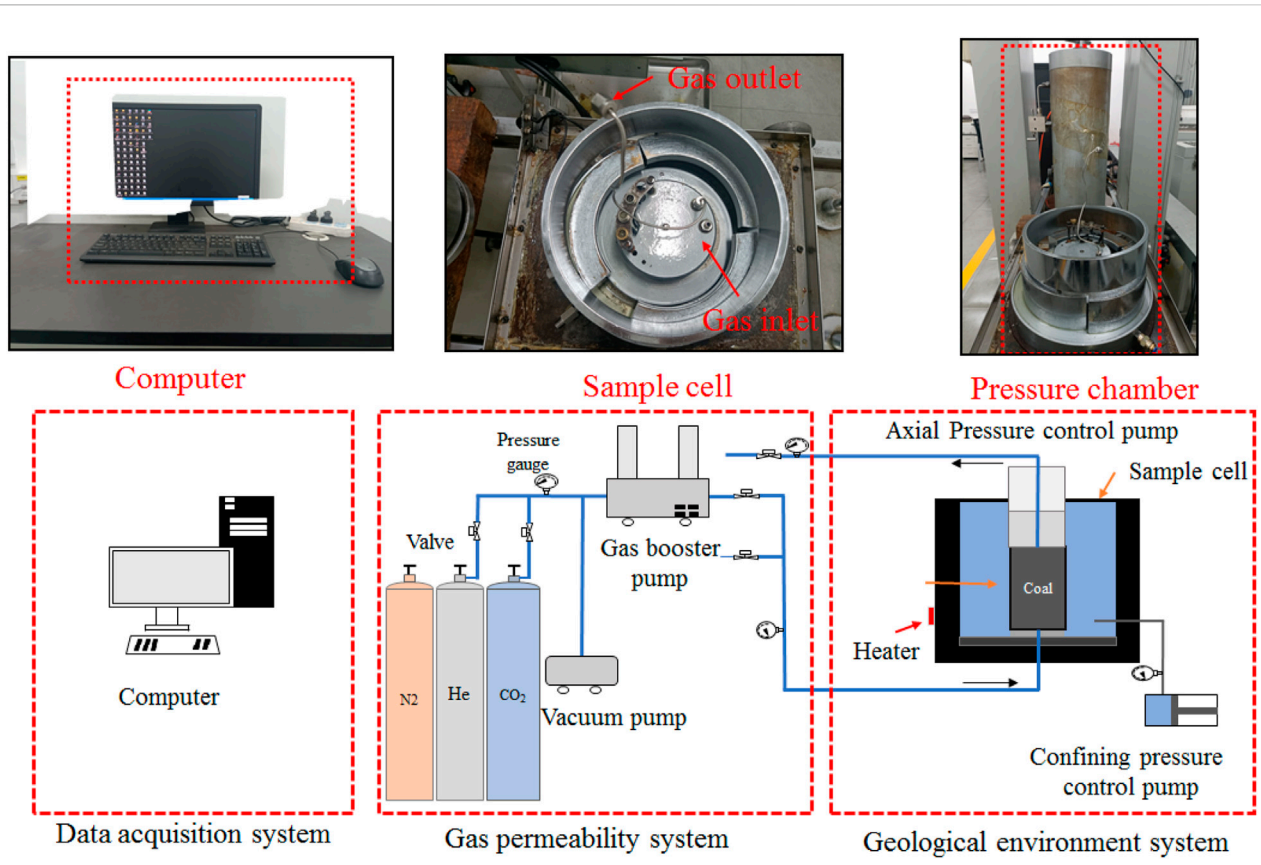

FIGURE 3
The experimental equipment of seepage test.

$$\sigma_e = \frac{1}{3}(\sigma_a + 2\sigma_c) - \frac{1}{2}(P_1 + P_2) \quad (1)$$

Where σ_e is the average effective stress, MPa; σ_a is the axial stress, MPa; σ_c is the confining pressures, MPa; P_1 is the inlet pressure, MPa; P_2 is the outlet pressure, MPa.

The steady-state test method was used in the experiments. For compressible gases, the expansion of fluid can affect the measurement of permeability. Assuming that the permeation of gas through the sample is an isothermal process and that the ideal gas law is applicable. So the gas permeability was calculated according to Darcy's law (Liu X. et al., 2020):

$$k = \frac{2\mu P_a L Q}{A(P_1^2 + P_2^2)} \quad (2)$$

Where k is the permeability, mD; Q is the gas flow rate, cm^3/s; P_a is the atmospheric pressure, 0.1 MPa; A is the cross-sectional area of the sample, cm^2; L is the length of the sample, m; P_1 and P_2 are the inlet and outlet pressures, MPa.

The experimental procedure was conducted as follows: (1) The coal sample was placed in the reaction chamber and the temperature was raised to 35°C. The effective stress was adjusted to 3 MPa and 10 MPa, respectively. Helium (He) was injected to measure the initial permeability of the bituminous coal before $ScCO_2$ treatment. (2) The He injection was stopped, and the axial and radial stress were adjusted to 10 MPa to simulate geological conditions at a depth of 1,000 m underground (Du et al., 2020). Then, $ScCO_2$ of 8 MPa was injected after discharging the residual gas. Previous studies have pointed out that the maximum expansion strain occurs within 3–4 h after CO_2 injection, so an 8-hour period is sufficient to investigate the effect of $ScCO_2$-H_2O on coal. And the coal samples were left to fully absorb and react for 8 h (Cheng et al., 2021). (3) After complete CO_2 adsorption and desorption of the coal samples, step (1) was repeated to measure the permeability of the coal sample after $ScCO_2$ treatment.

2.3 Low temperature liquid nitrogen adsorption test

The low temperature liquid nitrogen adsorption tests were conducted by using a fully automated multistation specific surface area and pore size analyzer, Quadrasorb 2 MP, manufactured by Conta Instruments, USA. Prior to the experiments, the coal samples were processed into 60–80 mesh powder and then pretreated by drying and degassing at 110°C for 24 h. The tests were used to measure the specific surface area, pore size distribution, and pore volume of the coal samples.

2.4 XRD test

The mineral components of the coal samples were analyzed by using a high efficiency conventional powder X-ray diffractometer

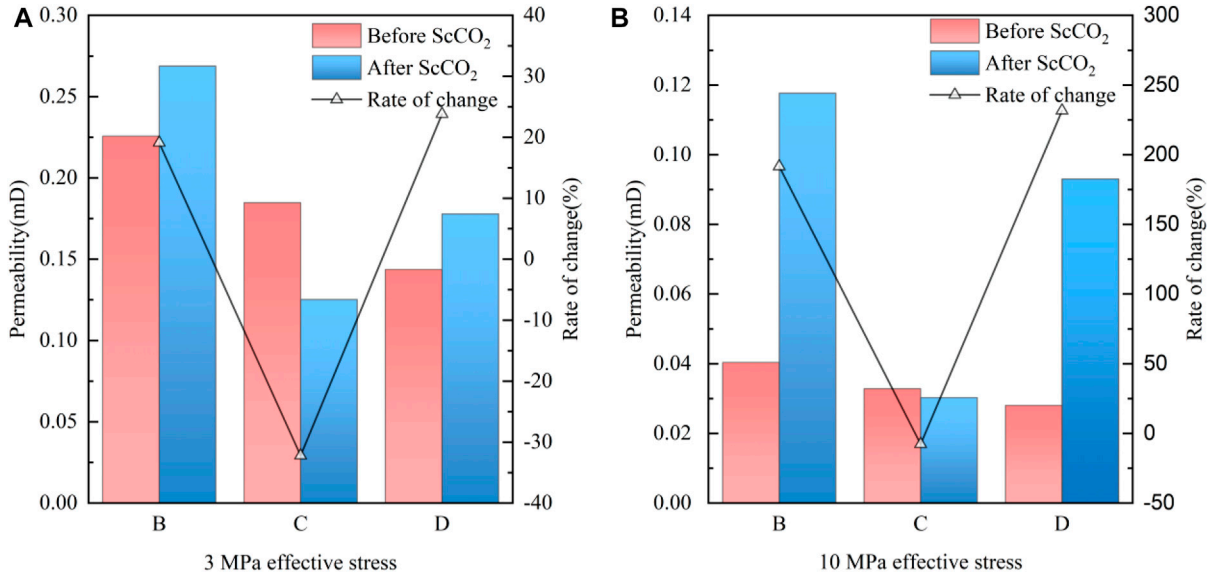

FIGURE 4
Permeability of the coal samples before and after $ScCO_2$ treatment at different effective stresses. **(A)** 3 MPa effecitve stress, **(B)** 10 MPa effective stress.

from Spectris, the Netherlands. The coal samples were ground into a powder of 200 mesh size and were pretreated prior to the experiments. The crystallographic information of the coal samples was obtained by scanning angles ranging from 5°–80° with a scanning time of 20 min.

3 Results and Discusssion

3.1 Permeability characteristics

He seepage tests were performed on bituminous coal samples with varying water saturation levels before and after treatment to examine the effects of $ScCO_2$-H_2O on permeability characteristics. Figure 4 presents the measured permeability values.

Figure 4 indicates that the permeability of bituminous coal is primarily influenced by the moisture content of the coal samples prior to $ScCO_2$ treatments (Zhang X. et al., 2019). Specifically, the permeability of coal samples declines from 0.226 mD to 0.144 mD with the increase of water saturation at 3 MPa effective stress. Similarly, the permeability of coal samples drops from 0.040 mD to 0.028 mD as water saturation increases at 10 MPa effective stress, which aligns with earlier research findings (Pan et al., 2010). The decline can be attributed to the combination of seepage channels such as the pores blockage by water and the squeezing effect caused by internal water absorption expansion (Teng et al., 2017; Talapatra et al., 2020). Moreover, the permeability of coal samples decreases due to compression of the seepage channels caused by increased stress as effective stress increases, which was the result of the continuous closure of pores and fractures as the effective stress increases (Niu et al., 2019).

In order to describe the changes of coal samples' permeability before and after $ScCO_2$ treatment better, the permeability change index k_c of coal samples is defined as follows:

$$k_c = \frac{k_1 - k_0}{k_0} \times 100\% \quad (3)$$

Where, k_0 is the permeability before $ScCO_2$ treatment, mD; k_1 is the permeability after $ScCO_2$ treatment, mD; k_c is the permeability change index, %.

Upon comparing the permeability of coal samples before and after $ScCO_2$ treatment, it is evident that the permeability of samples B and D increased after CO_2 treatment. The permeability of sample B increased from 0.226 mD to 0.269 mD at 3 MPa effective stress with the growth rate of 19.09%. Similarly, the permeability of sample D increased from 0.144 mD to 0.178 mD at 3 MPa effective stress with a growth rate of 23.81%. The physical-chemical reactions of $ScCO_2$ on the minerals of coal samples such as dissolution and extraction resulted in the widening of pores and fractures and improved pore connectivity, leading to an increase of permeability (Zhang G. et al., 2019). Moreover, the permeability of sample B increased from 0.040 mD to 0.118 mD at 10 MPa effective stress with a growth rate of 191.53%, and sample D's permeability increased from 0.028 mD to 0.093 mD with a growth rate of 231.71%. The k_c of sample D is much higher than that of sample B. Because the increase in moisture in the coal samples promotes the dissolution of internal minerals, which broadens and connects the pores better. Moreover, the k_c of coal samples at 10 MPa effective stress was found to be much higher than the k_c at 3 MPa effective stress. Because the cracks in the coal samples are largely closed as the effective stress increases. Therefore, the permeability of coal samples is controlled by pores at high effective stress, while it is controlled by fractures at low effective stress. The contact area between $ScCO_2$-H_2O and pore surface is larger, the reaction is more sufficient, and the pore connectivity is better. Therefore, the growth of permeability is more obvious at high effective stress.

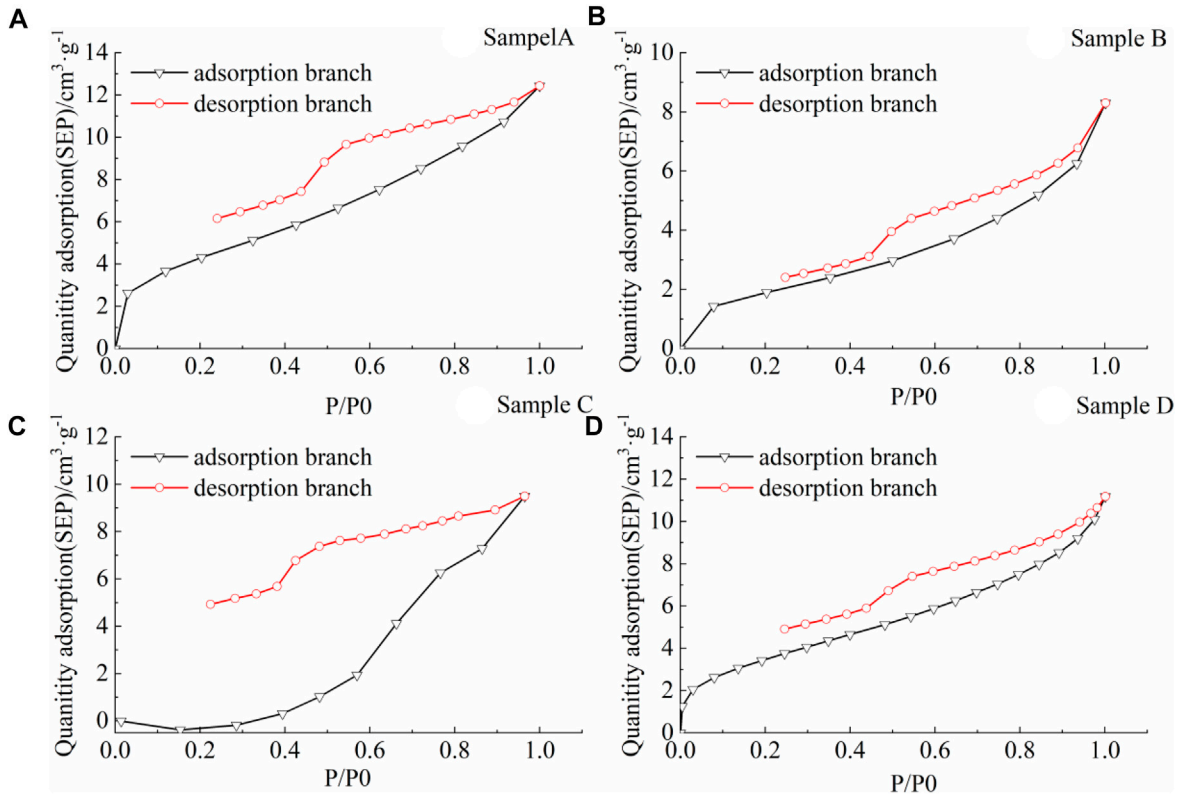

FIGURE 5
Low temperature liquid nitrogen adsorption-desorption curve. **(A)** sample A, **(B)** sample B, **(C)** sample C, **(D)** sample D.

Additionally, Figure 4 shows that the permeability of sample C decreases after $ScCO_2$ treatment. There are two possible reasons for the phenomenon. Firstly, the *in situ* stress conditions may have caused the collapse of the pores in the coal samples, leading to the blockage of seepage channels despite the modification of pore fissures by $ScCO_2$. Secondly, $ScCO_2$ treatment may have caused the generation of new mineral precipitations in sample C, which could have blocked the pore channels and had a negative impact on the permeability.

3.2 Pore characteristics

Coal is a naturally occurring organic rock with a dual pore structure that is influenced by various factors such as the freeze-thaw effect, effective stress and the action of $ScCO_2$ (Huang et al., 2017; Li et al., 2020; Chen et al., 2022). The pore structure is considered to be the most significant factor affecting the efficiency of ECBM and the stability of CGS (Wang et al., 2015; Zhang et al., 2020). The strong interaction of $ScCO_2$-H_2O and coal results in significant changes in the pore structure (Pan et al., 2018). The low temperature liquid nitrogen adsorption tests were conducted on coal samples before and after $ScCO_2$ treatment to investigate the effect of $ScCO_2$ on the pore characteristics of water-bearing coal samples. The adsorption and desorption capacity at different relative pressures were measured, and important parameters such as adsorption-desorption isotherms, pore size distribution, pore volume, specific surface area, and average pore size were calculated (Yi et al., 2012; Ni et al., 2020; Liu et al., 2022).

Experiments were conducted on both the original coal (sample A) and the $ScCO_2$-treated coal (samples B, C and D), and the resulting adsorption-desorption curves are displayed in Figure 5. The curves demonstrate varying trends, which can be classified into two types based on their morphological characteristics as defined in this paper.

Type A is characterized by a sharp decrease in the desorption branch at the relative pressure of 0.9–1.0, followed by a slow decrease as the relative pressure decreases. Then there is a certain decreasing inflection point at the relative pressure of about 0.5. When the relative pressure is below 0.1, the adsorption and desorption branches are not closed, and the distance between them is relatively small (Figures 5A, B, D). This type is caused by the existence of permeable pores with open ends and ink bottle type pores in the coal samples.

Similar to Type A, type B is characterized by a sharp decrease in the desorption branch at the relative pressure of 0.9–1.0, followed by a slow decrease as the relative pressure decreases. Then there is a certain inflection point at the relative pressure of about 0.5. When the relative pressure is below 0.1, the adsorption and desorption branches are not completely closed, and the distance between them is relatively large (Figure 5C). This type is caused by the development of pore narrow crevice pores, ink bottle pores, and permeable pores with open ends of the coal samples.

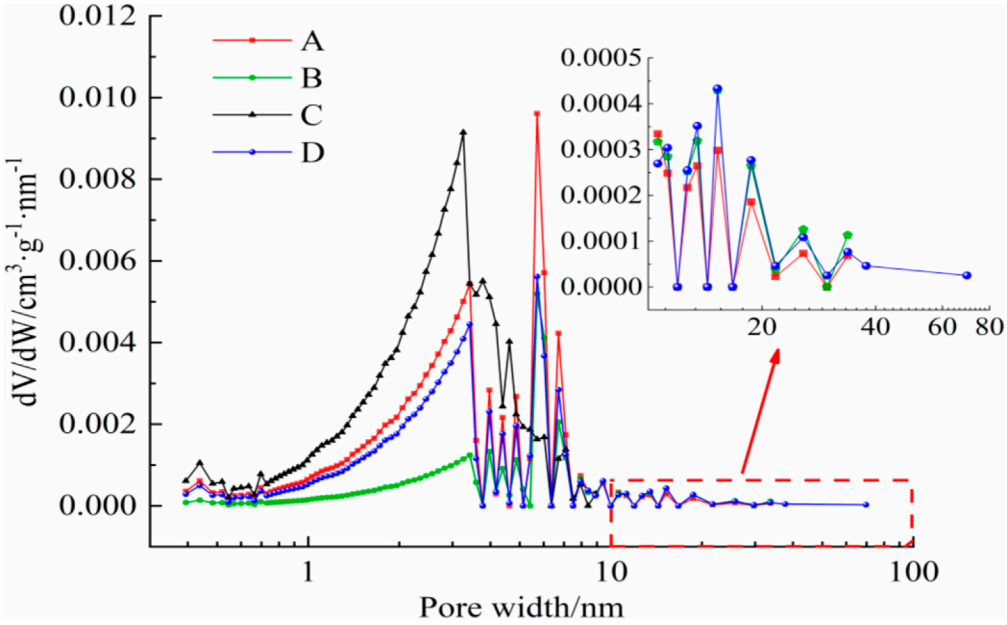

FIGURE 6
Pore size distribution characteristics of the coal samples.

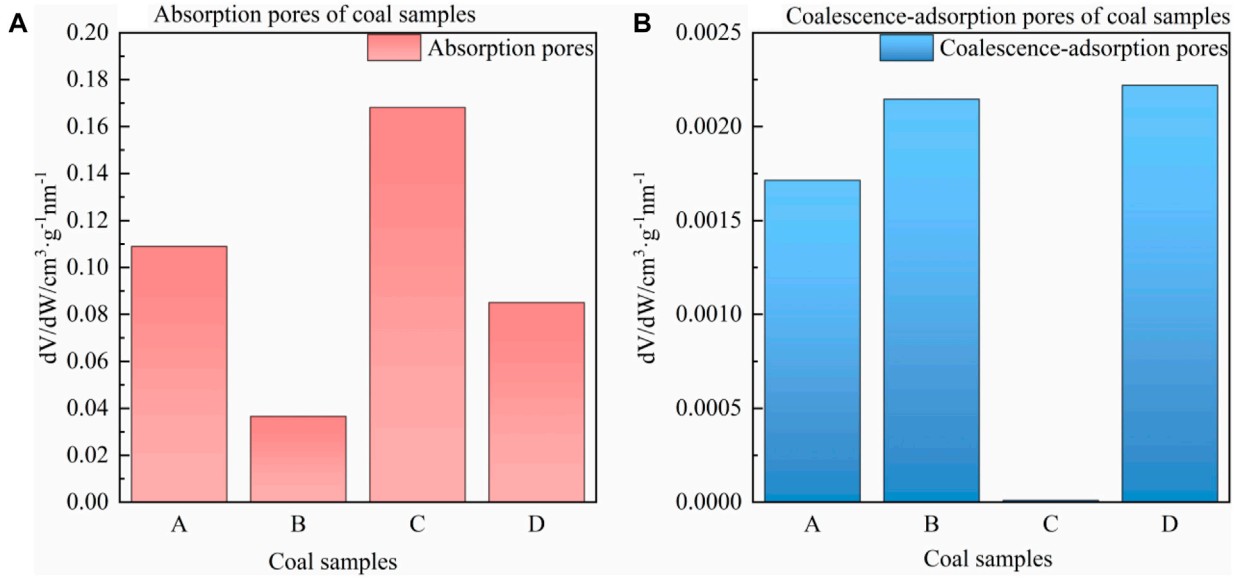

FIGURE 7
Adsorption pore volume of coal samples. **(A)** Adsorption pores, **(B)** Coalescence-adsorption pores.

Based on Kelvin's capillary coalescence theory, we used the BJH pore size analysis model to analyze the pores in the paper, which is widely accepted (Hu et al., 2021). The pore size distribution of the coal samples was plotted with BJH pore size (W) as the horizontal coordinate and the differential of pore volume to pore size (dV/dW) as the vertical coordinate, as shown in Figure 6.

The pore size distribution curves of the four coal samples in Figure 6 show similar trends that most pores falling within the 1–10 nm size range, and two main peaks observed between 2–5 nm and 5–8 nm. Additionally, there are several small peaks in the 10 nm range for three of the coal samples. As can be seen from Figure 6, the pore sizes of samples B and D tend to increase, while the pore sizes of

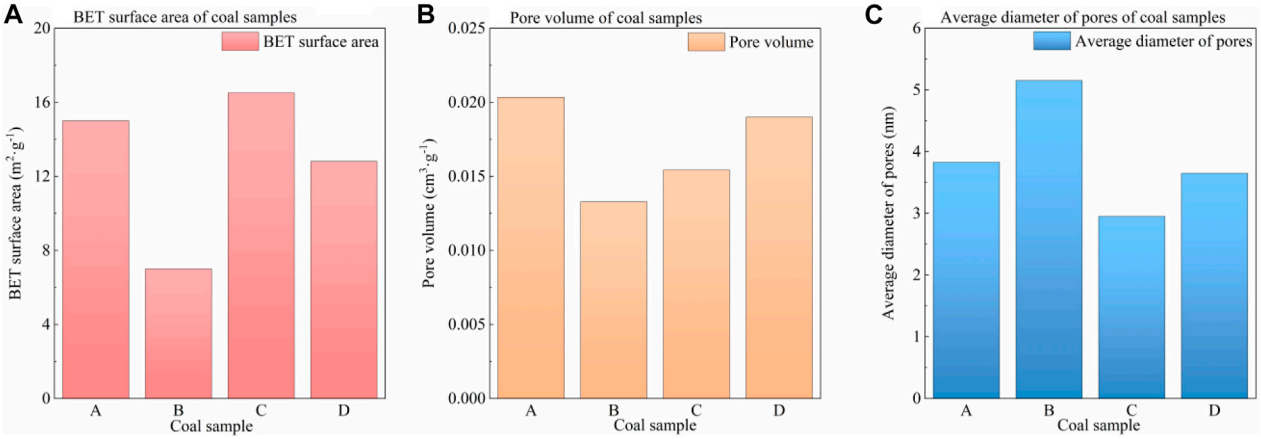

FIGURE 8
Pore parameters of coal samples. **(A)** BET surface area, **(B)** Pore volume, **(C)** Average diameter of pores.

sample C tend to decrease. Coal pore sizes can generally be categorized into adsorption pores (<100 nm) and seepage pores (>100 nm) (Mou et al., 2021). And the adsorption pores can be divided into coagulation-adsorption pores (10–100 nm) and absorption pores (<10 nm) further (Ni et al., 2020). The results in Figure 6 indicate that the pore size distribution of coal samples changed significantly after $ScCO_2$ treatment. Consequently, the volumes of adsorption pores and coagulation-adsorption pores for each of the four coal samples were calculated and are shown in Figure 7.

As depicted in Figure 7, the pore volumes of the four coal samples display distinct changes. Samples B and D show a decrease in the adsorption pore volumes, while sample C exhibits an increase. Conversely, the volumes of the coalescence-adsorption pore of samples B and D increase, while sample C shows a decrease. These findings indicate that the pores of coal samples undergo transformations after $ScCO_2$ treatment, where the pore size of samples B and D increases while the pore size of sample C decreases. Based on the changes in pore size, the samples can be categorized as either pore broadening type (samples B, D) or pore shrinkage type (sample C). The trend in pore changes in coal samples is consistent with the permeability changes discussed earlier. The BJH pore size analysis model was employed to determine the average pore size, pore volume, and specific surface area of the four coal samples. The specific parameters are presented in Figure 8.

Figure 8A shows that the specific surface area of samples B and D decreased after $ScCO_2$ treatment compared to raw coal (sample A) before $ScCO_2$ treatment. This is caused by the conversion of adsorption pores into seepage pores in coal samples, which is not conducive to gas adsorption. In contrast, the specific surface area of sample C increased after $ScCO_2$ treatment, providing more space for CO_2 adsorption and improving the stability of CO_2 sequestration.

It is evident that the pore volumes of samples B, C, and D decreased to varying degrees in Figure 8B. The decrease in pore volumes of the three coal samples is caused by axial and radial stress compression during $ScCO_2$ treatment. Then the transformation effect of $ScCO_2$ on coal is enhanced as the water content increases, and the pore volume of coal samples is restored to a certain extent. Therefore, the pore volume of coal samples continuously increases as the water content increases.

Figure 8C illustrates that the average pore size of sample B increases, while the average pore size of samples C and D decreases. This trend is opposite to that of the specific surface area due to the fact that the small pores provide more specific surface area than large pores.

The results above indicate that $ScCO_2$ promotes the development of seepage pores in dry and water saturated coal samples, leading to an increase in permeability and enhancement of CBM extraction efficiency. Furthermore, $ScCO_2$ causes the transformation of macropores into micropores and small pores of the half-saturated coal samples, providing more space for CO_2 adsorption and improving the capacity of CO_2 sequestration.

3.3 Mineral composition

XRD tests were performed on the four coal samples. The resulting data were analyzed by Jade 6 software to determine the mineral composition of the different water-saturated coal samples, which is shown in Figure 9. The analysis reveals that the minerals present in the raw coal samples include 25.1% calcite ($CaCO_3$), 20.0% dolomite ($CaMg(CO_3)_2$), 15.1% quartz (SiO_2), 2.3% pyrite (FeS_2), and 37.5% clay minerals, with illite ($K_3Fe_4Si1_4Al_7O_{40}(OH)_8$) and kaolinite ($Al_2Si_2O_5(OH)_4$) accounting for 11.2% and 26.3% of the clay minerals, respectively.

As shown in Figure 9, the $ScCO_2$ treatment resulted in a decrease in the content of carbonate minerals and an increase in the content of clay minerals in samples B, C, and D. This can be attributed to the strong dissolution reaction of carbonate minerals which are more sensitive to acidic environments (Zhang K. et al., 2019; Fatah et al., 2021; Ozotta et al., 2021). Although clay minerals can also be dissolved, the reaction rate is relatively slow, leading to an increase in their content. Specifically, the dolomite in sample B was violently dissolved, while calcite was slowly dissolved, resulting in a relatively higher content of the remaining minerals. Similarly,

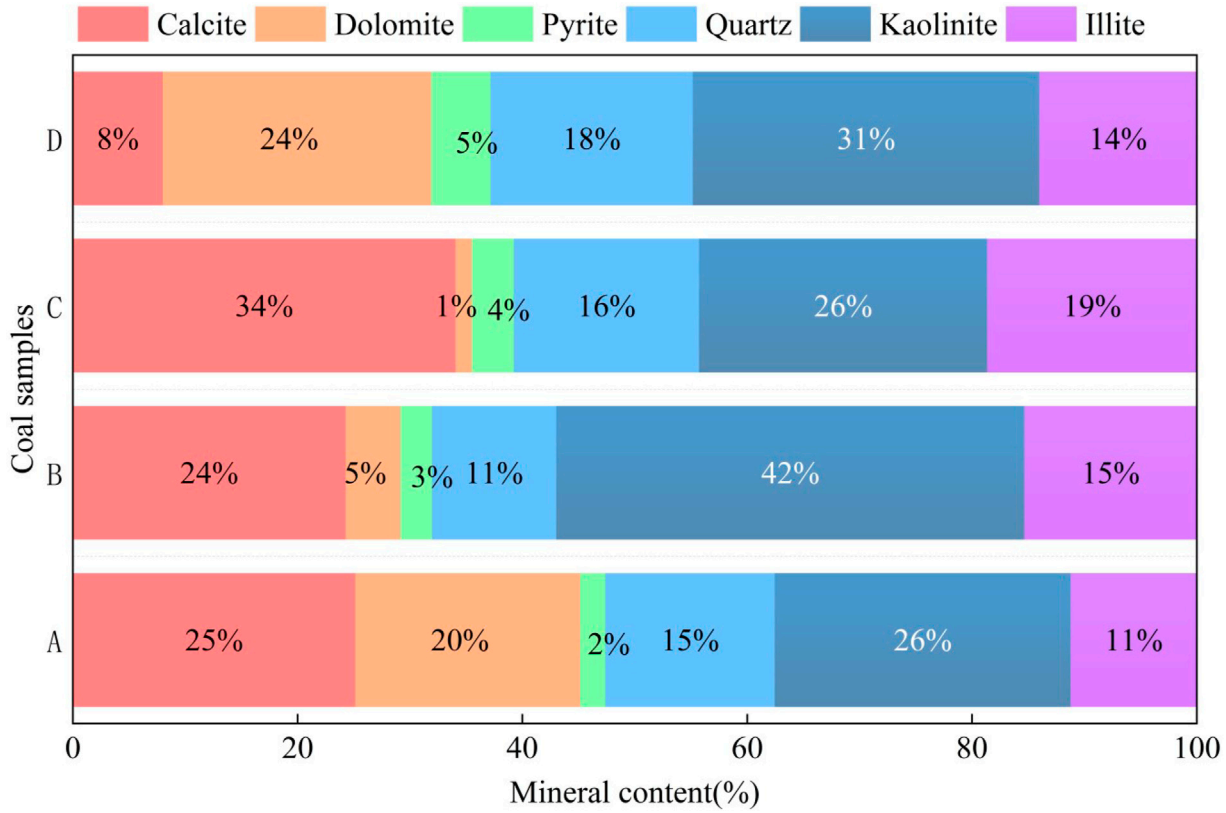

FIGURE 9
Mineral content changes.

the violent dissolution of calcite led to a relatively higher content of other minerals in sample D. The reaction above promoted the expansion of pores in samples B and D and improved the connectivity of pores. Therefore, their adsorption pores decrease and permeability increases.

Notably, the content of dolomite in sample C decreased significantly, while the content of calcite increased. This can be explained by the fact that the water in sample C reduced the pH value of the solution compared to sample D, intensifying the dissolution of dolomite. However, the large amount of Ca^{2+} and Mg^{2+} generated by the dolomite reaction could not be completely dissolved by the water in coal sample C. Moreover, the solubility of Ca^{2+} is lower than that of Mg^{2+}, causing Ca^{2+} to combine with CO_3^{2-} to precipitate as new calcite and increase the relative content of calcite. Moreover, a large amount of newly formed calcite precipitates in key seepage channels such as pore throats, dividing the original pores, resulting in an increase in BET specific surface area and a decrease in permeability.

3.4 Reaction mechanism

The combination of $ScCO_2$ and water generates H_2CO_3, which has strong extraction and corrosion effects on coal. Consequently, the microstructure of coal samples with different water saturation changes drastically after $ScCO_2$ treatment, leading to changes of permeability. The transformation mechanism is illustrated in Figure 10.

There is a series of geochemical reactions minerals in coal after $ScCO_2$ injection, and the specific reactions are as follows (Wang Z. et al., 2021; Ozotta et al., 2021):

$$CO_2 + H_2O \rightarrow H^+ + HCO_3^- \rightarrow H^+ + CO_3^{2-} \quad (4)$$

$$CaCO_3 + 2H^+ \rightarrow Ca^{2+} + H_2O + CO_2 \quad (5)$$

$$CaMg(CO_3)_2 + 4H^+ \rightarrow Ca^{2+} + Mg^{2+} + 2H_2O + 2CO_2 \quad (6)$$

$$FeS_2 + 2H^+ \rightarrow Fe^{2+} + H_2S + S \quad (7)$$

$$Al_2Si_2O_5(OH)_4 + 6H^+ \rightarrow 2Al^{3+} + 2SiO_2 + 5H_2O \quad (8)$$

$$K_3Fe_4Si_{14}Al_7O_{40}(OH)_8 + 88H^+ \rightarrow 7Al^{3+} + 3K^+ + 4Fe^{2+} + 14Si^{4+} + 48H_2O \quad (9)$$

Dolomite in the coal samples undergoes significant dissolution after $ScCO_2$ treatment, while the dissolution rate of clay minerals is relatively slow, resulting in an increased content of clay minerals. The content of quartz increases as the water saturation increases, although it does not undergo any significant reaction. This can be attributed to two reasons: (1) the dissolution of clay minerals produces new quartz minerals; (2) the violent dissolution of carbonate minerals leads to the relative increase in the content of quartz due to a decrease in the content of carbonate minerals.

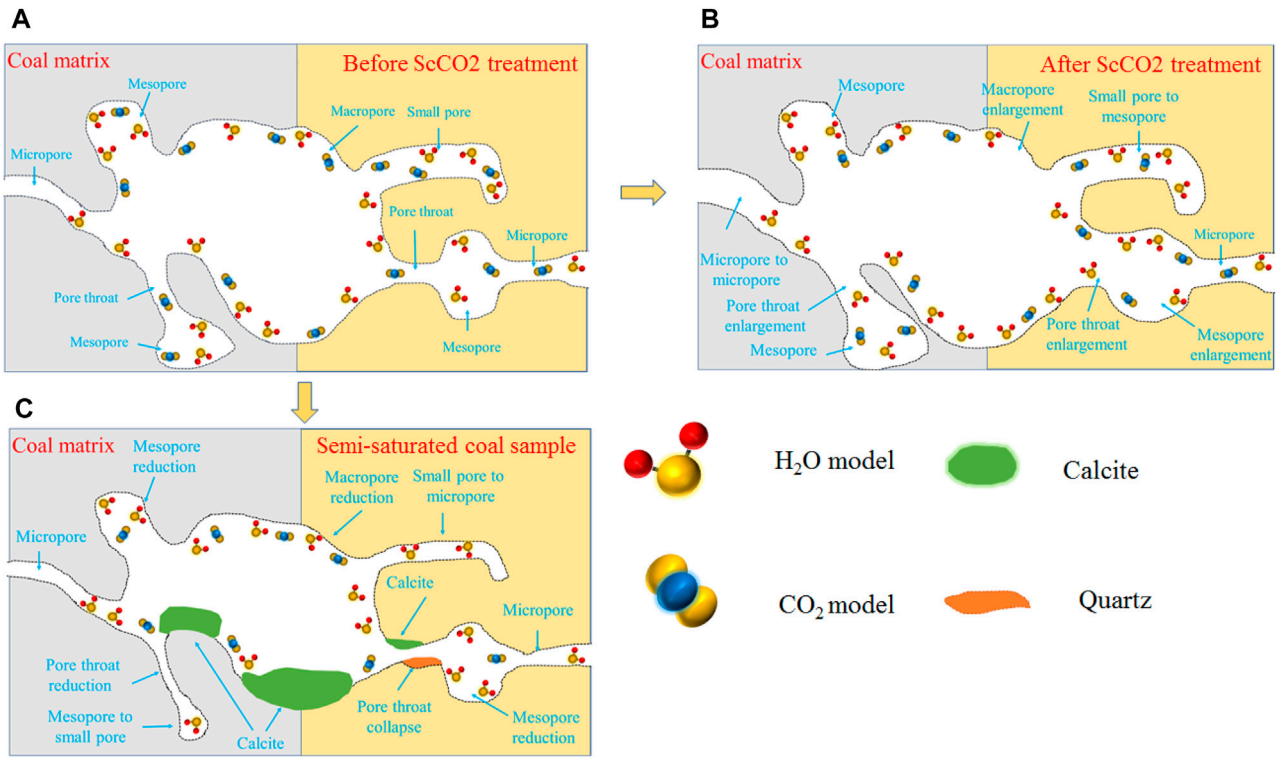

FIGURE 10
Reaction mechanism. **(A)** Before $ScCO_2$ treatment, **(B)** After $ScCO_2$ treatment, **(C)** Semi-saturated coal sample.

In Figure 10B, it can be observed that the injection of $ScCO_2$ results in significant dissolution of carbonate minerals in samples B and D. This dissolution widens the original pores and fractures, transforms the micropores into macropores, and improves the connectivity of seepage channels, thus enhancing the permeability of the coal samples. The formation of H_2CO_3 due to the CO_2-H_2O reaction in sample D leads to a lower pH and faster dissolution rate of carbonate minerals. Additionally, the presence of sufficient water increases the solubility of Ca^{2+} and Mg^{2+} which promotes the reaction progress and increases the connectivity of seepage pores further (Jiang et al., 2019). Therefore, the permeability growth of sample D is higher after $ScCO_2$ treatment comparing to sample B. However, this reaction also results in a reduction of initial adsorption pores and BET specific surface area, which is negative for CO_2 adsorption and stable storage.

In Figure 10C, it is shown that the dissolution of dolomite in sample C results in a substantial increase in Ca^{2+} and Mg^{2+}. However, the water in the sample C is unable to dissolve these ions completely comparing to sample D. As a result, the Ca^{2+} combines with CO_3^{2-} in the solution, leading to the precipitation of calcite. The newly formed calcite aggregates in the original seepage channels and pore throats, obstructing the seepage channels and reducing the size of the original macropores. This leads to a decrease in the pore size and an increase in the specific BET surface area of the coal samples. Consequently, the permeability of sample C decreases. However, the increased BET specific surface area provides more sites for CO_2 adsorption.

The fractures in coal samples are closed at high stress conditions, and the permeability is controlled by the seepage pores. However, the contact area between the $ScCO_2$ and pores surface is greater comparing to fractures, and the reaction is more efficient, resulting in better transformation effects. Therefore, the seepage growth of coal samples at high stress conditions is higher.

4 Conclusion

The $ScCO_2$-H_2O reaction experiments on coal samples with varying water saturation levels at *in situ* stress were conducted. Then the seepage tests, low temperature liquid nitrogen adsorption tests, and XRD tests was conducted to analyze the changes of the samples before and after treatment. The key findings are summarized below:

(1) $ScCO_2$ treatment significantly increases the permeability of both dry and water saturated coal samples at *in situ* stress conditions, which is more effective for water saturated coal samples. The growth rates of permeability as the effective stress increases due to the improved pore transformation. However, the permeability of semi-saturated coal samples decreases after $ScCO_2$ treatment due to the effects of stress compression and seepage channel blockage caused by new mineral precipitation.
(2) The low temperature liquid nitrogen adsorption tests revealed that $ScCO_2$ treatment effectively increased the pore size of dry and water saturated coal samples. And the pore volume of coal samples increases as the moisture content increases. However,

$ScCO_2$ treatment significantly increased the size of adsorption pores in semi-saturated coal samples, which provided more space for CO_2 adsorption.

(3) XRD analysis showed that $ScCO_2$ treatment makes the carbonate mineral content decrease and silicate minerals content increase in coal samples, which facilitated pore connectivity. Although the dissolution of dolomite increased the pore size of semi-saturated coal samples, the newly formed calcite and quartz clogged the pore throats and divided the pores, leading to a reduction in seepage pores.

(4) The experimental and analytical results show that the reaction mechanism of coal samples with different moisture content after $ScCO_2$ injection is different. $ScCO_2$ effectively improves the pore connectivity of dry and water saturated coal samples. This effect is even greater for saturated coal samples. Although the pores of semi saturated coal samples have been expanded after $ScCO_2$ treatment, the newly formed minerals such as quartz and calcite have a negative impact on pore connectivity and permeability.

The study compared the changes of mineral composition, pore structure, and permeability of coal samples with different water saturations before and after $ScCO_2$ treatment, and the change mechanism of bituminous coal with different water saturations was analyzed, which is significant for CGS and ECBM. However, the explanation for the change of semi-saturated bituminous coal after $ScCO_2$ treatment is still unclear. Therefore, it is necessary to further analyze the change rules and mechanisms of bituminous coal with different moisture content under the action of $ScCO_2$ in detail.

Data availability statement

The original contributions presented in the study are included in the article/supplementary material, further inquiries can be directed to the corresponding authors.

Author contributions

CL, JZ, and SH conceived and designed the experiments; CL performed the experiments; CL analyzed the data; CL and JZ contributed materials and analysis tools; CL and JZ wrote the paper. SH reviewed and edited.

Funding

The authors acknowledge fundings by National Natural Science Foundation of China (No. 42202155), China Postdoctoral Science Foundation (No. 2021MD703807), Heilongjiang Provincial Postdoctoral Science Foundation (No. LBH-Z20121).

Acknowledgments

We thank Chongqing University and Northeast Petroleum University for the financial support to this study.

Conflict of interest

The authors declare that the research was conducted in the absence of any commercial or financial relationships that could be construed as a potential conflict of interest.

Publisher's note

References

Chen, K., Liu, X., Nie, B., Zhang, C., Song, D., Wang, L., et al. (2022). Mineral dissolution and pore alteration of coal induced by interactions with supercritical CO_2. *Energy* 248, 123627. doi:10.1016/j.energy.2022.123627

Cheng, Y., Zhang, X., Lu, Z., Pan, Z. j., Zeng, M., Du, X., et al. (2021). The effect of subcritical and supercritical CO2 on the pore structure of bituminous coals. *J. Nat. Gas. Sci. Eng.* 94, 104132. doi:10.1016/j.jngse.2021.104132

Chiquet, P., Daridon, J.-L., Broseta, D., and Thibeau, S. (2007). CO_2/water interfacial tensions under pressure and temperature conditions of CO_2 geological storage. *Energy Convers. manage.* 48 (3), 736–744. doi:10.1016/j.enconman.2006.09.011

Cui, G., Yang, L., Fang, J., Qiu, Z., Wang, Y., and Ren, S. (2021). Geochemical reactions and their influence on petrophysical properties of ultra-low permeability oil reservoirs during water and CO_2 flooding. *J. Pet. Sci. Eng.* 203, 108672. doi:10.1016/j.petrol.2021.108672

Dawson, G. K. W., Golding, S. D., Massarotto, P., and Esterle, J. S. (2011). Experimental supercritical CO_2 and water interactions with coal under simulated *in situ* conditions. *Energy Procedia* 4, 3139–3146. doi:10.1016/j.egypro.2011.02.228

Du, Y., Fu, C., Pan, Z., Sang, S., Wang, W., Liu, S., et al. (2020). Geochemistry effects of supercritical CO_2 and H_2O on the mesopore and macropore structures of high-rank coal from the Qinshui Basin, China. *Int. J. Coal Geol.* 223, 103467. doi:10.1016/j.coal.2020.103467

Du, Y., Sang, S., Wang, W., Liu, S., Wang, T., and Fang, H. (2018). Experimental study of the reactions of supercritical CO_2 and minerals in high-rank coal under formation conditions. *Energy Fuel* 32 (2), 1115–1125. doi:10.1021/acs.energyfuels.7b02650

Fatah, A., Mahmud, H. B., Bennour, Z., Hossain, M., and Gholami, R. (2021). Effect of supercritical CO_2 treatment on physical properties and functional groups of shales. *Fuel* 303, 121310. doi:10.1016/j.fuel.2021.121310

Gao, S., Jia, L., Zhou, Q., Cheng, H., and Wang, Y. (2022). Microscopic pore structure changes in coal induced by a CO_2-H_2O reaction system. *J. Pet. Sci. Eng.* 208, 109361. doi:10.1016/j.petrol.2021.109361

Hu, Z., Li, C., and Zhang, D. (2021). Interactions of dynamic supercritical CO_2 fluid with different rank moisture-equilibrated coals: Implications for CO_2 sequestration in coal seams. *Chin. J. Chem. Eng.* 35, 288–301. doi:10.1016/j.cjche.2020.10.020

Huang, S., Liu, D., Yao, Y., Gan, Q., Cai, Y., and Xu, L. (2017). Natural fractures initiation and fracture type prediction in coal reservoir under different *in-situ* stresses during hydraulic fracturing. *J. Nat. Gas. Sci. Eng.* 43, 69–80. doi:10.1016/j.jngse.2017.03.022

Jiang, R., and Yu, H. (2019). Interaction between sequestered supercritical CO_2 and minerals in deep coal seams. *Int. J. Coal Geol.* 202, 1–13. doi:10.1016/j.coal.2018.12.001

Li, R., Ge, Z., Wang, Z., Zhou, Z., Zhou, J., and Li, C. (2022b). Effect of supercritical carbon dioxide ($ScCO_2$) on the microstructure of bituminous coal with different moisture contents in the process of $ScCO_2$ enhanced coalbed methane and CO_2 geological sequestration. *Energy Fuel.* 36 (7), 3680–3694. doi:10.1021/acs.energyfuels.1c04027

Li, X., Wei, N., Liu, Y., Fang, Z., Dahowski, R. T., and Davidson, C. L. (2009). CO_2 point emission and geological storage capacity in China. *Energy Procedia* 1 (1), 2793–2800. doi:10.1016/j.egypro.2009.02.051

Li, X., Yu, H., Lebedev, M., Lu, M., Yuan, Y., Yang, Z., et al. (2022a). The influence of CO2 saturated brine on microstructure of coal: Implications for carbon geo-sequestration. *Front. Energy Res.* 10. doi:10.3389/fenrg.2022.802883

Li, Y., Tang, S., Zhang, S., Xi, Z., and Wang, P. (2019). Biogeochemistry and water–rock interactions of coalbed methane Co-produced water in the shizhuangnan block of the southern Qinshui Basin, China. *China.* ***Water*** 12 (1), 130. doi:10.3390/w12010130

Li, Z., Yang, G., and Liu, H. (2020). The influence of regional freeze–thaw cycles on loess landslides: Analysis of strength deterioration of loess with changes in pore structure. *Water* 12 (11), 3047. doi:10.3390/w12113047

Liu, J., Xie, L., He, B., Gan, Q., and Zhao, P. (2021). Influence of anisotropic and heterogeneous permeability coupled with *in-situ* stress on CO2 sequestration with simultaneous enhanced gas recovery in shale: Quantitative modeling and case study. *Int. J. Greenh. Gas Control* 104, 103208. doi:10.1016/j.ijggc.2020.103208

Liu, J., Xie, L., Yao, Y., Gan, Q., Zhao, P., and Du, L. (2019). Preliminary study of influence factors and estimation model of the enhanced gas recovery stimulated by carbon dioxide utilization in shale. *ACS Sustain. Chem. Eng.* 7 (24), 20114–20125. doi:10.1021/acssuschemeng.9b06005

Liu, S., Yang, K., Sun, H., Wang, D., Zhang, D., Li, X., et al. (2022). Adsorption and deformation characteristics of coal under liquid nitrogen cold soaking. *Fuel* 316, 123026. doi:10.1016/j.fuel.2021.123026

Liu, X., Yu, J., Wu, D., and Xiao, X. (2020b). Permeability characteristics of coal after supercritical CO_2 adsorption at different temperatures. *Geofluids* 2020, 1–8. doi:10.1155/2020/8836349

Liu, Z., Liu, D., Cai, Y., and Pan, Z. (2020a). Experimental study of the effective stress coefficient for coal anisotropic permeability. *Energy Fuel.* 34 (5), 5856–5867. doi:10.1021/acs.energyfuels.0c00907

Mirzaeian, M., and Hall, P. J. (2006). The interactions of coal with CO_2 and its effects on coal structure. *Energy Fuel.* 20 (5), 2022–2027. doi:10.1021/ef060040+

Mou, P., Pan, J., Niu, Q., Wang, Z., Li, Y., and Song, D. (2021). Coal pores: Methods, types, and characteristics. *Energy Fuel.* 35 (9), 7467–7484. doi:10.1021/acs.energyfuels.1c00344

Ni, G., Li, S., Rahman, S., Xun, M., Wang, H., Xu, Y., et al. (2020). Effect of nitric acid on the pore structure and fractal characteristics of coal based on the low-temperature nitrogen adsorption method. *Powder Technol.* 367, 506–516. doi:10.1016/j.powtec.2020.04.011

Niu, Q., Cao, L., Sang, S., Zhou, X., and Liu, S. (2019). Experimental study of permeability changes and its influencing factors with CO_2 injection in coal. *J. Nat. Gas. Sci. Eng.* 61, 215–225. doi:10.1016/j.jngse.2018.09.024

Niu, Q., Cao, L., Sang, S., Zhou, X., and Wang, Z. (2018). Anisotropic adsorption swelling and permeability characteristics with injecting CO_2 in coal. *Energy Fuel.* 32 (2), 1979–1991. doi:10.1021/acs.energyfuels.7b03087

Ozotta, O., Ostadhassan, M., Liu, K., Liu, B., Kolawole, O., and Hadavimoghaddam, F. (2021). Reassessment of CO_2 sequestration in tight reservoirs and associated formations. *J. Pet. Sci. Eng.* 206, 109071. doi:10.1016/j.petrol.2021.109071

Pan, Y., Hui, D., Luo, P., Zhang, Y., Sun, L., and Wang, K. (2018). Experimental investigation of the geochemical interactions between supercritical CO_2 and shale: Implications for CO_2 storage in gas-bearing shale formations. *Energy Fuel* 32 (2), 1963–1978. doi:10.1021/acs.energyfuels.7b03074

Pan, Z., Connell, L. D., Camilleri, M., and Connelly, L. (2010). Effects of matrix moisture on gas diffusion and flow in coal. *Fuel* 89 (11), 3207–3217. doi:10.1016/j.fuel.2010.05.038

Perera, M. S. A., Ranjith, P. G., Choi, S. K., and Airey, D. (2011). The effects of sub-critical and super-critical carbon dioxide adsorption-induced coal matrix swelling on the permeability of naturally fractured black coal. *Energy* 36 (11), 6442–6450. doi:10.1016/j.energy.2011.09.023

Qu, S., Yang, J., and Liu, Z. (2012). CO_2 sorption on coals: Contribution of minerals and influence of supercritical CO_2 pre-exposure. *Energy Fuel.* 26 (6), 3928–3934. doi:10.1021/ef300123s

Song, Y., Zou, Q., Su, E., Zhang, Y., and Sun, Y. (2020). Changes in the microstructure of low-rank coal after supercritical CO_2 and water treatment. *Fuel* 279, 118493. doi:10.1016/j.fuel.2020.118493

Talapatra, A., and Karim, M. M. (2020). The influence of moisture content on coal deformation and coal permeability during coalbed methane (CBM) production in wet reservoirs. *J. Pet. Explor. Prod. Te.* 10 (5), 1907–1920. doi:10.1007/s13202-020-00880-x

Teng, T., Gao, F., Ju, Y., and Xue, Y. (2017). How moisture loss affects coal porosity and permeability during gas recovery in wet reservoirs? *Int. J. Min. Sci. Techno.* 27 (6), 899–906. doi:10.1016/j.ijmst.2017.06.016

Wang, H., Fu, X., Jian, K., Li, T., and Luo, P. (2015). Changes in coal pore structure and permeability during N_2 injection. *J. Nat. Gas. Sci. Eng.* 27, 1234–1241. doi:10.1016/j.jngse.2015.09.068

Wang, X., Zhang, D., Geng, J., Jin, Z., Wang, C., and Ren, K. (2022b). Effects of CO_2 intrusion on pore structure characteristics of mineral-bearing coal: Implication for CO_2 injection pressure. *J. Nat. Gas. Sci. Eng.* 108, 104808. doi:10.1016/j.jngse.2022.104808

Wang, Y., Guo, C., Du, C., Chen, X., Jia, L., Guo, X., et al. (2021a). Carbon peak and carbon neutrality in China: Goals, implementation path, and prospects. *China Geol.* 4 (0), 1–27. doi:10.31035/cg2021083

Wang, Z., Ge, Z., Li, R., Zhou, Z., Hou, Y., and Zhang, H. (2022a). Coupling effect of temperature, gas, and viscoelastic surfactant fracturing fluid on the chemical structure of deep coal: An experimental study. *Energy Fuel.* 36 (7), 3468–3480. doi:10.1021/acs.energyfuels.1c03796

Wang, Z., Ge, Z., Li, R., Zhou, Z., Hou, Y., and Zhang, H. (2021b). Coupling effect of temperature, gas, and viscoelastic surfactant fracturing fluid on the microstructure and its fractal characteristics of deep coal. *Energy Fuel.* 35 (23), 19423–19436. doi:10.1021/acs.energyfuels.1c02809

Xu, H., Zhu, S., and Shi, H. (2022). Is it possible to reduce agricultural carbon emissions through more efficient irrigation: Empirical evidence from China. *Water* 14 (8), 1218. doi:10.3390/w14081218

Yi, Z., Xiaomin, F., Xue, H., Zeyu, N., and Jun, X. (2012). Evaluation of coal bed methane content using BET adsorption isotherm equation. *Glob. Geol.* 15, 74–77. doi:10.3969/j.issn.1673-9736.2012.01.11

Zepeng, W., Zhaolong, G., Ruihui, L., Xianfeng, L., Haoming, W., and Shihui, G. (2022). Effects of acid-based fracturing fluids with variable hydrochloric acid contents on the microstructure of bituminous coal: An experimental study. *Energy* 244, 122621. doi:10.1016/j.energy.2021.122621

Zhang, G., Ranjith, P. G., Wu, B., Perera, M. S. A., Haque, A., and Li, D. (2019b). Synchrotron X-ray tomographic characterization of microstructural evolution in coal due to supercritical CO_2 injection at *in-situ* conditions. *Fuel* 255, 115696. doi:10.1016/j.fuel.2019.115696

Zhang, K., Cheng, Y., Li, W., Wu, D., and Liu, Z. (2017). Influence of supercritical CO_2 on pore structure and functional groups of coal: Implications for CO_2 sequestration. *J. Nat. Gas. Sci. Eng.* 40, 288–298. doi:10.1016/j.jngse.2017.02.031

Zhang, K., Sang, S., Liu, C., Ma, M., and Zhou, X. (2019c). Experimental study the influences of geochemical reaction on coal structure during the CO_2 geological storage in deep coal seam. *J. Pet. Sci. Eng.* 178, 1006–1017. doi:10.1016/j.petrol.2019.03.082

Zhang, S., Wu, C., and Liu, H. (2020). Comprehensive characteristics of pore structure and factors influencing micropore development in the Laochang mining area, eastern Yunnan, China. *J. Pet. Sci. Eng.* 190, 107090. doi:10.1016/j.petrol.2020.107090

Zhang, X., Wu, C., and Wang, Z. (2019a). Experimental study of the effective stress coefficient for coal permeability with different water saturations. *J. Pet. Sci. Eng.* 182, 106282. doi:10.1016/j.petrol.2019.106282

frontiers | Frontiers in Earth Science

TYPE Original Research
PUBLISHED 07 July 2023
DOI 10.3389/feart.2023.1185936

OPEN ACCESS

EDITED BY
Peng Tan,
CNPC Engineering Technology R&D Company Limited, China

REVIEWED BY
Jie Chi,
China University of Petroleum (Huadong), China
Ang Li,
Jilin University, China

*CORRESPONDENCE
Bo Zhang,
zhang_bo17@ctg.com.cn

RECEIVED 14 March 2023
ACCEPTED 14 April 2023
PUBLISHED 07 July 2023

CITATION
Wang Z, Zhang B, Yin L, Yang L, Fan Y, Yin H, Zhao P and Liu J (2023), The number of production wells affects the heat extraction performance of an enhanced geothermal system: insights from engineering-scale 3D THM coupling numerical simulations. *Front. Earth Sci.* 11:1185936. doi: 10.3389/feart.2023.1185936

The number of production wells affects the heat extraction performance of an enhanced geothermal system: insights from engineering-scale 3D THM coupling numerical simulations

Ziwei Wang[1], Bo Zhang[1,2]*, Likun Yin[1], Liming Yang[1], Yifan Fan[1], Hongmei Yin[1], Peng Zhao[3,4] and Jun Liu[4]

[1]Science and Technology Research Institute, China Three Gorges Corporation, Beijing, China, [2]Guizhou Branch, China Three Gorges Corporation, Guiyang, Guizhou, China, [3]State Key Laboratory of Geohazard Prevention and Geoenvironment Protection, Chengdu University of Technology, Chengdu, China, [4]Key Laboratory of Deep Underground Science and Engineering (Ministry of Education), Institute of New Energy and Low-Carbon Technology, Sichuan University, Chengdu, Sichuan, China

Enhanced geothermal systems (EGSs) are expected to be one of the most promising methods of supplying energy to meet the world's increasing energy demand. However, little attention has been paid to the influence of the number of production wells on the heat extraction performance of an EGS. A series of numerical simulations is organized in this work with three cases: Case 1 (one production well), Case 2 (two production wells), and Case 3 (three production wells). The results indicate that a slight temperature difference exists among the three simulation cases at the planes X-Y (Z = 0) and Y-Z (X = 0), while Case 1 ensures a greater cooling area, and the more production wells, the smaller the cooling area during the heat extraction in plane X-Z (Y = 0). In addition, the continuous injection of cooling water from the injection well and its arrival at different reference points enable the temperature at each point to declining with a variable amplitude of variation. This work also sets an efficiency (*ef*) to investigate the temperature variation in the EGS, where Case 1 exhibits a similar variation as Case 2, which is also similar to Case 3. It is hoped that this work will play a guiding role in EGS-related exploration and exploitation.

KEYWORDS

enhanced geothermal system, heat extraction performance, temperature variation, production well, numerical modeling

1 Introduction

Global energy consumption has experienced a sharp increase under the rapid development of the global economy, accompanied by the desire for green and low-carbon processes (Olasolo et al., 2016; Zheng et al., 2018; Zheng et al., 2019; Cheng et al., 2021; Zhao et al., 2022). In this context, unconventional oil/gas resources, such as shale oil/gas and tight sandstone gas, and clean energy, such as solar energy, wind energy, and enhanced geothermal systems (EGS), have emerged (Liu et al., 2017; Kumari and Ranjith, 2019; Hao et al., 2021; Lin et al., 2021; Steffen et al., 2021). Among them, the EGS is

assumed to have the potential to meet the increasing global energy demand as it is theoretically considered to be an infinite resource that is cheaper than conventional fuels and globally available (Lu, 2018; Zhao et al., 2023). This renewable energy resource needs to be supported by highly effective development. As an emerging technique, EGS has the advantage of promoting clean and low-carbon energy; therefore, much attention has been given to this technique, including attempts to guide EGS toward a commercially viable platform, including technology validation, cost reduction, and improved performance (Lu, 2018). Accordingly, many studies have revealed some sound and recognized achievements (Fairley et al., 2010; Olasolo et al., 2016).

EGS is no longer a new concept. It is also known as an engineered geothermal system. The terms hot dry rock (HDR) and hot sedimentary aquifers have been applied in previous research (Kuriyagawa and Tenma, 1999; Christ et al., 2017; Lu, 2018). Regarding the EGS-related work, preliminary investigations on the construction of an artificial geothermal reservoir and heat exchange and transport have been organized (Zhu et al., 2010; Feng et al., 2012). The heat extraction process in an EGS in the Songliao Basin of northeast China over 30 years was addressed, and the main influencing parameters were discussed (Huang et al., 2014; Huang et al., 2015). The variable EGS outcomes in long-term operation processes under different geological conditions were predicted (Chen et al., 2013a; Chen et al., 2013b). In addition, Gan et al. (2021) and Spycher and Pruess (2010)studied the EGS using CO_2 instead of water as a working fluid. The fracture network simulation methodologies were used to analyze the hydraulic fracturing process for an EGS reservoir (Wang and Zhang, 2011). Although these studies focused on different points, they have one thing in common: they all used numerical modeling. Having reviewed previous achievements in EGSs, it is noted that little attention has been paid to the influence of the number of production wells on the heat extraction performance, which may limit the deployment of the relative locations of injection wells for working fluid and production wells for heat extraction.

In recent years, numerical approaches have been widely adopted in geological resources research, especially for those working on an engineering scale, which is rarely conducted in an ordinary experimental setup (Fairley et al., 2010; Cheng et al., 2021; Liu et al., 2021; Zhao et al., 2021). In this work, numerical modeling is introduced to simulate the heat extraction process from an EGS system in which the number of production wells is set as a variable to evaluate their influence on the heat extraction performance. Here, the efficiency of heat extraction is also compared under different operating conditions for a quantitative investigation into how the number of production wells affects the heat extraction from an EGS. This numerical investigation is conducted on an engineering scale, offers a fresh perspective, and will provide guidance to a certain degree to the field of EGS-related exploration and exploitation.

2 Numerical model descriptions

On an engineering scale, this numerical work uses an HDR model with a size of X: 400 m × Y: 400 m × Z: 400 m, and the EGS is placed in the center of it with a size of X: 250 m × Y: 250 m × Z: 150 m (Figure 1). The roof and bottom of this simulated reservoir have a buried depth of 300 m and 600 m, respectively. To discuss how the number of production wells influences the heat extraction performance, an injection well and a production well are deployed in the EGS. Three cases are organized here, in which each model has one injection well with a 50 m length, and the coordinate of its midpoint is X: −100 × Y: 0 × Z: 0 (Figure 2). The origin point is located at the center of this EGS, as shown in Figure 1. Case 1 has one production well, and the coordinate of its midpoint is X: 100 × Y: 0 × Z: 0; Case 2 has two production wells, and the coordinates of its midpoints are X: 100 × Y: 50 × Z: 0 and X: 100 × Y: −50 × Z: 0, respectively (Figure 2). For Case 3, three production wells are set, and the coordinates of the midpoints are X: 100 × Y: 50 × Z: 0, X: 100 × Y: 0 × Z: 0, and X: 100 × Y: −50 × Z: 0, respectively (Figure 2).

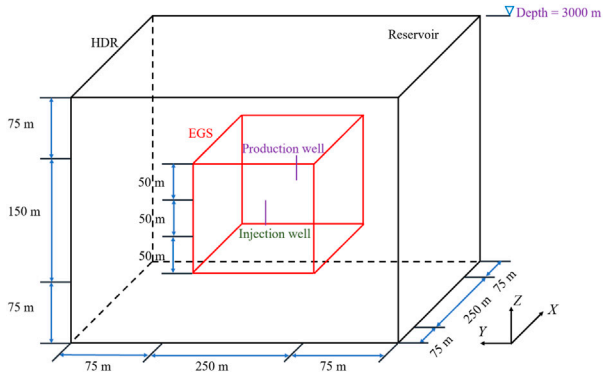

FIGURE 1
Numerical model used in this work.

3 Governing equations for model development

3.1 Model assumptions

To simulate the process of heat extraction from HDR, a 3D thermo-hydro-mechanical (THM) coupling model is developed in this study using several assumptions regarding fluid flow and heat transfer (Aliyu and Chen, 2017; Ye et al., 2021; Zhou et al., 2022; Huang et al., 2023).

(1) In the heat extraction process, water is utilized as the working fluid and exists in liquid form in the pores.
(2) The original EGS is treated as saturated with water. Fluid flow in the matrix is laminar flow and yields Darcy's law.
(3) Fourier's law describes the heat transfer process in the matrix. Local thermal equilibrium is assumed between the working fluid and rock mass.

These assumptions are widely set forth in the numerical studies of EGSs (Lu, 2018; Zhao et al., 2023) and are treated as reasonable conditions.

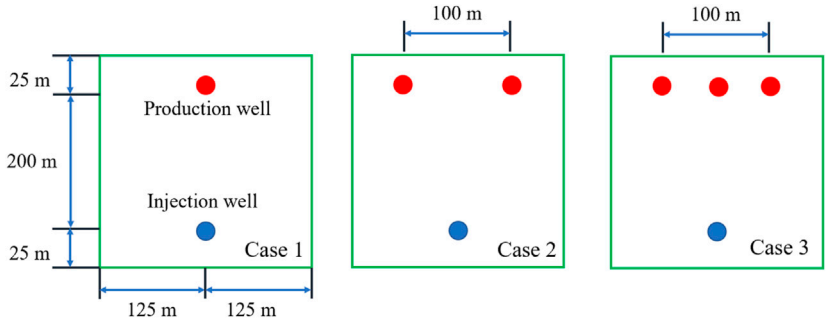

FIGURE 2
Description of the modeling cases for the EGS injection well platform.

3.2 Governing equations

The primary governing equations of this model for the simulated process of heat extraction are as follows (Sun et al., 2019; Han et al., 2020; Aliyu and Archer, 2021; Tan et al., 2021; Yu et al., 2021; Zinsalo et al., 2021; Zhou et al., 2022; Zhao et al., 2023):

In the seepage field, the working fluid flow in the porous medium is described by the mass conservation law. In Eq. 1.,

$$S\frac{\partial p}{\partial t} + \nabla \cdot q = -Q_f, \tag{1}$$

where S is the storage coefficient of the rock matrix, Pa^{-1}; p is the pore pressure, Pa; t is the time, s; q is the Darcy velocity, m/s; q_f is the Darcy velocity in the fracture, m/s; and Q_f is the source, 1/s.

In addition, the expressions of q are determined by Darcy's law.

$$q = -\frac{k}{\mu_f}\nabla \cdot (p + \rho_w g z), \tag{2}$$

where k is the permeability of the rock matrix, m^2; μ_f is the dynamic fluid viscosity, Pa·s; ρ_w is the fluid density, kg/m^3; g is the gravitational acceleration, m/s^2; and z is the unit vector in the vertical direction.

In the temperature field, the heat exchange between the rock surface and the cryogenic fluid is described by the local thermal equilibrium. The temperatures of the solid and the liquid are the same at each position. Then, based on the energy conservation law, the governing equations of the temperature field are written as [27]:

$$\left(\rho c_p\right)_m \frac{\partial T}{\partial t} + \nabla \cdot \left(\rho_w c_{p,w} q T\right) - \nabla \cdot (\lambda_m \nabla T) = -Q_{f,E}, \tag{3}$$

where T is the temperature, K; $c_{p,w}$ is the heat capacity of the fluid, J/(kg·K); $Q_{f,E}$ is the heat source, W/m^3; $(\rho c_p)_m$ is the effective volumetric heat capacity of the matrix, $J/(m^3 \cdot K)$; and λ_m is the effective thermal conductivity of the matrix, W/(m·K).

$$\left(\rho c_p\right)_m = (1-\varphi)\rho_s c_{p,s} + \varphi \rho_w c_{p,w}, \tag{4}$$

$$\lambda_m = (1-\varphi)\lambda_s + \varphi \lambda_w, \tag{5}$$

where φ is the porosity of the matrix; ρ_s is the solid density, (kg/m^3); $c_{p,s}$ is the solid heat capacity, J/(kg·K); and λ_s and λ_w are the thermal conductivities of the solid and the fluid, respectively, W/(m·K).

3.3 Effect of temperature on the properties of water

Some physical properties of water are determined by the temperature, such as the dynamic fluid viscosity (μ_f), the heat capacity ($c_{p,w}$), the thermal conductivities (λ_w), and the density (ρ_w). The relationships between the temperature and the physical properties are expressed as follows (Sun et al., 2019; Han et al., 2020; Aliyu and Archer, 2021; Yu et al., 2021; Zinsalo et al., 2021; Zhou et al., 2022; Zhao et al., 2023):

$$\mu_f = \begin{cases} 1.3799 - 0.0212T + 1.3604 \times 10^{-4}T^2 - 4.6454 \times 10^{-7}T^3 + 8.9043 \times 10^{-10}T^4 \\ -9.0791 \times 10^{-13}T^5 + 3.8457 \times 10^{-16}T^6 \quad 273.15K \le T \le 413.15K \\ 0.004 - 2.1075 \times 10^{-5}T + 3.8577 \times 10^{-8}T^2 - 2.3973 \times 10^{-11}T^3 \quad 413.15K \le T \le 573.15K, \end{cases} \tag{6}$$

$$c_{p,w} = 12010 - 80.4T + 0.3T^2 - 5.4 \times 10^{-4}T^3 + 3.6 \times 10^{-7}T^4 \quad 273.15K \le T \le 573.15K, \tag{7}$$

$$\lambda_w = 7.9754 \times 10^{-9}T^3 - 1.5837 \times 10^{-5}T^2 + 0.0089T - 0.8691 \quad 273.15K \le T \le 573.15K, \tag{8}$$

$$\rho_w = 838.4661 + 1.4005T - 3 \times 10^{-3}T^2 - 3.7182 \times 10^{-7}T^3 \quad 273.15K \le T \le 573.15K. \tag{9}$$

The initial and boundary conditions of the numerical model mentioned in this work are listed in Table 1, and all modeling cases were run for 30 years during this simulated process. The primary reservoir physical parameters are exhibited in Table 2. Here, the initial/boundary conditions and properties are referred to from previous achievements (Sun et al., 2019; Han et al., 2020; Aliyu and Archer, 2021; Yu et al., 2021; Zinsalo et al., 2021; Zhou et al., 2022; Zhao et al., 2023).

4 Mathematical results and discussion

The temperature is an important parameter to evaluate the heat extraction performance of an EGS (Majorowicz and Grasby, 2010; Rodriguez et al., 2013; Fallah et al., 2016; Guo et al., 2018; Yang et al., 2021). Therefore, in this work, the temperature of the EGS system is introduced to compare the heat extraction performance during the EGS utilization, where water is adopted as the working fluid. Here, the overall situation of the temperature in the whole EGS is investigated, and then three reference points in the EGS are set

TABLE 1 Initial and boundary conditions employed for the simulations.

Physical field	Boundary	Initial and boundary conditions
Seepage field	Initial pressure	30 MPa
	Injection rate	10 kg/s
	Production pressure	20 MPa
	Upper and lower boundaries	Impermeable
Temperature field	Initial temperature	473.15 K
	Injection temperature	303.15 K
	Upper and lower boundaries	Thermal insulation

TABLE 2 Physical properties of the reservoir.

Parameter	Value	Unit
Matrix density	2,700	kg/m^3
Matrix porosity	0.2	-
Matrix permeability	5e−15	m^2
Matrix heat capacity	950	J/(kg·K)
Matrix thermal conductivity	2.8	W/(m·K)
Fluid compressibility	1e-8	1/Pa
Biot coefficient	1	-

to determine the detailed variation for specific operation cases. Then, the temperature changes in the whole system for three simulated cases are compared.

4.1 Overall temperature variation tendency in an EGS for variable simulated cases

In this 3D numerical model, three planes were selected to demonstrate the variation tendency of temperature in the EGS: plane X-Y (Z = 0), plane Y-Z (X = 0), and plane X-Z (Y = 0); the coordinate system is shown in Figure 1. Here, these three planes are selected to show the temperature variation tendency in different directions for different simulated cases in this work.

1) X-Y plane

The X-Y plane is a slide that is perpendicular to the wellbore of the injection/production well. This work is set to investigate the temperature variation in the horizontal direction of the EGS. For all operation cases, the cooling area increases with time after water is injected into the injection well, and there is a tendency for the area to be extended from the injection well to the production well (Figure 3). However, by comparison, no matter the number of production wells (1, 2, or 3), the temperature variation in the X-Y plane seems to have a similar extension tendency, in which the difference is not obvious among all simulated cases. This could be due to two reasons: 1) for each case, the amount of injected water is the same in this numerical process, where the injection rate stabilizes at 10 kg/s, and 2) the low permeability of the EGS means that the injected, relatively low-temperature water does not travel far to hardly transport large-scale and makes the water seepage affected by the water extracted from the production well. From an intuitive perspective, the number of production wells barely affects the horizontal temperature variation for an EGS that is not fractured.

2) X-Z plane

The X-Z plane is a slide that penetrates the injection well and the EGS center, where Y = 0 in Figure 2. Here, this perspective is introduced to investigate the temperature variation along the direction from the injection well to the production well as shown in Figure 4. Generally, the cooling area increases after the injection, and this area tends to spread in the direction of the production well. Similar to the situation in the X-Y plane (Figure 3), the difference between the three simulations is not obvious in the X-Z plane. The reason for this phenomenon is similar to the analysis for the X-Y plane investigation.

3) Y-Z plane

The Y-Z plane is a slide with the X value set to 0 in the coordinate system in Figure 1, which is across the center of the EGS. From the exhibit in Figure 5, the continuous injection of water from the injection well enables the cooling area to increase with time. In addition, the area involved among the three cases differs under the condition of injecting the same amount of water from the injection well but with different production well settings. Compared with the aforementioned X-Y plane and the X-Z plane, there is a clear difference in temperature variation among the three cases, where one production well ensures a larger cooling area, and the more production wells, the smaller the cooling area during the heat extraction. Furthermore, because the difference between the X-Y plane and the X-Z plane is not obvious, it could be speculated that the temperature variation difference induced by the production well mainly occurs in the Y-Z plane, and this variation could cause the volume difference in the cooled rock during the heat extraction.

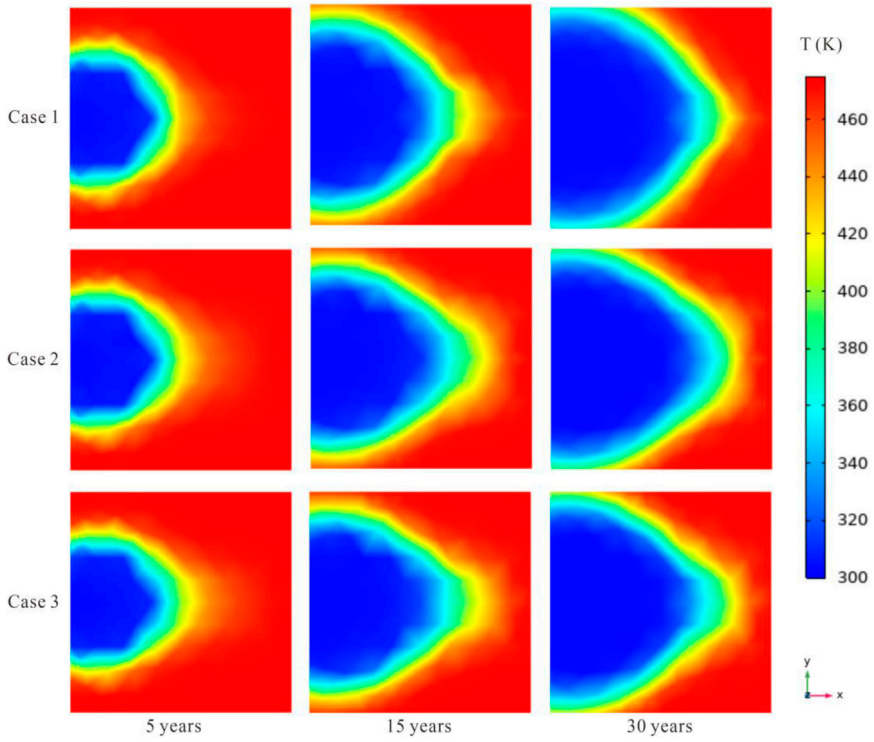

FIGURE 3
Temperature variation in the X-Y plane (Z = 0) during the heat extraction (coordinate system is shown in Figure 1).

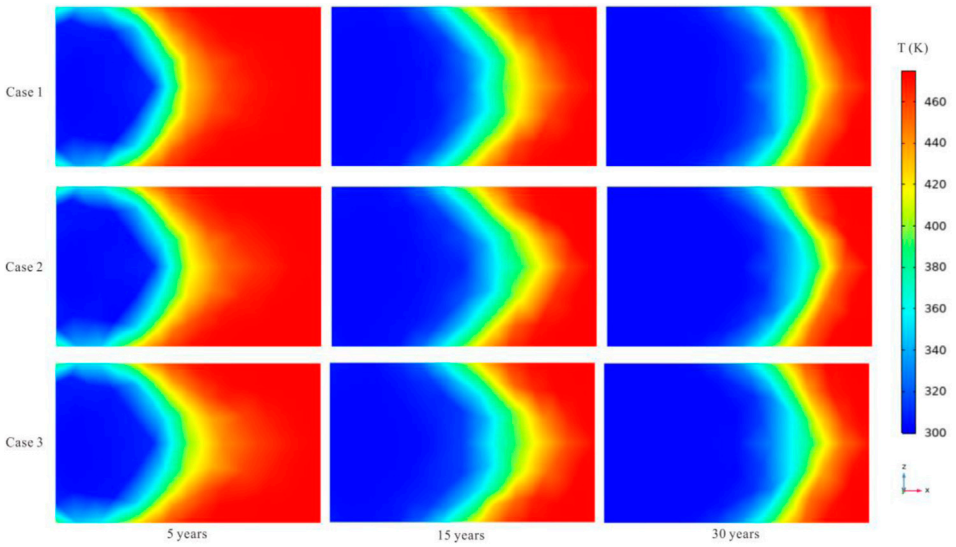

FIGURE 4
Temperature variation in the X-Z plane (Y = 0) during the heat extraction (coordinate system is shown in Figure 1).

4.2 Variation of temperature at reference points in an EGS for variable simulated cases

To further exhibit the temperature variation in different simulation cases, three reference points are chosen to quantitatively investigate the dynamic change in temperature during heat extraction. Here, the reference points are (X = 100: Y = 50: Z = 25), (X = 100: Y = 0: Z = 25), and (X = 100: Y = −50: Z = 25), using the coordinate system shown in Figure 1. The temperature variations at three representative points are shown in Figures 6–8, respectively.

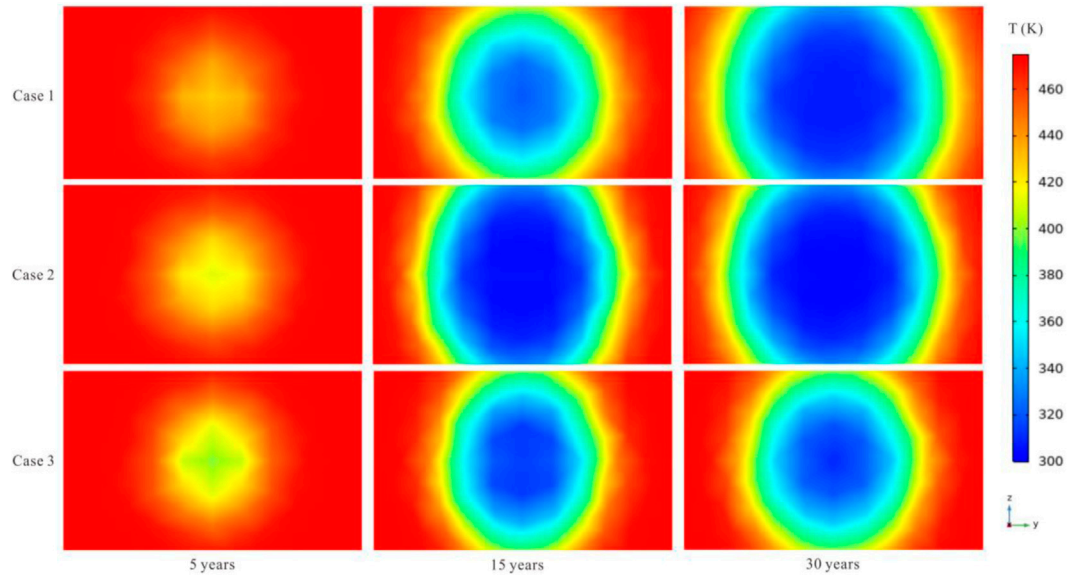

FIGURE 5
Temperature variation in the Y-Z plane (X = 0) during the heat extraction (coordinate system is shown in Figure 1).

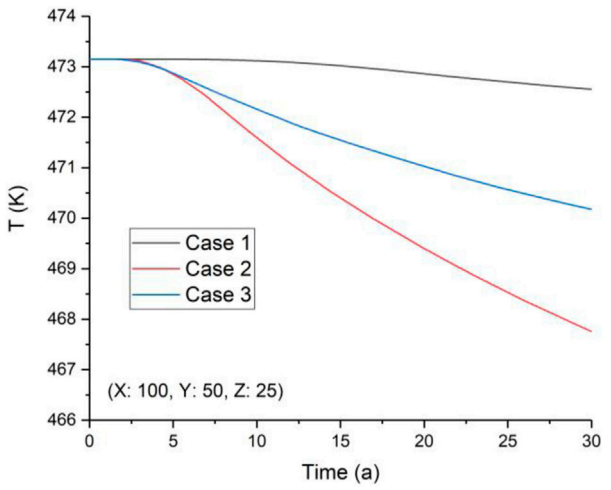

FIGURE 6
Variation of reference point temperature at (X = 100: Y = 50: Z = 25) (coordinate system is shown in Figure 1).

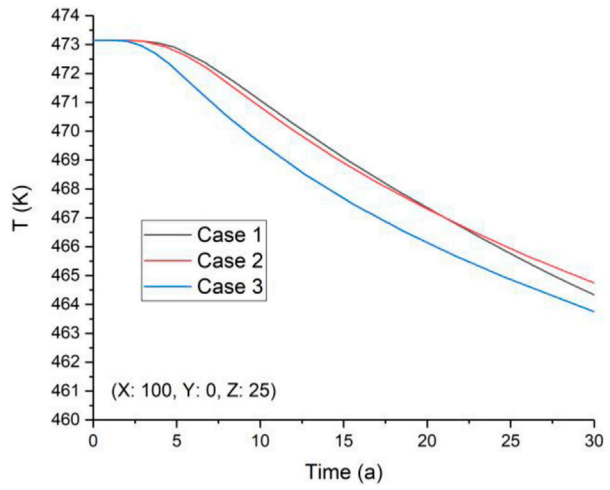

FIGURE 7
Variation of reference point temperature at (X = 100: Y = 0: Z = 25) (coordinate system is shown in Figure 1).

The temperature varies sparingly in the first ~3 years at each reference point for every simulation case (Figures 6–8) because the injected cooling water has not yet arrived at that point and the hot water extracted from the production well slightly affects the EGS temperature. Afterward, with the continuous injection of cooling water and its arrival at the reference points, the temperature there begins to decline with a variable amplitude of variation. At the point where (X = 100: Y = 50: Z = 25), for Case 1, the temperature experiences a small variation during the total heat extraction period because the water pressure difference between the injection well and the production well drives the cooling water to flow toward the production well. Therefore, in Case 1, point (X = 100: Y = 50: Z = 25) receives little of the injected cooling water, and the temperature there remains almost constant (Figure 6). However, for Case 2 and Case 3, the injected cooling water arrives at point (X = 100: Y = 50: Z = 25) because the hot water extracted from the production well induces the cooling water seepage toward this point. In Case 2, more cooling water flows to the point (X = 100: Y = 50: Z = 25) than in Case 3. This phenomenon occurs because the injected cooling water tends to flow toward the production well due to the fluid pressure difference, and more cooling water flows toward the point (X =

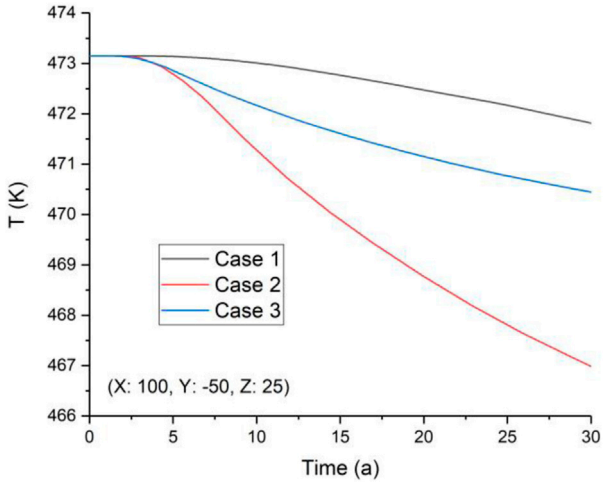

FIGURE 8
Variation of reference point temperature at (X = 100: Y = −50: Z = 25) (coordinate system is shown in Figure 1).

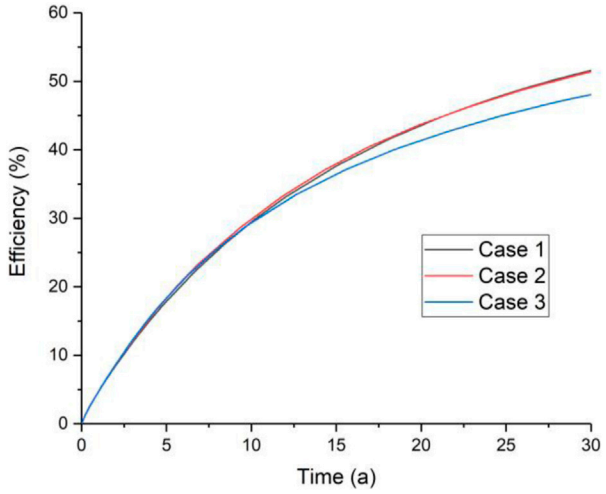

FIGURE 9
Heat extraction efficiency (*ef*) over 30 years of numerical simulations for each case.

100: Y = 50: Z = 25) in Case 2 because the middle production well in Case 3 has a tendency to shunt the injected cooling water (Figure 6).

As for the point where (X = 100: Y = 0: Z = 25) in the three cases, the temperature variation follows a similar rule and undergoes a similar tendency (Figure 7). This is because, at the point where (X = 100: Y = 0: Z = 25), the cooling water has a similar seepage space and flow condition to reach this point, indicating that the fluid pressure difference between the injection well and the point (X = 100: Y = 0: Z = 25) is similar in both simulation cases in this work. Moreover, for point (X = 100: Y = −50: Z = 25), the temperature variation there (Figure 8) is similar to the phenomenon at the point where (X = 100: Y = 50: Z = 25) (Figure 6), and the mechanism is also similar to the previous one.

4.3 Attenuation process of temperature in the whole EGS

In this work, following the previous work (Zhao et al., 2023), a heat extraction efficiency (denoted as *ef*) is introduced to investigate the attenuation process during the temperature variation in the EGS, which represents the heat recovery divided by the total heat stored in the EGS and yields:

$$e_f = \frac{\iiint_{V_s} \rho_s c_{p,s} (T_0 - T) dV}{\iiint_{V_s} \rho_s c_{p,s} (T_0 - T_{inj}) dV} \tag{10}$$

where V_S means the heat extraction zone in the EGS, T_0 is the initial temperature, and T_{inj} is the injection temperature of the fluid (namely, the cooling water).

According to Eq. 10, the *ef* performance for each numerical case is exhibited in Figure 9. Per the calculation results (Figure 9), little difference is demonstrated among the variable simulations. For all cases, the *ef* tends to increase faster during the first 15 years and experiences a relatively slower increase during the last 15 years. During the heat extraction process, Case 1 and Case 2 show a similar variation regarding the *ef*, while Case 3 has a slightly lower *ef* than Case 1 and Case 2. This phenomenon is unexpected because the temperature difference in representative slides or points exhibited a difference among the three cases (Figures 5–8). Therefore, this work speculates that there is a complicated coupling process in the EGS regarding the temperature variation during the heat extraction process that will require more attention.

5 Conclusion

This work reports on three cases to investigate the influence of the number of production wells on the heat extraction performance of an EGS system. The temperature variation with respect to the representative slides and reference points is systematically investigated for Case 1, Case 2, and Case 3. Furthermore, the *ef* is introduced and defined to represent the temperature variation of the EGS. Accordingly, the following points are made:

For the plane X-Y (Z = 0), plane Y-Z (X = 0), and plane X-Z (Y = 0), the temperature variation during the heat extraction process from the EGS is hardly different among the three simulation cases at the plane X-Y (Z = 0) and plane Y-Z (X = 0). Moreover, the results show that one production well (Case 1) ensures a larger cooling area, and the more production wells in a field (Case 2 and Case 3), the smaller the cooling area during the heat extraction in the X-Z plane (Y = 0).

Based on the investigation of the points of (X = 100: Y = 50: Z = 25), (X = 100: Y = 0: Z = 25), and (X = 100: Y = −50: Z = 25), the continuous injection of cooling water and its arrival at the reference points allow the temperature at each point to begin to decrease with a variable amplitude of variation. Relatively, the difference of temperature variation at points (X = 100: Y = 50: Z = 25) and

(X = 100: Y = −50: Z = 25) is greater among three numerical cases, while that at point (X = 100: Y = 0: Z = 25) is smaller.

Regarding the *ef*, Case 1 exhibits the same variation as Case 2, which is also similar to that of Case 3. This indicates that the number of production wells during the heat extraction has little influence on the *ef* for an EGS, even though temperature differences exist on the representative slides or reference points. This issue may be due to a complicated coupling process, and this possibility requires additional investigation.

Data availability statement

The original contributions presented in the study are included in the article/supplementary material; further inquiries can be directed to the corresponding author.

Author contributions

ZW, BZ, and JL organized the project. PZ, BZ, LkY, and LmY conducted the numerical simulations. HY, PZ, and JL performed the data analysis. PZ, ZW, and JL wrote the manuscript. JL revised the manuscript. All authors contributed to the discussions.

Funding

This study was financially supported by the Science and Technology Department of Sichuan Province (Grant No. 2021YFH0118), the Natural Science Foundation of Chongqing, China (No. CSTB2022NSCQ-BHX0721), and the project funded by the China Postdoctoral Science Foundation (Grant No. 2022T150774).

Conflict of interest

Authors ZW, BZ, LkY, LmY, YF, and HY are employed by China Three Gorges Corporation.

The remaining authors declare that the research was conducted in the absence of any commercial or financial relationships that could be construed as a potential conflict of interest.

Publisher's note

References

Aliyu, M., and Archer, R. A. (2021). A thermo-hydro-mechanical model of a hot dry rock geothermal reservoir. *Renew. Energy* 176, 475–493. doi:10.1016/j.renene.2021.05.070

Aliyu, M., and Chen, H. (2017). Optimum control parameters and long-term productivity of geothermal reservoirs using coupled thermo-hydraulic process modelling. *Renew. Energy* 112, 151–165. doi:10.1016/j.renene.2017.05.032

Chen, J., Jiang, F., Luo, L., Zacharek, A., Cui, X., Cui, Y., et al. (2013). Neuroprotective effect of human placenta-derived cell treatment of stroke in rats. *Chin. J. Comput. Phys.* 30, 871–879. doi:10.3727/096368911X637380

Chen, J., Lou, L., and Jiang, F. (2013). Thermal compensation of rocks encircling heat reservoir in heat extraction of enhanced geothermal system. *Chin. J. Comput. Phys.* 30, 862–870.

Cheng, L., Li, D., Wang, W., and Liu, J. (2021). Heterogeneous transport of free CH_4 and free CO_2 in dual-porosity media controlled by anisotropic *in situ* stress during shale gas production by CO_2 flooding: Implications for CO_2 geological storage and utilization. *ACS Omega* 6, 26756–26765. doi:10.1021/acsomega.1c04220

Christ, A., Rahimi, B., Regenauer-Lieb, K., and Chua, H. T. (2017). Techno-economic analysis of geothermal desalination using hot sedimentary aquifers: A pre-feasibility study for western Australia. *Desalination* 404, 167–181. doi:10.1016/j.desal.2016.11.009

Fairley, J. P., Ingebritsen, S. E., and Podgorney, R. K. (2010). Challenges for numerical modeling of enhanced geothermal systems. *Ground Water* 48, 482–483. doi:10.1111/j.1745-6584.2010.00716.x

Fallah, M., Mohammad, S., Mahmoudi, S., and Akbarpour Ghiasi, R. (2016). Advanced exergy analysis of the Kalina cycle applied for low temperature enhanced geothermal system. *Energy Convers. Manag.* 108, 190–201. doi:10.1016/j.enconman.2015.11.017

Feng, Z., Zhao, Y., Zhou, A., and Zhang, N. (2012). Development program of hot dry rock geothermal resource in the Yangbajing Basin of China. *Renew. Energy* 39, 490–495. doi:10.1016/j.renene.2011.09.005

Gan, Q., Candela, T., Wassing, B., Wasch, L., Liu, J., and Elsworth, D. (2021). The use of supercritical CO_2 in deep geothermal reservoirs as a working fluid: Insights from coupled THMC modeling. *Int. J. Rock Mech. Min. Sci.* 147, 104872. doi:10.1016/j.ijrmms.2021.104872

Guo, L. L., Zhang, Y. B., Zhang, Y. J., Yu, Z. W., and Zhang, J. N. (2018). Experimental investigation of granite properties under different temperatures and pressures and numerical analysis of damage effect in enhanced geothermal system. *Renew. Energy* 126, 107–125. doi:10.1016/j.renene.2018.02.117

Han, S., Cheng, Y., Gao, Q., Yan, C., and Zhang, J. (2020). Numerical study on heat extraction performance of multistage fracturing Enhanced Geothermal System. *Renew. Energy* 149, 1214–1226. doi:10.1016/j.renene.2019.10.114

Hao, L., Zhou, M., Song, Y., Ma, X., Wu, J., Zhu, Q., et al. (2021). Tin-based perovskite solar cells: Further improve the performance of the electron transport layer-free structure by device simulation. *Sol. Energy* 230, 345–354. doi:10.1016/j.solener.2021.09.091

Huang, L. K., He, R., Yang, Z. Z., Tan, P., Chen, W., Li, X., et al. (2023). Exploring hydraulic fracture behavior in glutenite formation with strong heterogeneity and variable lithology based on DEM simulation. *Eng. Fract. Mech.* 278, 109020. doi:10.1016/j.engfracmech.2022.109020

Huang, X., Zhu, J., and Li, J. (2015). "Analysis of wellbore heat transfer in enhanced geothermal system using CFD modeling," in Proceedings of the world geothermal congress 2015, April 2015, Melbourne, Australia.

Huang, X., Zhu, J., Niu, C., Li, J., and Jin, X. (2014). Heat extraction and power production forecast of a prospective enhanced geothermal system site in Songliao Basin, China. *Energy* 75, 360–370. doi:10.1016/j.energy.2014.07.085

Kumari, W., and Ranjith, P. G. (2019). Sustainable development of enhanced geothermal systems based on geotechnical research – a review. *Earth-Science Rev.* 199, 102955. doi:10.1016/j.earscirev.2019.102955

Kuriyagawa, M., and Tenma, N. (1999). Development of hot dry rock technology at the Hijiori test site. *Geothermics* 28, 627–636. doi:10.1016/s0375-6505(99)00033-4

Lin, T., Liu, X., Zhang, J., Bai, Y., Liu, J., Zhang, Y., et al. (2021). Characterization of multi-component and multi-phase fluids in the Upper Cretaceous oil shale from the Songliao basin (NE China) using T_1–T_2 NMR correlation maps. *Petroleum Sci. Technol.* 39, 1060–1070. doi:10.1080/10916466.2021.1990318

Liu, J., Xie, L. Z., He, B., Gan, Q., and Zhao, P. (2021). Influence of anisotropic and heterogeneous permeability coupled with *in-situ* stress on CO_2 sequestration with simultaneous enhanced gas recovery in shale: Quantitative modeling and case study. *Int. J. Greenh. Gas Control* 104, 103208. doi:10.1016/j.ijggc.2020.103208

Liu, J., Yao, Y., Liu, D., and Elsworth, D. (2017). Experimental evaluation of CO_2 enhanced recovery of adsorbed-gas from shale. *Int. J. Coal Geol.* 179, 211–218. doi:10.1016/j.coal.2017.06.006

Lu, S. M. (2018). A global review of enhanced geothermal system (EGS). *Renew. Sustain. Energy Rev.* 81, 2902–2921. doi:10.1016/j.rser.2017.06.097

Majorowicz, J., and Grasby, S. E. (2010). Heat flow, depth-temperature variations and stored thermal energy for enhanced geothermal systems in Canada. *J. Geophys. Eng.* 7, 232–241. doi:10.1088/1742-2132/7/3/002

Olasolo, P., Juárez, M., Olasolo, J., Morales, M., and Valdani, D. (2016). Economic analysis of Enhanced Geothermal Systems (EGS). A review of software packages for estimating and simulating costs. *Appl. Therm. Eng.* 104, 647–658. doi:10.1016/j.applthermaleng.2016.05.073

Rodriguez, C. E. C., Palacio, J. C. E., Venturini, O. J., Silva Lora, E. E., Cobas, V. M., Marques dos Santos, D., et al. (2013). Exergetic and economic comparison of ORC and Kalina cycle for low temperature enhanced geothermal system in Brazil. *Appl. Therm. Eng.* 52, 109–119. doi:10.1016/j.applthermaleng.2012.11.012

Spycher, N., and Pruess, K. (2010). A phase-partitioning model for CO_2-brine mixtures at elevated temperatures and pressures: Application to CO_2-enhanced geothermal systems. *Transp. Porous Media* 82, 173–196. doi:10.1007/s11242-009-9425-y

Steffen, J., Lengsfeld, S., Jung, M., Ponick, B., Herranz Gracia, M., Spagnolo, A., et al. (2021). Design of a medium voltage generator with DC-cascade for high power wind energy conversion systems. *Energies* 14, 3106. doi:10.3390/en14113106

Sun, X., Liao, Y., Wang, Z., and Sun, B. (2019). Geothermal exploitation by circulating supercritical CO_2 in a closed horizontal wellbore. *Fuel* 254, 115566. doi:10.1016/j.fuel.2019.05.149

Tan, P., Jin, Y., and Pang, H. W. (2021). Hydraulic fracture vertical propagation behavior in transversely isotropic layered shale formation with transition zone using XFEM-based CZM method. *Eng. Fract. Mech.* 248, 107707. doi:10.1016/j.engfracmech.2021.107707

Wang, Y., and Zhang, K. (2011). Modeling approaches for fractures in enhanced geothermal system (EGS). *Shanghai Land Resour.* 32, 77–80.

Yang, R. Y., Hong, C. Y., Liu, W., Wu, X., Wang, T., and Huang, Z. (2021). Non-contaminating cryogenic fluid access to high-temperature resources: Liquid nitrogen fracturing in a lab-scale Enhanced Geothermal System. *Renew. Energy* 165, 125–138. doi:10.1016/j.renene.2020.11.006

Ye, Z., Wang, J., and Hu, B. (2021). Comparative study on heat extraction performance of geothermal reservoirs with presupposed shapes and permeability heterogeneity in the stimulated reservoir volume. *J. Petroleum Ence Eng.* 206, 109023. doi:10.1016/j.petrol.2021.109023

Yu, P., Dempsey, D., and Archer, R. (2021). A three-dimensional coupled thermo-hydro-mechanical numerical model with partially bridging multi-stage contact fractures in horizontal-well enhanced geothermal system. *Int. J. Rock Mech. Min.* 143, 104787. doi:10.1016/j.ijrmms.2021.104787

Zhao, P., He, B., Zhang, B., and Liu, J. (2022). Porosity of gas shale: Is the NMR-based measurement reliable? *Petroleum Sci.* 19, 509–517. doi:10.1016/j.petsci.2021.12.013

Zhao, P., Liu, J., and Elsworth, D. (2023). Numerical study on a multifracture enhanced geothermal system considering matrix permeability enhancement induced by thermal unloading. *Renew. Energy* 203, 33–44. doi:10.1016/j.renene.2022.12.056

Zhao, P., Xie, L. Z., He, B., and Liu, J. (2021). Anisotropic permeability influencing the performance of free CH_4 and free CO_2 during the process of CO_2 sequestration and enhanced gas recovery (CS-EGR) from shale. *ACS Sustain. Chem. Eng.* 9, 914–926. doi:10.1021/acssuschemeng.0c08058

Zheng, S. J., Yao, Y. B., Liu, D. M., and Cai, Y. (2018). Characterizations of full-scale pore size distribution, porosity and permeability of coals: A novel methodology by nuclear magnetic resonance and fractal analysis theory. *Int. J. Coal Geol.* 196, 148–158. doi:10.1016/j.coal.2018.07.008

Zheng, S. J., Yao, Y. B., Liu, D. M., Cai, Y., and Li, X. (2019). Nuclear magnetic resonance T_2 cutoffs of coals: A novel method by multifractal analysis theory. *Fuel* 241, 715–724. doi:10.1016/j.fuel.2018.12.044

Zhou, L., Zhu, Z., Xie, X., and Hu, Y. (2022). Coupled thermal-hydraulic-mechanical model for an enhanced geothermal system and numerical analysis of its heat mining performance. *Renew. Energy* 181, 1440–1458. doi:10.1016/j.renene.2021.10.014

Zhu, L., Chen, W., Li, W., et al. (2010). Experiment of stainless corrosion and scaling in geothermal water supply pipeline. *J. Jiangsu Univ. Nat. Sci. Ed.* 31, 292–295.

Zinsalo, J., Lamarche, L., and Raymond, J. (2021). Design and optimization of multiple wells layout for electricity generation in a multi-fracture enhanced geothermal system. *Sustain Energy Techn* 47, 101365. doi:10.1016/j.seta.2021.101365

frontiers | Frontiers in Environmental Science

TYPE Original Research
PUBLISHED 27 July 2023
DOI 10.3389/fenvs.2023.1244543

OPEN ACCESS

EDITED BY
Shiming Wei,
China University of Petroleum, China

REVIEWED BY
Can Shi,
Chengdu University of Technology, China
Zhi Chang,
CNPC Engineering Technology R & D Company Limited, China

*CORRESPONDENCE
Guangming Zhang,
1849798714@qq.com

RECEIVED 22 June 2023
ACCEPTED 17 July 2023
PUBLISHED 27 July 2023

CITATION
Liu W and Zhang G (2023), Enhancing oil-water flow simulation in shale reservoirs with fractal theory and meshless method. *Front. Environ. Sci.* 11:1244543. doi: 10.3389/fenvs.2023.1244543

Enhancing oil-water flow simulation in shale reservoirs with fractal theory and meshless method

Wenbo Liu and Guangming Zhang*

School of Petroleum Engineering, Yangtze University, Wuhan, China

Introduction: Simulating oil and water flow in shale reservoirs is challenging due to heterogeneity caused by fractures. Conventional grid-based methods often have convergence issues. We propose a new approach using fractal theory and meshless methods to accurately model flow.

Methods: A mathematical model describing oil-water flow in fractured horizontal shale wells was developed. The meshless weighted least squares (MWLS) method was used to numerically solve the model. Modeling points were placed flexibly, informed by fractal theory.

Results: The MWLS solution aligned well with reference solutions but had enhanced flexibility. Comprehensive analysis showed the effects of modeling parameters like fracture properties on production.

Discussion: The proposed methodology enabled accurate prediction of shale oil production. Convergence was improved compared to grid-based methods. The flexible modeling approach can be tailored to specific reservoir conditions. Further work could expand the model complexity and types of reservoirs.

KEYWORDS

shale reservoir, oil-water flow, MWLS method, multi-fractured horizontal well, reservoir simulation

1 Introduction

Shale oil is an unconventional type of oil found in organic-rich black shale or nanoscale pores in shale. With vast reserves distributed worldwide, shale oil has become the most promising unconventional oil resource for development. However, shale oil reservoirs exhibit low matrix pore permeability and significant heterogeneity (Jia et al., 2019). Consequently, low fracture flowback rates often occur during the flowback process (Zhang et al., 2019), making accurate prediction of the oil and water flow in shale reservoirs crucial (Daneshy, 2004; Bertoncello et al., 2014; Su et al., 2016).

Due to the multi-scale nature and complex fluid distribution in shale oil reservoirs, traditional Darcy flow equations are insufficient for accurately depicting their flow characteristics. Researchers have adopted apparent porosity and permeability models to characterize the unique migration mechanisms in shales. These models can be grouped into three primary categories: Javadour models (based on fracture aperture) (Javadpour, 2009; Akkutlu et al., 2015; Singh and Javadpour, 2016), Civan models (based on the Knudsen number) (Civan, 2010; Wu et al., 2015; Song et al., 2016), Civan models (based on the Knudsen number) (Mason et al., 1983; Li et al., 2017; Zeng et al., 2017). In the study of oil

behavior within nanopores, researchers have explored the use of organic/inorganic apparent porosity models. These models offer a valuable approach to characterize the oil state within nanopores, considering the influence of both organic and inorganic components. By incorporating the concept of apparent porosity, researchers aim to gain a deeper understanding of the distribution and behavior of oil within these nanoscale spaces (Sheng et al., 2019; Sheng et al., 2020). Furthermore, integrating the conventional dual-medium model with apparent permeability/porosity models has been found to provide a more accurate depiction of shale oil flow behavior (Sheng et al., 2018).

The heterogeneity of porosity and permeability in shale oil reservoirs poses challenges for numerical simulation, such as high computational costs and poor convergence (Li et al., 2023). Conventional grid-based finite difference methods are complex and not suitable for complex boundary conditions. Wei (Wei et al., 2021a) proposed a discontinuous discrete fracture model for coupled flow and geomechanics and used the finite element method to optimize the reservoir stress evolution (Shiming et al., 2022) and fracturing schemes for encrypted wells throughout the drilling-fracturing-producing wells (Wei et al., 2021b). Finite element meshes may experience severe distortion, requiring remeshing, which increases computational time and significantly affects accuracy. Describing complex geometric computational domains becomes cumbersome as further mesh refinement complicates preprocessing. Finite difference/volume methods are known for their accuracy; however, they have limitations when it comes to grid uniformity. High-precision difference schemes are often designed for regular Cartesian grids, which poses challenges when dealing with complex boundaries or reservoirs with intricate geological conditions. As a result, handling such situations becomes difficult using traditional finite difference/volume methods (Rao et al., 2020; Rao et al., 2022). Given the limitations of conventional numerical methods in simulating shale oil reservoirs, the meshless method emerges as a promising and efficient alternative. This method entails positioning points throughout the reservoir area to precisely delineate the intricate boundary of the shale oil reservoir. In this manner, the meshless technique develops a potent numerical model to emulate the movement of oil and water inside the shale oil deposit.

Introduced by Lucy in 1977, the Smoothed Particle Hydrodynamics (SPH) method is a mesh-free approach that has found success in addressing astrophysical problems. This method has been widely utilized in the simulation of various astrophysical phenomena, showcasing its effectiveness in capturing complex dynamics and fluid behavior without relying on traditional meshes (Lucy, 1977). Radial Basis Function (RBF) interpolation is an effective approach for generating smooth, continuous approximations of scattered data. In this technique, a collection of radial basis functions, such as Gaussian or multiquadric functions, are employed to estimate the solution at any point within the domain (Wright, 2003). The Element-free Galerkin (EFG) method is a meshless alternative to the Galerkin method, which is widely used in finite element analysis. Utilizing moving least squares (MLS) approximation, EFG constructs shape functions and integrates the PDE's weak form throughout the domain. This method is applicable to both linear and nonlinear problems. (Belytschko et al., 1995). Li (Yu-kun, 2007) proposed the Mesh-Free Weighted Least Squares (MWLS) method, which has been recognized for its high accuracy and excellent stability, particularly in generating a symmetric coefficient matrix. Unlike the Galerkin method, the MWLS method does not require Gaussian integration, making it more efficient. Xu and Rao (Rao et al., 2021; Xu et al., 2021) applied the MWLS method to study shale gas water seepage problems, analyzing the influence of weight functions and nodes in the MWLS method. However, they did not specifically analyze the characteristics of shale oil.

In this paper, the concept of fractal permeability is introduced, and a numerical model is developed to simulate oil and water flow in a fractured horizontal well situated in a fractal shale oil reservoir. The Mesh-Free Weighted Least Squares (MWLS) method is employed to solve the problem. Additionally, a comparative analysis is conducted to evaluate the impacts of fracture distribution patterns, initial water saturation, and reservoir reconstruction degree on reservoir utilization scope and production performance. Through this analysis, insights are gained into the effective utilization and production performance of reservoirs under different conditions.

2 Equations for the meshless method in modeling oil-water flow in shale oil reservoirs

The meshless technique employs a collection of field nodes distributed across the computational domain's boundary and body to delineate the boundary and the domain itself. Because these field nodes do not form any mesh, this technique can overcome the constraints of the finite difference approach, which necessitates a Cartesian mesh, as well as the finite element approach, which demands high-quality mesh production and remodeling.

The meshless method unfolds in three primary stages:

Step 1. Field Nodes in Meshless Techniques for Conveying Field Variable Values

Within the meshless approach, field variable values, encompassing unknown functions, are expressed by the nodal values assigned to field points. The precision of the computation is directly impacted by the concentration of these field points, which are typically spread evenly across the domain.

Step 2. Localized Approximation of Field Variables in Meshless Techniques

In meshless techniques, where a grid is not utilized, the field variables at a specific point $x=(x_1,x_2)$ within the computational domain are approximated through interpolation using the field node values within the localized superconductive area centered around that point. This approach enables accurate estimation of field variable values at arbitrary locations, ensuring precise representation of the underlying physical phenomena.

$$u(x) = \sum_{i=1}^{n} \phi_i(x) u_i = \Phi^T(x) U_s \tag{1}$$

Where, n denotes quantity of field nodes within a specific point's local support domain x, u_i signifies the nodes's value of the ith field node; U_s is The vector composed of the values at each field node; and

$\varphi_i(x)$ represents the shape function associated with the ith node in the support region of a given point x.

Step 3. Deriving Nodal Values of the Unknown Function in Meshless Techniques

Through the application of localized field variable approximations, the derivation of the shape function is done for the field points. The MLS approach is proficient in providing a shape function of high continuity across the overall problem sphere. Generally, when considering a global optimization problem, MLS simplifies the attainment of a globally optimal solution. Consequently, this paper leverages the MLS approach for the local approximation of field variables. In the scope of MLS, the approximation of the unknown function $u(x)$ within x's influence domain is performed.

$$u^h(x) = \sum_{i=1}^{m} p_i(x) a_i(x) = p^T(x) a(x) \tag{2}$$

Here, x represents the position in space of every node within the support region Ω_x of the node under consideration, $p_i(x)$ operates as the principle basis function, m denotes the count of basis functions, and $a_i(x)$ denotes the vector of coefficients tied to the location coordinates. In the context of the MLS approximation $a_i(x)$, The decision on coefficients ensures the validity of the approximation function $u^h(x)$ optimally approximates the function to be solved in terms of the least squares within the Ω_x of the node under review. These coefficients minimize the weighted norm in Eq. 3.

$$J = \sum_{i=1}^{n} \hat{W}(x - x_i) \left[p^T(x_i) a(x) - u_i \right]^2 \tag{3}$$

Where n represents the quantity of nodes held in the support domain of the weight function $\hat{W}(x - x_i) \neq 0$, and u_i indicates the nodal parameter at the location x equals to xi.

The necessary condition of making Eq. 3 minimum is

$$\frac{\partial J}{\partial a} = 0 \tag{4}$$

That is,

$$A(x) a(x) = B(x) U_s \tag{5}$$

In which,

$$\begin{aligned} A(x) &= \sum_{i=1}^{n} \hat{W}(x - x_i) p(x_i) p^T(x_i) \\ B(x) &= \left[\hat{W}(x - x_1) p(x_1), \ldots, \hat{W}(x - x_n) p(x_n) \right] \end{aligned} \tag{6}$$

Then $a(x)$ is:

$$a(x) = A^{-1}(x) B(x) U_s \tag{7}$$

On substituting Eq. 6 into Eq. 2, it leads us to the conclusion that

$$u^h(x) = \sum_{i=1}^{n} \phi_i(x) u_i = \Phi^T(x) U_s \tag{8}$$

In this context, $\Phi(x)$ represents a vector built from shape functions, determined by

$$\Phi^T(x) = \{\phi_1(x) \phi_2(x) \cdots \phi_n(x)\} = p^T(x) A^{-1}(x) B(x) \tag{9}$$

So $\varphi_i(x)$ is defined as

$$\phi_i(x) = \sum_{j=1}^{m} p_j(x) \left(A^{-1}(x) B(x) \right)_{ji} = p^T(x) \left(A^{-1} B \right)_i \tag{10}$$

It is important to note that while the shape function constructed on the basis of the point interpolation local approximation method possesses the Kronecker property, its usage of the local support domain fails to ensure compatibility throughout the entire domain.

2.1 Oil-water flow model of shale oil reservoir

In the geologic model for fractured horizontal wells within shale oil reservoirs, a binary porosity medium is proposed, comprised of two parts: the matrix substance and the fracture web. The matrix substance functions as the primary storage space, while the fracture network operates as the main channel for shale oil. Both oil and water have the capacity to move within the fractures, however, only oil has the ability to flow within the matrix. The dual-porosity model encompasses both the matrix and fracture systems: the former is the chief repository for shale oil, and the latter is the primary passage for it. Three basic assumptions are taken into account:

(1) The flow of oil-water takes place in the fracture system, while solely single-phase shale oil migrates towards fractures in the matrix, disregarding the flow within the matrix system;
(2) The influence of gravity and capillary forces is disregarded;
(3) Fluids exhibit minor compressibility, while rock material remains incompressible.

2.1.1 Flow model for the matrix system

Adhering to the principles of mass conservation and the Darcy flow equation, the oil flow equation within the matrix can be articulated as follows:

$$-\frac{\sigma \rho_o k_{app}}{\mu_o} \left(p_m - p_f \right) = \frac{\partial \left(\phi_{app} \rho_o \right)}{\partial t} \tag{11}$$

where μ_o denotes the oil viscosity, in mPa·s; ρ_o denotes the oil density, in kg/m^3; k_{app} represents the matrix apparent permeability, in mD; p_m refers to the matrix pressure, in MPa; p_f signifies the fracture network pressure, in MPa; φ_{app} stands for the matrix apparent porosity and t denotes time; σ denotes the interfacial flow coefficient, 1/m^2.

The fracture system under scrutiny in this study is planar, possessing a uniform fracture spacing equal to 12/Lm, where Lm corresponds to the length of the matrix rock block's side.

2.1.2 Flow model for the fracture system

Considering the principle of mass conservation along with Darcy's law of flow, the equation for the water phase within a fracture system can be expressed as follows:

$$\nabla \left[\frac{\rho_w k_f k_{rw}}{\mu_w} \nabla p_{wf} \right] + Q_m = \frac{\partial \left(\rho_w \phi_f S_w \right)}{\partial t} \tag{12}$$

The oil flow within the fracture is described as follows:

$$\nabla\left[\frac{\rho_o k_f k_{ro}}{\mu_o}\nabla p_{of}\right] + Q_m = \frac{\partial\left(\rho_o \phi_f S_o\right)}{\partial t} \tag{13}$$

where ρ_w signifies the water's density, kg/m^3; k_{rw}, k_{ro} denote the relative permeability of water and oil, respectively, mD; k_f represents the fracture's permeability, mD;μ_w is the water's viscosity, mPa•s; p_{wf} is the pressure within the water phase of the fracture, in MPa; φ_f is the fracture's porosity; S_w and S_o indicate the water and oil saturations within the fracture, respectively; Q_{mo} is the mass flow rate, as shown in Eq. 14,

$$Q_m = \rho_i \frac{\sigma k_m}{\mu_i}\left(p_m - p_f\right) \tag{14}$$

Characteristics of the fracture system, like porosity and permeability, can be articulated as follows:

$$\phi_f(x) = \phi_w\left(\frac{x}{x_w}\right)^{D_f-2-\theta_f}$$
$$k_f(x) = k_w\left(\frac{x}{x_w}\right)^{D_f-2-\theta_f}$$

in this context, x denotes the distance from the origin, measured in meters (m), and x_w refers to the hydraulic fracture's width, also measured in meters (m). The parameters ϕ_w and kw represent the starting point's porosity and permeability, respectively, in the matrix and fracture system medium, stated in millidarcies (mD). D_f is utilized to depict the fracture system medium's geometric attributes, capturing the fractal fracture's geometric nuances and intricacy. The anomaly diffusion index of the fracture system medium is conveyed by ϕ_f.

2.1.3 Supporting equations

For the purpose of this analysis, capillary forces are not considered. Therefore, the pressure of the oil within the fracture system equilibrates with the pressure of the water phase, resulting in the flow of only oil within the matrix system. Consequently, the pressures within the fracture and the matrix are denoted by P_f and P_m, respectively.

$$S_o + S_w = 1 \tag{15}$$
$$P_{wf} = P_{of} = P_f \tag{16}$$

Initial:

$$p_i = p_f(x, y, z, 0) = p_m(x, y, z, 0) \tag{17}$$

2.2 Model solution

The meshless method, which is based on the weighted residual technique, utilizes the moving least squares (MLS) strategy to construct the approximation function. The governing equation is discretized using the least square method, resulting in the development of MWLS, a meshless technique. For a comprehensive understanding of the MWLS, please refer to the cited literature. (Yu-kun, 2007).

By reorganizing Eqs 11–13, we can derive the subsequent Eq. 18.

$$\begin{cases} \nabla\left(\lambda_{fg}^t \nabla p_f^{t+1}\right) + \nabla\left(\lambda_{fw}^t \nabla p_f^{t+1}\right) + q_{mg}^t - \left(\phi_f C_{tf}\right)^t \dfrac{p_f^{t+1} - p_f^t}{\partial t} = 0 & ① \\ \nabla\left(\lambda_{fw}^t \nabla p_f^{t+1}\right) - \phi_f^t \dfrac{S_w^{t+1} - S_w^t}{\partial t} = 0 & ② \\ \dfrac{\sigma k_m}{\mu_g}\left(p_m^{t+1} - p_f^{t+1}\right) + \phi_m C_{tm} \dfrac{p_m^{t+1} - p_m^t}{\partial t} = 0 & ③ \end{cases} \tag{18}$$

In the process of executing MWLS for inferential purposes, the problem domain, represented by Ω, and its boundary, denoted by Γ, undergo discretization through the use of n points. The fracture system's pressure and water saturation are then modeled by meshless approximate functions, established courtesy of MLS, which can be expressed following the template of Eq. 19.

$$p_f \approx \sum_{i=1}^{n} N_i P_{fi} = N d_f \tag{19}$$

where $N = [N_1(x)\, N_2(x) N_3(x) \cdots N_n(x)]$ is a shape function, $d_f = [p_{f1}\, p_{f2}\, p_{f3} \cdots p_{fn}]^T$.

By replacing Eq. 18-①) with Eq. 19 from above, the residual can be derived, as depicted in Eq. 20.

$$R_{p_f} = \nabla\left(\lambda_{fw}^t\left(\nabla N d_f^{t+1}\right)\right) + \nabla\left(\lambda_{fg}^t \nabla\left(N d_f^{t+1}\right)\right) + \frac{\sigma k_m}{\mu_g}\left(p_m^t - N d_f^{t+1}\right) - \left(\frac{\phi_f C_{tf}}{\Delta t}\right)^t \left(N d_f^{t+1} - N d_f^t\right) = 0 \tag{20}$$

Thus, the computational scheme of MWLS for determining the pressure in the fracture system unfolds as follows:

$$\Pi_{p_f} = \int_{\Omega} \left(R_{p_f}\right)^T R_{p_f} d\Omega + \int_{\Gamma_1} \alpha_1\left(N d_f^{t+1} - p_{fc}\right)\left(N d_f^{t+1} - p_{fc}\right) d\Gamma + \int_{\Gamma_2} \alpha_2 \left(\frac{\partial p_f^{t+1}}{\partial x}\right)\left(\frac{\partial p_f^{t+1}}{\partial x}\right) d\Gamma \tag{21}$$

In Eq. 21, α_1 and α_2 symbolize the penalty functions for the boundary conditions. By identifying the least value of Eq. 21 and transposing it into a discrete format, we arrive at Eq. 22:

$$\delta\Pi_{p_f} = \sum_{s=1}^{n} \delta R_{p_f} R_{p_f}\big|_{x=x_s} + \sum_{s=1}^{n_1} \alpha_1 \delta p_f^{t+1} N^T\left(N d_f^{t+1} - p_{fc}\right)\big|_{x=x_s} + \sum_{s=1}^{n_2} \alpha_2 \delta p_f^{t+1} \nabla N^T \nabla N\big|_{x=x_s} = 0 \tag{22}$$

By transforming Eq. 22 into matrix system and taking into account the freedom of p_f^{t+1} , we derive Eq. 23.

$$K_1 p_f^{t+1} = F_1 \tag{23}$$

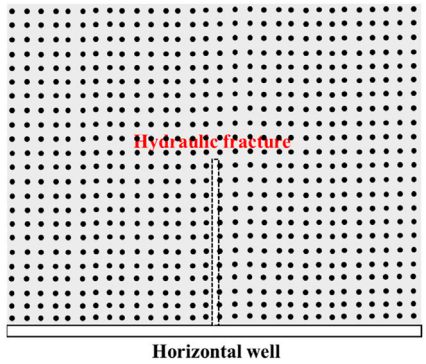

FIGURE 1
Model figure.

Among them:

$$K_1 = \sum_{s=1}^{n} \delta R_{p_f} \left(\nabla \lambda_f^t \nabla (\nabla N) - \frac{\sigma k_m}{\mu_g} N - \left(\frac{\phi_f C_{tf}}{\Delta t} \right)^t N \right) + \sum_{s=1}^{n_1} \alpha_1 N^T N + \sum_{s=1}^{n_1} \alpha_2 \nabla N^T \nabla N$$

$$F_1 = \sum_{s=1}^{n} \delta R_{p_f} \left(-\frac{\sigma k_m}{\mu_g} p_{gm}^t - \left(\frac{\phi_f C_{tf}}{\Delta t} \right)^t d_f^t \right) + \sum_{s=1}^{n_1} N^T p_{fc}$$

Eq. 24 provides the fracture's pressure at the t+1 time step. This value is then utilized in Eq. (18-②) for substitution. Subsequently, the MLS method is employed to construct an approximate equation for the *Sw* in the fracture. Ultimately, Eq. 24 is derived:

$$K_2 S_w^{t+1} = F_2 \tag{24}$$

Eq. 24 provides the fracture's *Sw* at the next time step. The variables and parameters involved are as follows:

$$K_2 = \sum_{s=1}^{n} N^T N + \sum_{s=1}^{n_1} \alpha_1 N^T N + \sum_{s=1}^{n_2} \alpha_2 \nabla N^T \nabla N$$

$$F_2 = \sum_{s=1}^{n} N^T \left(e_{\mathrm{wf}}^t + \frac{\Delta t}{\phi_f} \left(\nabla \lambda_w^t \left(\nabla p_f^{t+1} \right) \right) \right) + \sum_{s=1}^{n_1} \alpha_1 N^T S_{wfc}^t$$

The matrix system's pressure can be determined using a similar approach. By inserting the fracture system's pressure at the next time step into formula (18-③), the final MWLS equation can be derived:

$$K_3 p_m^{t+1} = F_3 \tag{25}$$

Eq. 25 provides the matrix's pressure at the next time step. The variables and parameters involved are as follows:

$$K_3 = \sum_{s=1}^{n} \delta R_{p_m} \left(\frac{\sigma k_m}{\mu_g} N + \frac{\phi_m C_{tm} N}{dt} \right) + \sum_{s=1}^{n_1} \alpha_1 N^T N + \sum_{s=1}^{n_2} \alpha_2 \nabla N^T \nabla N$$

TABLE 1 Parameters of reservoir.

Parameters	Values
Initial pressure p_i/Bar	300
Wellbore flow pressure p_{wf}/Bar	150
Fracture system porosityφ_f/%	0.4
Fracture starting point's permeability k_w/mD	100000
Initial *Sw*/%	20
Fractal index *a*	−0.1
Matrix mass size l_m/m	10

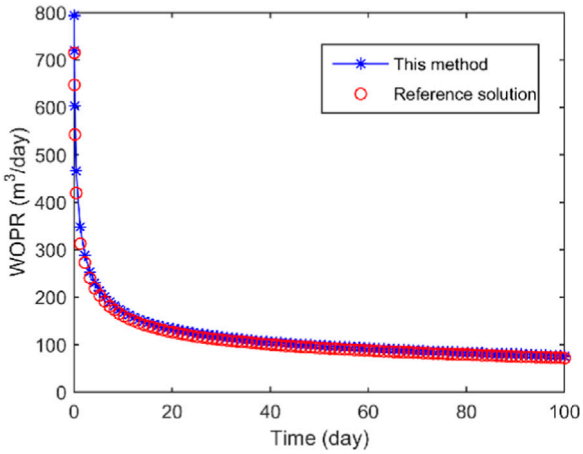

FIGURE 2
WOPR.

$$F_3 = \sum_{s=1}^{n} \delta R_{p_m} \left(\frac{\sigma k_m}{\mu_g} d_f^{t+1} + \frac{\phi_m C_{tm}}{dt} p_m^t \right) + \sum_{s=1}^{n_1} \alpha_1 N^T p_{m\Gamma_1}^t$$

Where *s* represents the number of points used for calculations; Let *n* represent t the total number of points used for calculations within the neighborhood Ω, and let *ni* (i = 1,2) represent the total number of points used for calculations on boundary *Γi*.

3 Examining and confirming the accuracy of computational examples

3.1 Model validation

A field case was constructed to validate the model's accuracy, considering the fractal features in a shale oil reservoir where the horizontal well is fractured. The reservoir area are 500 m × 400 m × 10m, with the model and layout depicted in Figure 1. The

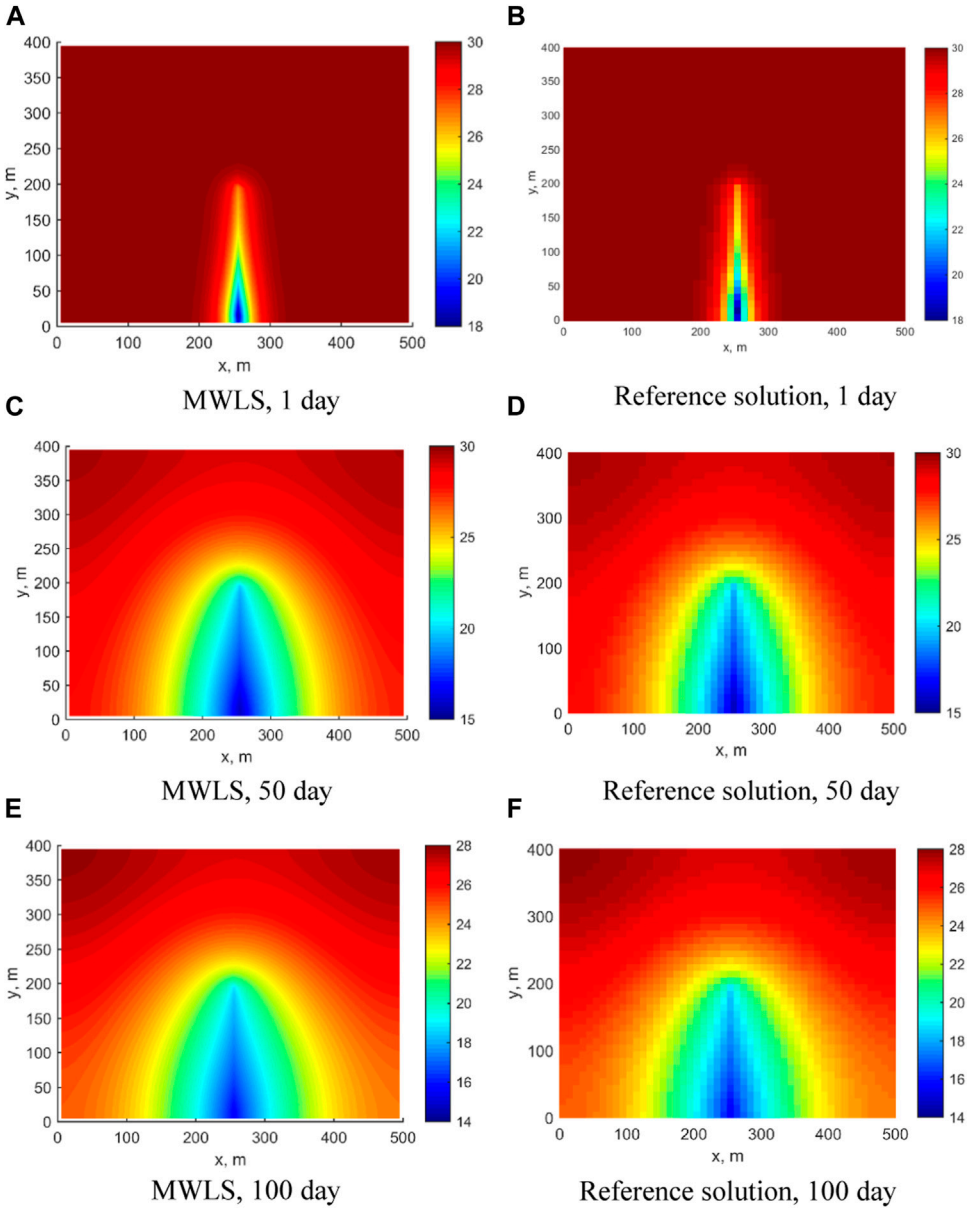

FIGURE 3
The Distribution of fracture pressure. **(A)** MWLS, 1 day; **(B)** Refence solution, 1 day; **(C)** MWLS, 50 day; **(D)** Refence solution, 50 day; **(E)** MWLS, 100 day; **(F)** Refence solution, 100 day.

corresponding physical properties of the reservoir can be found in Table 1. Due to its superior continuity and higher computational accuracy, we used the Gaussian formulation as the weighting function in the grid-independent approach. The layout scheme used is 50 × 40, and a node spacing of 3 times (30 m) is used for the node influence domain.

This study incorporated Table 1 data into the oil-water flow fractal shale reservoir model to obtain daily oil production variations. This paper set a result calculated using EDFM as the reference solution. The results were then compared to those of a reference solution, as shown in Figure 2. The proposed method closely matched the reference solution, demonstrating its reliability, accuracy, and high computational efficiency. Furthermore, Figure 3 presents the pressure distribution at different times, showing that the matrix pressure gradually decreases during production. Although there were some discrepancies between the reference solution and the MWLS results, these errors fall within acceptable bounds and can be attributed to inherent differences between the approaches.

3.2 Sensitivity analysis of nodal influence domain

After applying the theories and solutions mentioned earlier, a sensitivity analysis of the nodal influence domain is conducted to

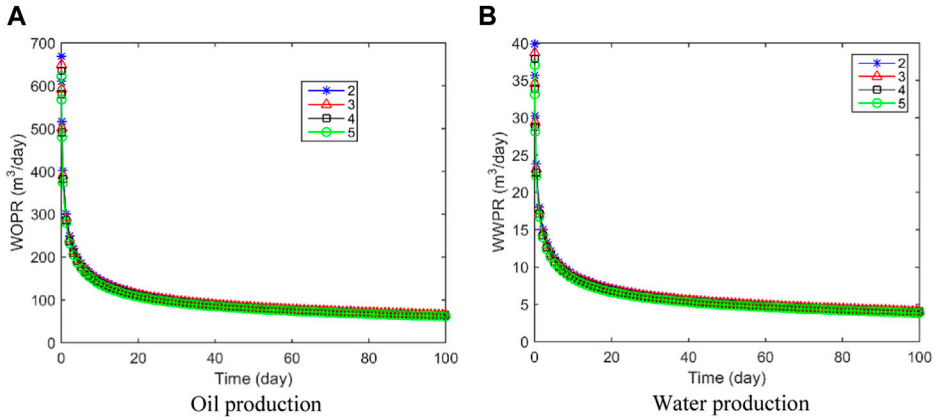

FIGURE 4
Comparsion of production. **(A)** Oil production; **(B)** Water production.

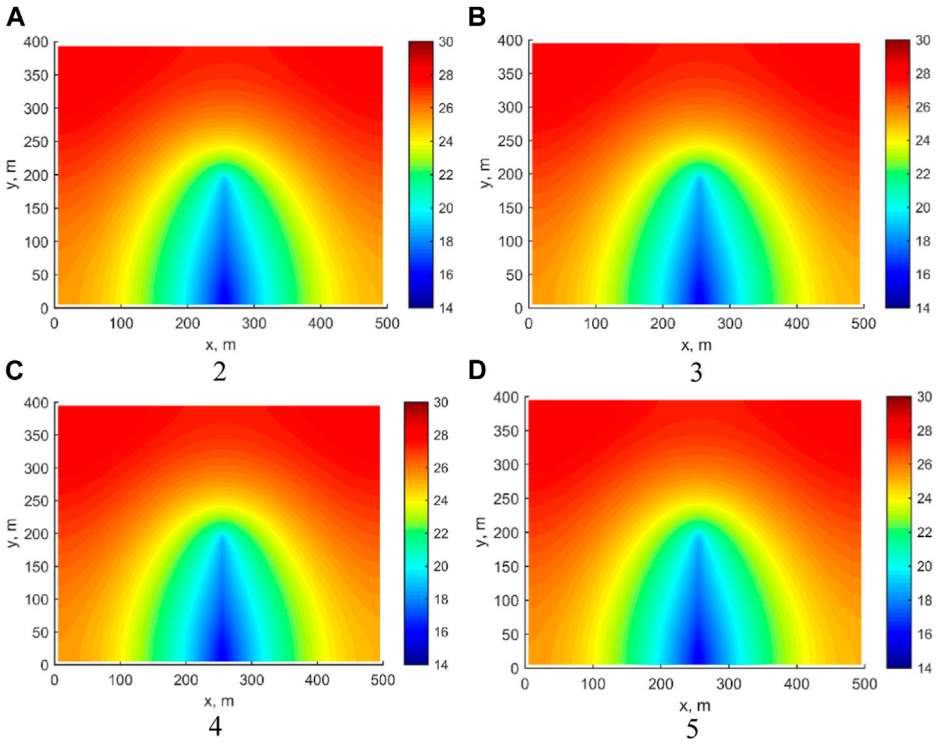

FIGURE 5
The distribution of frature pressure under different node influence domains. **(A)** 2; **(B)** 3; **(C)** 4; **(D)** 5.

evaluate its impact on the accuracy of meshless method computations. The solution of the flow of oil and water in horizontally fractured wells. is used to verify the validity of the method. While the MWLS method is inherently precise, the accuracy of its results is also dependent on the process of choosing the nodal influence domain. The optimal parameter values vary depending on the specific problem at hand.

Consequently, the nodal influence domain was chosen to be 2, 3, 4, and 5 times the nodal spacing (10 m), with the initial water saturation is 0.25 while keeping other parameters constant. By doing so, the established mathematical model is further validated and analyzed to ensure its reliability and applicability in solving real-world problems associated with the flow of oil and water in horizontally fractured wells.

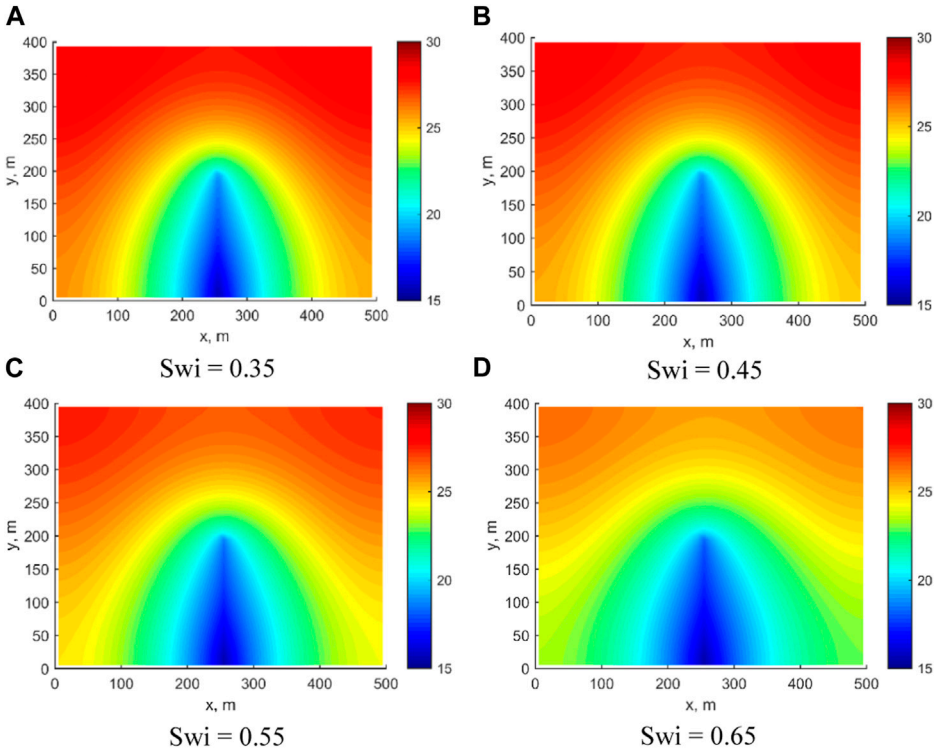

FIGURE 6
Pressure distribution under different initial Sw. **(A)** Swi = 0.35; **(B)** Swi = 0.45; **(C)** Swi = 0.55; **(D)** Swi = 0.65.

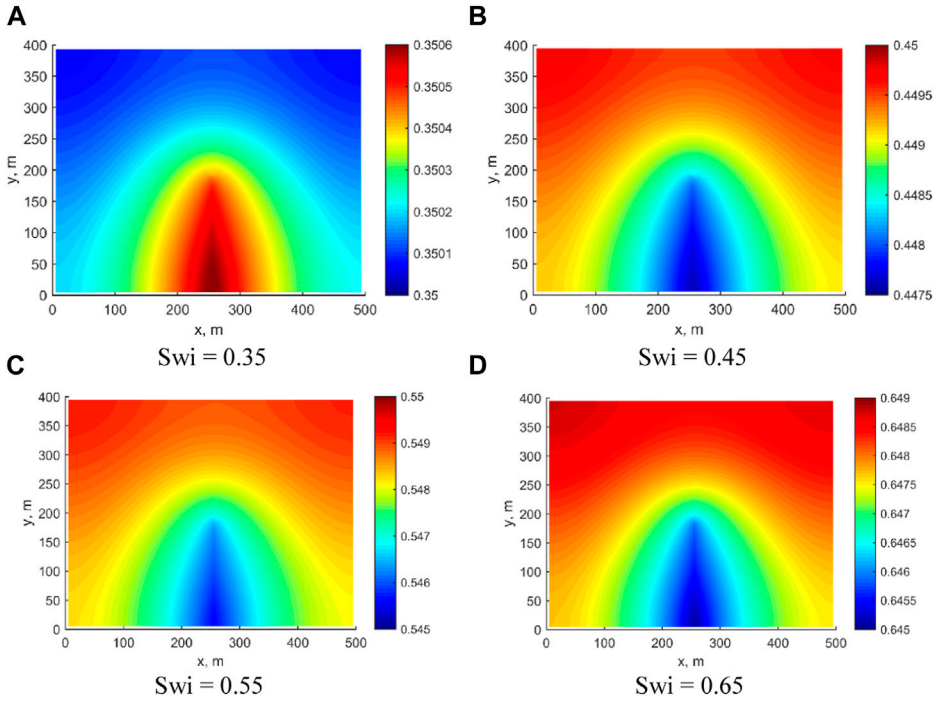

FIGURE 7
Fracture *Sw* distribution under different initial *Sw*. **(A)** Swi = 0.35; **(B)** Swi = 0.45; **(C)** Swi = 0.55; **(D)** Swi = 0.65.

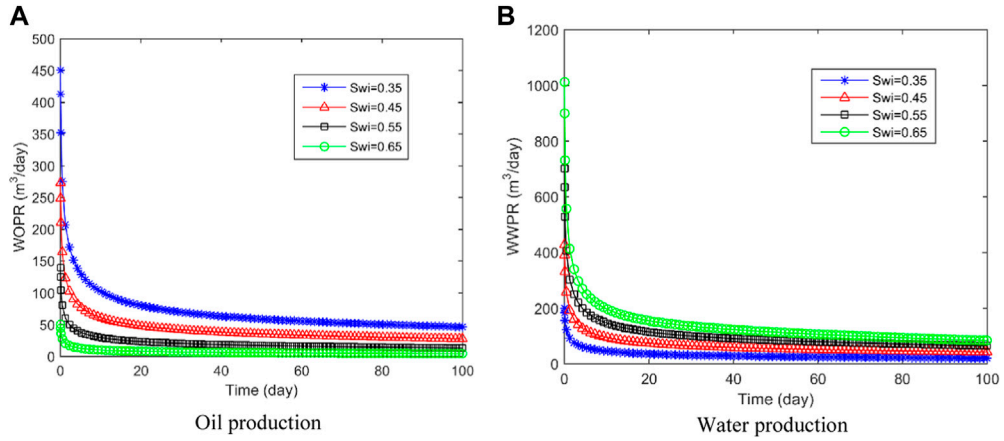

FIGURE 8
Production of different initial water saturation conditions. **(A)** Oil production; **(B)** Water production.

Figure 4 demonstrates the variation curves of daily oil and water production for different nodal influence domains. The calculated results demonstrate varying levels of consistency when the nodal influence domain is set at 2, 3, 4, and 5 times the nodal spacing. This suggests that the method is characterized by good stability and convergence in its calculations. This validates its effectiveness and robustness for simulating the flow of oil and water in horizontally fractured wells. Figure 5 shows the crack pressure distribution at 100 days for different nodal influence domains. The calculated crack pressure distributions do not differ significantly under different conditions. When the influence domain size is 5 times the nodal spacing, the pressure drop area is marginally larger than that for the influence domain size of 2, 3, and 4 times the nodal spacing. However, the overall difference is less than 2% because the area of pressure drop increases slightly with the size of the influence domain.

3.3 Sensitivity analysis of initial *Sw*

The initial *Sw* level is a crucial factor affecting shale oil production. To investigate the impact of different initial *Sw* levels on reservoir recovery and fractured well production while keeping other parameters constant, data from Table 1 were utilized. The initial *Sw* values were set at 0.35, 0.45, 0.55, and 0.65. Figure 6 illustrates the pressure in the reservoir for different initial levels of Sw after 100 days of production. It is evident that an increase in the initial *Sw* level leads to a reduction in the pressure difference between the matrix and fracture in the reservoir. This underscores the importance of accurately modeling and understanding initial *Sw* when simulating and predicting shale oil production. At an initial *Sw* of 0.35, the matrix pressure in the upper part of the model is about 30 MPa at 100 days, while at this value of 0.65, the matrix pressure in the upper part of the model is only about 26 MPa.

In Figure 7, the *Sw* distribution in the reservoir at 100 days are shown for different initial *Sw* levels. When the initial *Sw* is set at 0.35, the *Sw* at the fracture increases slightly to 0.3506 after 100 days. However, as the initial *Sw* level increases, the *Sw* at the fracture decreases after 100 days. This phenomenon is mainly due to the increase in *Sw*, which results in a significant rise in water flow capacity. Accurately modeling and predicting the behavior of oil-water flow in shale reservoirs requires an understanding of the relationship between initial *Sw* and its impact on fracture *Sw* over time.

In Figure 8, the fluid production under different initial *Sw* conditions is displayed. As the initial *Sw* increases, there is less free oil stored in the fractures and reservoirs. Consequently, the initial oil production is significantly reduced when the initial *Sw* is higher. Moreover, higher *Sw* reduces the relative permeability of the oil phase, hindering oil flow within the reservoir. Thus, larger initial *Sw* levels result in lower daily oil production and higher daily water production. For instance, when the initial *Sw* is set at 0.65, the initial daily well water production rate can reach 1024 m^3/day. Understanding these relationships is crucial for optimizing reservoir management and production strategies.

3.4 Sensitivity analysis of fracture half-lengths

We investigate the effects of different fracture half-lengths on the proposed model by setting the values to 100 m, 150 m, 200 m, 250 m, and 300 m, while keeping other parameters unchanged. This analysis helps to understand how variations in fracture half-length and SRV influence the production performance and recovery efficiency in shale oil reservoirs.

Figure 9 displays the pressure distribution field for different fracture half-lengths at 100 days. Increasing the fracture half-length results in a more rapid and extensive drop in matrix

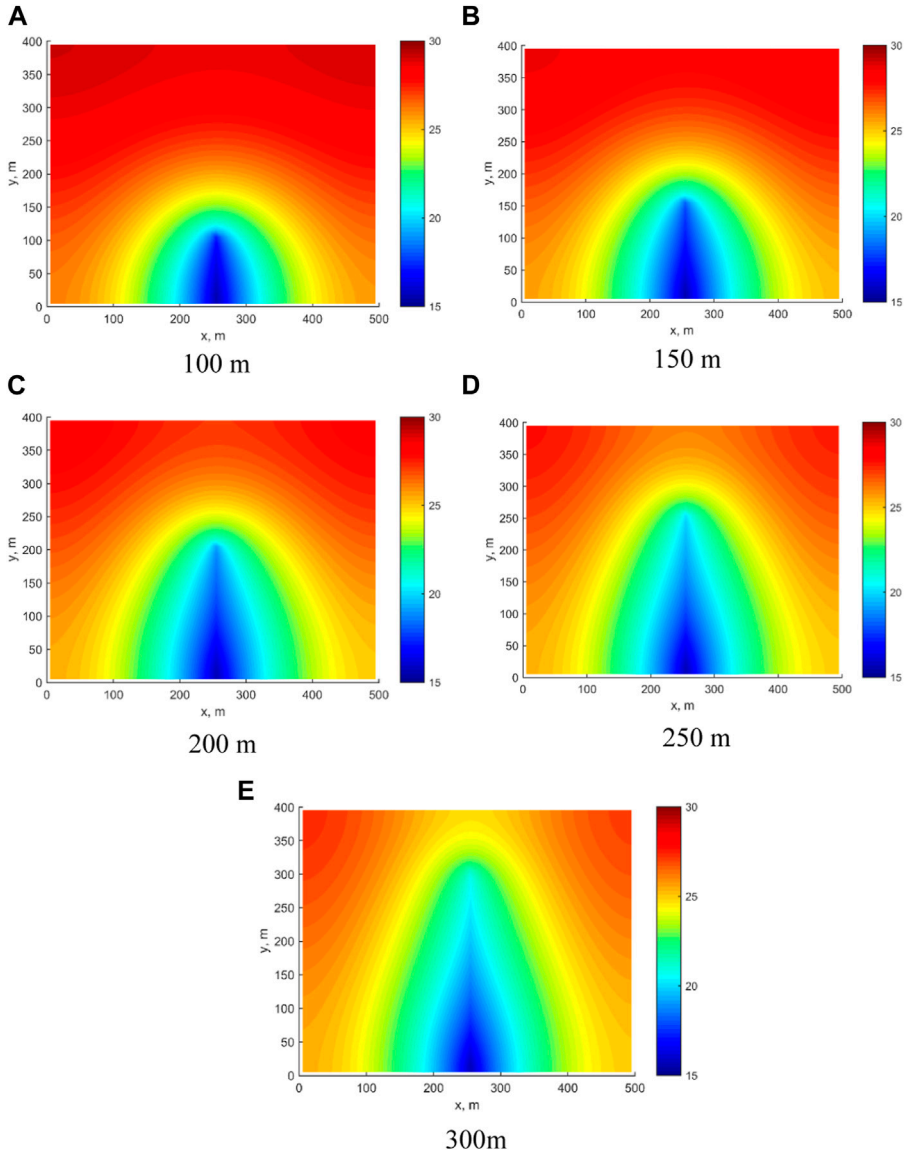

FIGURE 9
Pressure distribution of different fracture half-lengths. **(A)** 100 m; **(B)** 150 m; **(C)** 200 m; **(D)** 250 m; **(E)** 300 m.

pressure. For instance, with a fracture half-length of 100 m, the matrix pressure in the upper part of the reservoir was maintained at 30 MPa, while at a fracture half-length of 300 m, it decreased to 27 MPa.

Figure 10 depicts the comparison curves of daily and cumulative oil production for various fracture half-lengths. Daily oil production rises with an increase in the fracture half-length, as shown in Figure 10A. Figure 10B indicates a positive correlation between cumulative oil production and fracture half-length, mainly due to the larger stimulated reservoir volume and pressure ripple area as the fracture half-length increases. Despite this, the incremental gain in cumulative oil production diminishes as the fracture half-length increases. For example, when the fracture half-length is 100 m, the cumulative oil production for 100 days is 8075 m^3. When the fracture half-length is extended to 150 m, the cumulative oil production increases by 1556 m^3 to reach 9631 m^3. However, when the fracture half-length is increased from 250 m to 300 m, the increase in cumulative oil production is only 602 m^3.

3.5 Effects of fracture numbers

There are multiple factors affecting oil well productivity, among which the number of fractures is one of the key factors. The optimization of fracture numbers is also an important aspect of design of hydraulic fractures for horizontal wells. By fixing fracture half-length at 200 m, setting the initial *Sw* at 0.65, we change the number of fractures to 2, 3, 4, and 5, keeping other parameters consistent with the previous example.

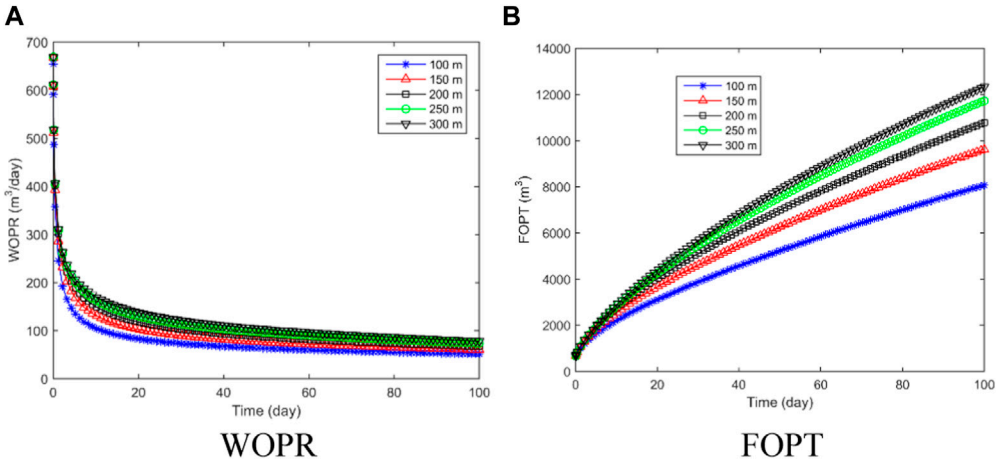

FIGURE 10
WOPR and FOPT of different fracture half-lengths. **(A)** WOPR; **(B)** FOPT.

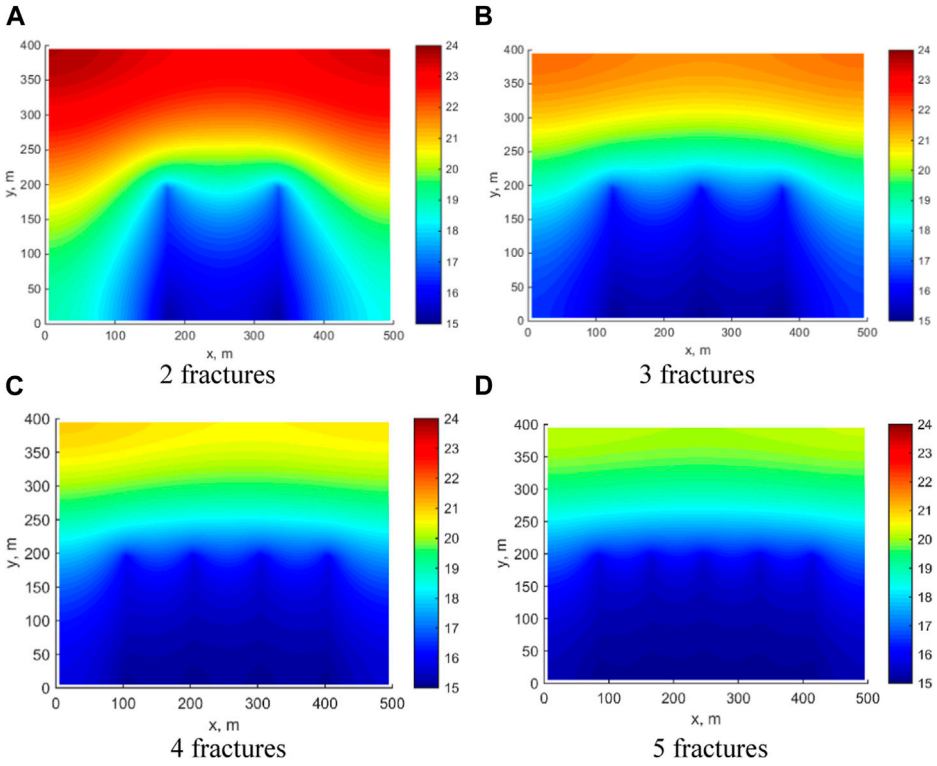

FIGURE 11
Pressure distribution at 100 days. **(A)** 2 fractures; **(B)** 23 fractures; **(C)** 4 fractures; **(D)** 5 fractures.

The pressure distribution at 100 days for different fracture numbers is displayed in Figure 11. The relationship between the number of fractures and the pressure in the reservoir is evident, with an increase in fractures leading to a more rapid decline in pressure and a larger affected area. For example, when there are 2 fractures, the matrix pressure at the upper end of the reservoir can still be maintained at 25 MPa. However, when there are 5 fractures, the matrix pressure at the upper end of the reservoir is only 20 MPa. Figure 12 presents the changes in production capacity under different fracture numbers. Figures 12A, B display the wopr and wwpr curves, respectively,

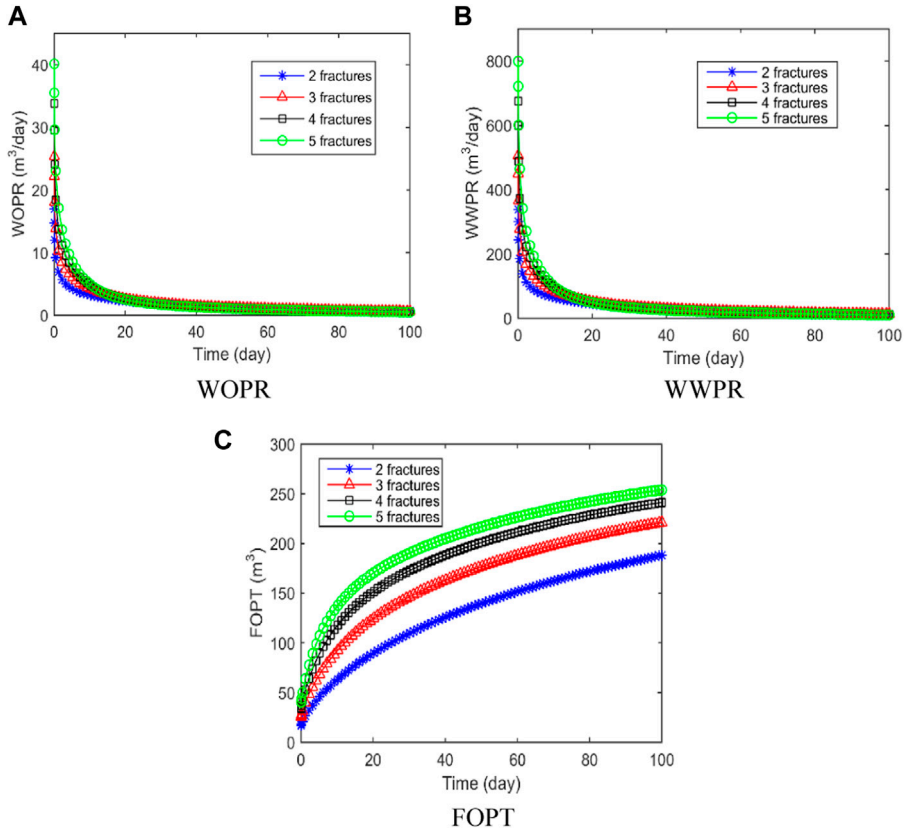

FIGURE 12
Production capacity analysis. **(A)** WOPR; **(B)** WWPR; **(C)** FOPT.

indicating that as the number of fractures increases, the corresponding WOPR and WWPR also increase. Figure 12C shows the FOPT curve, which is also shows a positive correlation with the number of fractures, but the rate of increase is diminishing. Increasing the number of fractures from 2 to 4 results in a 1.28-fold increase in cumulative oil production. However, increasing the number of fractures from 4 to 5 only leads to a 1.05-fold increase in cumulative oil production.

4 Conclusion

1) A mathematical model for oil-water fractal diffusion in fractured horizontal wells considering fracture network heterogeneity was developed and numerically solved using the MWLS method. Field example validation confirmed the model's accuracy.
2) The impact of nodal domains in MWLS method was explored. The method shows robust stability. With an expanding nodal influence domain, the calculated results converge towards true values.
3) Employing the model, we examined the effects of initial Sw and reservoir modification on reservoir utilization and production. Increasing initial Sw increases oil flow resistance, hence reducing oil production. During reservoir modification, expanding fracture half-length and count enhances oil production, but with diminishing growth rate.

Data availability statement

The raw data supporting the conclusion of this article will be made available by the authors, without undue reservation.

Author contributions

WL conceptualization, methodology, software, writing—original draft, formal analysis GZ supervision, Project administration. All authors contributed to the article and approved the submitted version.

Conflict of interest

The authors declare that the research was conducted in the absence of any commercial or financial relationships that could be construed as a potential conflict of interest.

Publisher's note

References

Akkutlu, I. Y., Efendiev, Y., and Savatorova, V. J. T. i. P. M. (2015). Multi-scale asymptotic analysis of gas transport in shale matrix. *Transp. Porous Media* 107, 235–260. doi:10.1007/s11242-014-0435-z

Belytschko, T., Lu, Y. Y., Gu, L., and Tabbara, M. (1995). Element-free Galerkin methods for static and dynamic fracture. *Int. J. Solids Struct.* 32, 2547–2570. doi:10.1016/0020-7683(94)00282-2

Bertoncello, A., Wallace, J., Blyton, C., Honarpour, M., and Kabir, C. (2014). Imbibition and water blockage in unconventional reservoirs: well-management implications during flowback and early production. *SPE Res. Eval. & Eng.* 17, 497–506. doi:10.2118/167698-PA

Civan, F. (2010). Effective correlation of apparent gas permeability in tight porous media. *Transp. Porous Media* 82, 375–384. doi:10.1007/s11242-009-9432-z

Daneshy, A. (2004). "Analysis of off-balance fracture extension and fall-off pressures," in SPE International Symposium and Exhibition on Formation Damage Control, Lafayette, Louisiana, February 2004. doi:10.2118/86471-MS

Javadpour, F. J. J. o. C. P. T. (2009). Nanopores and apparent permeability of gas flow in mudrocks (shales and siltstone). *J. Can. Pet. Technol.* 48, 16–21. doi:10.2118/09-08-16-da

Jia, B., Tsau, J. S., and Barati, R. (2019). A review of the current progress of CO2 injection EOR and carbon storage in shale oil reservoirs. *Fuel* 236, 404–427. doi:10.1016/j.fuel.2018.08.103

Li, Z., Lei, Z., Shen, W., Martyushev, D. A., and Hu, X. (2023). A comprehensive review of the oil flow mechanism and numerical simulations in shale oil reservoirs. *Energies* 16, 3516. doi:10.3390/en16083516

Li, Z., Zhang, X., and Liu, Y. J. G. (2017). Pore-scale simulation of gas diffusion in unsaturated soil aggregates: Accuracy of the dusty-gas model and the impact of saturation. *Geoderma* 303, 196–203. doi:10.1016/j.geoderma.2017.05.008

Lucy, L. B. (1977). A numerical approach to the testing of the fission hypothesis. *Astronomical J.* 82, 1013–1024. doi:10.1086/112164

Mason, E. A., Ea, M., and Ap, M.(1983). *Gas transportin porous media: The dusty-gas model*.

Rao, X., Cheng, L., Cao, R., Jia, P., Liu, H., and Du, X. (2020). A modified projection-based embedded discrete fracture model (pEDFM) for practical and accurate numerical simulation of fractured reservoir. *J. Petroleum Sci. Eng.* 187, 106852. doi:10.1016/j.petrol.2019.106852

Rao, X., Xin, L., He, Y., Fang, X., Gong, R., Wang, F., et al. (2022). Numerical simulation of two-phase heat and mass transfer in fractured reservoirs based on projection-based embedded discrete fracture model (pEDFM). *J. Petroleum Sci. Eng.* 208, 109323. doi:10.1016/j.petrol.2021.109323

Rao, X., Zhan, W., Zhao, H., Xu, Y., Liu, D., Dai, W., et al. (2021). Application of the least-square meshless method to gas-water flow simulation of complex-shape shale gas reservoirs. *Eng. Analysis Bound. Elem.* 129, 39–54. doi:10.1016/j.enganabound.2021.04.018

Sheng, G., Javadpour, F., and Su, Y. (2018). Effect of microscale compressibility on apparent porosity and permeability in shale gas reservoirs. *Int. J. Heat Mass Transf.* 120, 56–65. doi:10.1016/j.ijheatmasstransfer.2017.12.014

Sheng, G., Javadpour, F., and Su, Y. J. F. (2019). Dynamic porosity and apparent permeability in porous organic matter of shale gas reservoirs. *Fuel* 251, 341–351. doi:10.1016/j.fuel.2019.04.044

Sheng, G., Zhao, H., Su, Y., Javadpour, F., Wang, C., Zhou, Y., et al. (2020). An analytical model to couple gas storage and transport capacity in organic matter with noncircular pores. *Fuel* 268, 117288. doi:10.1016/j.fuel.2020.117288

Shiming, W., Yan, J., Jiawei, K., Yang, X., and Botao, L. (2022). Reservoir stress evolution and fracture optimization of infill wells during the drilling-fracturing-production process. *Acta Pet. Sin.* 43, 1305. doi:10.7623/syxb202209009

Singh, H., and Javadpour, F. J. F. (2016). Langmuir slip-Langmuir sorption permeability model of shale. *Fuel* 164, 28–37. doi:10.1016/j.fuel.2015.09.073

Song, W., Yao, J., Li, Y., Sun, H., Zhang, L., Yang, Y., et al. (2016). Apparent gas permeability in an organic-rich shale reservoir. *Fuel* 181, 973–984. doi:10.1016/j.fuel.2016.05.011

Su, Y., Sheng, G., Wang, W., Zhang, Q., Lu, M., and Ren, L. J. F. (2016). A mixed-fractal flow model for stimulated fractured vertical wells in tight oil reservoirs. *Fractals* 24, 1650006. doi:10.1142/s0218348x16500067

Wei, S., Jin, Y., Liu, X., and Xia, Y. (2021b). "The optimization of infill well fracturing using an integrated numerical simulation method of fracturing and production processes," in Abu Dhabi International Petroleum Exhibition & Conference, Abu Dhabi, UAE, November 2021. doi:10.2118/207978-MS

Wei, S., Kao, J., Jin, Y., Shi, C., and Liu, S. (2021a). A discontinuous discrete fracture model for coupled flow and geomechanics based on FEM. *J. Petroleum Sci. Eng.* 204, 108677. doi:10.1016/j.petrol.2021.108677

Wright, G. B. (2003). *Radial basis function interpolation: Numerical and analytical developments*. Colorado: University of Colorado at Boulder.

Wu, K., Li, X., Wang, C., Chen, Z., and Yu, W. J. A. J. (2015). A model for gas transport in microfractures of shale and tight gas reservoirs. *AIChE J.* 61, 2079–2088. doi:10.1002/aic.14791

Xu, Y., Sheng, G., Zhao, H., Hui, Y., Zhou, Y., Ma, J., et al. (2021). A new approach for gas-water flow simulation in multi-fractured horizontal wells of shale gas reservoirs. *J. Petroleum Sci. Eng.* 199, 108292. doi:10.1016/j.petrol.2020.108292

Yu-kun, L. (2007). *Meshless numerical well-test on complex fault-block reservoir*.

Zeng, Y., Ning, Z., Lei, Y., Huang, L., Lv, C., and Hou, Y. (2017). "Analytical model for shale gas transportation from matrix to fracture network," in SPE Europec featured at 79th EAGE Conference and Exhibition, Paris, France, June 2017. doi:10.2118/185794-MS

Zhang, G., Chen, R., Hu, G., Huang, W., zhang, X., and liu, H. (2019). Low-cost drilling Technology for horizontal wells with atmospheric shale gas in the outer margin of sichuan basin. *IOP Conf. Ser. Earth Environ. Sci.* 295, 042098. doi:10.1088/1755-1315/295/4/042098

frontiers | Frontiers in Environmental Science

TYPE Original Research
PUBLISHED 03 August 2023
DOI 10.3389/fenvs.2023.1243854

OPEN ACCESS

EDITED BY
Bamidele Victor Ayodele,
University of Technology Petronas, Malaysia

REVIEWED BY
Wentong Zhang,
Xi'an Shiyou University, China
Kaixuan Qiu,
Jiangmen Laboratory of Carbon Science and Technology, China

*CORRESPONDENCE
Shiqiang Guo,
guoshiqiang30@163.com

RECEIVED 21 June 2023
ACCEPTED 24 July 2023
PUBLISHED 03 August 2023

CITATION
Kang Y, Zhang L, Luo J, Guo Y, Cheng S, Wu D, Li K and Guo S (2023), Molecular dynamics simulation of CO_2 dissolution-diffusion in multi-component crude oil. *Front. Environ. Sci.* 11:1243854. doi: 10.3389/fenvs.2023.1243854

Molecular dynamics simulation of CO_2 dissolution-diffusion in multi-component crude oil

Yulong Kang[1], Lei Zhang[1], Juan Luo[2], Yuchuan Guo[2], Shiying Cheng[2], Di Wu[2], Kaifen Li[2] and Shiqiang Guo[2]*

[1]Research Institute of Yanchang Petroleum (Group) Co., Ltd., Xi'an, China, [2]State Key Laboratory of Petroleum Resources and Prospecting, China University of Petroleum (Beijing), Beijing, China

In order to study the dissolution-diffusion process and mechanism of CO_2 in multi-component crude oil, a model of multi-component crude oil system with octane as the main component and 16 other alkanes as a compound was constructed by using molecular dynamics simulation method. We estimated the CO_2 density distribution in crude oil model and the shift in crude oil model volume change. We then investigated the microscopic influence mechanism of CO_2 dissolution-diffusion on the volume expansion of crude oil by simulating the action of CO_2 dissolution-diffusion in the multi-component crude oil model. Based on the variation law of mean square displacement between crude oil molecules, the dissolution and diffusion coefficients of CO_2 were predicted, and the influence of CO_2 dissolution-diffusion on crude oil mobility was analyzed. It is found that temperature intensifies the molecular thermal motion and increases the voids between alkane molecules, which promotes the dissolution of CO_2 and encourages CO_2 molecules to transmit, making the crude oil expand and viscosity decrease, and improving the flow ability of crude oil; with the enhancement of given pressure, the potential energy difference between the inside and outside of the crude oil model becomes larger, and the voids between alkane molecules become larger, which is favorable to the dissolution of CO_2. Nevertheless, the action of CO_2 molecules' diffusing in the crude oil sample is significantly limited or even tends to zero, besides, the mobility of crude oil is affected due to the advance of external pressure. The mechanism of CO_2 dissolution and diffusion in multi-component crude oil is revealed at the microscopic level, and provides theoretical guidance for the development of CO_2 flooding.

KEYWORDS

CO_2, dissolution-diffusion, multi-component crude oil system, molecular dynamics simulation, mobility

1 Introduction

CCUS, the abbreviation for Carbon Capture Utilization and Storage technology, has been developed in recent years with the global attention to greenhouse gas emissions and other ecological issues. CCUS technology is not only effective in improving global warming, but also significant for achieving zero carbon emissions by 2050. According to the International Energy Agency, CCUS technology will achieve 38% of the emission reduction in the chemical and engineering industry and is expected to contribute about 14% of the CO_2 emission reduction by 2050 (Mi and Ma, 2019; Jin and Chen, 2020; Qin et al.,

2020; Zhang et al., 2022). CCUS technology can be further divided into oil and gas reservoir utilization (CCUS-EOR/EGR), chemical utilization, and biological utilization depending on the utilization method. CCUS-EOR technology is to inject the captured CO_2 into a reservoir in the development stage with complete geological structure and adequate basic information, to enhance the recovery of crude oil through CO_2 flooding and to achieve CO_2 burial (Ku et al., 2023). This technology is not only highly economically viable, but also has a wide range of applications and a very promising future.

Overseas CO_2 flooding originated in the 1950s (Whorton et al., 1952). In the 1980s, it was gradually applied in the oil field and began to be promoted commercially. Since 2000, the globe concern about environmental issues and the continuous development of engineering technology have further promoted the innovation of CO_2 flooding technology (Shen and Liao, 2009). Around the 1960s, China started to pay close attention to CO_2 flooding technology and conducted indoor flooding experiments, and carried out field tests in layer 4-7 of Pulin Daqing oilfield and in the eastern transition zone of Sanan; during the 1990s, Jiangsu Fumin oilfield carried out experiments on CO_2 huff and puff (Chen et al., 2011). Before entering the 21st century, due to the lack of understanding and experimental support for this technology, coupled with the lack of CO_2 gas sources in China and serious gas channeling in the oilfield experiments, the development of CO_2 flooding technology in China had been slow (Gao et al., 2014; Zhao et al., 2017; Li, 2018). Over past 10 years, the internal CO_2 flooding and storage field tests had made a remarkable progress which had three phases: pre-experiments, extended tests and industrial application, with increasingly abundant types of reservoirs and scales of tests, achieving certain results and accumulating some practical experience (Luo et al., 2013). Among all enhance oil recovery (EOR) technologies, the most well-known and effective way to enhance the oil production efficiency is to inject CO_2 into the reservoir, furthermore, the injected CO_2 can achieve the goal of CCUS energy saving and emission reduction (Yuan et al., 2020). The reasons in terms of mechanism why CO_2 flooding can enhance oil recovery is that the solution of CO_2 in the crude petroleum causes volume expansion of crude oil and increases oil saturation in the pore; in addition, CO_2 can diffuse easily inside oil and water, giving the opportunity that the CO_2 can redistribute and stabilize the balance of phase system, which acts an effective part in the relative permeability of oil and water (Hu et al., 2017; Guo et al., 2018; Jia et al., 2019; Li et al., 2019; Li, 2020; Jia et al., 2021).

To take into account the limitations of the complex dissolving and diffusing action of CO_2 inside oil and water, and the inability of indoor experiments to simulate the microscopic oil drive efficiency of CO_2, the author chose the molecular dynamics simulation method to carry out the research. Molecular dynamics simulation is a non-quantum mechanical method to work out problems at the molecular level based on the fundamental theory of classical Newtonian mechanics. The calculation process mainly relies on the position or average configuration of the nucleus to establish the required force field function to describe the molecular structure and energy, which is a more widely used calculation method, and it has certain advantages in analyzing the changes of microscopic properties such as intermolecular forces and molecular morphology. A crude oil system model which contains multiple alkane components is constructed and the action of dissolution-diffusion of CO_2 in the multi-component crude oil model is simulated by applying the simulation method of molecular dynamics in this article. The CO_2 density distribution in crude oil as well as the volume change of crude oil are calculated, and the microscopic impact mechanism of CO_2 dissolution-diffusion on the volume expansion of crude oil is further analyzed. The dissolution and diffusion coefficients of CO_2 were predicted based on the variation law of mean square displacement between crude oil molecules, and the impact of CO_2 dissolution diffusion on crude oil mobility was analyzed. The mechanism of CO_2 dissolution-diffusion in multi-component crude oil is revealed at the microscopic level, and provides theoretical guidance for the development of CO_2 flooding.

TABLE 1 Oil composition analysis data.

Component	Mole %	Plus fraction analysis	Mole %
C1	14.446		
C2	6.487	C1–C4	41.793
C3	12.674	C5+	58.207
C4	8.186		
C5	3.958		
C6	3.223	C1–C8	66.605
C7	4.893	C9+	33.395
C8	12.738		
C9	7.632		
C10	7.162	C1–C16	97.856
C11	3.577	C17	2.144
C12	3.109		
C13	2.969		
C14	2.527		
C15	2.368		
C16	1.907		
C17	2.144		
Total	100		

2 Construction of the multi-component crude oil system model

Primarily based on the results of laboratory determination of the chemical compositions of crude oil, a model of crude oil was constructed within our paper, the crude oil model is mainly composed of octane, including 17 kinds of alkane components such as methane and ethane (Table 1), the density at 20°C of this model is 0.82 g/cm^3. The Visualize module in Material Studio software was used to build a model of each alkane molecule in the crude oil component (as shown in Figure 1). In addition, a molecular model of CO_2 (shown in Figure 2) was constructed for

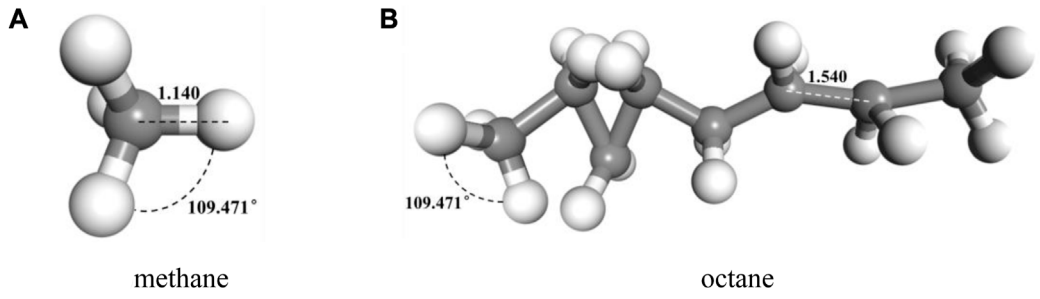

FIGURE 1
Typical molecular model of components of oil. **(A)** methane **(B)** octane.

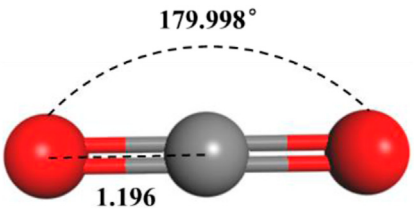

FIGURE 2
CO_2 molecular model.

subsequent simulation of the CO_2 motion in the crude oil model (Jia et al., 2021).

In accordance with the established molecular models of alkanes and CO_2 above, the geometry and energy optimization of each molecular model were carried out and the optimized the molecular model structure was obtained by using the Forcite component, as shown in Figure 3. Figure 4 indicated that we used the Construction tool which is belong to the Amorphous Cell Tools component to build the multi-component crude oil molecular system model in accordance with the experimental testing consequences of crude oil components with the dimensions of 42.67 × 42.67 × 42.67 $Å^3$ and the density of it is set to 0.82 g/cm^3 in accordance with the real crude oil density. To ensure that the properties of the system remain unchanged during the simulation process, the crude oil system model is therefore subjected to three-dimensional periodic boundary conditions. CO_2 was added to the multi-component crude oil molecular system model, and the temperature were set to 313 K, 353 K, 393 K and the pressure were set to 10–50 MPa, in units of 10 MPa respectively in order to be similar to the reservoir properties. This part is a preparation for the research of the action of the CO_2 dissolution and diffusion in crude oil under different reservoir conditions. It should be noted that the idea of establishing the model is also applicable to other multi-component fluids including two phases of oil and gas or three phases of oil, gas and water, but it needs to be further determined according to experimental results and research objectives. Multi-component fluids are more reasonable in real formation fluid characterization and simulation.

3 Simulation method and validation

Author used the BIOVIA Material Studio 2019 software package for molecular dynamics simulations. First, the geometric and energy optimization of the multicomponent crude oil model was performed using steepest descent method to obtain the optimized structures for different temperature and pressure conditions. After that, the kinetic equilibrium was performed, and the force field parameters for both CO_2 and n-alkanes were assigned using the COMPASS force field developed by Sun et al. which is suitable for organic molecules and

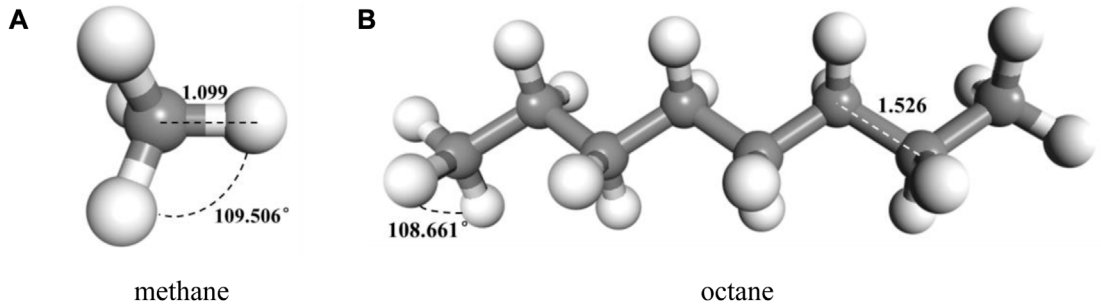

FIGURE 3
Typical molecular model of components of oil after geometric and energy optimization **(A)** methane **(B)** octane.

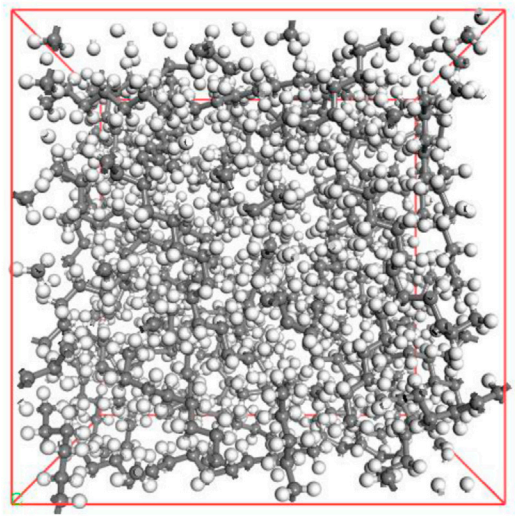

FIGURE 4
Multicomponent oil system model.

inorganic covalent bond molecular systems, and its potential energy function form is expressed as:

$$Etotal = Ebond + Eangle + Etorsion + Ecross + Evdw + Ecoulombic \quad (1)$$

where the first previous four terms show the bonding energy and the last two terms denote the non-bonding interaction energy. The non-bonding interaction energy can be represented by the Lennard-Jones 9-6 potential and the Coulomb electrostatic potential. The Lennard-Jones 9-6 potential describes the potential energy due to the weak repulsive and gravitational forces of the van der Waals force. Its specific form is:

$$E = \sum_{i>j} \frac{qiqj}{rij} + \sum_{i>j} Eij\left[2\left(\frac{r_{ij}^0}{rij}\right)^9 - 3\left(\frac{r_{ij}^0}{rij}\right)^6\right] \quad (2)$$

$$r_{ij}^0 = \left(\frac{(r_i^0)^6 + (r_j^0)^6}{2}\right)^{\frac{1}{6}} \quad (3)$$

where ij denotes an atomic pair, E_{ij} is the potential well depth, r_{ij}^0 is the zero potential distance of the atomic pair, and r is the distance between two atoms.

The other kinetic simulation parameters are: the canonical ensemble (NVT), temperature control using the Nosé-Hoover method, with the temperature set to 313, 353, and 393 K respectively; after that, the isothermal isobaric system synthesis (NPT) is selected, with the pressure set to 10–50 MPa, in units of 10 MPa, respectively, and the Berendsen method for pressure control. All other parameters were consistent in both equilibria, including: Ewald and Atom Based ways were adopted for electrostatic interaction as well as van der Waals interaction, separately. The dynamic simulation of 1 ns (1,000,000 steps) was performed with a step size of 1 fs at a distance of 1.25 nm. The consequences of the simulation procedure were exported every 1,000 steps which divided into two parts, the first part including 400 ps, they were applied to maintain the balance of the system, and the other part containing 600 ps was utilized for collecting the density data in whole system.

The way in which we calculate the crude oil molecular system density at a temperature of 20°C is to apply the simulation of molecular dynamics, afterwards, we compared it with the US NIST database, as shown in Figure 5. The difference between the value of crude oil system density as determined via molecular dynamics simulation that used in our article and the density value of reference given by NIST database is slight, which indicating that the established multi-component crude oil system model and procedure of simulation are reasonable.

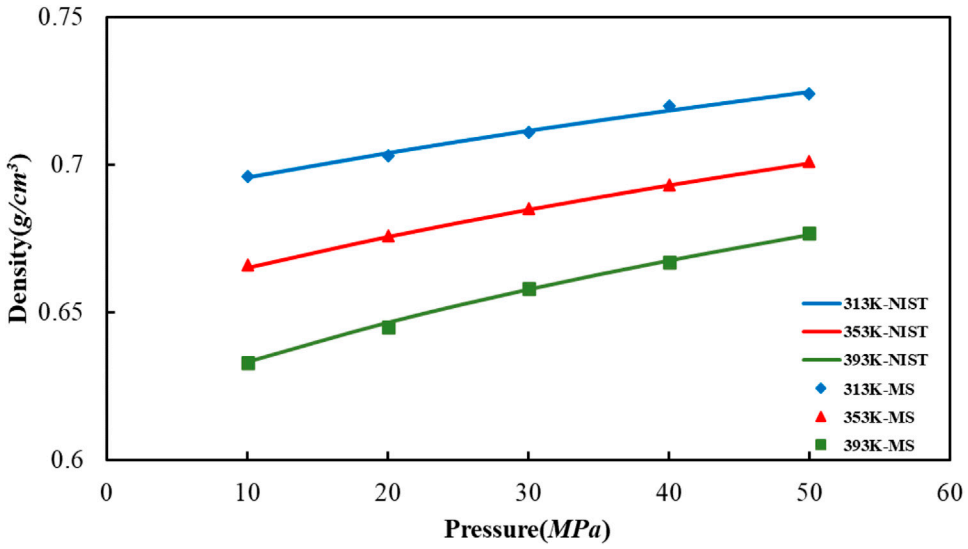

FIGURE 5
Comparison of octane density values in oil models under different temperature and pressure conditions.

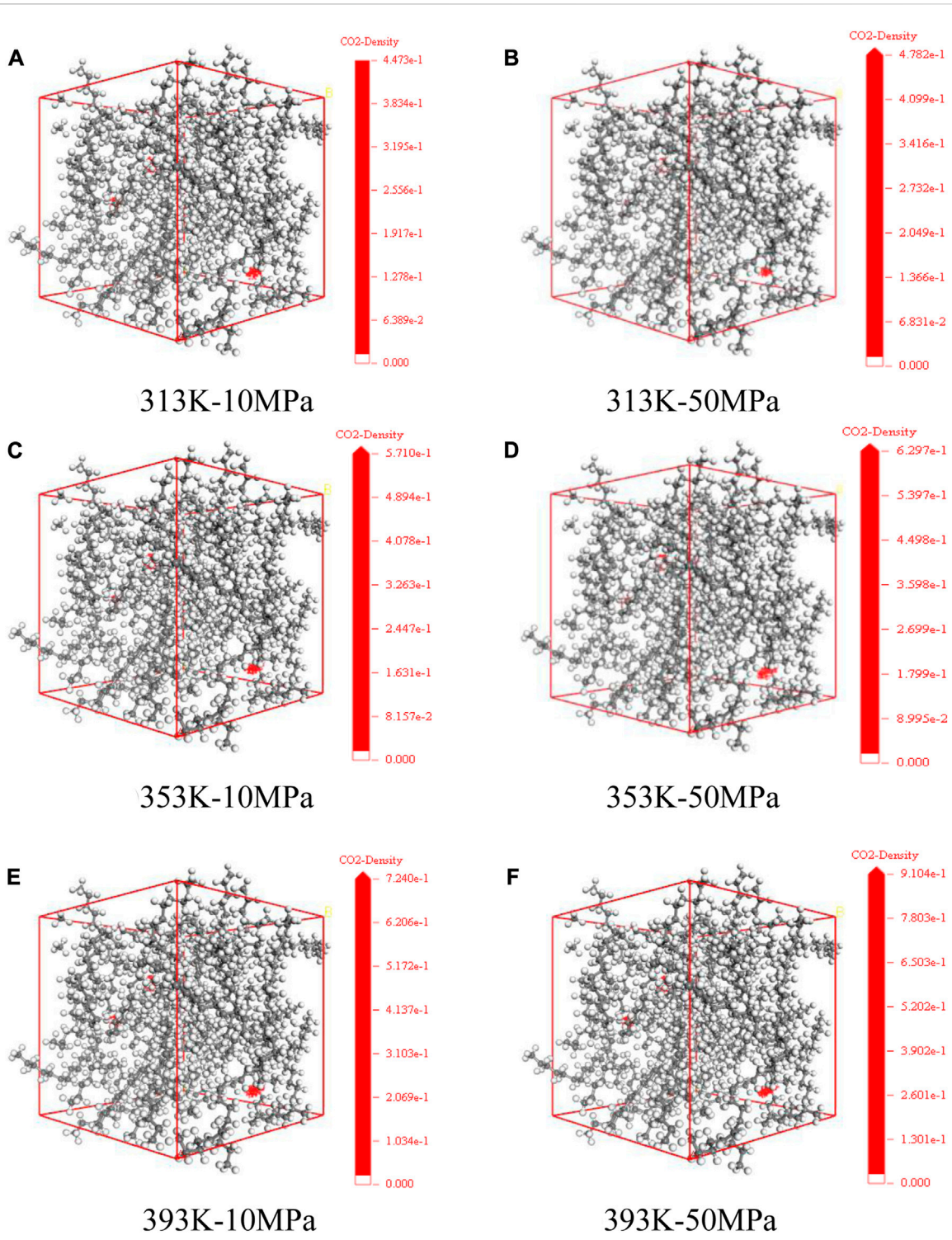

FIGURE 6
Dissolution density distribution of CO_2 in oil system model under varying temperature and pressure conditions **(A)** 313 K-10 MPa **(B)** 313 K-50 MPa **(C)** 353 K-10 MPa **(D)** 353 K-50 MPa **(E)** 393 K-10 MPa **(F)** 393 K-50 MPa.

4 Dissolution diffusion coefficient and crude oil mobility

Zhao et al. (2016a) used a PVT instrument to measure the solubility change of CO_2 in crude oil and formation water under reservoir conditions respectively and express those changes through curve representation. It was found that with the enhancement of reservoir pressure, the ability of CO_2 solution in both oil and water enhanced, and the ability of CO_2 solution within oil phase was about 7 times that in water.

TABLE 2 Volume change of oil system at 313 K.

Condition	Pressure MPa	Final model volume Å^3	Volume change Å^3	Rate of volume change %
Before CO_2 dissolution	10	79690.983	2000.481	2.57
	20	78970.768	1280.266	1.64
	30	78323.617	633.115	0.81
	40	77990.168	299.666	0.39
	50	77817.122	126.620	0.16
After CO_2 dissolution	10	80841.625	3151.123	4.06
	20	80155.734	2465.232	3.17
	30	79452.643	1762.141	2.27
	40	78702.051	1011.549	1.30
	50	78243.050	552.548	0.71

TABLE 3 Volume change of oil system at 353 K.

Condition	Pressure MPa	Final model volume Å^3	Volume change Å^3	Rate of volume change %
Before CO_2 dissolution	10	82838.956	5148.454	6.63
	20	81842.447	4151.945	5.34
	30	81333.928	3643.426	4.69
	40	80376.023	2685.521	3.46
	50	79339.13	1648.628	2.12
After CO_2 dissolution	10	84905.656	7215.154	9.29
	20	84111.661	6421.159	8.27
	30	83224.991	5534.489	7.12
	40	82042.791	4352.289	5.60
	50	80974.986	3284.484	4.23

TABLE 4 Volume change of oil system at 393 K.

Condition	Pressure MPa	Final model volume Å^3	Volume change Å^3	Rate of volume change %
Before CO_2 dissolution	10	87146.066	9455.564	12.17
	20	86125.836	8435.334	10.86
	30	85145.046	7454.544	9.60
	40	83643.014	5952.512	7.66
	50	81906.377	4215.875	5.43
After CO_2 dissolution	10	89014.656	11324.15	14.58
	20	88255.055	10564.55	13.60
	30	86815.055	9125.553	11.75
	40	85815.347	8124.845	10.46
	50	84906.157	7215.655	9.29

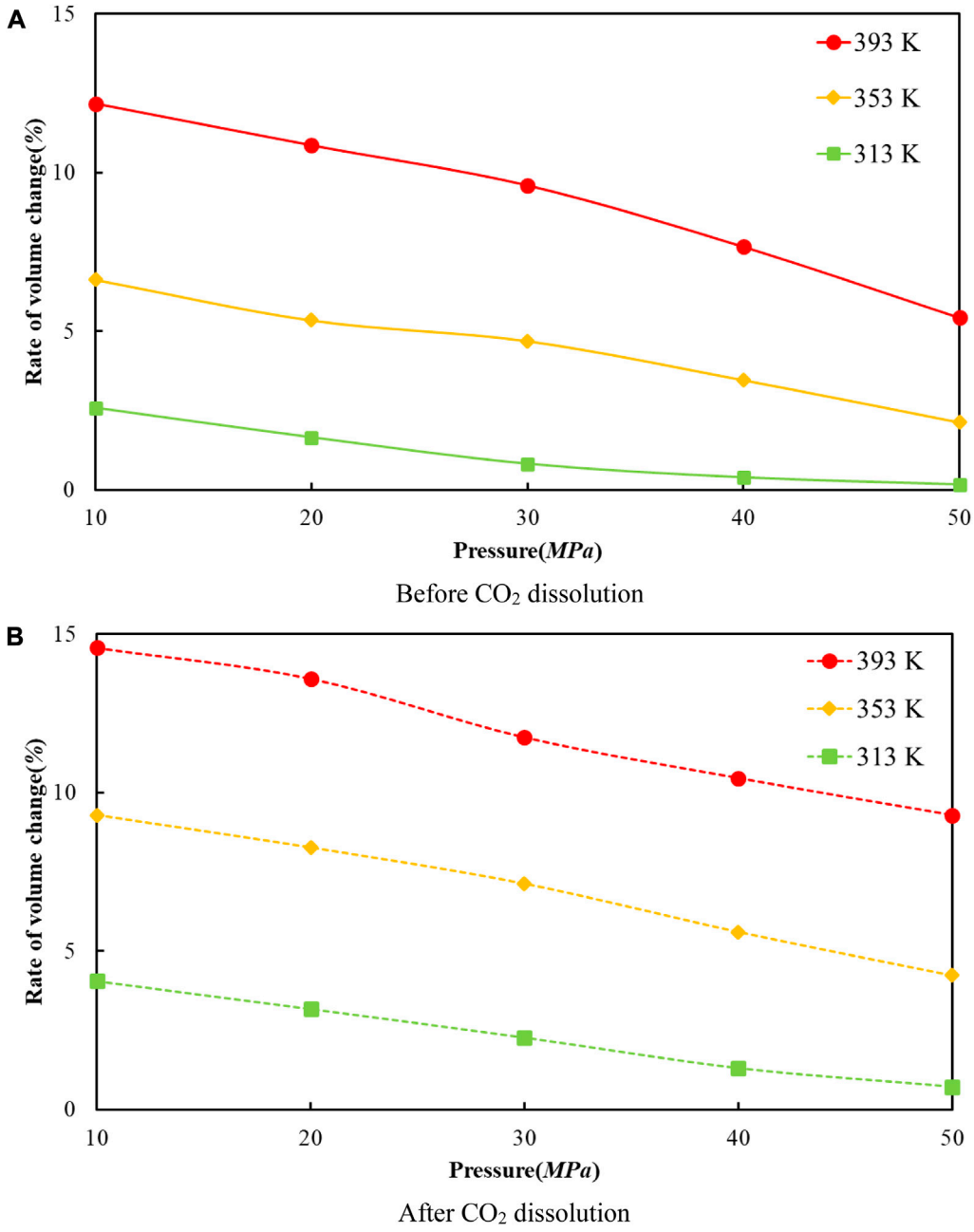

FIGURE 7
The correlation between the volume change rate and pressure of oil system model before and after CO_2 dissolution at different temperatures. **(A)** Before CO_2 dissolution. **(B)** After CO_2 dissolution.

Ao et al. (2019) studied the dissolution and diffusion law in crude oil and brine layer by using the pressure depletion method, and found that the reservoir pressure, temperature and brine concentration all directly affect the dissolution process of CO_2 in brine layer. The higher the salt concentration in the brine layer, the lower the CO_2 dissolution and the slower the diffusion rate.

At a certain temperature, the adsorption isotherm is plotted by calculating the number of small molecules adsorbed in the periodic box at different pressure points, which represents the relationship between the concentration of adsorbed gas and its partial pressure p at a certain temperature. Where the slope of the adsorption isotherm for a pressure value of 0 is the dissolution coefficient S (Jin et al., 2020; Jia et al., 2023):

$$S = \lim_{p \longrightarrow 0} \frac{c}{p} \tag{4}$$

where S is the dissolution coefficient, dimensionless. This factor represents the maximum number of grams of solute dissolved in 100 g of solution at a given temperature and pressure.

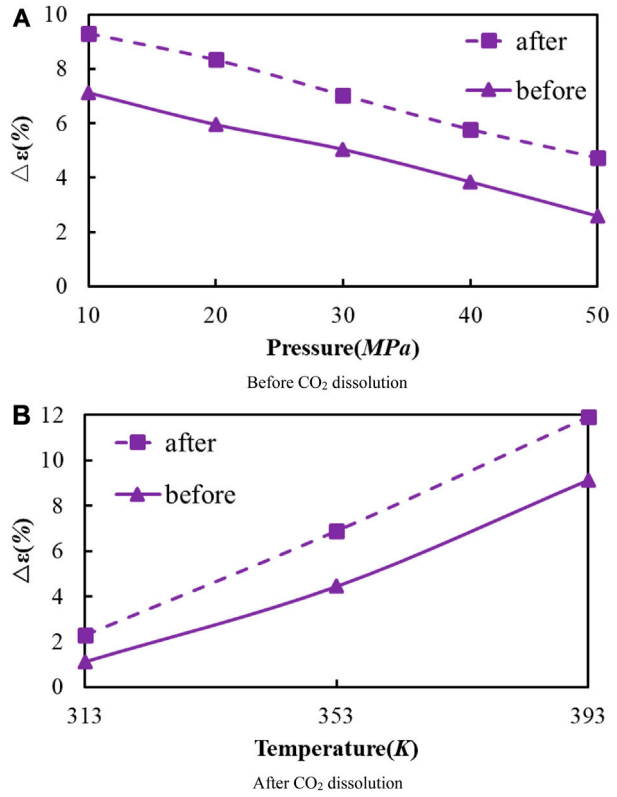

FIGURE 8
Volume change rate of oil system model before and after CO_2 dissolution under different temperature and pressure conditions. **(A)** Before CO_2 dissolution. **(B)** After CO_2 dissolution.

The dissolution coefficient decreases with the increasing temperature. While determining the dissolution rate and final CO_2 dissolution in crude oil is the diffusion coefficient, the larger the diffusion coefficient, the larger the diffusion flux, which determines the gas distribution in the reservoir at different times and affects and improves the physical characteristics of crude oil (Chen et al., 2010). Grogan and Pinczewski (1984) established a mathematical model for the diffusion coefficient under atmospheric pressure conditions by directly observing the interfacial movement of the oil or water phase during CO_2 diffusion. Renner (1988) used artificial cores to test the coefficients of CO_2 and rich gas diffusing motion in crude oil at high pressure. Riazi (1996) used the pressure drop method to study the diffusion coefficients between gas and crude oil (Zhang et al., 2000). Wang (1996) systematically described the CO_2 mixed-phase drive diffusion percolation equation, molecular diffusion coefficient and physical dispersion coefficient models and related experimental determination methods (Li et al., 2001; Fu et al., 2003). Zhao et al. (2016b) proposed an approximate calculation model of the variable diffusion coefficient applicable to the pressure drop method, but the effect of crude oil expansion on diffusion was not considered. In response to the inability of previous authors to comprehensively consider the impacts of varying temperatures and pressures on the diffusion of dissolved CO_2 in crude oil in indoor experiments. This paper takes advantage of molecular dynamics simulations at the microscopic level to carry out simulation studies.

The diffusion coefficient in this paper is calculated from the mean square displacement and is mainly expressed as (Jin and Chen, 2019; Jin et al., 2020):

$$D = \frac{1}{6N\alpha} \lim_{t \to \infty} \frac{d}{dt} \sum_{i=1}^{N\alpha} \langle [ri(t) - ri(0)]^2 \rangle \tag{5}$$

where Nα denotes the diffusion of atoms in the system and *ri(t)* represents the displacement vector of molecule i from 0 to time t. The diffusion coefficient is obtained from the best trend line of the MSD curve y = ax + b. It is specifically obtained from the following equation:

$$D = \frac{a}{6} \tag{6}$$

According to the Stokes-Einstein formula, different diffusion coefficients of CO_2 lead to different viscosities of crude oil and ultimately different crude oil fluidity. The two show an inverse relationship, mainly calculated by the following equation:

$$\mu = \frac{kT}{6\pi\alpha D} \tag{7}$$

where T represents the simulated temperature, α represents the molecular radius of CO_2, which is approximately 1.65×10^{-8} cm, k denotes the Boltzmann constant, which is 1.38×10^{-23} J/K, D denotes the diffusion coefficient, as well as μ represents the crude oil viscosity.

The dissolution and diffusion coefficients of CO_2 were calculated mainly by Material Studio software. In the simulation process, the software will count the specific dissolution amount of CO_2 at different times, and according to these dissolution amounts, the dissolution coefficient of CO_2 at different times can be calculated. The diffusion coefficient was calculated by calculating the change of Mean Square Displacement of CO_2 over a period of time, and then solving the diffusion coefficient according to linear regression fitting.

5 Results and discussion

5.1 The density distribution of CO_2

Figure 6 shows the distribution state of CO_2 dissolution density in the model of crude oil system that we set up under various temperature and pressure conditions. The red part represents the concentration distribution of CO_2 molecules dissolved in different systems. We count the specific distribution density of CO_2, as shown in the following figure. At the same temperature, with the enhancement of pressure, the dissolving amount of CO_2 within the crude system also increases, and the dissolution density distribution of CO_2 in the crude oil system model enhances. Meanwhile, the ability of CO_2 solubility increases as the temperature rises at the same pressure. This is because of the existence of vast voids among alkane molecules. With the change of external conditions, the movement of CO_2 molecules is intensified, prompting it to enter the voids between alkane molecules.

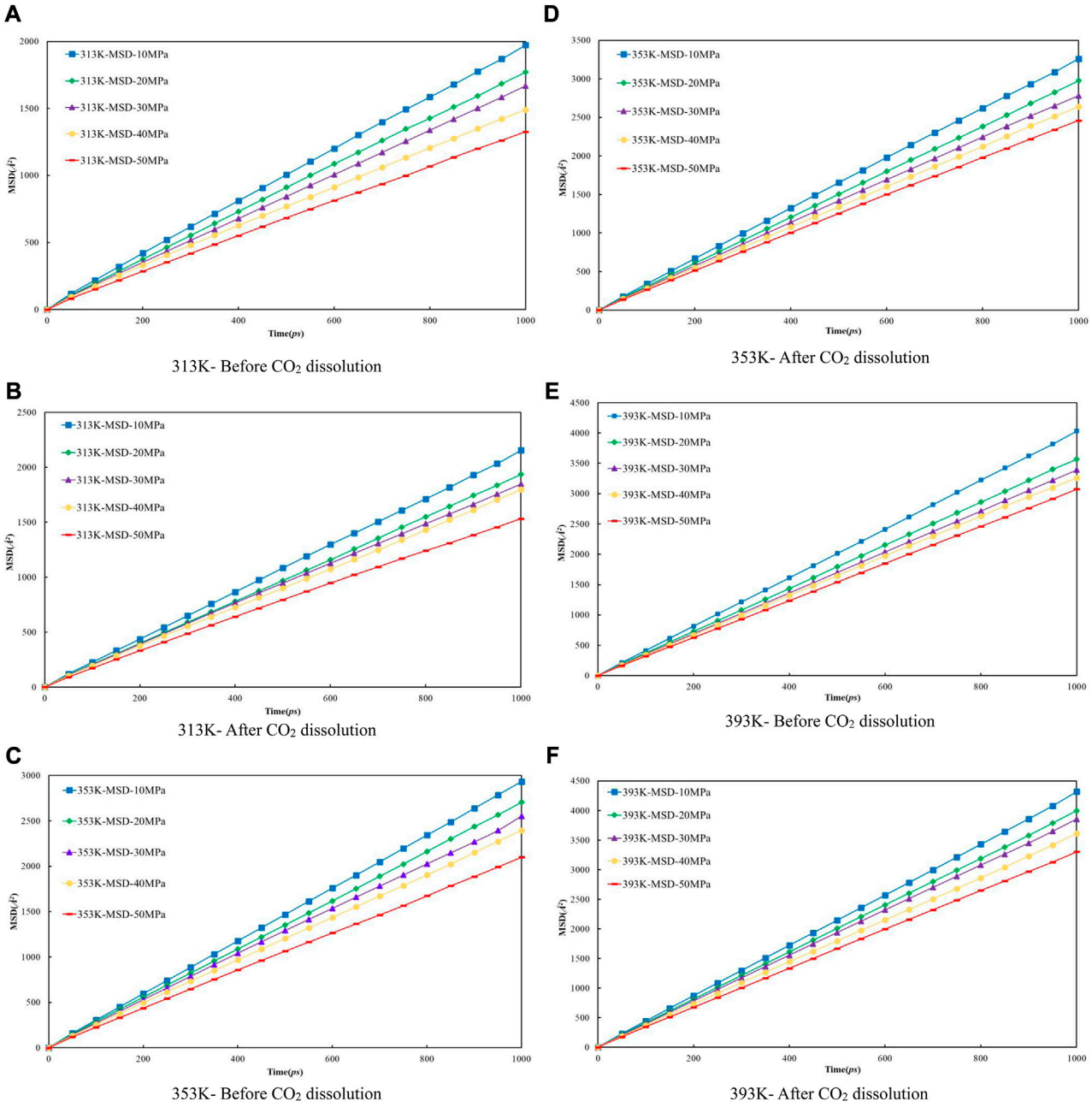

FIGURE 9
The relationship between molecular mean azimuth movement of oil molecular and simulation time under different temperature and pressure conditions. **(A)** 313 K- Before CO_2 dissolution **(B)** 313 K-After CO_2 dissolution **(C)** 353 K-Before CO_2 dissolution **(D)** 353 K-After CO_2 dissolution **(E)** 393 K-Before CO_2 dissolution **(F)** 393 K-After CO_2 dissolution.

5.2 The expansion law of crude oil model

Since the action of the dissolution of CO_2 into crude oil was done, it promotes the expansion of crude oil. However, the change of external temperature and pressure will make the volume of crude oil model show different variation rules. We calculated the volume of the crude oil model after CO_2 dissolution under different reservoir conditions and found that: the pressure increases, the crude oil system model is compressed and becomes smaller. And the increase of temperature causes the crude oil model to expand further and become larger in volume. We calculated the system change rate of crude oil system model under different temperature and pressure conditions, as demonstrated in Tables 2, 3, 4 below:

Figure 7 reveals the trends of the volumes of the crude oil system models before and after dissolving CO_2 under varying thermal and pressure conditions. As the pressure increases, the crude oil system model is compressed and the volume of each model decreases. After dissolving CO_2, the volume change rate of the crude oil model reduces linearly, and the volume change rate of each model is comparable to which in the undissolved CO_2 model and smaller

TABLE 5 Diffusion coefficient of oil before and after dissolving CO_2.

Condition	Pressure	Diffusion coefficient	Condition	Pressure	Diffusion coefficient
	MPa	$\times 10^{-4}$ cm^2·s^{-1}		MPa	$\times 10^{-4}$ cm^2·s^{-1}
313 K-Before CO_2 dissolution	10	0.3255	313 K-After CO_2 dissolution	10	0.3559
	20	0.2931		20	0.3203
	30	0.2751		30	0.3050
	40	0.2451		40	0.2954
	50	0.2202		50	0.2533
353 K-Before CO_2 dissolution	10	0.4864	353 K-After CO_2 dissolution	10	0.5415
	20	0.4475		20	0.4942
	30	0.4182		30	0.4632
	40	0.3947		40	0.4385
	50	0.3462		50	0.4081
393 K-Before CO_2 dissolution	10	0.6696	393 K-After CO_2 dissolution	10	0.7137
	20	0.5939		20	0.6620
	30	0.5633		30	0.6385
	40	0.5431		40	0.5956
	50	0.5101		50	0.5485

than that of the undissolved CO_2 model. The interpretation for this phenomenon is that the potential energy difference value from the inner to outer system becomes smaller after CO_2 enters the space between alkane molecules through dissolution and diffusion. At the critical point of dissolution and diffusion, these systems will be in dynamic equilibrium and the influence of external environment becomes weak.

As the temperature increases, the crude oil system model expands and becomes larger in volume. From the simulation results at 313, 353, and 393 K, the average swelling rate of the crude oil model before dissolving CO_2 molecules is 4.01% per 40 K increase.

The average swelling rate after dissolving CO_2 molecules was 4.82% (Figure 8). The increase in temperature promotes the dissolution and diffusion of CO_2 molecules while also prompting the crude oil model to undergo expansion. It is attributed to the enhancement of temperature results in the rise of molecules kinetic energy, the increase of distance between molecules, the increase of space between alkanes, and the extension of the crude oil model system. The enhancement in CO_2 molecules kinetic energy makes it easier to enter into the gaps between alkane molecules, resulting in the increase in dissolution and diffusion ability. As a result, the dissolved amount of CO_2 also increases.

5.3 The prediction of dissolution-diffusion coefficients

Firstly, the density distribution of alkane molecules was calculated, and the distribution of CO_2 density in the models that we established under various conditions was obtained by simulation to predict the CO_2 dissolving coefficients in the crude oil system and use the coefficients to figure the diffusion coefficient of multi-component crude oil molecules. Figure 9 shows the mean-square displacement (MSD) versus simulation time for the crude oil system model under different pressure conditions. Based on the gradient of the MSD curves, the diffusion coefficients of multicomponent crude oil were calculated as shown in Table 5.

The external pressure has an impact on the volume change rate of the crude oil system model, making it fall off with the pressure increasing, it is due to the decrease of diffusion coefficient before and after the dissolution of CO_2. The diffusion coefficients after dissolving CO_2 are all larger than those before dissolving CO_2, and the diffusion coefficients at all temperature regimes decrease with increasing pressure, among which: the diffusion coefficients for the 313 K regime decrease from 0.3255×10^{-4} cm^2/s at 10 MPa to 0.2202×10^{-4} cm^2/s at 50 MPa and from 0.3559×10^{-4} cm^2/s at 10 MPa to 0.2533×10^{-4} cm^2/s at 50 MPa respectively; the diffusion coefficients of the 353 K system decreased from 0.4864×10^{-4} cm^2/s at 10 MPa to 0.3462×10^{-4} cm^2/s at 50 MPa and from 0.5415×10^{-4} cm^2/s at 10 MPa to 0.4081×10^{-4} cm^2/s at 50 MPa respectively; the diffusion coefficients of the 393 K system decreased from 0.6696×10^{-4} cm^2/s at 10 MPa to 0.5101×10^{-4} cm^2/s at 50 MPa and from 0.7137×10^{-4} cm^2/s at 10 MPa to 0.5485×10^{-4} cm^2/s at 50 MPa respectively.

The molecular kinetic energy and the diffusion coefficient going up while the temperature rises. For example, the diffusion coefficients at 10 MPa pressure increased from 0.3255×10^{-4} cm^2/s at 313 K to 0.6696×10^{-4} cm^2/s at 393 K and from 0.3559×10^{-4} cm^2/s at 313 K to 0.7137×10^{-4} cm^2/s at 393 K

before and after dissolving CO_2, respectively. From these data and analysis in Figure 9, it is able to be indicated that the coefficients of diffusion of the crude oil system after dissolving CO_2 is generally larger than that before dissolution. This is because the dissolved CO_2 occupies the voids of alkane molecules, thus reducing the interaction forces between alkane molecules.

5.4 The influence mechanism of crude oil flow law

The diffusion coefficient of multi-component crude oil before and after dissolving CO_2 is calculated, and the variation of crude oil viscosity can be further calculated according to Eq. 7. The coefficient of diffusion is inversely proportional to the viscosity. The increase of temperature and the dissolution of CO_2 can reduce the viscosity of crude oil and improve the fluidity of crude oil, but the effect of temperature is stronger. Moreover, the increase of temperature accelerates the diffusion of CO_2 molecules into the matrix, which is conducive to the adsorption of CO_2 on the wall and the displacement of crude oil (Lashgari et al., 2019; Chen et al., 2011).

The increase of pressure will increase the intermolecular force of crude oil, inhibit the diffusion, and slightly enhance the crude oil viscosity. However, the enhancement of pressure will promote the dissolution of CO_2, and minish the crude oil viscosity to a certain extent. In general, the increase of pressure will have a weak viscosity reduction effect. Although the increase of pressure will inhibit the diffusion of CO_2 in the crude oil, more CO_2 will enter the reservoir to achieve reservoir acidizing to solve plugging, and also improve permeability and flow capacity (Jia et al., 2021; Gao et al., 2023).

6 Conclusion

In this paper, we established a multi-component model close to the real formation crude oil and employed molecular dynamics simulations to investigate the dissolution and diffusion process of CO_2 in the crude oil systems, and its influence on the mobility of crude oil was examined. By establishing a multi-component crude oil model consistent with the results of experiments, the dissolution-diffusion procedure of CO_2 in multi-component crude oil at 313 K, 353 K, 393 K and 10–50 MPa, in units of 10 MPa were simulated. Our aims were to quantitatively characterize the density distribution of CO_2 dissolved in crude oil, reveal the mechanism of crude oil expansion and improvement of the crude oil mobility due to CO_2 dissolution and diffusion, and systematically analyze the effects of temperature and pressure on the dissolution and diffusion of CO_2. In addition, the research ideas in this manuscript are also applicable to the molecular dynamics simulations of other fluid models. We expect that our study will provide some insights into the mechanism of CO_2-EOR and provide some ideas for molecular dynamics simulations. The following conclusions were obtained:

1) By simulating the reservoir status including temperature and pressure, the dissolving process of CO_2 in multi-component crude oil was observed as well as the density distribution of CO_2 was analyzed; with the change of temperature or pressure, the movement of CO_2 was intensified and driven into the interstices of alkane molecules.
2) The variation of crude oil volume since dissolving CO_2 and the mechanism of varying temperature and pressure on the expansion of crude oil were analyzed. It is concluded that both temperature and pressure promote the action of CO_2 dissolving in petroleum, as well as the crude volume expansion along with temperature enhancing, while compression occurs while the pressure increasing.
3) The coefficient of crude oil diffusion before and after CO_2 dissolution is predicted. The variation trend of diffusing coefficient before and in the back of CO_2 dissolving in crude oil is analyzed, and the impact mechanism of temperature and pressure on diffusing coefficient is clarified.
4) The effects of temperature, pressure as well as CO_2 dissolving on the fluidity of crude oil are studied by combining the variation of diffusion coefficient and SE equation. The increase of temperature and the dissolution of CO_2 can lower the crude oil viscosity and improve the fluid ability of crude oil, but the influence of temperature is stronger. The increase of pressure will have a weak viscosity reduction effect.

Data availability statement

The original contributions presented in the study are included in the article/Supplementary Material, further inquiries can be directed to the corresponding author.

Author contributions

YG: Conceptualization; DW and KL: Investigation; JL: Methodology; LZ: Software; SC: Validation; YK: Writing—original draft; SG: Writing—review and editing. All authors contributed to the article and approved the submitted version.

Acknowledgments

Thanks to all the co-authors for their support and help during the study.

Conflict of interest

Authors YK and LZ were employed by Research Institute of Yanchang Petroleum (Group) Co., Ltd.

The remaining authors declare that the research was conducted in the absence of any commercial or financial relationships that could be construed as a potential conflict of interest.

Publisher's note

References

Ao, W. J., Zhao, R. B., Li, H., Zheng, J. D., Kong, L. P., and Zuo, Q. Q. (2019). Solution-diffusion law of CO2 in crude oil and brine. *Complex Hydrocarb. Reserv.* 12 (3), 51–54. doi:10.16181/j.cnki.fzyqc.2019.03.010

Chen, Y. F., Liao, X. W., Zhao, H. J., and Zhao, X. L. (2010). Determination two key dissolution coefficients in calculation of CO2 storage capacity. *Sci. Technol. Rev.* 28 (01), 98–101. doi:10.1360/972009-1380

Chen, Z. H., Yu, K., and Liu, W. (2011). A preliminary study on the injection-production characteristics and development effects of CO2 miscible flooding: Take the Subei Caoshe oil field as an example. *Eval. Dev. Oil Gas Reserv.* 34 (1), 37–41. doi:10.3969/j.issn.2095-1426.2011.01.007

Fu, G., Du, C. G., Meng, Q. F., and Zhang, G. F. (2003). Diffusion characteristic and loss amount of carbon dioxide gas in FS9 well. *J. Daqing petroleum Inst.* 27 (4), 1–4. doi:10.3969/j.issn.2095-4107.2003.04.001

Gao, H., Wang, C., Cheng, Z. L., Li, T., Dou, L., Zhao, K., et al. (2023). Effect of pressure pulse stimulation on imbibition displacement within a tight sandstone reservoir with local variations in porosity. *Geoenergy Sci. Eng.* 226, 211811. doi:10.1016/j.geoen.2023.211811

Gao, Y. C., Zhao, M. F., Wang, J. B., and Zong, C. (2014). Performance and gas breakthrough during CO2 immiscible flooding in ultra-low permeability reservoirs. *Petroleum Explor. Dev.* 41 (1), 88–95. doi:10.1016/s1876-3804(14)60010-0

Grogan, A. T., and Pinczewski, W. V. (1984). The role of molecular diffusion processes in tertiary CO2 flooding. *Soc. Pet. Eng. AIME, Pap. (United States)* 39 (5), 591–602. doi:10.2118/12706-pa

Guo, M. L., Huang, C. X., Dong, X. G., Zou, Y., and Tang, R. J., (2018). CO2 EOR mechanism of tight sandstone reservoir in Yanchang oilfield. *Chem. Eng. Oil Gas* 47 (2), 75–79. doi:10.3969/j.issn.1007-3426.2018.02.014

Hu, W., Lu, C. Y., Wang, R., Yang, Y., and Wang, X. (2017). Mechanism of CO2 immiscible flooding and distribution of remaining oil in water drive oil reservoir. *Editor. Dep. Petroleum Geol. Recovery Effic.* 24 (5), 99–105. doi:10.13673/j.cnki.cn37-1359/te.2017.05.015

Jia, C. Q., Huang, Z. Q., Sepehrnoori, K., and Yao, J. (2021a). Modification of two-scale continuum model and numerical studies for carbonate matrix acidizing. *J. Petroleum Sci. Eng.* 197, 107972. doi:10.1016/j.petrol.2020.107972

Jia, C. Q., Ren, B., Sepehrnoori, K., Delshad, M., Liu, B., Sun, H., et al. (2023). Numerical studies of hydrogen buoyant flow in storage aquifers. *Fuel* 349, 128755. doi:10.1016/j.fuel.2023.128755

Jia, C. Q., Sepehrnoori, K., Huang, Z. Q., and Yao, J. (2021b). Modeling and analysis of carbonate matrix acidizing using a new two-scale continuum model. *SPE J.* 26 (05), 2570–2599. doi:10.2118/205012-pa

Jia, K. F., Ji, D. C., and Gao, J. D. (2019). The existing state of enhanced oil recovery by CO 2 flooding in low permeability reservoirs. *Unconv. Oil Gas* 6 (1), 107–114.

Jin, Y., and Chen, K. P. (2019). Fundamental equations for primary fluid recovery from porous media. *J. Fluid Mech.* 860, 300–317. doi:10.1017/jfm.2018.874

Jin, Y., Wei, S. M., Chen, K. P., and Xia, Y. (2020). Self-diffusion seepage model. *Acta Pet. Sin.* 41 (6), 737–744.

Ku, H. C., Miao, Y. H., Wang, Y. Z., Chen, X., Zhu, X., Lu, H., et al. (2023). Frontier science and challenges on offshore carbon storage. *Front. Environ. Sci. Eng.* 17 (7), 80. doi:10.1007/s11783-023-1680-6

Lashgari, H. R., Sun, A., Zhang, T. W., Pope, G. A., and Lake, L. W. (2019). Evaluation of carbon dioxide storage and miscible gas EOR in shale oil reservoirs. *Fuel* 241, 1223–1235. doi:10.1016/j.fuel.2018.11.076

Li, C. L. (2018). Gas channeling influencing factors and patterns of CO2-flooding in ultra-low permeability oil reservoir. *Special Oil Gas Reservoirs* 25 (3), 82–86. doi:10.3969/j.issn.1006-6535.2018.03.016

Li, H. Y., Fu, G., and Peng, S. M. (2001). Experimental study on the diffusion coefficients of natural gas. *Petroleum Geol. Exp.* 23 (1), 108–112.

Li, S. L., Tang, Y., and Hou, C. X. (2019). Present situation and development trend of CO2 injection enhanced oil recovery technology. *Reserv. Eval. Dev.* 9 (3), 1–8.

Li, Y., Xiao, K., Huang, C., Wang, J., Gao, M., Hu, A., et al. (2020). Enhanced potassium-ion storage of the 3D carbon superstructure by manipulating the nitrogen-doped species and morphology. *Editor. Dep. Petroleum Geol. Recovery Effic.* 27 (1), 1–10. doi:10.1007/s40820-020-00525-y

Luo, R. H., Hu, Y. L., and Li, B. Z. (2013). Practice of increasing production rate by injecting CO2 into oil and gas fields in China. *Special Oil Gas Reservoirs* 20 (2), 1–7. doi:10.3969/j.issn.1006-6535.2013.02.001

Mi, J. F., and Ma, X. F. (2019). Development trend analysis of carbon capture, utilization and storage technology in China. *Proc. CSEE* 39 (1), 2537–2542. doi:10.13334/j.0258-8013.pcsee.190375

Qin, J. S., Li, Y. L., and Wu, D. B. (2020). CCUS global progress and China's policy suggestions. *Editor. Dep. Petroleum Geol. Recovery Effic.* 27 (1), 20–28. doi:10.13673/j.cnki.cn37-1359/te.2020.01.003

Renner, T. (1988). Measurement and correlation of diffusion coefficients for CO2 and rich-gas applications. *SPE Reserv. Eng.* 3 (2), 517–523. doi:10.2118/15391-pa

Riazi, M. R. (1996). A new method for experimental measurement of diffusion coefficients in reservoir fluids. *J. Petroleum Sci. Eng.* 14 (3/4), 235–250. doi:10.1016/0920-4105(95)00035-6

Shen, P. P., and Liao, X. W. (2009). *The technology of carbon dioxide stored in geological media and enhanced oil recovery*. Beijing: The Press of the Petroleum Industry.

Wang, L. S. (1996). Convective diffusion of driving gases in reservoir fluids(I). *PED* 23 (6), 62–66.

Whorton, L. P., Brownscombe, E. R., and Dyes, A. B. (1952). *Method for producing oil by means of carbon dioxide*. Washington, U.S. Patent No. 2,623,596.

Yuan, S. Y., Wang, Q., Li, J. S., and Han, H. S. (2020). Technology progress and prospects of enhanced oil recovery by gas injection. *Acta Pet. Sin.* 41 (12), 1623. doi:10.7623/syxb202012014

Zhang, Y. J., Zou, Y., Zhang, Y., Wang, L., Liu, D., Sun, J., et al. (2022). Experimental study on characteristics and mechanisms of matrix pressure transmission near the fracture surface during post-fracturing shut-in in tight oil reservoirs. *J. Petroleum Sci. Eng.* 219, 111133. doi:10.1016/j.petrol.2022.111133

Zhang, Y. P., Hyndman, C. L., and Maini, B. B. (2000). Measurement of gas diffusivity in heavy oils. *J. Petroleum Sci. Eng.* 25 (1/2), 37–47. doi:10.1016/s0920-4105(99)00031-5

Zhao, R. B., Ao, W. J., Xiao, A. G., Yan, W., Yu, Z. H., and Xia, X. T. (2016a). Diffusion law and measurement of variable diffusion coefficient of CO2 in oil. *J. China Univ. Petroleum (Ed. Nat. Sci.* 40 (3), 136–142. doi:10.3969/j.issn.1673-5005.2016.03.018

Zhao, S. X., Wang, R., Lv, C. Y., Lun, Z. M., and Zhou, Y. (2016b). Influences of the dissolution on the relative permeability for CO2 flooded low-permeability oil reservoirs. *Petroleum Geol. oilfield Dev. Daqing* 35 (03), 126–129. doi:10.3969/J.ISSN.1000-3754.2016.03.024

Zhao, X. S., Shi, L. H., Wang, W. B., Bai, Y., and Tian, F., (2017). CO2 channeling sealing in ultra-low-permeability reservoirs. *J. Southwest Petroleum Univ. Sci. Technol. Ed.* 39 (6), 131–139. doi:10.11885/j.issn.1674-5086.2016.05.01.61

frontiers | Frontiers in Earth Science

TYPE Mini Review
PUBLISHED 29 August 2023
DOI 10.3389/feart.2023.1268103

OPEN ACCESS

EDITED BY
Shiming Wei,
China University of Petroleum, Beijing, China

REVIEWED BY
Zhipeng Wang,
China University of Petroleum, Beijing, China
Yan Zhang,
China National Petroleum Corporation, China

*CORRESPONDENCE
Zhiquan Zhang,
79957026@qq.com
Yuhui Zhou,
zhou.yuhui@qq.com

RECEIVED 27 July 2023
ACCEPTED 14 August 2023
PUBLISHED 29 August 2023

CITATION
Xu Y, Zhang Z and Zhou Y (2023), A brief review of steam flooding and its applications in fractured oil shale reservoirs.
Front. Earth Sci. 11:1268103.
doi: 10.3389/feart.2023.1268103

A brief review of steam flooding and its applications in fractured oil shale reservoirs

Yunfeng Xu, Zhiquan Zhang* and Yuhui Zhou*

School of Petroleum Engineering, Yangtze University, Wuhan, China

Steam flooding is an important thermal recovery method for heavy oil reservoirs, and convective heating technology is used to fracture oil shale reservoirs with good results. This paper reviews the main prediction methods, optimization approaches for steam flooding performance, and its application in fractured oil shale reservoirs. The prediction methods include experimental, numerical simulation, and statistical models. These provide insights into steam override, heat transfer, and production dynamics. To optimize steam flooding, parameters like quality, temperature, injection rate, and allocation need to be coordinated based on reservoir conditions and monitoring data. Real-time injection control, economic analysis, and sweep efficiency improvements should also be considered in optimization workflows. Although progress has been made, more field studies are needed to establish systematic optimization practices utilizing advanced technologies. This review summarizes the key developments in steam flooding modeling and optimization, providing a reference for further research and field applications.

KEYWORDS

fractured oil shale reservoirs, steam flooding, production prediction, schedule optimization, thermal recovery

1 Introduction

Steam flooding is an important thermal recovery technique that uses heat to mobilize and produce heavy and viscous crude oil. It helps reduce oil viscosity through various mechanisms and improves recovery from depleted or marginal reservoirs. This paper reviews key developments in modeling and optimizing steam flooding performance for conventional heavy oil as well as applications in fractured reservoirs like oil shale. Prediction methods provide insights into complex heat and fluid flow dynamics during steam flooding. Various technical parameters need to be optimized based on reservoir conditions to improve project economics. Convective heating technologies have been applied in fractured reservoirs including oil shale with good results. Further studies on systematic optimization workflows are still needed to maximize the potential of steam flooding (Rao et al., 2022; Xu et al., 2022). This review summarizes progress in this area to provide a reference for future research and field applications.

2 Steam flooding reservoir prediction methods

The main methods for dynamic prediction of steam flooding development are mine-site experimental method (Zhao, 2020), numerical simulation method (Falta et al., 1992;

Mozaffari et al., 2013), and statistical model method (Shafiei et al., 2013). The mine-site experimental method mainly summarizes the steam overriding phenomena in the block based on the production situation of the block, combined with geological characteristics, and analyzes some rules of steam overriding (Sander et al., 1991). Lauwerier (1955) was the first scholar to start the theoretical research on steam flooding and make some progress. Through his studies on reservoir heat transfer problems such as injecting steam and other hot fluids, he obtained the laws of reservoir heat transfer in the reservoir and near the injection wells. Langeheim and Marx proposed a classic mathematical model for steam injection and thermal oil recovery by viscosity reduction. This became the theoretical basis for subsequent scholars to study thermal oil recovery by steam. Through Langeheim and Marx's theory, the speed of heat penetration, cumulative heated area, and the economic limit of injecting heat into an ideal reservoir at a constant temperature rate can be roughly estimated (Marx and Langenheim, 1959).

Ramey (1959) further expanded the above steam flooding theoretical model in 1959. Ramey changed the original fixed steam injection rate to variable steam injection rate, which was Ramey's major contribution to steam flooding theory. Willman et al. (1961) derived an equation that can roughly estimate the heating radius under a fixed steam injection rate. This method was used to predict the required steam injection rate for a fixed steam volumetric flow rate in radial flow reservoirs.

The research results of the above scholars assume that the temperature distribution in the reservoir is step-wise, dividing the fluid flow regions in the steam flooding process into hot and cold zones. This theoretical assumption was broken by Mandl-Volek (1969)'s innovation on physical models in 1969. The model incorporates heat exchange at the steam front in the steam flooded reservoir, and introduces the concept of "critical time" into the model. Based on Mandl-Volek's theory, Myhill-Stegemeier (1978) proposed a set of steam front displacement theories through in-depth research. The premise of this method assumes that the oil displacement is equal to the crude oil production. If the calculation is based on this assumption, the results will be biased high.

Through sensitivity analysis of various parameters on the Kern River block, Gomma (1980) established a new steam flooding model. His analysis revealed the relationship between key parameters such as formation thickness, net to gross ratio, and initial oil saturation for this type of steam flooded reservoir. The calculation formula can be used to obtain reservoirs with similar fluid properties or physical similarities to the Kern River block. However, this method is only applicable to reservoirs similar to the Kern River block.

Based on the theoretical foundations of the above models, Jones (1981) proposed a mathematical model for one-dimensional steam flooding. The Jones model combines 3 empirical coefficients from actual field production to predict steam flooding production dynamics. However, the empirical coefficients of this model can only be applied to reservoirs with similar properties to the Kern River field. To apply it to other oilfields, the empirical coefficients must be history matched against actual field data to obtain accurate coefficients.

Considering steam override, Farouq Ali (1982) proposed a steam flooding model based on the Van Lookeren model theory. The most obvious advantage is the use of the principles of conservation of mass and energy. It considers heat loss without relying on empirical data. However, the shortcoming is that some parameters of this model are difficult to obtain, and temperature has a significant impact on relative permeability. Therefore, the experimental results hardly reflect the real situation. To facilitate screening and evaluating reservoirs for suitability of applying steam flooding for improved oil recovery, Aydelotte and Pope (1983)

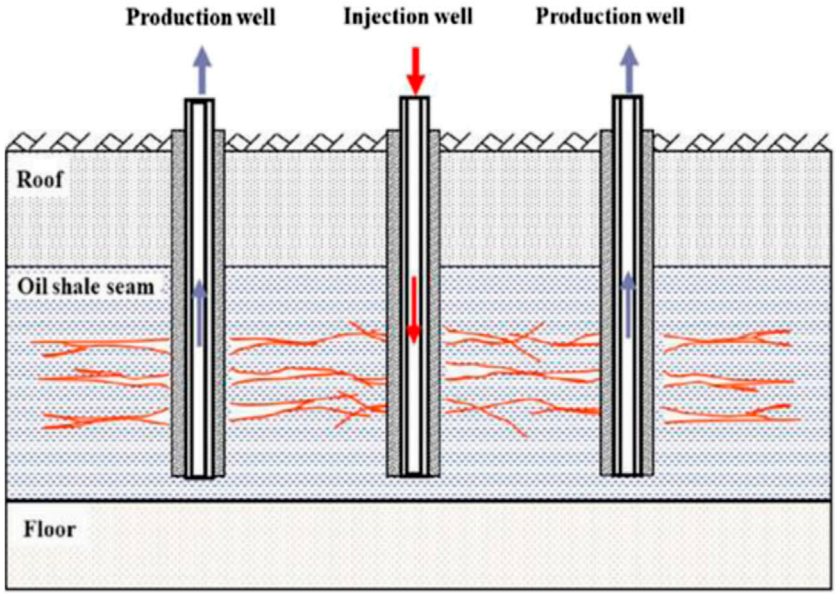

FIGURE 1
Schematic of oil shale in-situ retorting technology by superheated steam injection (MTI) (Kang et al., 2020).

constructed a simplified predictive model for steam flooding. This model expanded the Van Lookeren model and designed a more general computer program.

Neuman C.H. (Neuman, 1975; Newman, 1975; Neuman, 1985) proposed a new model. This model assumes that the steam zone grows vertically and considers steam override. Miller-Leung (Miller and Leung, 1985) divided the reservoir into three zones - the steam zone, condensation zone and cold oil zone, and established a predictive steam flooding model considering steam override. The model established by Torabzadeh-Kumar (Torabzadeh et al., 1990) has standardized the historical dynamics of the same or similar oilfields. However, the relationship between normalized recovery factor and injected steam was fitted using polynomials. Kohei Miura and Jin Wang (Miura and Wang, 2012) proposed a simplified analytical model for predicting cumulative steam-oil ratio during steam assisted gravity drainage process (Figure 1).

3 Steam flooding production optimization

With the advancement of steam flooding technologies for heavy oil recovery, optimizing steam flooding performance has received increasing attention in both academic research and field applications (Alvarez and Han, 2013; Dong et al., 2019). The key objectives of steam flooding optimization are to maximize heat efficiency, improve sweep efficiency, delay steam breakthrough time, and enhance oil production in an economic manner (Kirmani et al., 2021). This requires optimizing multiple technical parameters throughout the entire process from pilot design to late field development (Huang et al., 2018). Recent studies have proposed various approaches to optimize steam injection parameters based on reservoir conditions (Shin and Polikar, 2007). Dong et al. (2019) optimized quality and temperature of high pressure steam injection for a deep reservoir and achieved higher oil rates than normal pressure. Sun et al. (2017) optimized injection rate to balance heat efficiency and oil production.

With the help of monitoring technologies like distributed temperature sensing (DTS), real-time injection control and optimization has become viable. Patel et al. (2018) designed a closed-loop approach to continuously optimize steam rate based on DTS data and simulator predictions. Teletzke et al. (2010) adjusted injector-producer spacing based on monitoring to mitigate steam override issues. These practices have proven effective in increasing sweep efficiency and reducing steam loss.

To address reservoir heterogeneity, steam allocation optimization has been applied. Yan et al. (2018) optimized zone-based steam allocation with a multi-objective genetic algorithm and improved Net Present Value. Such optimization helps utilize steam energy more efficiently. Economic analysis should be incorporated in steam flooding optimization. Kannah et al. (2021) performed economic evaluation on various steam operational strategies. The optimal strategy balances oil rate, heat efficiency and project life to maximize profitability. Economic optimization helps justify optimization practices and improve overall field development value.

Steam quality is the mass fraction of the vapor to the liquid phase (Guo et al., 2022). It represents a dimensionless number between 0 and 1 indicating the amount of water converted to steam. Steam quality affects displacement efficiency as well as viscosity reduction and other mechanisms, which helps determine optimal flooding conditions (Srochviksit and Maneeintr, 2016). Compared to high injection rates, lower injection rates but higher steam quality can increase recovery to a greater extent (Al Shaibi and Al Abri, 2018). Steam optimization utilizes proper steam allocation to increase oil production in a cost-effective monitoring program, while maintenance, variation in steam quality and restricted steam distribution have negatively impacted steam flooding (Castrup, 2019). Based on these studies, a proper and optimized steam injection scheme can be recommended that activates recovery mechanisms by adjusting steam quality and temperature. This research helps select injection schemes that consider the challenges of steam flooding and maximize total field production from heavy oil reservoirs under economic conditions.

In summary, optimizing steam flooding requires coordinating multiple technical parameters over the entire project life based on continuous monitoring and updated reservoir data. More field studies are still needed to establish robust and systematic optimization workflows with the aid of advanced technologies.

4 Application of steam flooding in fractured oil shale reservoirs

An important technique for developing oil shale reservoirs is convective heating technology, which uses high-temperature fluids to heat the oil shale *in situ*. Several heating and production wells are first drilled in the oil shale formation, and hydraulic fracturing is used to interconnect the heating and production wells (Wei et al., 2021a; Wei et al., 2021b; Shiming et al., 1305). Then the positions of the production and heating wells are alternated periodically. High-temperature fluids are injected into the oil shale layer through the heating wells, heating up the oil shale formation and thermally cracking kerogen to generate oil and gas. The produced oil and gas are carried out to the surface by the cooler fluids or condensed water through the production wells. The cracking and release of pyrolysis gases from the oil shale generates numerous microfractures, which helps improve the matrix permeability of the oil shale and enhance flow channels (Fan et al., 2010). Compared to electrical heating for in-situ development, the in-situ development of oil shale using fluid heating is more complex, requiring consideration of more factors in numerical simulation. These factors include heat transfer, temperature field, pressure field, fluid flow, and the influence of fractures.

Kang et al. (2008) studied in-situ development techniques for oil shale using steam injection heating, and performed coupled analysis of the fluid flow, temperature, and chemical fields. Li (2017) carried out numerical simulation studies on the temperature field, kerogen concentration, and oil production during steam injection in-situ development of oil shale. Based on hydraulic fracturing to connect the injection and production wells in oil shale formations, Wang (2011) performed simulation analysis of steam injection heating techniques for oil shale. The effects of fracture position on oil shale heating were discussed, but only two-dimensional reservoirs were simulated.

Xue (2007) discovered through numerical simulation that using high temperature and high pressure steam can effectively pyrolyze

oil shale and carry away the generated shale oil. High temperature and high-pressure steam can also significantly increase the number of fractures inside the oil shale, improving its permeability. Jiang et al. (2015) performed numerical simulation studies on nitrogen gas injection from production wells for heating and heat transfer. Based on extending the functions of open-source fluid simulation software from Los Alamos National Laboratory in the US, Kelkar (Kelkar et al.) carried out numerical simulation studies of coupled thermal-hydrological-mechanical-chemical processes during in-situ conversion and production, and provided some simple simulation examples. Zhao (2013) performed coupled thermal-flow-solid simulations of the interaction processes between oil and gas components during underground co-gasification of oil shale and coal, obtaining the evolution laws of underground temperature fields and coupling characteristics in the co-gasification process. Li (2017) used CMG numerical simulation software to simulate oil shale pyrolysis experiments, designed the model as a dual-porosity geological model. The kerogen decomposition chemical reactions used an alternative reaction mechanism, simplifying the decomposition process into three chemical reaction equations. Based on IFCD technology, Liu (2019) combined experimental research with numerical simulation to summarize the physical property evolution laws of oil shale during heating. The temperature, stress and strain field variations in the oil shale layer during in-situ development were also analyzed.

5 Results

This review summarizes key developments in modeling and optimizing steam flooding performance. Prediction models provide insights into complex dynamics like steam override and heat efficiency. Optimizing parameters such as quality, temperature, injection rate and allocation can improve performance based on reservoir conditions. Real-time injection control and dynamic optimization enabled by monitoring technologies have been implemented. Economic analysis is vital for justifying optimization practices. Convective heating shows potential in fractured reservoirs like oil shale, by thermally cracking kerogen and enhancing permeability. Further studies are needed to develop systematic optimization workflows using advanced technologies. This review of modeling and optimization advances provides a valuable reference for steam flooding research and applications.

Author contributions

YX: Writing–original draft, Writing–review and editing. ZZ: Conceptualization, Visualization, Writing–review and editing. YZ: Project administration, Supervision, Validation, Writing–original draft, Writing–review and editing.

Funding

The author(s) declare financial support was received for the research, authorship, and/or publication of this article. This study was supported by the Natural Science Foundation of Xinjiang Uygur Autonomous Region (No. 2022D01A330) the National Natural Science Foundation of China (No. 52274030) and “Tianchi Talent” Introduction Plan of Xinjiang Uygur Autonomous Region (2022).

Acknowledgments

The authors thank the support from Yangtze University.

Conflict of interest

The authors declare that the research was conducted in the absence of any commercial or financial relationships that could be construed as a potential conflict of interest.

Publisher’s note

References

Al Shaibi, R., and Al Abri, A. “Steam optimization topic, injection rate reduction vs. Surface steam quality reduction,” in Proceedings of the SPE EOR Conference at Oil and Gas West Asia, Muscat, Oman, March 2018.

Ali, S. “Steam injection theories-A unified approach,” in Proceedings of the SPE California Regional Meeting, San Francisco, California, March 1982.

Alvarez, J., and Han, S. (2013). Current overview of cyclic steam injection process. *J. Petroleum Sci. Res.* 2. https://www.academia.edu/26208229/Current_Overview_of_Cyclic_Steam_Injection_Process.

Aydelotte, S. R., and Pope, G. A. (1983). A simplified predictive model for steamdrive performance. *J. Petroleum Technol.* 35, 991–1002. doi:10.2118/10748-pa

Castrup, S. “Data analytics for steam injection projects,” in Proceedings of the SPE Western Regional Meeting, San Jose, California, USA, April 2019, D031S011R002.

Dong, X., Liu, H., Chen, Z., Wu, K., Lu, N., and Zhang, Q. (2019). Enhanced oil recovery techniques for heavy oil and oilsands reservoirs after steam injection. *Appl. energy* 239, 1190–1211. doi:10.1016/j.apenergy.2019.01.244

Falta, R. W., Pruess, K., Javandel, I., and Witherspoon, P. A. (1992). Numerical modeling of steam injection for the removal of nonaqueous phase liquids from the subsurface: 1. Numerical formulation. *Water Resour. Res.* 28, 433–449. doi:10.1029/91wr02526

Fan, Y., Durlofsky, L. J., and Tchelepi, H. A. (2010). Numerical simulation of the *in-situ* upgrading of oil shale. *SPE J.* 15, 368–381. doi:10.2118/118958-pa

Gomaa, E. E. (1980). Correlations for predicting oil recovery by steamflood. *J. Petroleum Technol.* 32, 325–332. doi:10.2118/6169-pa

Guo, X., Wang, Y., Zhang, J., Ci, F., Ding, G., and Chen, Y. (2022). Online fully-automatic high precision steam dryness monitoring system. *Measurement* 190, 110642. doi:10.1016/j.measurement.2021.110642

Huang, S., Chen, X., Liu, H., Jiang, J., Cao, M., and Xia, Y. (2018). Experimental and numerical study of solvent optimization during horizontal-well solvent-enhanced steam flooding in thin heavy-oil reservoirs. *Fuel* 228, 379–389. doi:10.1016/j.fuel.2018.05.001

Jiang, P., Sun, Y., Guo, W., and Li, Q. (2015). Heating technology and heat transfer simulation for oil shale of in-situ pyrolysis by fracturing and nitrogen injection. *J. Northeast. Univ. Nat. Sci.* 36, 1353. doi:10.3969/j.issn.1005-3026.2015.09.029

Jones, J. (1981). Steam drive model for hand-held programmable calculators. *J. Petroleum Technol.* 33, 1583–1598. doi:10.2118/8882-pa

Kang, Z., Zhao, Y., and Yang, D. (2008). Physical principle and numerical analysis of oil shale development using *in-situ* conversion process technology. *Acta Pet. Sin.* 29, 592–595. doi:10.7623/syxb200804022

Kang, Z., Zhao, Y., Yang, D., Tian, L., and Li, X. (2020). A pilot investigation of pyrolysis from oil and gas extraction from oil shale by *in-situ* superheated steam injection. *J. Petroleum Sci. Eng.* 186, 106785. doi:10.1016/j.petrol.2019.106785

Kannah, R. Y., Kavitha, S., Karthikeyan, O. P., Kumar, G., Dai-Viet, N. V., Banu, J. R., et al. (2021). Techno-economic assessment of various hydrogen production methods–A review. *Bioresour. Technol.* 319, 124175. doi:10.1016/j.biortech.2020.124175

Kelkar, S., Pawar, R., and Hoda, N. *Numerical simulation of coupled thermal-hydrological-mechanical-chemical processes during* in situ *conversion and production of oil shale*, 1–8.

Kirmani, F. U. D., Raza, A., Gholami, R., Haidar, M. Z., and Fareed, C. S. (2021). Analyzing the effect of steam quality and injection temperature on the performance of steam flooding. *Energy Geosci.* 2, 83–86. doi:10.1016/j.engeos.2020.11.002

Lauwerier, H. A. (1955). The transport of heat in an oil layer caused by the injection of hot fluid. *Appl. Sci. Res. Sect. A* 5, 145–150. doi:10.1007/bf03184614

Li, Z. (2017). *Numerical simulation study on in-situ steam injection development of oil shale*.

Liu, Z. (2019). *Numerical simulation study of coupled processes in in-situ development of oil shale*.

Mandl, G., and Volek, C. (1969). Heat and mass transport in steam-drive processes. *Soc. Petroleum Eng. J.* 9, 59–79. doi:10.2118/2049-pa

Marx, J., and Langenheim, R. (1959). Reservoir heating by hot fluid injection. *Trans. AIME* 216, 312–315. doi:10.2118/1266-g

Miller, M., and Leung, W. "A simple gravity override model of steamdrive," in Proceedings of the SPE Annual Technical Conference and Exhibition, Las Vegas, Nevada, United States, September 1985.

Miura, K., and Wang, J. (2012). An analytical model to predict cumulative steam/oil ratio (CSOR) in thermal-recovery SAGD process. *J. Can. Petroleum Technol.* 51, 268–275. doi:10.2118/137604-pa

Mozaffari, S., Nikookar, M., Ehsani, M. R., Sahranavard, L., Roayaie, E., and Mohammadi, A. H. (2013). Numerical modeling of steam injection in heavy oil reservoirs. *Fuel* 112, 185–192. doi:10.1016/j.fuel.2013.04.084

Myhill, N., and Stegemeier, G. (1978). Steam-Drive correlation and prediction. *JPT* 30 (2), 173–182. doi:10.2118/5572-PA

Neuman, C. (1985). A gravity override model of steamdrive. *J. petroleum Technol.* 37, 163–169. doi:10.2118/13348-pa

Neuman, C. "A mathematical model of the steam drive process applications," in Proceedings of the SPE California Regional Meeting, Ventura, California, April 1975.

Newman, C. "A mathematical model of the steam drive process-derivation," in Proceedings of the SPE California Regional Meeting, Ventura, California, April 1975.

Patel, R., Guevara, J. L., and Trivedi, J. "Closed-loop reservoir management using nonlinear model predictive control: A field case study," in Proceedings of the European Association of Geoscientists & Engineers, Barcelona, Spain, September 2018, 1–25.

Ramey, H., Jr (1959). Discussion on the paper by Marx and Langenheim. *Trans. AIME* 21, 364.

Rao, X., Xin, L., He, Y., Fang, X., Gong, R., Wang, F., et al. (2022). Numerical simulation of two-phase heat and mass transfer in fractured reservoirs based on projection-based embedded discrete fracture model (pEDFM). *J. Petroleum Sci. Eng.* 208, 109323. doi:10.1016/j.petrol.2021.109323

Sander, P. R., Clark, G. J., and Lau, E. C. "Steam-foam diversion process developed to overcome steam override in Athabasca," in Proceedings of the SPE Annual Technical Conference and Exhibition, October 1991 (Dallas, Texas, United States.

Shafiei, A., Dusseault, M. B., Zendehboudi, S., and Chatzis, I. (2013). A new screening tool for evaluation of steamflooding performance in Naturally Fractured Carbonate Reservoirs. *Fuel* 108, 502–514. doi:10.1016/j.fuel.2013.01.056

Shiming, W., Yan, J., Jiawei, K., Yang, X., and Botao, L., Reservoir stress evolution and fracture optimization of infill wells during the drilling-fracturing-production process. *Acta Pet. Sin.* 43, 1305.

Shin, H., and Polikar, M. (2007). Review of reservoir parameters to optimize SAGD and Fast-SAGD operating conditions. *J. Can. Petroleum Technol.* 46. doi:10.2118/07-01-04

Srochviksit, S., and Maneeintr, K. (2016). Simulation on heavy oil production from steam-flooding. *EDP Sci.* 68, 07002. doi:10.1051/matecconf/20166807002

Sun, F., Yao, Y., Chen, M., Li, X., Zhao, L., Meng, Y., et al. (2017). Performance analysis of superheated steam injection for heavy oil recovery and modeling of wellbore heat efficiency. *Energy* 125, 795–804. doi:10.1016/j.energy.2017.02.114

Teletzke, G. F., Wattenbarger, R. C., and Wilkinson, J. R. (2010). Enhanced oil recovery pilot testing best practices. *SPE Reserv. Eval. Eng.* 13, 143–154. doi:10.2118/118055-pa

Torabzadeh, S. J., Kumar, M., and Hoang, V. T. "Performance correlations for steamflood field projects," in Proceedings of the SPE California Regional Meeting, Ventura, California, April 1990.

Wang, J. (2011). *Numerical simulation of temperature field in in-situ development of oil shale*.

Wei, S., Jin, Y., Liu, X., and Xia, Y. "The optimization of infill well fracturing using an integrated numerical simulation method of fracturing and production processes," in Proceedings of the Abu Dhabi International Petroleum Exhibition & Conference, Abu Dhabi, UAE, November 2021, D012S136R001.

Wei, S., Kao, J., Jin, Y., Shi, C., and Liu, S. (2021a). A discontinuous discrete fracture model for coupled flow and geomechanics based on FEM. *J. Petroleum Sci. Eng.* 204, 108677. doi:10.1016/j.petrol.2021.108677

Willman, B., Valleroy, V., Runberg, G., Cornelius, A., and Powers, L. (1961). Laboratory studies of oil recovery by steam injection. *J. Petroleum Technol.* 13, 681–690. doi:10.2118/1537-g

Xu, Y., Hu, Y., Rao, X., Zhao, H., Zhong, X., Peng, X., et al. (2022). A fractal physics-based data-driven model for water-flooding reservoir (FlowNet-fractal). *J. Petroleum Sci. Eng.* 210, 109960. doi:10.1016/j.petrol.2021.109960

Xue, J. (2007). *Experimental study on physical and mechanical properties of oil shale and unsteady heat conduction mathematical modeling of its in-situ development*.

Yan, Z., Sha, J., Liu, B., Tian, W., and Lu, J. (2018). An ameliorative whale optimization algorithm for multi-objective optimal allocation of water resources in Handan, China. *Water* 10, 87. doi:10.3390/w10010087

Zhao, L. (2013). *Study on coupled processes of in-situ pyrolysis of oil shale and underground gasification of coal*.

Zhao, Y. (2020). Laboratory experiment and field application of high pressure and high quality steam flooding. *J. Petroleum Sci. Eng.* 189, 107016. doi:10.1016/j.petrol.2020.107016

Frontiers in Earth Science

Investigates the processes operating within the major spheres of our planet

Advances our understanding across the earth sciences, providing a theoretical background for better use of our planet's resources and equipping us to face major environmental challenges.

Discover the latest Research Topics

See more →

Frontiers

Avenue du Tribunal-Fédéral 34
1005 Lausanne, Switzerland
frontiersin.org

Contact us

+41 (0)21 510 17 00
frontiersin.org/about/contact